Quantum light source and detector metrology

Rachel Nicole Clark

Supervisors: Professor Anthony J. Bennett, Dr Philip R. Dolan, Dr Ian Farrer.

School of Engineering, College of Physical Sciences and Engineering

This thesis is being submitted in partial fulfilment of the requirements for the degree of Doctor of Philosophy.

20th December 2023

Abstract

Single-photon technology forms the foundation upon which emerging quantum technologies are being developed and experimentally verified. Both the generation and detection of single-photons are crucial to many photonic technologies, most notably quantum communications and computing. If these technologies are to be deployed in the same way that classical computing and telecommunications has in recent decades, scalable fabrication processes must be established. Additionally, our understanding and characterisation techniques to assess the performance of novel devices must continue to develop alongside their increasingly demanding measurement requirements. To implement these devices to the best of their promised potential, new metrological techniques that push the boundaries of experimental uncertainty must be explored.

In this thesis, I will present my work on single-photon source and detector metrology. First, experimental and computational considerations for measuring photon correlation of second- and third-order will be discussed. Then, a numerical model will be presented to demonstrate how real single-photon detectors are incapable of accurately resolving correlation at high incident photon rates. Next, a process for fabricating bright and pure single-photon sources based on quantum dots in semiconductor micropillar structures will be presented, and the single-photon characteristics confirmed with hallmark measurements. Finally, a metrological study of these quantum dot sources closes the quantum radiometry gap by traceably linking the single-photon flux to the SI, and applications for applying this flux to calibrate single-photon detectors is discussed. With this work, new insights into experimental applications of bunched and antibunched light sources for single-photon detector characterisation have been demonstrated.

Acknowledgements

There are so many people to thank for helping me to achieve everything written in this thesis. To begin with, I have to thank the CDT and my Cohort 1 colleagues for being with me since day 1. Terri and Sarah, you are both superstars - thank you for looking after us all. Bogdan, Tristan, Paradeisa, Cobi and Seyed - it was a real pleasure to go through the four years with you guys! To the rest of the CDT, I can't wait to see you all succeed and flourish. To my second supervisor, Dr Ian Farrer - thank you for all the wonderful quantum dots and cavities you have grown for us, and the excellent hosting at UK Semi. To the staff in the Institute for Compound Semiconductors cleanroom - especially Tom, Stu, Angela and Saleem, thank you for sharing your expertise and helping us make some fantastic looking micropillar cavities. A big thanks also has to go to my examiners, Dr Francesco Masia and Prof Robert Hadfield, for a fascinating and enjoyable discussion during my viva examination, and for giving such valuable insight and knowledge to improve and correct my thesis.

During my PhD, the QLab team have been an immense support network for me. Firstly I have to thank Dr Petros Androvitsaneas for teaching me almost everything I know about quantum dots and big scary lasers. Thank you for your patience and all of your help over the years. To the rest of Q Lab, past and present - Dr J. P Hadden, Dr Sherif Ibrahim, Dr Reza Hekmati, Yanzhao, Bilge, Annie, Matthew, Cobi, Davey, Katie, Miguel - it's been so wonderful working alongside all of you and I'm sad to be leaving a great team. A special thank you to Joseph - my day 1 desk buddy - for always being such a brilliant colleague and friend. I am so grateful to have met you and gone on this journey together.

I was incredibly fortunate to spend five months working with the quantum photonics team at the National Physical Laboratory. I owe huge thanks especially to Dr Ted Santana, Luke, Benyam and Adam - your help in the lab, your wisdom in the office and the many pints in the Adelaide were all enormously helpful at various times! Another big thanks has to go to Dr Chris Chunnilall and Simon Hall for facilitating my secondment and collaborations. Finally, for being involved in my project from the beginning, a very heartfelt thanks to both Dr Alastair Sinclair, and my supervisor Dr Philip Dolan. Thanks for never being angry when I misaligned the confocal microscope Phil. The self-confidence and knowledge that I gained from my time working with you at NPL has been transformative for my scientific self-esteem and career, without a doubt. Last but certainly not least, a big thank you to Laura and Rob for taking me in as a lodger and being my placement parents!

The biggest thanks has to go to five people in particular. Firstly, Dr Sam Bishop, for always helping me in lab and being patient, and discussing ideas and problems on our daily commute for the past two years. And of course - LabVIEW! Prof. Anthony Bennett, the leader of Q Lab - I cannot overstate how grateful I am to have worked with you these past three years. Thank you for always believing in me and always being happy to draw a cartoon for me when I'm confused. You are the best. Finally, everyone in my huge family who has supported and believed in me along the way, but especially my parents - Mum, Malc and Dad. Everything I am, I owe to you. I hope to continue making you proud, and I love you very much.

Contents

List of Figures

List of Tables

List of acronyms

List of symbols

Symbol	Parameter	Usage
τ_c	Correlation timescale	Chapters 3,4
τ_{ij}	Time difference between detection channels i,j	Chapters 3,4, 5, 6
$g^{(n)}(\tau_{12}, ..., \tau_{1n})$	n^{th} order correlation function	Chapters 3,4, 5, 6
f	Focal length	Chapters 2, 4, 5,6
T	Integration time	Chapters 2, 3, 6
$\eta(t)$	Time-dependent detection efficiency	Chapter 4
ε	Time-averaged detection efficiency	Chapter 4
T_{dead}	Detector dead time	Chapters 4, 6
$t_{\text{detection}}$	Time of photon detection	Chapter 4
R	Incident photons	Chapter 4
R'	Detected photons	Chapter 4
T_{reset}	Detector reset time	Chapter 4
T_{recovery}	Detector recovery time	Chapter 4
$\Omega(\tau)$	Waiting time distribution	Chapter 4
$\bar{\tau}$	Mean waiting time	Chapter 4
η_{H}	Heaviside detector efficiency function	Chapter 4
η_{real}	Real detector efficiency function	Chapter 4
Ω	Rabi frequency	Chapter 5
Q	Cavity Q-factor	Chapter 5
$\Delta\omega_{\text{cav}}$	Cavity mode width	Chapter 5
Γ	Cavity mode decay rate	Chapter 5
γ	Non-cavity mode decay rate	Chapter 5
β	Spontaneous emission coupling factor	Chapter 5
F_P	Purcell factor	Chapter 5
X^0	Neutral exciton	Chapter 5
T_1	Radiative lifetime	Chapter 5
T_2	Coherence time	Chapter 5
P	Optical power	Chapters 5, 6
V	Voltage	Chapter 6
R	Photodetector responsivity	Chapter 6
G	Amplifier gain	Chapter 6
σ_i	Error on measurand i	Chapter 6
k	Coverage factor	Chapter 6
v_{eff}	Combined degrees of freedom	Chapter 6
P_{det}	Detection probability	Chapter 6
N_{counts}	Detected photon counts	Chapter 6
N_{det}	Detected photon counts minus background	Chapter 6
N_{in}	Incident photon counts	Chapter 6
η	Average detection efficiency	Chapter 6

List of publications

- *Evanescent-field assisted photon collection from quantum emitters under a solid immersion lens.* S. G. Bishop, J. K. Cannon, H. B. Yağcı, **R. N. Clark**, J. P. Hadden, W. Langbein, A. J. Bennett. New Journal of Physics, Vol. 24, Issue 10, 103027. October 2022.

- *Direct-write projection lithography of quantum dot micropillar single photon sources.* P. Androvitsaneas, **R. N. Clark**, M. Jordan, M. A. Perez, T. Peach, S. Thomas, S. Shabbir, A. D. Sobiesierski, A. Trapalis, I. A. Farrer, W. Langbein, A. J. Bennett. Applied Physics Letters, Vol. 123, Issue 9. August 2023.

- *Probing Purcell enhancement and photon collection efficiency of InAs quantum dots at nodes of the cavity electric field.* M. Jordan, P. Androvitsaneas, **R. N. Clark**, A. Trapalis, I. A. Farrer, W. Langbein, A. J. Bennett. Awaiting publication in Physical Review Research.

- *Dynamics of photon emission from quantum emitters in aluminium nitride.* Y. Guo, J. P. Hadden, **R. N. Clark**, S. G. Bishop, A. J. Bennett. Under review.

- *Measuring photon correlation using imperfect detectors.* **R. N. Clark**, S. G. Bishop, J. K. Cannon, J. P. Hadden, P. R. Dolan, A. G. Sinclair, A. J. Bennett. Under review.

List of conference proceedings

- *Towards the quantum candela: a calibrated flux of five million single-photons per second delivered by single-mode fibre.* **R. N. Clark**, P. Androvitsaneas, L. Arabskyj, P. R. Dolan, T. S. Santana, C. J. Chunnilall, A. G. Sinclair, I. A. Farrer, A. J. Bennett. Semiconductor integrated optoelectronics (SIOE) 2023, Cardiff, United Kingdom. Oral presentation.

- *Towards the quantum candela: a calibrated flux of five million single-photons per second delivered by single-mode fibre.* **R. N. Clark**, P. Androvitsaneas, L. Arabskyj, P. R. Dolan, T. S. Santana, C. J. Chunnilall, A. G. Sinclair, I. A. Farrer, A. J. Bennett. SPIE Photonics for Quantum 2023, Rochester, New York. Oral presentation.

- *Towards the quantum candela: a calibrated flux of five million single-photons per second delivered by single-mode fibre.* **R. N. Clark**, P. Androvitsaneas, L. Arabskyj, P. R. Dolan, T. S. Santana, C. J. Chunnilall, A. G. Sinclair, I. A. Farrer, A. J. Bennett. NewRAD 2023, National Physical Laboratory, United Kingdom. Poster presentation.

CHAPTER 1

INTRODUCTION

The new understanding of light and matter afforded to humanity at the turn of the 20$^{\text{th}}$ century rapidly advanced our scientific and technological capabilities. The proposal of discretised energy states for electromagnetic waves by Planck,[1] proportional to their frequency by a constant now named in his honour, was the very beginning of the quantum era. These packets or *quanta* of electromagnetic energy were able to interact with other particles, such as electrons in a solid, as described by Einstein.[2] Soon after, Bohr used Planck's theory to develop a new model of the atom.[3] In this description light behaved as a particle[4] (or *photons*, as coined by Lewis[5]) and carried momentum.[6,7]

In the decades that followed, advances in semiconductor devices,[8] and inventions such as the maser[9] and later the laser,[10] generated enormous progress within computing and telecommunications. Simultaneously, work on the quantum nature of light was being examined thanks to experimental developments such as intensity interferometry[11] and photodetection techniques.[12] In 1963, three influential articles by Glauber[13–15] described the statistics of different light fields in terms of *coherence*, as well as the first report of a particular state of light that is entirely quantum-mechanical in nature, described by well-defined number states of photons. This analysis was developed by Mandel and Wolf[16] in the following decades, while experiments confirmed the existence of sources that can emit one photon at a time with an inherently quantum statistical signature, known as *antibunching*.[17,18] These pioneering works are considered the beginnings of *quantum optics*. Applying this intriguing new form of quantum light to translate existing classical technology, such as computing, cryptography, sensing, to a new quantum paradigm, is an ongoing research effort. The promise of such *quantum technology* marks the next stage of this continuing evolution.

The power of a quantum computer is tied to fundamental features of quantum mechanics such as superposition and entanglement[19,20] by virtue of its quantum

mechanical units of information - qubits. These aspects can be exploited to solve classes of problems that are difficult for classical computers.[21,22] For example, the intractability of the prime factorisation problem for classical computers is the basis for the security of the RSA cryptographic protocol.[23] An algorithm for solving this problem on a quantum computer is able to complete in polynomial time,[24] thus rendering RSA insecure. Fortunately, a potential solution to this issue is also granted by quantum technology - unconditional security in a cryptographic sense is possible with quantum key distribution,[25,26] protocols for which were famously developed by Bennett and Brassard[27] and later, Ekert.[28] Specifically for a qubit based on a photon - the no-cloning theorem[29] forbids secret eavesdropping. The conditions for physically implementable quantum computation were outlined by the DiVincenzo criteria.[30] Knill et al[31] proposed an implementable scheme for quantum computation based solely on linear optics. In this scheme, a single-photon source emitting on-demand, indistinguishable photons, can produce qubits that satisfy the DiVincenzo criteria and precipitate efficient quantum computation. This unforeseen conclusion triggered new experimental endeavours in creating an ideal single-photon source, as well as instruments for measuring them - single-photon detectors. The development of these sources and detectors is encompassed in the general term *single-photon technology*. The rest of this chapter will provide some context of current research efforts in both single-photon sources and detectors, an overview of experimental achievements using both, and the outline of this thesis within these contexts. In the next two subsections, the advancements of devices comprising single-photon sources and detectors in turn will be reviewed, and some criteria for their ideal parameters will be identified.

1.1 Generating single photons

Sources of single photons have been discovered in a wide range of physical systems, each with benefits and disadvantages. In order to present some examples from the literature and draw a comparison, we will introduce a definition and key parameters to describe the "ideal" single-photon source. The general term 'quantum light' may refer to a number of different light states that are only well understood in terms of quantum mechanics, for example squeezed light. For the purposes of this thesis, the term 'quantum light source' or 'emitter' refers to some physical system that emits photons one at a time. The canonical single-photon source is a device that emits antibunched light, described in quantum mechanics by Fock states, on demand. The definition of a single-photon source from Oxborrow and Sinclair[32] is:

> A device for ensuring that one or several spatio-temporal modes will, after the source has acted on them, contain precisely one photon, where the

> spatio-temporal modes in receipt of the photon can be selected by, or are at least known to, the experimenter in advance of the said photon's detection.

From this definition, it is possible to identify desirable characteristics for single-photon sources:

- **On-demand**: A single photon is emitted instantaneously with a trigger from the user.
- **Purity**: Following a single trigger, the probability of emitting a single photon is 100%, and the probability of a multi-photon event is 0%.
- **Brightness**: The user can trigger at an arbitrarily fast repetition rate.
- **Efficiency**: For every trigger, the user collects a single photon in a well-defined spatio-temporal mode.

Depending on the specific end application, other advantageous features may include things such as **indistinguishability**, i.e. how identical the subsequent single photons are to the previous, and **emission wavelength**, for example 1550 nm for applications in telecommunications. Alongside these key features, practicality must also be considered. The ability to easily-integrate the source into large scale experiments and technologies will be limited by factors such as its native substrate material and operational temperature. Single-photon sources based in the solid state are therefore preferential candidates.

The first reports of single-photon emission were based on the measurement of heralded non-classical statistics in atomic transitions.[17,18,38] By the early 2000s, single-photon emission had been reported in several physical systems: single molecules;[39–42] semiconductor QD;[43–46] atoms and ions in cavities;[47–50] the NV centre in diamond[51,52] and other crystal defects.[53,54] At the time of writing, the record for the brightest[36] and purest[58] single-photon source are QDs in microcavity structures.[59] However the current state of the art QDs are typically operated at cryogenic temperatures, and self-assembled growth leads to non-uniform emission spectra, meaning that either extensive searching through samples or tunable devices are required for ideal operation. Room temperature sources of antibunched light have been demonstrated in crystal defects including the diamond NV centre[51] and colour centres in compound semiconductors such as AlN,[60] GaN[61] and SiC.[62] However, they typically suffer from broad spectra at room temperature and low count rates in bulk structures. In the last decade, quantum emitters were also discovered in two-dimensional materials such as tungsten diselenide (WSe_2)[63] and hBN.[34] Monolayers of these materials exhibit room temperature antibunching, and present the possibility of integrated growth or transfer techniques onto bulk substrates. Current research efforts in single-photon sources focus on the engineering of semiconductor nanostructures to enhance spontaneous emission and improve collection efficiency. The

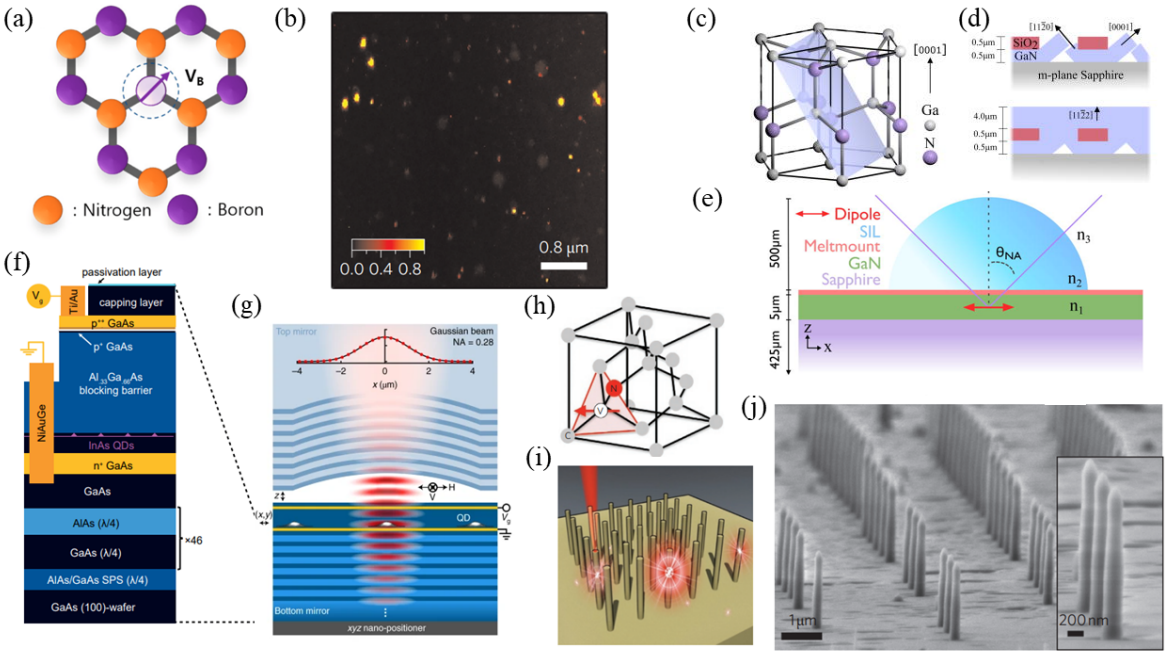

Figure 1.1.1: Single-photon sources in a range of solid state systems. **(a)** The 2D structure of hexagonal boron nitride (hBN) with a boron vacancy, taken from Kim *et al.*;[33] **(b)** a photoluminescence scan map of hBN at room temperature, taken from Tran *et al.*[34] **(c)** The crystal structure and **(d)** growth regime for semi-polar gallium nitride (GaN) which hosts colour centres that emit antibunched light at room temperature. **(e)** A solid immersion lens (SIL) structure used to enhance the collection efficiency of antibunched light from a colour centre in GaN. Figures **(c)**, **(d)** and **(e)** taken from Bishop *et al.*[35] **(f)**: A schematic of the tunable microcavity structure based on III-V semiconductor Bragg mirrors and **(g)**: the tunable microcavity can be adjusted with nano-positioners to guide the resulting Gaussian beam (red, simulated) for enhanced collection efficiency of single photons from a quantum dot (QD), taken from Tomm *et al.*[36] **(h)**: The crystal structure of the nitrogen-vacancy (NV) centre in diamond, and **(i)**: a schematic and **(j)** scanning electron microscope image of diamond nanowires, taken from Babinec *et al.*[37]

SIL is a micro-scale hemisphere of high refractive index material such as ZrO_2 which forms a plano-convex lens.[64] These structures have been shown to enhance the collection efficiency of fluorescence[65] and may be placed deterministically[35,66,67] to selectively enhance emitters in bulk materials. A schematic of a typical SIL structure is shown in Figure 1.1.1(e). Bullseye antennae are resonant cavities formed by concentric circular dielectric layers, with the layer thicknesses and spacing dictated by the Bragg interference condition. These structures can be designed to enhance collection efficiency up to 80%[68] and demonstrate polarisation sensitivity.[69] Experimental demonstrations with these structures have enhanced and guided single-photon emission into the far field for quantum dots,[70–72] colour centres in bulk semiconductors[73,74] and 2D materials.[75] Micropillar cavities based on alternating semiconductor layers that form distributed Bragg reflectors (DBRs) are a popular choice for optical cavities enhancing QD emission.[76] These heterostructures are typically grown via molecular beam epitaxy (MBE),[77] allowing

System	Emission range, nm	Purity	Brightness, cps	Operating temp., K	Notes
Single molecule (DBT:Ac)[55]	780	92%	1.36×10^6	3	Non-resonant CW excitation
NV centre in diamond nanowire[37]	600 to 750	~70%	1.7×10^5	293	Non-resonant CW excitation
Colour centre in aluminium nitride (AlN) with SIL[56]	560 to 770	88%	7.4×10^5	293	Non-resonant CW excitation
Colour centre in silicon carbide (SiC) nanoparticles[57]	600 to 850	70%	7×10^6	293	Non-resonant CW excitation
Electrically tunable QD in cavity[36]	940	~98%	4×10^7	4.2	Pulsed resonant excitation; end-to-end efficiency > 50%
Defect in hBN[34]	600 to 700	61%	4.2×10^6	293	Non-resonant CW excitation

Table 1.1.1: A table summarising the current state-of-the-art in single-photon sources based in the solid state, where the list is non-exhaustive, and reports the highest operational rates and temperatures.

fine control of the layer thicknesses and hence high quality factor cavities,[78] as well as embedded active layers containing QDs. The shape of these structures promotes well-collimated emission into a particular mode, an ideal far-field projection for optimising collection into single-mode fibre.[64] QDs in micropillar structures have demonstrated exceptional collection efficiency and brightnesses.[58,79,80] This specific form of resonator structure will be the subject of Chapter 5, and a thorough mathematical description of cavity-enhanced emission will be presented there. A comparison of the current state-of-the-art sources are summarised in Table 1.1.1, and a range of schematics for some of the listed devices are shown in Figure 1.1.1.

1.2 Detecting single photons

In a similar manner to their generation, the detection of single photons is an active research field that is rapidly advancing. Devices sensitive enough to detect single photons are now commercially available and can be simple to use. These devices may be based on different materials systems and physical mechanisms to generate a readout, but in general, they will provide a 'click' per incident photon as an electrical signal. The different physical systems can lead to a variance in advantages and disadvantages with respect to their

performance metrics. As implied, the key difference between a single-photon detector and a classical photodetector is the need for a noise floor which is orders of magnitude lower in order to detect the much weaker optical power associated with a single-photon flux. The ideal single-photon detector according to Natarajan *et al.*[81] is described by the following:

> An ideal single-photon detector generates an electrical signal only upon absorption of a photon. The signal level is well defined above the noise; in the absence of illumination, no electrical signal is returned.

Accordingly, some of the main parameters used to characterise single-photon detectors include:

- **Detection rate**: The maximum incident photon rate at which the detector can safely and accurately resolve single-photons.
- **Efficiency**: The ratio of detection events to photon arrivals.
- **Dark count rate**: The number of detection events that were not caused by a photon arrival.
- **Jitter**: The uncertainty in photon arrival time.
- **Dead time**: The time following a detection event for which the detector is unable to count incoming photons.
- **Afterpulsing probability**: The probability of a false detection event which is correlated to a previous true detection event.

Outside of these features, things such as operational temperature, wavelength range, system complexity and cost play a role in the overall suitability of a particular single-photon detector over another.

The earliest devices used to detect single photons were photomultiplier tubes (PMT),[91] a technology based on vacuum tubes and an arrangement of dynodes that provide the 'multiplication' of the system. These devices provided high gain and good optical collection, but were large and difficult to maintain due to poor mechanical stability, with relatively low detection efficiencies.[92] In the last few decades, the avalanche photodiode (APD) has been used for single-photon detection by operating in Geiger mode.[82,93] For detecting light between 400 to 1000nm, SPAD based on a silicon p-n junction can offer peak detection efficiencies of around 70% for timing jitters of $\sim$ hundreds of ps and dark counts of $\sim$ hundreds of Hz.[94] Novel device designs are summarised in Figure 1.2.1. For detection beyond the visible and near infrared, an especially important endeavour for quantum photonics and communications, different junction materials are

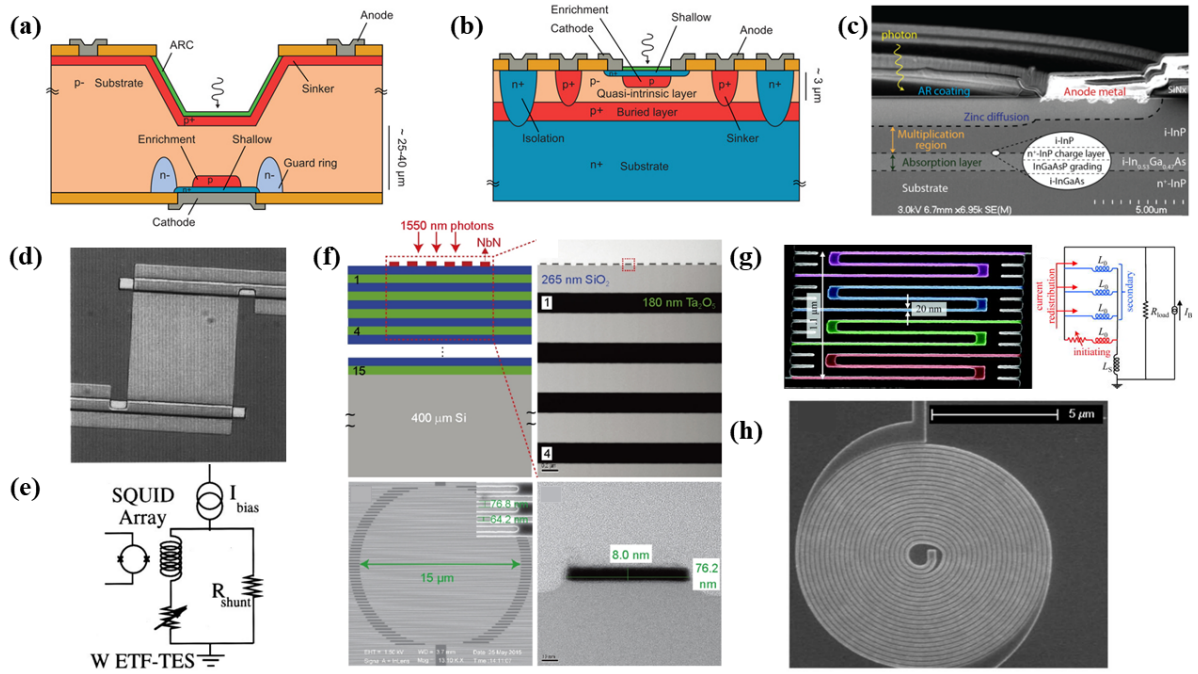

Figure 1.2.1: Single-photon detector designs. **(a)**: A 'reach-through' (SPCM) single-photon avalanche diode (SPAD) design developed by Dautet *et al.*[82] **(b)**: A planar thin junction SPAD design developed by Ghioni *et al.*[83,84] Both **(a)** and **(b)** taken from Figure 2 in Ceccarelli *et al.*[85] **(c)**: Device structure for indium gallium arsenide (InGaAs) SPAD by Tosi *et al.*[86] **(d)**: Image and **(e)**: schematic of electronic read out for tungsten-based transition edge sensor (TES), both taken from Cabrera *et al.*[87] **(f)**: Multi-panel plot from Zhang *et al.*[88] showing schematic, scanning electron and tunnelling electron microscope images of the nanowire-on-DBR design for a niobium nitride superconducting nanowire single-photon detector (SNSPD). **(g)**: The parallel architecture (with false colouring) of the superconducting nanowire avalanche photodetectors (SNAP) device and schematic of electronic readout, from Ejrnaes *et al.*[89] **(h)**: A scanning electron microscope (SEM) image of a spiral nanowire design in a niobium-tin based SNSPD, taken from Dorenbos *et al.*[90] which aims to reduce polarisation sensitivity.

under investigation. Devices based on InGaAs and indium phosphide (InP) can offer detection solutions up to 1670 nm, however suffer from worse noise due to an increased dark current contribution.[95] The standard structure of InGaAs/InP SPADs is based on a layered epitaxial structure[96] with separate absorption, charge and multiplication (SACM). Another solution for infrared detection is using germanium,[97,98] with a room-temperature cut-off wavelength of around 1879 nm. These types of SPADs exhibit lower detection efficiency and higher dark count rates[99] than their indium-based counterparts. Ge-on-Si devices have been shown to exhibit lower afterpulsing probability when compared to InGaAs/InP.[100]

Single-photon detectors based on superconducting materials comprise two main types: TES and SNSPD. Both technologies rely on incoming radiation disrupting the superconducting state of a thin film or nanowire, and therefore require cryogenic temperatures to keep the superconductor below its critical temperature. TESs are capable of high efficiency ($> 90\%$)[101] and even number-resolving detection[102] but at low count

rates (<1 MHz). SNSPDs exploit physical effects similar to those of a bolometer. Peacock *et al.*[103] developed a superconducting tunnel junction for spectroscopic applications, able to detect a few thousand photons per second in the wavelength range 200 to 500nm. This work was developed into a preliminary single-photon detection scheme by Semenov and Gol'tsman,[104] who used a superconducting film and voltage pulse read out to detect individual photons. Later the same year, this was developed further into a detector with picosecond resolution,[105] based on an ultrathin (5 nm) strip of niobium nitride (NbN) deposited on a sapphire substrate and patterned into 200 nm×1 µm 'microbridges'. To further improve the absorption efficiency of this design, a *meander* structure of the nanowire was developed[106] to increase the detection active area. In the following decade many optimisations of these principles ensued[107–110] before the modern meander design became well established. An alternative parallel architecture that exploits a cascading effect is used in SNAP,[89] result in improved dead time and therefore higher counting rates. SNSPDs are now commercially available from several companies, but at a much higher cost in comparison to SPADs because of the cryogenic and high vacuum technology required. A detailed guide of the underlying physics and working principles of both SPADs and SNSPDs will be presented in Chapter 2.

System	**Detection efficiency**	**Dark count rate, cps**	**Max count rate, cps**	**Timing jitter, ps**	**Notes**
Silicon SPAD[111]	62% at 800 nm	≈ 100	3.7×10^7	350	After-pulse probability 3%; operational temp up to 343 K.
InGaAs/InP SPAD[86]	30% at 1550 nm	≈ 5000	6.5×10^8	87	After-pulse probability 1.5% at 225 K.[112]
NbN SNSPD[88]	90% at 1550 nm	≈10	$< 2 \times 10^7$	79	Nanowires on top of DBR stack to enhance absorption. Requires <4.2 K cooling.
Molybdenum silicide (MoSi) SNSPD[113]	87.1% at 1542 nm	< 100	1×10^7	76	Nanowires embedded in optical stack to enhance absorption. Requires <1 K cooling.
Tungsten silicide (WSi) SNSPD[114]	93% at 1550 nm	≈ 1000	$< 2.5 \times 10^7$	150	Nanowires embedded in optical stack to enhance absorption. Requires <2 K cooling.

Table 1.2.1: A table summarising the current state-of-the-art in single-photon detectors.

1.3 Experimental demonstrations using single-photon technology

In summary - no individual source, or detector, can offer every desirable feature simultaneously. Most notably, the brightest single-photon sources (QDs) and the most sensitive single-photon detectors (SNSPDs) both require cryogenic temperatures, which is often considered to render them unfeasible for scalable quantum technologies. However, the best attributes of different sources and detectors have been harnessed in a variety of proof-of-concept demonstrations. In addition, advances in engineering techniques may improve the outlook of scalability and integration. This section will briefly review some high-impact applications of single-photon technologies and experimental demonstrations to date.

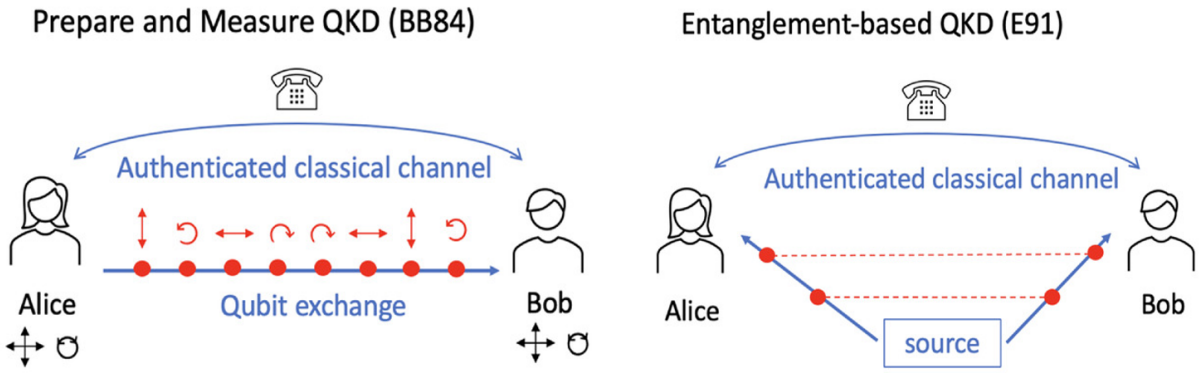

Figure 1.3.1: Two protocols introduced by Bennett and Brassard[27] and Ekert[28] for quantum key distribution (QKD). Figure taken from Vajner *et al.*[115]

Quantum key distribution (QKD) has been demonstrated experimentally with a variety of source and detector combinations. Waks *et al.* reported the advantages of sub-Poissonian light for the security of QKD.[116] Early reports employed the *prepare-and-measure* configuration, with individually encoded photons as bits and the BB84 protocol used for measurement. The first demonstrations using a single-photon source employed the diamond NV centre to transmit over free space[117,118] across tens of metres. The first demonstration using quantum dots as sources and SPADs as detectors in free space were in the early 2000s[119,120] and later also in-fibre.[121] Later advancements used telecommunication wavelength QDs[122] and SNSPDs as detectors,[123] with the latter demonstration by Takemoto *et al.* in 2015[123] being the longest fibre-based QKD demonstration with single-photon sources. More recent advancements of single-photon based QKD schemes employ the E91 protocol[28] and entangled two-photon states.[124–126] A very recent demonstration of entangled states from QDs achieved continuous operation in a metropolitan area over a 270 m free-space link.[127] In opposition to QKD with single-photon sources, so-called *practical* QKD based on weak coherent pulses of laser

light have been implemented both in fibre and free space using SPADs and SNSPDs. With a cooled (153 K) InGaAss/InP SPAD detection system, the *coherent one-way* (COW) protocol[128] was employed to demonstrate in-fibre QKD over 307 km.[129] The first demonstration of QKD using weak laser pulses for the BB84 protocol and SNSPDs was Hadfield *et al.*[130] This work demonstrated how the reduced dark count rates of SNSPDs when compared with InGaAs SPADs can improve the total distance of the transmitted secure keys. Takesue *et al.* built a system based on a *differential phase shift* (DPS) protocol and demonstrated a 200 km fibre link[131] with SNSPDs and a coherent source. The current record for in-fibre QKD uses the *twin-field* protocol[132,133] and SNSPDs, and transmits over a link of 830 km fibre.[134]

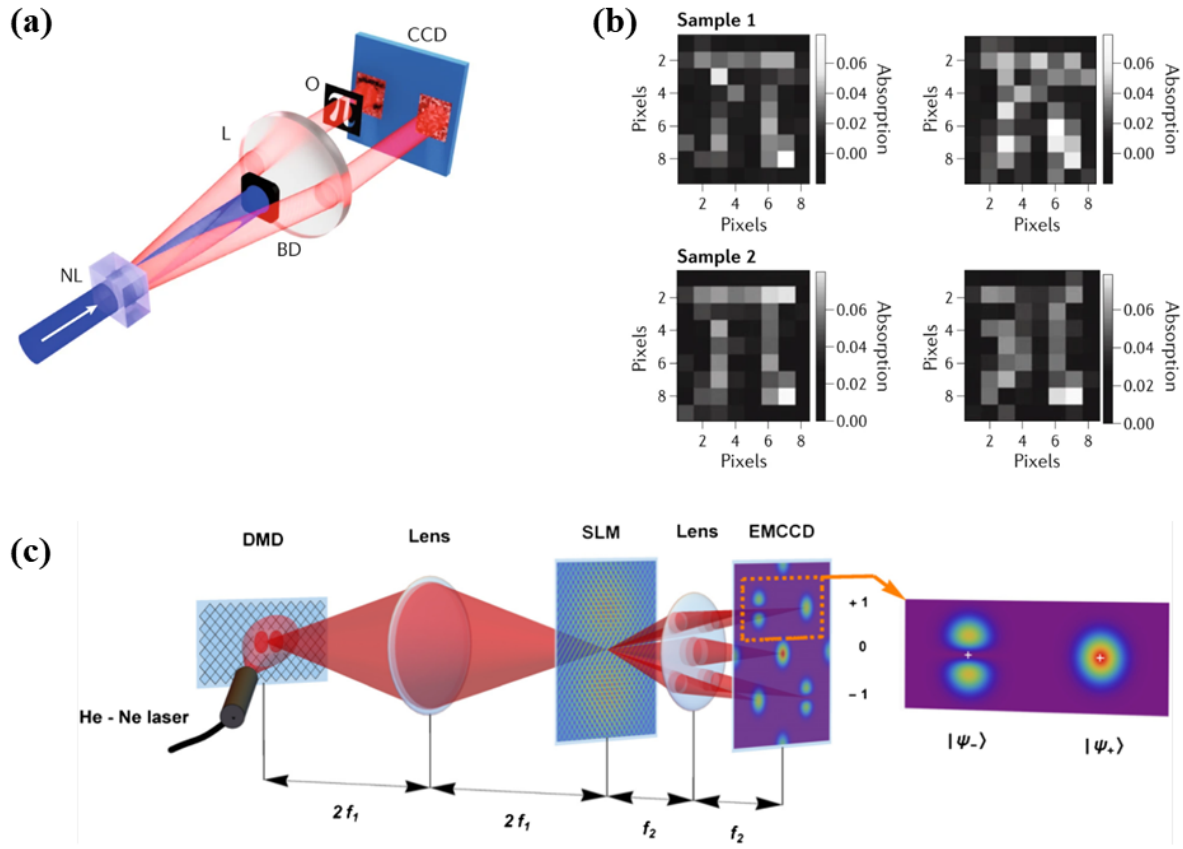

Figure 1.3.2: Examples of quantum-enhanced imaging and resolution. **(a)** Spontaneous down-conversion of light through a non-linear crystal is split and incident on a camera; spatial correlations between one path passing through an object and another directly on the camera allow the removal of shot noise generated in the image of the object. **(b)** Images on the left have been corrected with spatial correlations of the second beam, images on the right are raw camera images of the object. **(a)** and **(b)** taken from Moureau *et al.*[135] **(c)**: The experimental scheme for enhanced resolution, described by Paur *et al.*[136]

Quantum metrology is a field that aims to exploit quantum mechanical features to overcome the classical precision limits and determine the fundamental bounds of such techniques.[137–142] There are many examples specifically of optical metrology that is able

to benefit from the quantum nature of light. In interferometry, squeezed light,[143,144] entangled states[145] or Fock states[146] can be injected into input ports to beat the shot noise limit, the classical limit on the uncertainty associated with a measurement of the phase of light due to its Poissonian statistics. This sub-shot-noise paradigm can present a quantum advantage and has been experimentally demonstrated for techniques in imaging[147–151] and microscopy.[152–155] Perhaps most notably, sub-shot-noise measurements were implemented at LIGO for the observation of gravitational waves,[156,157] and to beat the diffraction limit.[136] Further experimental demonstrations of 'quantum enhanced' measurements were able to show improved resolution when imaging with colloidal QD[158,159] and the diamond NV centre.[160]

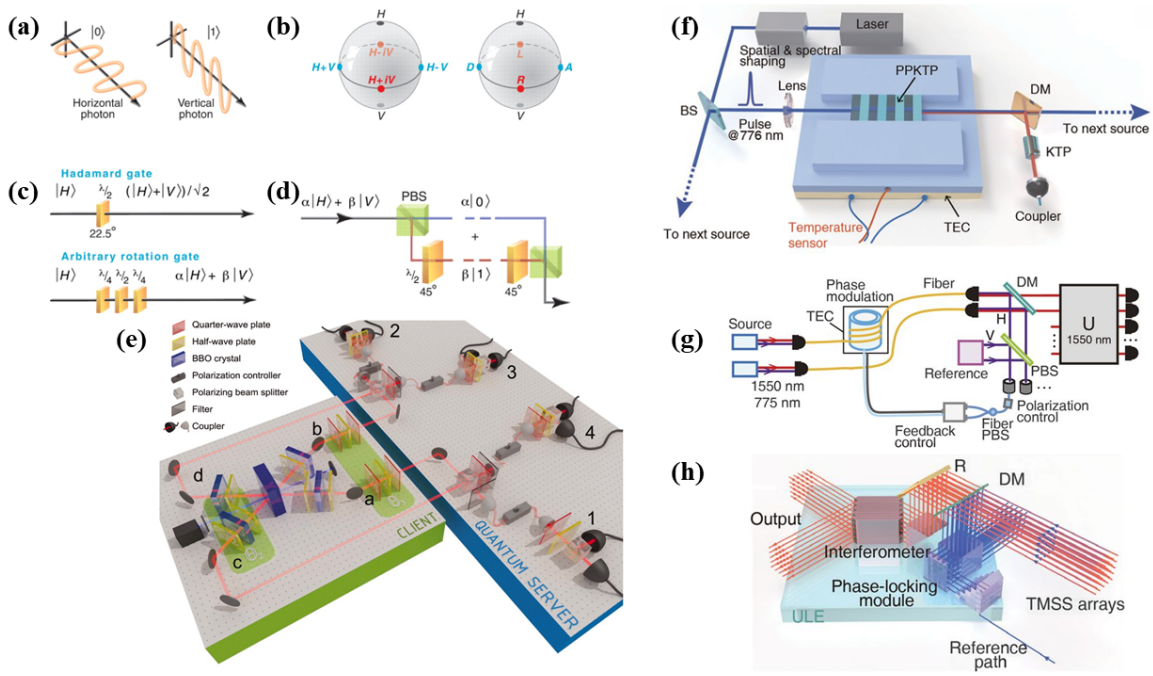

Figure 1.3.3: Experimental demonstrations of quantum computing with photons. Using single photons as qubits: **(a)** encoding a logical 0 or 1 with polarisation state; **(b)** representing an arbitrary state on the Bloch sphere; **(c)**: single-qubit gates for photons can be implemented with linear optical components; **(d)** readout achieved with polarisation optics. Figures **(a)**-**(d)** taken from O'Brien *et al.*[161] **(e)** Blind quantum computing achieved with linear optics. Blind cluster states are produced on the client side and measured on the quantum server side. Figure taken from Barz *et al.*.[162] Experimental set-up for **(f)**: generating squeezed states; **(g)**: phase locking and readout; **(h)**: the 50-spatial mode interferometer, taken from Zhong *et al.*[163]

Quantum computing with single photons is a desirable implementation scheme based on their low decoherence and ease of transmission, the latter permitting a straightforward integration with communication.[161] Photons have many distinct degrees of freedom which can be easily manipulated and read out, and thus used for encoding information. Demonstrated implementations of optical quantum computing include: a controlled-NOT (CNOT) gate;[164] *one-way* quantum computing[165] with four qubit cluster states;[166] demonstrations of Shor's algorithm[167,168] and Grover's algorithm;[169] a blind quantum

computing (BQC) protocol.[162] More recent experiments employing the *boson-sampling* protocol,[170] a technique that uses non-classical light to generate photon number- and path-entangled states,[171,172] have demonstrated a 100-mode interferometer yielding a 10^{14} rate improvement compared to state-of-the-art supercomputers.[163]

Beyond quantum information processing and metrology, a whole realm of unprecedented technologies is enabled by single-photon technology. The higher precision achievable with quantum light has applications in DNA sequencing,[173] while photon counting techniques are used in biological tissue imaging[174,175] and light detection and ranging (LIDAR).[176] The well-defined number-state of quantum light has further applications in quantum radiometry[177] - which is the subject of the final experimental chapter in this thesis.

1.4 Outline of thesis

This chapter has provided an overview of current research efforts in generating, detecting, and using single photons, within a range of physical systems and for a variety of high-impact applications. In this thesis I will present my work on developing characterisation techniques for both single-photon sources and detectors, approaches for high-throughput fabrication of QD micropillar sources, and applying these sources in a metrological study of single-photon detectors.

The structure of the three study chapters includes a brief and specific introduction, literature review and experimental methods. Chapter 2 will describe general experimental methods and instruments used in all study chapters. Chapter 3 provides a detailed mathematical background of correlation functions in optics, and presents some computational and experimental considerations for measuring and calculating these for a variety of sources and detectors. Chapter 4 presents a mathematical model of rate-dependent detection efficiency of a single-photon detector due to finite detector dead time, and experimental results to corroborate predicted effects on higher-order correlation functions. Chapter 5 details the workflow for fabricating micropillar cavities for semiconductor QDs, and their single-photon characteristics based on resonant fluorescence experiments. Chapter 6 presents the results obtained during a five-month secondment at the National Physical Laboratory (NPL), during which metrological measurements of the QDs micropillar samples were performed. Calibrated optical power measurements on low optical flux detectors (LOFDs) will be presented, and applying this source to calibrate a single-photon detector will be discussed. The thesis closes with concluding remarks and an outlook for this research in Chapter 7. Any additional information including mathematical derivations or analysis scripts may be found in the appendices.

CHAPTER 2

EXPERIMENTAL METHODS

Chapter 1 provided an overview of single-photon technology and the ideal single-photon source and detector. This chapter will present the experimental techniques that are employed throughout the thesis. In addition, further specific experimental methods are introduced in each subsequent chapter. Chapter 3 is dedicated to the theory and measurement of photon correlation, while a discussion of metrologically traceable calibration techniques is reserved until Chapter 6. Three experimental fields that are crucial to the characterisation of single-photon sources in particular are the focus of this chapter.

To generate single photons from a sample or device, it must be excited by some external source of energy in order to fluoresce. In this thesis, this is achieved with optical microscopy. Two configurations of confocal microscope were adopted to excite QDs and collect their single-photon flux. Both will be outlined in this section, with detailed discussion of the specific microscope components reserved for the relevant chapters (Chapter 5 and Chapter 6).

In order to probe the spectral information of the collected fluorescence from a sample, spectroscopic techniques are required. This can be achieved with a spectral grating and charge-coupled device (CCD) sensor - the optical spectrometer. Another method is laser scanning, where the excitation wavelength of a tunable laser is scanned over some range and changes in the resulting fluorescence is monitored.

Once the fluorescence from a device has been collected and its spectral features identified, information about the temporal dynamics can be probed with time-resolved measurements. These exploit photon counting using single-photon detectors. Throughout this thesis, two types of single-photon detectors were used and characterised. These devices and techniques will be discussed in detail, with measurement requirements considered.

2.1 Confocal microscopy

The field of optical microscopy has revolutionised a number of different scientific disciplines. The adaptable nature of an optical microscope, by using different configurations of the optical components, can allow enhanced resolution or contrast and custom-built systems for a range of use cases. A confocal microscope offers improved lateral and axial resolution when compared to a conventional wide field microscope. This improved resolution is achieved with a spatial pinhole that selectively filters out-of-focus light from the resulting image.[178] An often-cited absolute limit of the spatial resolution

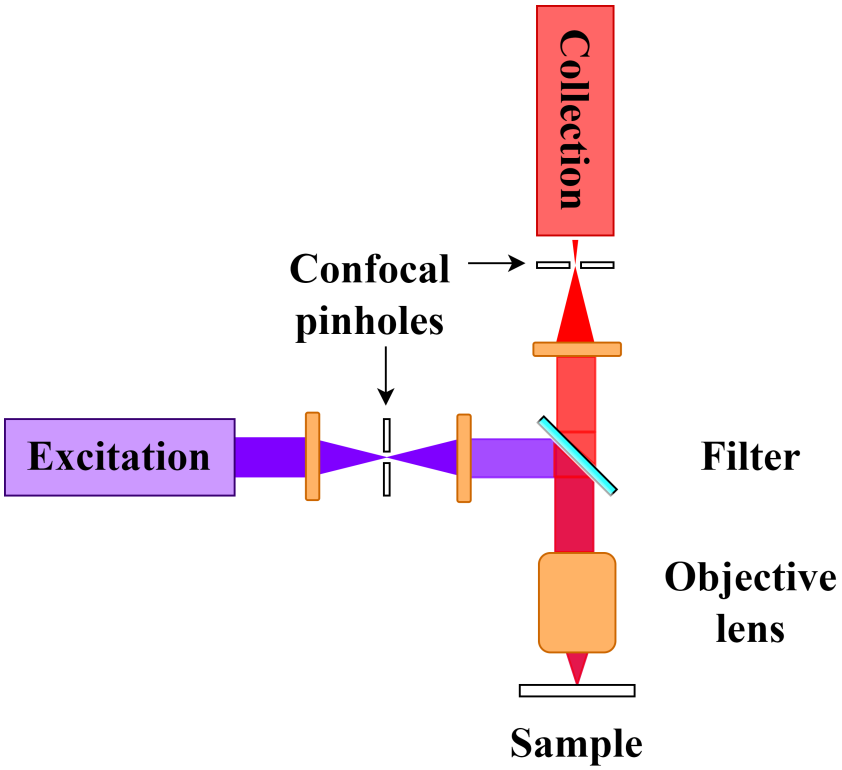

Figure 2.1.1: An illustration of the working principle of a confocal microscope. The excitation source passes through a pinhole and is focussed onto the sample by an objective lens, the numerical aperture of which determines the overall resolution of the system. The fluorescence emitted by the sample under investigation is collected by the same objective and directed through a filter, which may be a spectral or polarising optic. The pinhole before the detection scheme acts to filter out-of-focus rays, improving the image contrast.[179]

Δx of an imaging system is given by the Rayleigh criterion:[179]

$$\Delta x \approx 0.61 \frac{\lambda}{\mathrm{NA}}, \tag{2.1.1}$$

where λ is the wavelength of light and NA is the numerical aperture (NA) value of the objective lens, a value that defines a *cone of acceptance* of light that the objective can efficiently emit and collect.[180] Another resolution limit often applied in confocal microscopy is the Sparrow criterion,[181] which gives a smaller resolution based on the

assumption of an intensity plateau between two point emitters.

In this work, two different confocal microscopes were used to probe quantum dot samples held in a cryostat. In both cases, by launching the excitation from and collecting into single-mode fibre, the core acts as a pinhole to reject out-of-focus light. The first was a dark field resonant fluorescence microscope, which used polarisation optics to achieve high extinction ratio filtering, and mechanical piezo stages inside the cryostat to scan across the sample. This was used in QLab at Cardiff University for all of the measurements presented in Chapter 5. The second was a laser scanning confocal microscope (LSCM) which employed a $4f$ system to raster scan the excitation beam across the sample surface and collect spectrally filtered fluorescence. This was used in the single photons lab at the National Physical Laboratory (NPL) for all of the measurements presented in Chapter 6. Specific details, including a diagram of these microscopes, will be presented in the corresponding chapters. Sections 2.1.1 and 2.1.2 will provide a brief discussion of both confocal microscopes, and Section 2.1.3 will present an overview of the cryostat systems.

2.1.1 Polarisation filtering

Investigating a sample with an excitation beam that is *on resonance* with the transition of interest presents many experimental challenges. To efficiently collect the emitted fluorescence while extinguishing the (much more intense) excitation, it is necessary to use a high performance filtering method. A scheme for observing the resonant fluorescence from a semiconductor QD was first established based on guiding the fluorescence into a spatially orthogonal mode with embedded planar waveguides;[182] this *orthogonal excitation-detection geometry* scheme became standard.[183–185] This experimental set up was later adapted to exploit the polarisation of light[186] instead of its spatial mode, so that the separation of the two beams can be performed with free space optics rather than semiconductor fabrication techniques. This technique, known as *dark field microscopy*, defines an excitation and detection basis with linear polarisers (LPs) set at orthogonal positions and then separates scattered laser light and resonant fluorescence with a polarising beam splitter (PBS). Half waveplates (HWPs) and quarter waveplates (QWPs) can rotate the polarisation state to be any required linear or elliptical polarisation state. The extinction ratio - the ratio of fluorescence to excitation in the detection channel - must be a minimum of 10^4. In practice, extinction ratios as high as 10^7 or 10^8 may be achieved[186] with fine optimisation of the LP, PBS, HWP and QWP. A high-extinction polarisation-based darkfield microscope was used for the experiments in Chapter 5. This microscope was built by Dr Petros Androvitsaneas, and the specific optical components are introduced at the beginning of the chapter. A particular version of the Bloch sphere is used in optics to visualise polarisation states and mapping between them with waveplates - this is the Poincaré sphere.[187] The antipodes of the Poincaré sphere can

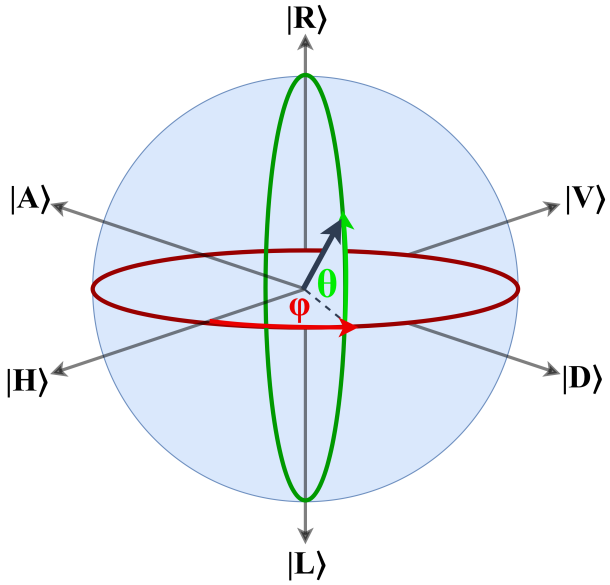

Figure 2.1.2: A visualisation of the Poincaré sphere, where antipodes on the surface correspond to orthogonal polarisation states. Moving around the sphere in terms of ϕ and θ is achieved with waveplates.

be described in pairs that relate to a specific polarisation state. In the Poincaré sphere picture, the antipodal pairs - namely, $|H\rangle$ and $|V\rangle$, $|D\rangle$ and $|A\rangle$, and $|R\rangle$ and $|L\rangle$ - are degenerate polarisation states that lie at orthogonal positions to one another. The linear polarisation states $|H\rangle$, $|V\rangle$, $|D\rangle$ and $|A\rangle$ lie along the equator separated by some spherical orientation angle, φ. The circular polarisation states $|R\rangle$ and $|L\rangle$ lie at the north and south pole respectively. Any elliptical polarisation state that consists of some linear and circular polarisation components can be represented on the Poincaré sphere as a pair of coordinates related to its relative linear polarisation angle φ (position along equator) and circular polarisation angle θ (vertical angle away from equator). The combination of one HWP and one QWP allows the mapping of any incoming polarisation state to any other on the Poincaré sphere. For the polarisation microscope, scanning the sample was achieved with piezoelectric controllers inside the cryostat attached to the sample stage. This system is preferred for a microscope whose performance depends strongly on precise position and spatial orthogonality of free space optics. Scanning in this way is inherently slower and may be subject to drift or instabilities. An alternative to mechanical movement of the sample stage is to raster scan the excitation beam across the sample and build up an image based on the photoluminescence response in the collection arm. This is how the second microscope, in the next subsection, was implemented. The details of this microscope, built by Dr Philip Dolan, and experiments performed with it can be found in Chapter 6.

2.1.2 Laser scanning confocal microscope

Raster-scanning an excitation beam across a sample can be achieved with a LSCM. This configuration makes use of the $4f$ optical system to transform a change of incidence angle on an aspheric lens to a lateral translation on the sample surface. Figure 2.1.3 shows a

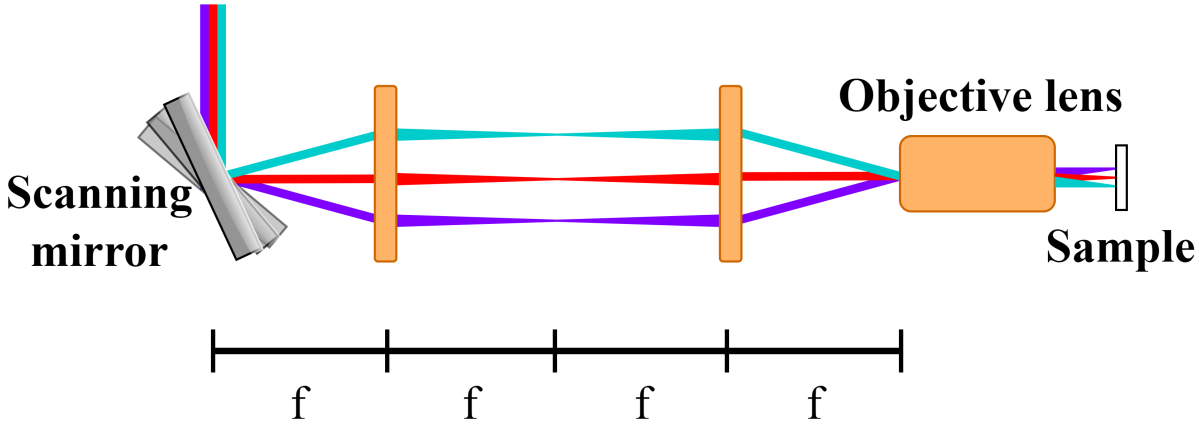

Figure 2.1.3: A schematic of a LSCM that uses a 4f system to move point-by-point across a sample.

example of a $4f$ system. Two aspheric lenses with equal focal lengths f are placed $2f$ apart, such that their focal points coincide in space. The scanning mirror is placed f away from the first lens; tilting this scanning mirror changes the angle at which the collimated beam is incident on the lens. The objective lens is placed f away from the second lens. As the angle of incidence at the first lens changes, the focussed beam coming out of the objective lens is moved laterally across the sample. By using a programmable scanning mirror, the excitation beam can be moved between a range of incidence angles on the first lens which equates to point-by-point scanning across the surface of the sample. The emitted fluorescence of the sample can be correlated to a physical location and analysed to build up an image.

2.1.3 Cryostat system

The cryostat systems used for the two confocal microscopes described in the previous sections were both closed-cycle attoDRY systems. These cryostats are sometimes referred to as 'dry cryostats', since they allow cooling with no liquid helium or other cryogens, instead recycling helium gas. In QLab, Cardiff, the resonant excitation microscope (Section 2.1.1) was built on a attachable breadboard which was mounted above the attoDRY1000[188] cryostat system. This system is tailored for ultra-low vibration measurements down to 4 K. The sample is mounted onto a base plate and secured with silver paste. The plate sits on a nanopositioner stack, comprised of piezoelectric motor-driven stages for X, Y and Z position control. These nanopositioners are driven

by control units that provide coarse- and fine- movement with different voltage steps. Within the stack is a heater stage for fine-temperature tuning. All of this sits inside a long stick tube which is inserted into the cryostat and secured with vacuum flanges when the system is warm. The cryostat insert is under exchange gas, 20 mbar at room temperature. In the Photonics group at NPL, the LSCM (Section 2.1.2) was built on an attoDRY800[189] system, which comprises an integrated optical table around the cryostat, with the sample mounted inside a vacuum shroud. The sample stage sat on top of XYZ nanopositioners, controlled with an ANC300 driver.

2.2 Spectroscopy

Optical spectroscopy involves probing the spectral characteristics of the fluorescence from a particular sample. In this thesis, spectroscopy techniques were used for analysing the cavity mode of semiconductor micropillar cavity structures containing QD, and the associated optically addressable transitions within the QD fine structure. The cavity mode measurements were performed using a broadband LED source for reflectivity measurements, and the QD transitions were examined with both non-resonant and resonant photoluminescence measurements. Spectral features of QD are typically bright ($> 10^4$ cps) and narrow (< 0.1nm). In Chapters 5 and 6, optical spectrometers are used to identify specific transitions using a diffraction grating and CCD. In Chapter 5 for high resolution spectral information regarding the QD fine structure, a tunable titanium sapphire laser is used to scan across wavelengths of picometre resolution.

2.2.1 Spectrometer

An optical spectrometer has three key components: an input slit, a diffraction grating, and a detector. The input slit is motorised and can be used to control the amount of light going into the instrument. The diffraction grating disperses the incident light accordingly. The irradiance pattern for light dispersed by a ruled grating depends on the incidence and diffraction angle, the ruling spacing and the wavelength of light. Better spectral resolution is achieved with smaller line spacing. The efficiency may be improved by *blazing* the grating. This results in triangular-shaped rulings that are slanted for a particular order.[190] The dispersed light beam may then be redirected towards a wide-field detection system, to analyse the spectrum of the incident light, or towards an output slit to deliver a spectrally filtered beam by choosing the grating angle and output slit width. In both of the optical spectrometers used in this thesis, the detection was performed with a CCD camera. These detection systems are based on a wide array of individual pixels that detect photons, and the spatial position of each pixel correlated to the incident intensity provides spectral information about the dispersed beam.[191] In Chapter 5, an Andor

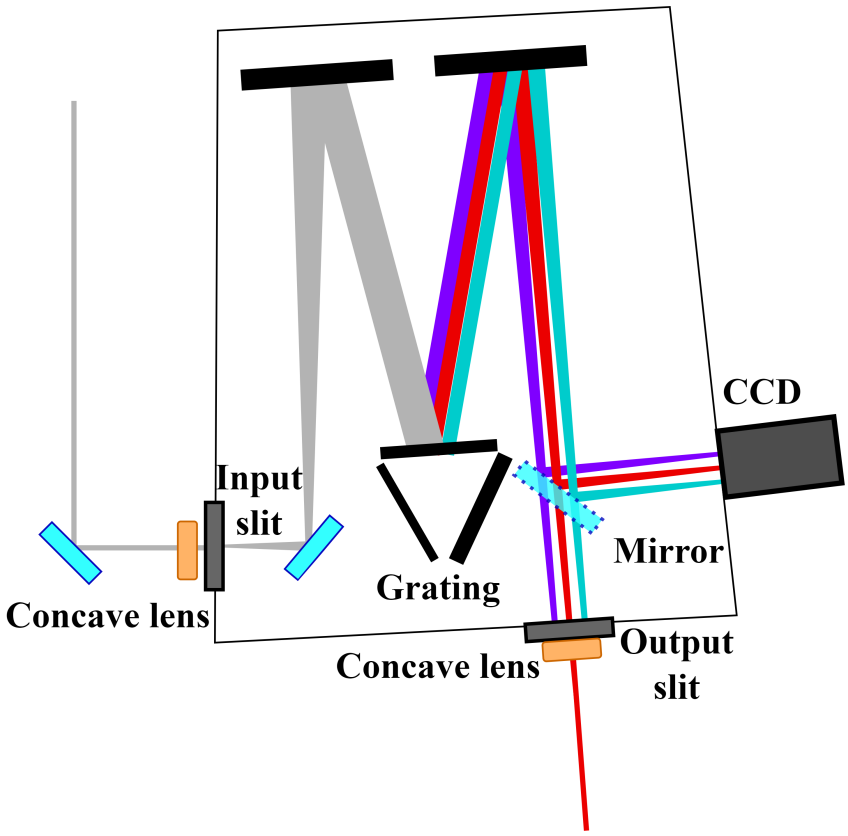

Figure 2.2.1: A schematic to demonstrate the working principle of a spectrometer. Collimated light is focussed onto the slit which expands the beam. The beam is dispersed by a grating, and the CCD correlates spatial position with wavelength.

Shamrock spectrometer and CCD system was used for taking spectral measurements and filtering. In Chapter 6, a Horiba spectrometer and Newton CCD were used for taking spectral measurements and filtering. A schematic of the spectrometer system used in Chapter 6 is shown in Figure 2.2.1. A collimated beam in free space is coupled into the instrument via a concave lens focussing the beam onto input slit. The expanded beam is re-collimated by a parabolic mirror, and then dispersed by a diffraction grating, chosen for a particular resolution. The separated light can then either be directed to the CCD to record spectral measurements, or out of the output slit for filtering. Details of the components in both spectrometer systems is given in the respective chapters.

2.2.2 Laser scanning

The tunable titanium sapphire laser is an essential tool for quantum optics experiments. A high-power (>5 W) pump beam, typically of ∼532 nm, is incident on a titanium-doped sapphire crystal to produce either ultrashort pulsed or continuous-wave (CW) laser light, tunable across a range typically between 600 to 1000nm.[192] In Chapter 5, a CW tunable titanium sapphire laser (M Squared SolsTiS) was used for spectroscopic analysis of quantum dot fine structure. This method involves scanning the excitation laser over

a specified spectral range while collecting the fluorescence and measuring its intensity at a detector. The M Squared laser was able to perform a function called 'TeraScan'[193] which smoothly and continuously tunes the laser over a user-defined range, down to a resolution of ∼tens of picometres, at rates from $1\,\mathrm{MHz\,s^{-1}}$ up to $20\,\mathrm{GHz\,s^{-1}}$. By correlating the intensity at the detector with the wavelength of the tunable excitation laser, the fine structure of the quantum dot, that is not resolvable with a conventional diffraction grating spectrometer set up, is revealed.

2.3 Photon collection and counting

After exciting and collecting a single-photon flux from a device, it is possible to probe the dynamics of the emission using time-resolved measurements. In this thesis, two types of single-photon detectors were used; the following subsections will provide an overview of their working principles, with advantages and disadvantages of both, especially in relation to the 'ideal characteristics' outlined in Chapter 1. A summary of these parameters is given in Tables 1.2.1 with respect to standard commercial models for both. To collect the fluorescence for photon counting measurements, the free-space beam is focussed into single-mode fibres directed to fibre-coupled detectors. This section begins with an overview of optical fibres.

2.3.1 Optical fibres

Optical fibres are devices comprised of a high index dielectric core surrounded by a lower refractive index cladding, designed to efficiently guide and transmit a particular mode of light based on total internal reflection. A multi-mode fibre has a wide core $>50\,\mu\mathrm{m}$ and is able to support multiple modes for higher bandwidth transmission. A single-mode fibre is designed to only support an individual mode of light and therefore has a smaller core size and angle of acceptance, acting similarly to a waveguide. The small core size acts as a pinhole to reject light from higher modes. Fibres can be connected with mating sleeves that correspond to the cut of their ferrule. If the ferrule heads are flat, they can be connected with FC/PC connectors, known as ferrule contact (FC). If the ferrule heads are angled, they can be connected with FC/APC connectors - corresponding to angled physical contact (APC).

2.3.2 Single-photon avalanche diodes

The single-photon avalanche diode (SPAD) is a device based on a biased semiconductor heterostructure, in which a p-n junction is reverse-biased under the breakdown voltage. Operating in this regime results in a gain process due to avalanche multiplication of charge

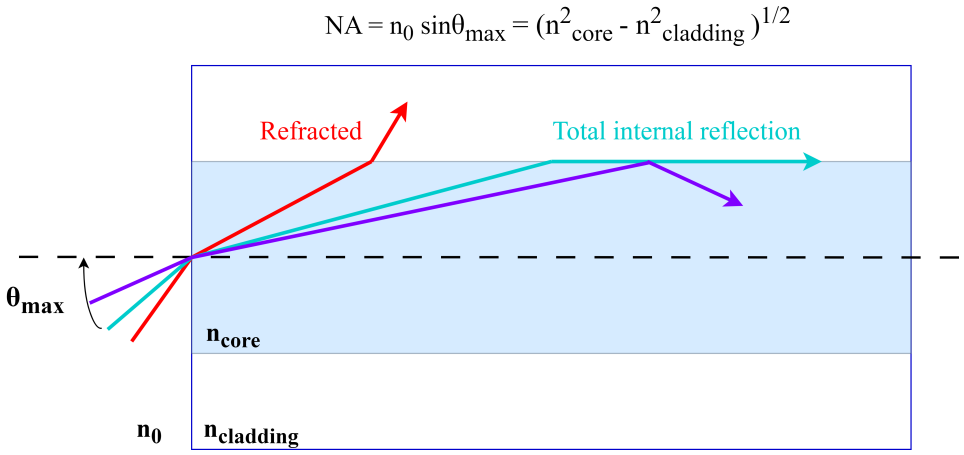

Figure 2.3.1: Working principle of a multimode optical fibre.

carriers across the junction, which allows incoming radiation to be detected. To achieve higher gains required for single-photon detection, the junction must be biased above the breakdown voltage. After the arrival of a photon, the impact ionisation process begins and the current grows due to the avalanche effect. To reset the device before another detection can occur, a *quenching circuit* is required to drive the voltage back down. The 'on-off' nature of the detection regime has given rise to the term 'Geiger mode' for operating with a bias above breakdown voltage.[94]

The standard single-photon detector metrics (see Chapter 1) such as detection efficiency, dark count rate and jitter, all depend on the bias voltage. The probability of triggering an avalanche process in the junction increases with bias voltage above the breakdown, hence detection efficiency improves at higher biases. The dark count rate for a SPAD depend on both the design of the heterostructure and the fabrication of its material. Local traps within the bandgap may result in the thermal generation of carriers, and band-to-band tunnelling can occur. In general, dark count rate increases with bias voltage above the breakdown due to an increased probability of thermally generated carriers. Timing jitter in SPADs is related to uncertainty between the photon arrival and the onset of the avalanche process. It is primarily related to the time taken for photo-generated carriers far from the depletion region to diffuse to the high field region and induce the avalanche; therefore, it depends on the thickness of the junction active region.[194] A parasitic effect, unique to SPADs, is *afterpulsing*. This phenomenon occurs as a result of charge carriers being trapped in deep intra-bandgap energy levels during the avalanche process - these carriers can be released after the quenching circuit has reset the device, and therefore trigger an anomalous event, conditionally related to the original photon arrival that resulted in an avalanche. This effect contributes to the dark count rate, and the probability increases with bias voltage above the breakdown. One method for reducing the effects of afterpulses is an extended quenching time to reduce the likelihood of triggering a false detection event, at the cost of reducing the detector

operational speed. Another undesirable feature of SPADs is the *breakdown flash*.[195,196] During an avalanche, charge carriers may recombine in the active region and emit light. For a fibre-coupled device, this can result in *backflashes*, where the emitted light travels in the opposite direction down the fibre, is reflected at some interface, and directed back towards the detector. The impact of backflashes on photon correlation is explored in more detail in Chapter 3.

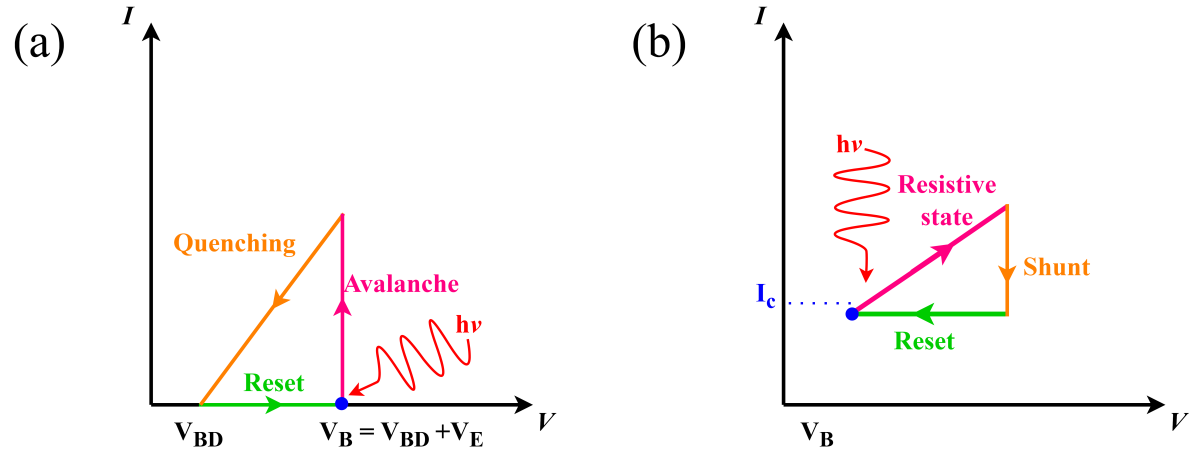

Figure 2.3.2: The IV characteristic describing the operation of **(a)**: SPADs (adapted from Migdall *et al.*[194]) and **(b)**: SNSPDs. On both graphs, the blue dot indicates the state of the detector before an incident photon, and V_B is the operational bias. **(a)**: The SPAD is held at some bias voltage V_B which is some excess V_E above the breakdown voltage V_{BD}. An incident photon incurs an avalanche response which generates a photocurrent. The quenching circuit reduces the current back to the off state, and the detector is reset. **(b)**: The SNSPD is held at V_B such that the supercurrent is just below the critical current. An incident photon creates a localised hotspot, creating a resistive region across the nanowire which grows until a finite voltage is measured as a 'click'. When the current gets to a certain value it is shunted to allow the superconducting state to recover and the detector to reset.

2.3.3 Superconducting-nanowire single-photon detectors

Superconducting nanowire single-photon detectors (SNSPD) are devices that exploit the 'hotspot'[197] created by incident radiation on a superconductor. An incident photon may break a Cooper pair[198] and produce two quasiparticles as a result. This region of 'hot' quasiparticles forms a local resistive region.[199,200] A nanowire, typically made of materials such as niobium nitride or molybdenum silicon (see Chapter 1 for a review of different devices), is used as the detector active area. The nanowire is held below its critical temperature and biased slightly below its critical current, in order to maintain the superconducting state. Incident single infrared photons are energetic enough to create a nanometre scale hotspot on a superconducting material. The sensitivity of a superconducting nanowire to incoming light of a particular wavelength is related to its superconducting energy gap, $\Delta(T)$. As a result of this nanoscopic resistive region, the

supercurrent is diverted to the wire edges. The local current density exceeds the critical current and a resistive region across the width of the nanowire impedes the supercurrent, allowing a voltage readout. Joule heating means that the resistive region continues to expand, until some threshold is reached and the bias current applied to the nanowire is shunted to allow the superconducting state to recover.[81] This process for the supercurrent is illustrated in Figure 2.3.2(b).

The detection efficiency is dependent on how well the nanowire can be illuminated, can absorb incoming radiation, and the likelihood that the voltage readout is generated from incoming radiation. Efficient coupling is enhanced using a variety of nanowire designs, such as the spiral[90] or the meander.[106] The meander design is typical for most commercial devices, but this arrangement does result in a polarisation sensitivity of the detector.[201] Nanowire absorption can be improved with cavity or waveguide structures, as discussed in Section 1.2. The efficiency of voltage readout can be enhanced with ultra-narrow nanowires,[110] or parallel nanowire architectures such as the SNAP.[89] The timescales associated with the voltage readout and current shunting processes dictate the detector jitter and dead time respectively, and readout electronics may affect the detector recovery, or induce an afterpulsing effect.[202] The largest contribution to the overall jitter of an SNSPD detection system is related to the noise associated with the readout electronics, but also depends on the intrinsic superconductor dynamics,[203] the operational temperature and bias current of the nanowires.[204] Generally, a higher bias current reduces the detector jitter,[203] and therefore this is also dependent on the choice of nanowire material since each superconductor has a different critical current. However, higher bias currents increase the dark count rate. The dark count rate is associated with counts registered due to blackbody radiation and the intrinsic dark count, thought to be due to complex dynamics in the superconducting state.[205] The latter is poorly understood, but several studies have shown the effects of filtering and fibre-coupling to reduce the effect of the former.[206,207] Reducing the detector dead time can be achieved with shorter nanowires,[208,209] however if this is done excessively then the hotspot does not have sufficient time to dissipate. This effect is known as *latching*,[210] and means that no further photons can be registered until the bias current is reduced. SNSPD systems are typically operated with closed-cycle vacuum cryostat systems, where a compressor continuously evaporates and condenses helium to maintain a constant temperature below ~4 K and an operational (when used for detection) temperature of 0.8 K. The electronic signal from the nanowire readout is amplified before being received by the time correlated single-photon counting module (TCSPCM). The optical fibres going into the system are single-mode and polarisation maintain for enhanced coupling.

CHAPTER 3

HIGHER-ORDER PHOTON CORRELATIONS

3.1 Introduction

Chapter 1 provided an overview of single-photon technology and typical performance metrics and Chapter 2 described characterisation techniques for assessing those metrics. This chapter will examine the experimental requirements of measuring *higher-order correlations*. The second-order correlation function, $g^{(2)}(\tau_{12})$, is a hallmark of single-photon purity. Obtaining a precise estimate of this function depends on many experimental parameters that must be considered. Being able to extract higher-order correlations of light sources $g^{(n)}(\tau_{12}, ..., \tau_{1n})$, where $n > 2$, is an attractive prospect in quantum light metrology. For every higher degree of photon correlation that can be verified, more statistical information about the photon number distribution can be obtained.[194] Third-order correlated light has been shown to reveal unexpected statistics in laser light,[211,212] have applications in imaging,[213–215] as well as probing time asymmetries[216] and multi-photon states.[217] Fourth-order light has been measured for pseudothermal light,[218] in multi-photon interference experiments[219] and for indistinguishability measurements.[220] However - with extra information comes added complexity, both in terms of experimental requirements and computational demand.

In this chapter I will present a thorough description of photon correlation, from theory through experimental considerations to data analysis. An overview of photon statistics will define three distinct light sources based on their correlation function. The experimental methods of photon counting for correlation will be outlined, and finally the development of a script for extracting higher-order correlations from timetagged data files will be described and its results shown.

3.2 Classical optics and coherence

In classical optics we consider light to act as an electromagnetic wave, which has properties such as wavelength, amplitude and phase associated with its electric field component. The propagation of this wave as a beam of light has an intensity related to its electric field strength.[180] Both the electric field amplitude and its intensity will be subject to fluctuations that occur with some characteristic timescale, in accordance with the physical mechanism behind the light generation. The *correlations* between these fluctuations can be investigated experimentally to learn about the *coherence* properties of the field. Light is coherent if it can interfere when superimposed spatially or temporally.[221]

The first-order coherence of a light field is related to the correlation of the electric field amplitudes. For a light field at two points in space and time, $E(\mathbf{r_1}, t_1)$ and $E(\mathbf{r_2}, t_2)$, the first order correlation function $g^{(1)}(\mathbf{r_1}t_1; \mathbf{r_2}t_2)$ is given in Equation 3.2.1, where $\langle ... \rangle$ denotes an ensemble average over dependent variables.

$$g^{(1)}(\mathbf{r_1}t_1; \mathbf{r_2}t_2) = \frac{\langle E^*(\mathbf{r_1}, t_1) E(\mathbf{r_2}, t_2) \rangle}{[\langle |E(\mathbf{r_1}, t_1)|^2 \rangle \langle |E(\mathbf{r_2}, t_2)|^2 \rangle]^{\frac{1}{2}}}. \tag{3.2.1}$$

Under the assumptions that: (i) the field is composed of one spatial mode such that $g^{(1)}(\underline{\mathbf{r}}) = g^{(1)}$; (ii) the field correlation is time invariant, such that it depends only on the time difference $\tau_{12} = t_2 - t_1$;[222] Equation 3.2.1 simplifies to Equation 3.2.2, where $\langle ... \rangle$ now denotes the time average:

$$g^{(1)}(\tau_{12}) = \frac{\langle E^*(t) E(t + \tau_{12}) \rangle}{\langle |E(t)^2| \rangle}. \tag{3.2.2}$$

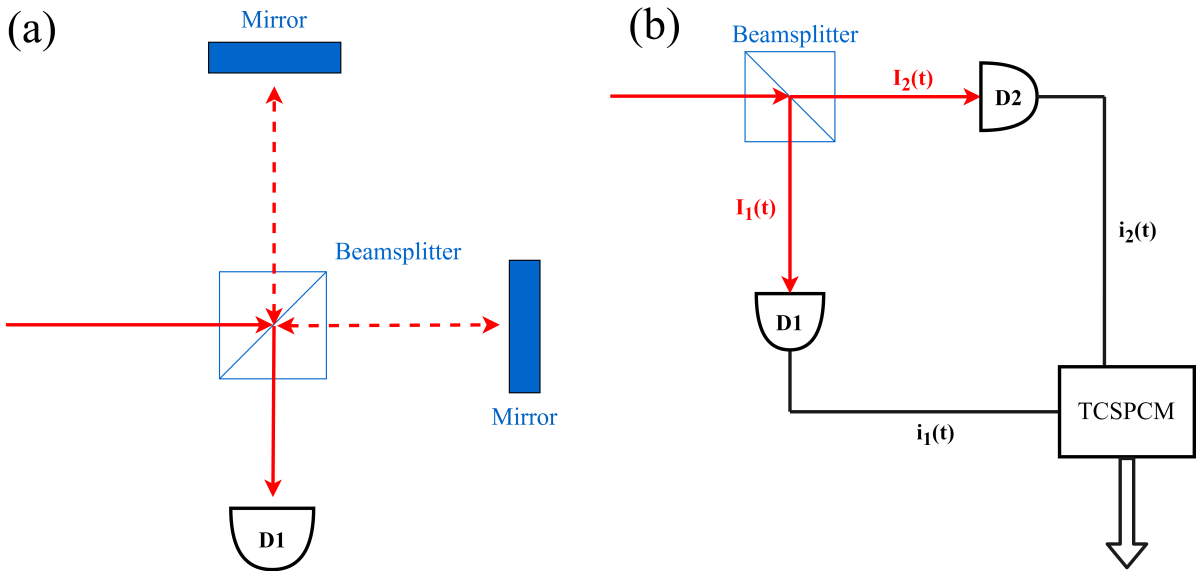

Figure 3.2.1: Optical experiments for probing the first and second order coherence of light. **(a)**: A Michelson interferometer. **(b)**: A Hanbury-Brown and Twiss interferometer.

It is possible to measure the first-order coherence of a particular light source using an optical interferometer, for example a Michelson or Mach-Zehnder interferometer.[16] Figure 3.2.1(a) shows a schematic of a Michelson interferometer. In this experiment, the light field is split into two by a beamsplitter, and each beam travels down an arm of different path length, thus introducing a time delay. The two beams are then recombined, and the resulting interference pattern is measured as a function of the path length difference. Since the first-order coherence is related to the electric field amplitude, whilst it can reveal information such as the coherence length of the light, it cannot verify the statistical nature of the intensity fluctuations. The second-order coherence is related to the correlation of the field intensities - as defined in Equation 3.2.3.

$$g^{(2)}\left(\mathbf{r_1}, t_1; \mathbf{r_2}, t_2\right) = \frac{\left\langle E^*\left(\mathbf{r_1}, t_1\right) E^*\left(\mathbf{r_2}, t_2\right) E\left(\mathbf{r_1}, t_1\right) E\left(\mathbf{r_2}, t_2\right)\right\rangle}{\left\langle \left|E\left(\mathbf{r_1}, t_1\right)\right|^2 \right\rangle \left\langle \left|E\left(\mathbf{r_2}, t_2\right)\right|^2 \right\rangle}. \tag{3.2.3}$$

Again, this expression can be simplified with the assumptions as before:

$$g^{(2)}\left(\tau_{12}\right) = \frac{\left\langle I\left(t\right) I\left(t+\tau_{12}\right)\right\rangle}{\left\langle I\left(t\right)\right\rangle^2}. \tag{3.2.4}$$

To probe intensity fluctuations the second-order coherence must be measured using a Hanbury-Brown Twiss experiment,[11] shown in Figure 3.2.1(b). The incident light beam is split into two and directed towards individual photodetectors, followed by a TCSPCM which counts photon arrivals at each detector. We can define three statistical signatures of light that occur with different $g^{(2)}\left(\tau_{12}\right)$ behaviour, shown in Figure 3.2.2. To further probe the relationship between the second-order correlation function and the three signatures observed in Figure 3.2.2, the idea of classical intensity must be related to the quantum mechanical concept of photons and number states.

3.3 Quantum optics and photon counting

Using a quantum mechanical description of light, we can develop a new interpretation of photon correlation. A full description of the quantum harmonic oscillator and creation and annihilation operators may be found in Appendix A.1. The intensity of light is directly proportional to the number of photons arriving at each detector, and so we can rewrite the $g^{(2)}\left(\tau_{12}\right)$ in terms of the creation and destruction operators, as in Equation 3.3.1.

$$g^{(2)}\left(\tau_{12}\right) = \frac{\left\langle \hat{a}^\dagger\left(t\right) \hat{a}^\dagger\left(t+\tau_{12}\right) \hat{a}\left(t\right) \hat{a}\left(t+\tau_{12}\right)\right\rangle}{\left\langle \hat{a}^\dagger\left(t\right) \hat{a}\left(t\right)\right\rangle^2}. \tag{3.3.1}$$

In the photon number picture of correlation, we can consider photons arriving at a detector, and the probability of finding n photons in a particular time bin, $P(n)$. Each stream of photons will have some associated average number per bin $\langle n \rangle$, and variance

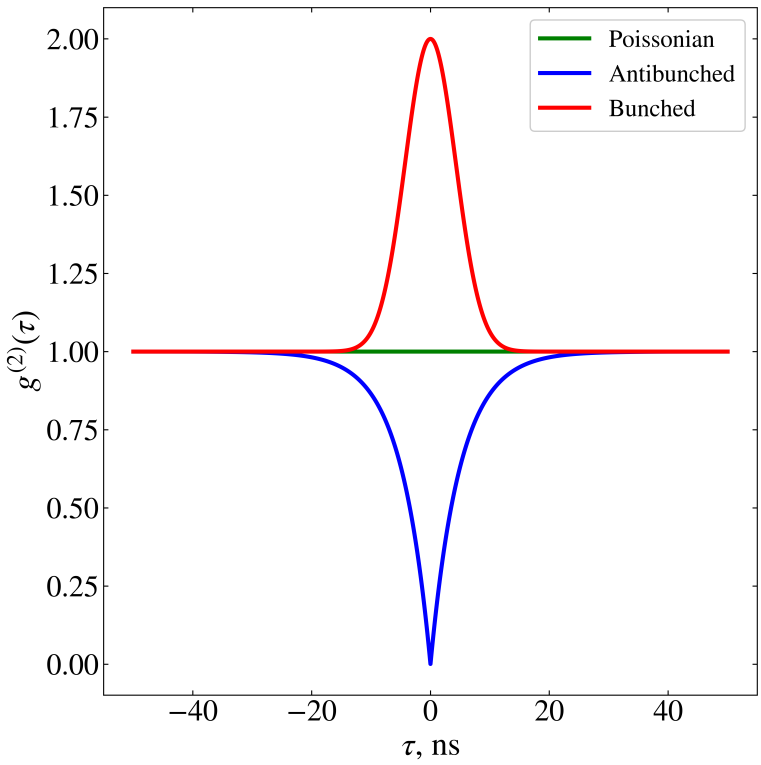

Figure 3.2.2: Examples of second-order correlation functions exhibiting bunched, antibunched and Poissonian characteristics. The associated correlation timescales are 5 ns. Here, the bunched function represents a thermal light source as $g^{(2)}(0) = 2$, and the antibunched function represents a two-level system under non-resonant excitation.

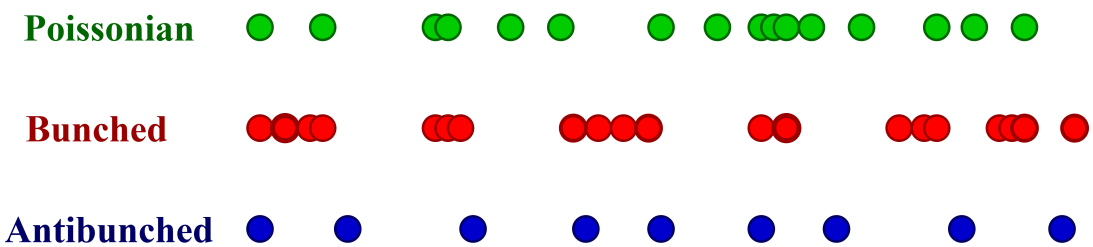

Figure 3.3.1: The three statistical signatures of light in terms of their photon number distribution arriving at a detector.

Δn^2. The probability distribution $P(n)$ of bunched light is given by the Bose-Einstein distribution and is therefore characterised by $\Delta n^2 > \langle n \rangle$. In semi-classical theory, this presents as fluctuating beam intensity. The term 'bunched' refers to the fact that at a photodetector the photons arrive in 'bunches', which appears as a blinking behaviour. Examples of this type of light are *thermal* and *chaotic* light. Poissonian light has a probability distribution $P(n)$ described by the Poisson distribution, which applies to random, discrete variables that occur in some time interval. It is characterised by $\Delta n^2 = \langle n \rangle$. An example of this is laser light, which can be described as having an overall average beam power and flux, but will still experience photon number fluctuations on small time scales or pulsed operation. Antibunched light has a probability distribution

$P(n)$ described by Fock number states. This regime of light cannot be described by semi-classical theory. The term 'antibunched' refers to the fact that in a given beam segment, photons are (somehow) more ordered than coherent light[223] - it is characterised by $\Delta n^2 < \langle n \rangle$. A summary of these probability distributions is given in Table 3.3.1, and Figure 3.3.2 shows examples of each probability distribution of light for some average photon number, $\langle n \rangle$. With Equation 3.3.1, it is clear that each regime will have a

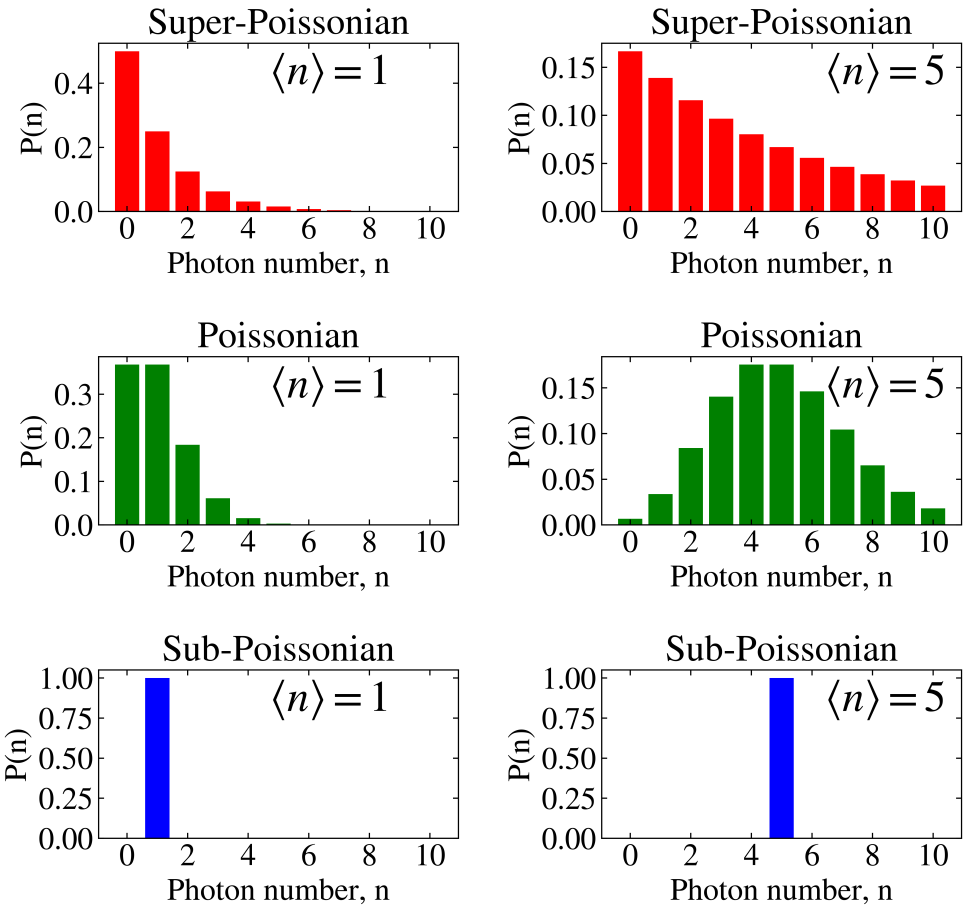

Figure 3.3.2: The probability distributions $P(n)$ defined in Table 3.3.1 for the three light statistics, showing the change in distribution for different mean photon numbers of $\langle n \rangle = 1,5$.

distinct $g^{(2)}(\tau_{12})$ as well, according to the underlying photon distribution $P(n)$. The value of $g^{(2)}(\tau_{12})$ at zero time delay, $\tau_{12} = 0$, defines the 'signature' of the light source being measured. These values are summarised in Table 3.3.1. A delay time τ_{12} of zero represents a photon arriving at both detectors at the same time - a coincidence. Therefore the value of $g^{(2)}(0)$ is effectively a measure of the likelihood of coincidence, relative to the uncorrelated Poissonian function. Photons in a beam described by Poissonian statistics arrive randomly at any time, and so we don't expect a coincidence to be more or less likely than any other time delay between arrivals - its $g^{(2)}(\tau_{12})$ is equal to 1 everywhere. Photons in a bunched light beam are more likely to arrive together, in 'bunches', and so

Photon statistics	**Photon number variance,** Δn^2	**Examples**
Super-Poissonian	$\Delta n^2 > \langle n \rangle$	Chaotic, incoherent, thermal; described by Bose-Einstein probability distribution.
Poissonian	$\Delta n^2 = \langle n \rangle$	Laser; described by Poissonian probability distribution.
Sub-Poissonian	$\Delta n^2 < \langle n \rangle$	Antibunched light, squeezed light; described by quantum mechanical operators e.g. Fock states, quadratures.

Table 3.3.1: The three statistically distinct modes of light, with their associated statistical parameters: the mean $\langle n \rangle$ and the variance Δn^2.

there will be a higher probability of coincidence relative to Poissonian over the correlation timescale. Since a perfect antibunching source will only ever emit one photon at a time, we should never see simultaneous arrivals at more than one detector, so the probability of a coincidence drops to zero over the correlation timescale. An important distinction to make is the separation between the characteristic intensity fluctuations of a source, and its temporal characteristics as defined by the photon distribution $P(n)$. A sub-Poissonian source will not necessarily have an antibunched $g^{(2)}(\tau_{12})$, and some light sources with a Poissonian $g^{(2)}(\tau_{12})$ may have higher intensity fluctuations than a laser beam, for example.

Experimentally, the $g^{(2)}(\tau_{12})$ is obtained by calculating the difference in arrival times between one detection channel and another. The Hanbury-Brown and Twiss experiment requires a beamsplitter, two photodetectors and a photon counting module, as shown in Figure 3.2.1(b). TCSPCM are typically capable of operating in two modes. The first is known as 'start-stop', where one detector is selected as the 'start' channel, and the other as the 'stop' channel. In this configuration the TCSPCM records the time differences between nearest-neighbour photon coincidences, and the software displays a histogram of these time differences, which reveals the second-order correlation function. The $g^{(2)}(\tau_{12})$ measured in this way will suffer from photon *pile up* and exponentially decay. This is because when examining nearest-neighbour coincidences only, the *waiting time distribution* is observed - explored in more detail in Chapter 4 - where the probability of long timescale correlations is decreasing. The second counting mode is *timetagging*, where the TCSPCM writes a *timestamp* of each photon arrival at the detector to a file. Depending on the TCSPCM model, the timetagged file may sometimes containing other information such as channel number and average rate. This method is more computationally intensive - the histogram of time differences must be calculated separately, after data collection, and the generated timetagged files can be large. However, it also provides complete information about the correlation between each and every

photon-photon event - this is the full auto-correlation function. For example, using timetagged data to extract a $g^{(2)}(\tau_{12})$ allows you to specify the bin width and span of τ retroactively, or monitor the count rate of the source over 10s of hours of experiment and remove anomalous timetags in hindsight.

In order to produce a sufficiently populated histogram, we must consider the number of histogram counts per bin accumulated for an uncorrelated source, as a baseline minimum. For a $g^{(2)}(\tau_{12})$, this is given in Equation 3.3.2:

$$N_{\text{count}} = R_1 \times R_2 \times \Delta t \times T, \tag{3.3.2}$$

where N_{count} is the number of counts per bin, $R_{1,2}$ are the detected photon rates on detection channels 1 and 2, Δt is the bin size and T is the experiment integration time.

3.4 Experimental methods for measuring correlation

The descriptions of expected $g^{(2)}(\tau_{12})$ values given in Sections 3.2 and 3.3 are idealised - in reality, there are many experimental imperfections that will lead to correlation functions with unexpected artefacts or non-perfect $g^{(2)}(0)$ values. In this section, experimental considerations when measuring photon correlation will be presented. Firstly the impact of signal-to-noise ratio will be discussed. Then, single-photon detector imperfections will be outlined, specifically detector jitter, which affects both SPADs and SNSPDs, and finally backflashes, which only affects SPADs. A feature of single-photon detectors known as the *dead time* leads to a rate-dependent detection efficiency and therefore, at high rates, can affect the measured $g^{(2)}(0)$ value. This is the subject of Chapter 4 and so will not be discussed within this section, but revisited there instead.

3.4.1 Signal-to-noise ratio

A perfect $g^{(2)}(\tau_{12})$ measurement of a correlated light source assumes that all light collected and counted at the detectors is from the source only. In practice, some background light will be measured. This may be ambient light in the laboratory, but is more commonly the excitation laser or dark counts on the detector. Most of these background sources are described by Poissonian statistics, which act to reduce the 'purity' of the correlated $g^{(2)}(\tau_{12})$ function, moving it towards the uncorrelated case of $g^{(2)}(\tau_{12}) = 1$. This leads to a dependence of correlated $g^{(2)}(\tau_{12})$ functions on signal-to-noise ratio (SNR). This effect can be quantified[224] with Equation 3.4.1

$$g^{(2)}_{\text{SNR}}(\tau) = 1 - P_s^2 + P_s^2\left(g^{(2)}_{\text{real}}(\tau)\right), \tag{3.4.1}$$

where P_s is the probability that a coincidence is due to the correlated signal (rather than uncorrelated background), given by the proportion of the correlated signal to all of the light being measured:

$$P_s = \frac{I_s}{I_s + I_b}. \tag{3.4.2}$$

Examples of this effect for antibunched and bunched sources are shown in Figures 3.4.1(a) and (b) respectively, with two different SNR.

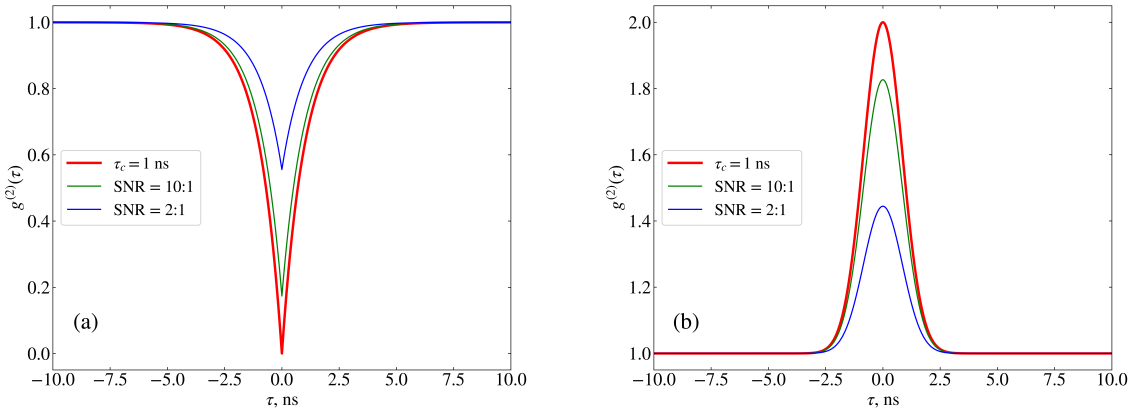

Figure 3.4.1: The impact of SNR on **(a)**: an antibunched correlation function and **(b)**: a bunched correlation function, where in both figures τ_c is the correlation timescale.

3.4.2 Detector jitter

Detector *jitter*, in relation to single-photon detectors and TCSPCM, can be thought of as some uncertainty in photon arrival time. Discussed in Chapter 2, it arises in single-photon detectors due to different physical mechanisms, and in TCSPCM due to the counting electronics. Often, the jitter of a single-photon detector is between tens and hundreds of picoseconds - for the ID Quantique SNSPDs discussed in Chapter 4, it is around 30 ps, and for typical Excelitas SPADs, it is around 300 ps. For a single-photon source with a correlation timescale τ_c that is comparable to the detector jitter, the exponential $g^{(2)}(\tau_{12})$ function becomes 'smeared', going from a sharp dip to a smooth curve. An example of this is shown in Figure 3.4.2(a). It is possible to obtain the 'real' correlation function $g^{(2)}_{\text{real}}(\tau)$ - that is, characteristic of the source only - with an instrument response function (IRF) convolution method. The IRF of the single-photon detector can be modelled as a Gaussian function of time $J(\tau)$, with a width σ defined by the jitter. Equation 3.4.3 gives the relation between the measured and real $g^{(2)}(\tau_{12})$ functions, $g^{(2)}_{\text{meas}}(\tau)$ and $g^{(2)}_{\text{real}}(\tau)$, and the Gaussian function describing the detector jitter, $J(\tau)$.

$$g^{(2)}_{\text{meas}}(\tau) = g^{(2)}_{\text{real}}(\tau) * J(\tau) = \left(1 - e^{\frac{-|\tau|}{\tau_c}}\right) * \left(\frac{1}{\sqrt{2\pi}\sigma} e^{-\frac{\tau^2}{2\sigma^2}}\right); \tag{3.4.3}$$

$$F(\tau) = g^{(2)}_{\text{fit}}(\tau) * J_{\text{fit}}(\tau) = \left(A_1 - B_1 e^{\frac{-|\tau - t_1|}{\tau_c}}\right) * \left(e^{\frac{(\tau - t_2)^2}{2\sigma^2}}\right); \tag{3.4.4}$$

where in both equations, τ_c is the corresponding correlation timescale. By fitting the measured correlation, $g^{(2)}_{\text{meas}}(\tau)$ with a function $F(\tau)$ based on a convolution of an ideal $g^{(2)}(\tau_{12})$ function and the detector IRF due to jitter $J(\tau)$, the $g^{(2)}(\tau_{12})$ parameters can be extracted. Equation 3.4.4 shows the fitting function for this process, where A_1, B_1, t_1, τ_c, t_2 are free fitting parameters, and σ is the detector jitter value. Once A_1, B_1, t_1 and τ_c have been found with this fitting routine, then these parameters give the 'real' $g^{(2)}(\tau_{12})$:

$$g^{(2)}_{\text{fit}}(\tau, A_1, B_1, t_1, \tau_c) = g^{(2)}_{\text{real}}(\tau). \tag{3.4.5}$$

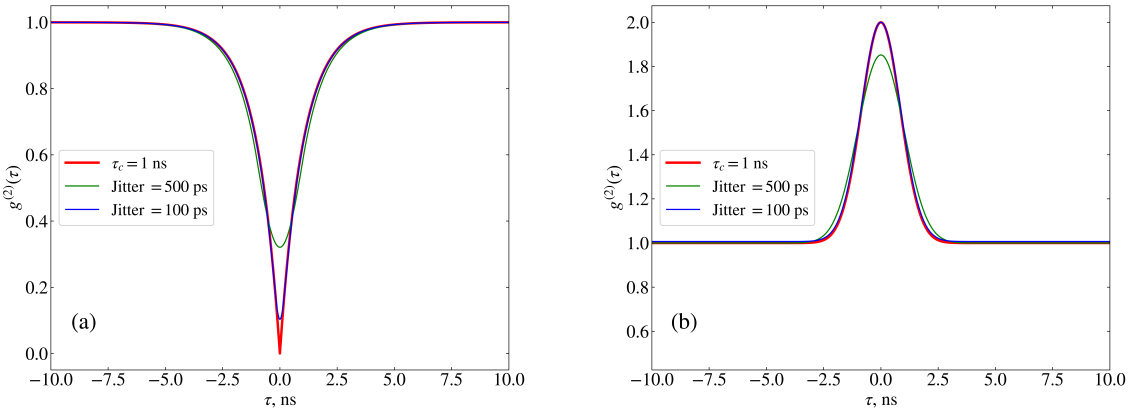

Figure 3.4.2: The impact of detector jitter on **(a)**: an antibunched correlation function and **(b)**: a bunched correlation function, where the correlation timescale τ_c is 1 ns in both cases.

3.4.3 Detector backflashes

A detector backflash is an effect in SPADs where the avalanche current following a detection event may probabilistically generate a photon, described in Chapter 2. This photon can be emitted and may travel back down the fibre coupled into the SPAD. If incident upon a reflecting surface, such as a beamsplitter or fibre end, it may be reflected back and counted again at the other SPAD. This effect can manifest itself as bunching on a correlation function, since coincidences at some point in time (due to being a fixed point in space along a fibre) are occurring with a higher likelihood than randomly. An example of this is shown in Figure 3.4.3(b). This figure, compared to (a), shows that bunching due to backflashes is more evident at lower count rate measurements. This is

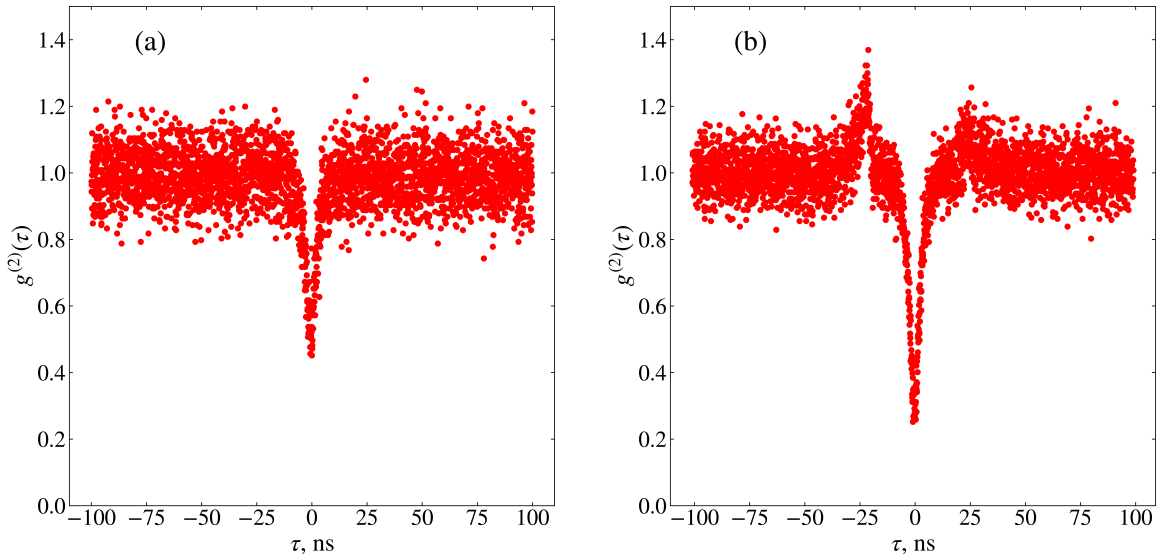

Figure 3.4.3: A second-order correlation function of the fluorescence from a QD transition under non-resonant continuous wave excitation, at two different count rates. **(a)**: The count rate at the SPADs was ∼250 kcps and the measurement was integrated for 5 minutes. Bunching due to reflections of backflashes are not visible here. **(b)**: The count rate at the SPADs was ∼20 kcps and the measurement was integrated for 16 hours. Bunching due to reflections of backflashes are visible at approximately ±30 ns.

because, while two-fold coincidences due to light correlation are built up with respect to the average rate squared, R^2_{avg} - the probability of a backflash causing a coincidence is proportional to the average rate, R_{avg}. Backflashes in SPADs can be reduced with several methods. As mentioned - higher rate measurements will reduce the severity of backflash coincidences compared to correlation coincidences. Spectral filtering can be implemented if the desired signal is at a different wavelength to the backflash, although this can be challenging as backflashes tend to occur across a broad spectral range.[225] If the reflection is thought to be caused by a fibre end launching into free space, this can be reduced by replacing flat fibres (FC) with angled fibres (APC), or by extending the fibre length so that the coincidence occurs at some timescale $\tau_{\text{BF}} >> \tau_c$.

3.5 Analysis methods for calculating correlation

Section 3.3 described timetagged data, how this can be used to extract second-order correlation functions, and the experimental requirements of building up a histogram to count two-fold coincidences. In this section, some computational considerations of extracting correlation functions from timetagged data will be described, and work on developing a MATLAB script to perform this analysis will be presented.

Equation 3.3.2 showed that the number of counts depends most strongly on the channel rates. However - the higher the incident rates on each channel, the more photon

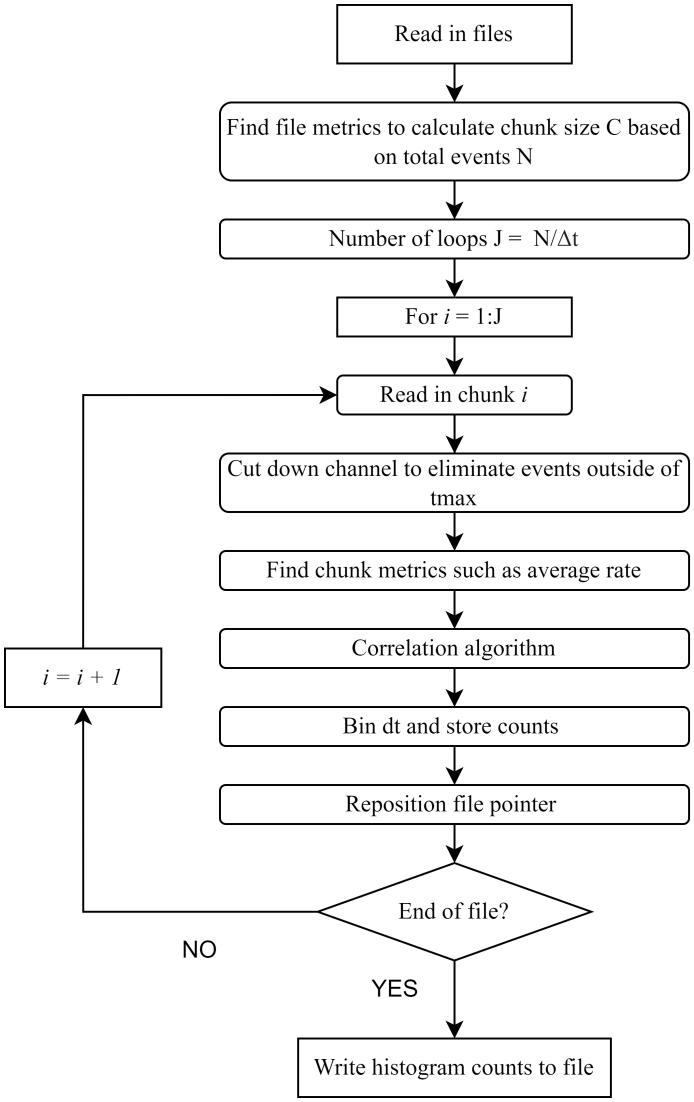

Figure 3.5.1: A simplified algorithm of the 'timestamping' code. This MATLAB script reads in binary files that contain timetagged data and extract the correlation function. The main components of the code are firstly reading the files in chunks, and secondly performing the correlation calculation within each chunk.

events, and the larger the timetagged files become, meaning that memory management is critical. For example - a photon rate of $\sim$ 100 kcps for an hour long experiment recorded on the ID900 time controller generates a binary file of $\sim$ 2.5 GB. To prevent memory overload, the timetagged data files must be read in 'chunks'. Figure 3.5.1 shows a simple flowchart describing the main elements of the timestamping MATLAB script, which will be described one by one.

1. **Read in files**: the binary file containing the timetagged data is opened with the function `fopen`.

2. **Find file metrics**: the last event, the total number of events, the average channel rate and the average spacing of events over the whole file are found using functions `fseek` to move the file pointer between bits, `ftell` to find the current position of

the file pointer, and `fread` to read the value of the data at a particular file pointer location. After these metrics have been found, `fseek` is used to move the pointer back to the beginning of the file before the calculation begins.

3. **Number of loops**: The chunk size of detection channel 1, `chunk1`, is chosen as the total number of events in the file, `events1`, divided by an arbitrary time window `chunk_factor` that defines the number of iterations of the main loop `J`, normally chosen as 5×10^4. Defining chunks related to the number of events in each file helps to keep them synchronised in time. For timetagged data of very high photon rates, >8 Mcps, `chunk_factor` needs to be adjusted so that the length of each chunk in time is much greater than the average spacing between photon arrivals. Before the main loop begins, data storage arrays are initialised and the histogram metrics are chosen: `t_max` gives the bounds of the search window for correlations; `bin_size` gives the bin width in time for the correlation function; `histrange` is defined as a linearly spaced vector from `-t_max` to `+t_max` in spaces of `bin_size`; `co12` is an empty array of length `histrange` - 1.

4. **Main loop**: The main `for` loop of this script moves between the file chunks until the entire reference channel file has been read in and searched.

5. **Cut down channel**: since for every element in channel 1 `c1[i]`, we want to locate elements in channel 2 that are $\pm$`t_max`, we can cut out the first and last `t_max` amount of values in channel 1 to reduce the search window.

6. **Find chunk metrics**: for this chunk, in iteration `i` of `J`, we store information about the data including `chunkrate1` and `chunkrate2` for each channel and `t_int` for average end time of each chunk. This allows us to monitor the count rate and time of the whole experiment at chunk level, which is useful for post-processing.

7. **Correlation algorithm**: The main calculation that finds the time differences between elements in channels 1 and 2. This process is outlined in Figure 3.5.2.

8. **Bin** `dt`: Once the time differences between the current chunk of channel 1 and channel 2, `dt12`, have been found - bin them over `histrange` using the function `histcounts`, and update the count vector `co12`.

9. **Reposition file pointer**: to ensure the file pointers in each channel remain approximately synchronous in experiment time, a time gradient `grad` is calculated based on the current pointer position relative to the final event in channel 2.

10. **End of file**: if `i=J`, or the array containing the channel data is empty, exit the main loop.

11. **Write counts to file**: Save the MATLAB workspace and write `histrange`,`co_12` to a .csv file.

The correlation calculation is done as a loop inside each chunk of the file. This loop iterates through the reference channel event by event, defines a search window in time, and uses a binary search to locate events in the second channel that fall within this window. This method is illustrated in Figure 3.5.2.

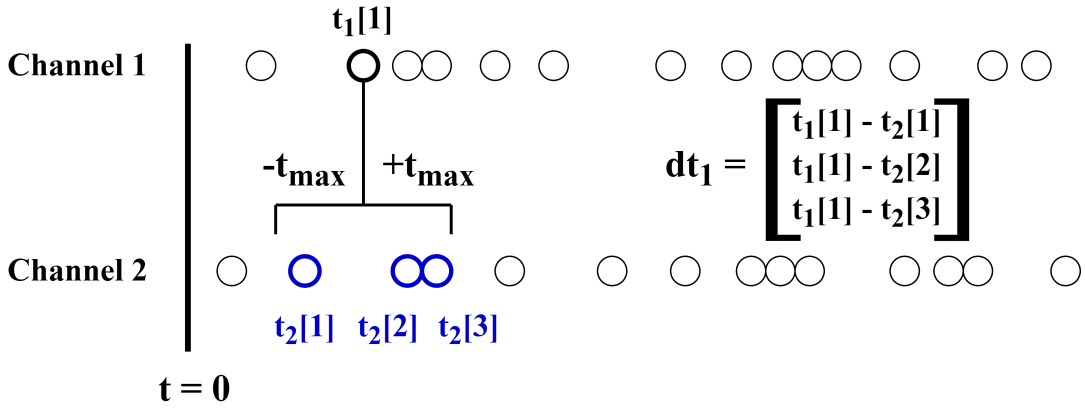

Figure 3.5.2: One detection channel is picked as the reference channel, and then iterated through element-by-element. For each element, the bounds of the 'search window' are defined as ±`t_max` centred on the element value, where `t_max` is a variable defined by the user, typically chosen to be 1 µs. Then, using a binary search algorithm, all elements $\{j\}$ that fall within these bounds in Channel 2 are selected, and the time differences $i - \{j\}$ are calculated. Instead of storing all time difference values, they are sorted into bins of size determined by the user, over the range ±`t_max`. This reduces memory overheads involved in storing large arrays of `dt` or having to write to file - instead, we are just storing a 1D count vector. This process is repeated until we have iterated through Channel 1 entirely.

Since the search window as defined by ±`t_max`, and `bin_size` for the coincidence histogram are user-defined variables, correlations over different timescales and with different resolutions can be obtained for the same dataset. The variable `bin_size` is limited to the size of the photon counter resolution, and this depends on its counting mode - for the ID900 Time Controller, high speed mode was limited to timetags of 100 ps resolution, and high resolution mode was limited to 13 ps. In order to avoid aliasing and incorrectly counting, the bin size of the histogram must be an integer number of these values.

3.6 Higher-order correlations

In the previous sections, we have discussed the theory, experimental and computational considerations of measuring second-order correlation functions for antibunched and bunched sources. In this section, the theory will be extended to consider *higher-order* correlations: $g^{(n)}(\tau_{12}, ..., \tau_{1n})$ where $n > 2$. Firstly, considerations for photon counting and

statistics will be reconsidered, and methods for extending the timestamping script will be discussed. Then, an experiment built and designed to test this code - an optical set-up for generating pseudothermal light - will be introduced and explained. Finally, some third-order correlation functions of the pseudothermal light source and an antibunching light source will be presented, with the analysis detailed and experimental imperfections discussed.

We can generalise the correlation function to an arbitrary n^{th} order:

$$g^{(n)}\left(\mathbf{r_1}, \mathbf{t_1}, ..., \mathbf{r_n}, \mathbf{t_n}\right) = \frac{\langle I\left(\mathbf{r_1}, \mathbf{t_1}\right) ... I\left(\mathbf{r_n}, \mathbf{t_n}\right)\rangle}{\langle I\left(\mathbf{r_1}, \mathbf{t_1}\right)\rangle ... \langle I\left(\mathbf{r_n}, \mathbf{t_n}\right)\rangle}, \tag{3.6.1}$$

and in terms of τ_{1n}:

$$g^{(n)}\left(\tau_{12}, ..., \tau_{1n}\right) = \frac{\langle I\left(t\right) ... I\left(t + \tau_{1n}\right)\rangle}{\langle I\left(t\right)\rangle^n}. \tag{3.6.2}$$

As with the $g^{(2)}\left(\tau_{12}\right)$ function and two-fold coincidences, we can say that the $g^{(n)}\left(\tau_{12}, ..., \tau_{1n}\right)$ function yields the relative likelihood of an n-fold coincidence. Experimentally - an n^{th} order correlation function requires n detection channels, and is searching for n photons arriving in n separate channels at times $\tau_{12}, ..., \tau_{1n}$. The number of histogram counts per bin for an n-fold coincidence is given by Equation 3.6.3

$$N_{\text{count}} = \prod_{i=1}^{n} R_i \times \left(\Delta t\right)^{(n-1)} \times T. \tag{3.6.3}$$

Figure 3.6.1 demonstrates the challenge in building up histogram counts for increasing orders of $g^{(n)}\left(\tau_{12}, ..., \tau_{1n}\right)$, and obtaining meaningful statistics. For N counts, the Poissonian counting error σ_N as a percentage is given by

$$\sigma_N = \frac{\sqrt{N}}{N}. \tag{3.6.4}$$

For an average channel rate of 500 kcps and a histogram bin size of 1 ns, a $g^{(2)}\left(\tau_{12}\right)$ with less than 1% counting error can be built up in minutes - but acquiring a $g^{(3)}\left(\tau_{12}, \tau_{13}\right)$ with this level of counting error will take $\sim 80,000$ seconds, or 22 hours. Over the limits of this graph, which runs to 1×10^6 second or 11 days, it is not possible to build up a $g^{(4)}\left(\tau_{12}, \tau_{13}, \tau_{14}\right)$ with less than 10% counting error for this count rate and bin size. There are a few significant points to raise here. Firstly, we note that in this figure, the rate of 500 kcps is an *average* channel rate - so, for a four-fold correlation, the source should have a total rate of 2 Mcps. Secondly, the number of histogram counts N is for an uncorrelated source - in general, for $g^{(n)}\left(\tau \to \infty\right)$. This means that building up the statistics of a bunched source around the correlation timescale will be quicker than indicated on Figure 3.6.1. The opposite is also true - in the case of an antibunched source, it will be slower. In fact, the better the single-photon source is - the closer $g^{(2)}\left(0\right)$ is to 0 - the longer it will

take to build up counts for $g^{(n)}(\tau_{12},...,\tau_{1n})$. Finally, a comment on normalisation - how to move from raw counts, sometimes denoted $G^{(n)}(\tau)$, to a normalised $g^{(n)}(\tau_{12},...,\tau_{1n})$ function. Considering Equation 3.6.3, it appears as though the uncorrelated events at long delay times can be normalised with this expression that depends on photon rate, bin size and integration time. However - this method may be unreliable[92] for varying count rates, and at high count rate where detected photon rate is different to incident photon rate - the latter is discussed in detail in Chapter 4. In general, normalising $g^{(n)}(\tau_{12},...,\tau_{1n})$ throughout this thesis is achieved by using the average of the histogram bin counts at $\tau \to \infty$. This is justified by accounting for the fluctuating count rates experienced for different sources in different experiments, described in the relevant sections in turn.

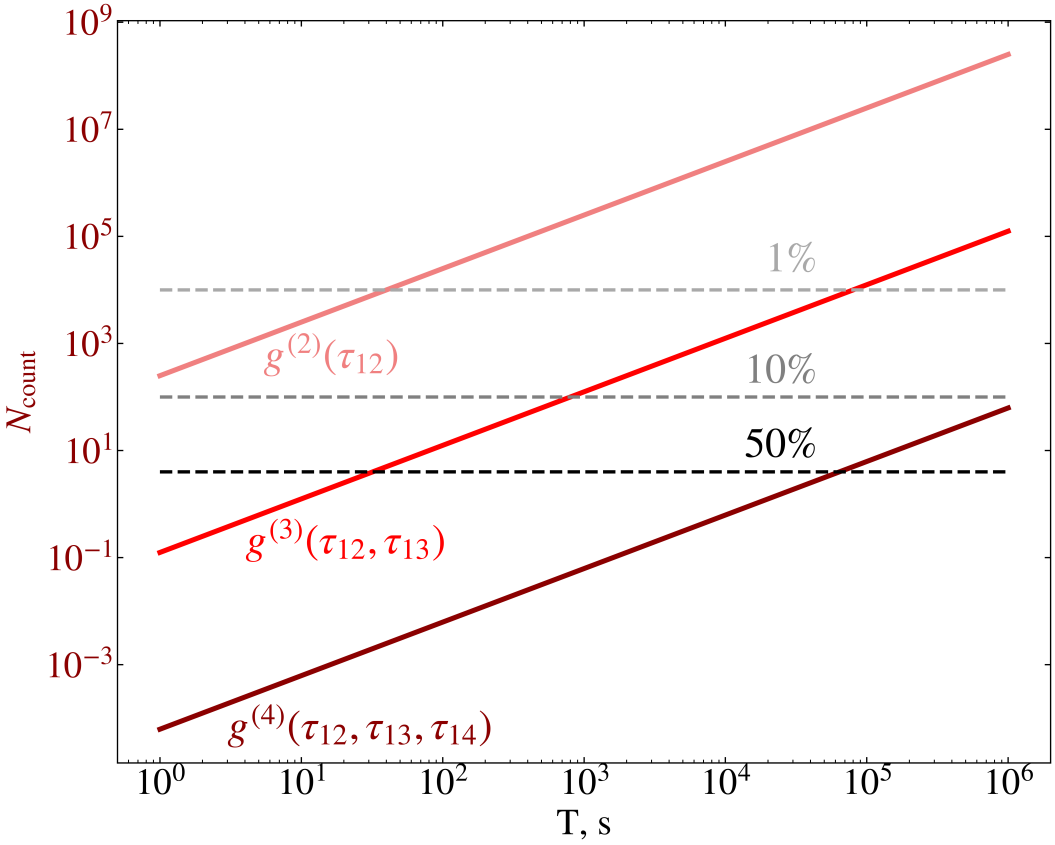

Figure 3.6.1: Building up histogram counts for $g^{(2)}(\tau_{12})$, $g^{(3)}(\tau_{12},\tau_{13})$ and $g^{(4)}(\tau_{12},\tau_{13},\tau_{14})$. Here, the coloured lines indicate the number of histogram counts built up in each respective $g^{(n)}(\tau_{12},...,\tau_{1n})$ function for an average channel count rate of 500 kcps and a bin size of 1 ns. The dashed grey lines mark the histogram count number N at which we have 1%, 10% and 50% counting error respectively.

3.6.1 Generating pseudothermal light

In order to investigate higher order correlations, and test the timestamping script, an experiment to generate pseudothermal light and take four-fold correlation measurements was developed. This is a highly adaptable experiment able to generate light that exhibited photon bunching over a tunable timescale. In this section, the physics and experimental considerations for this set-up will be presented.

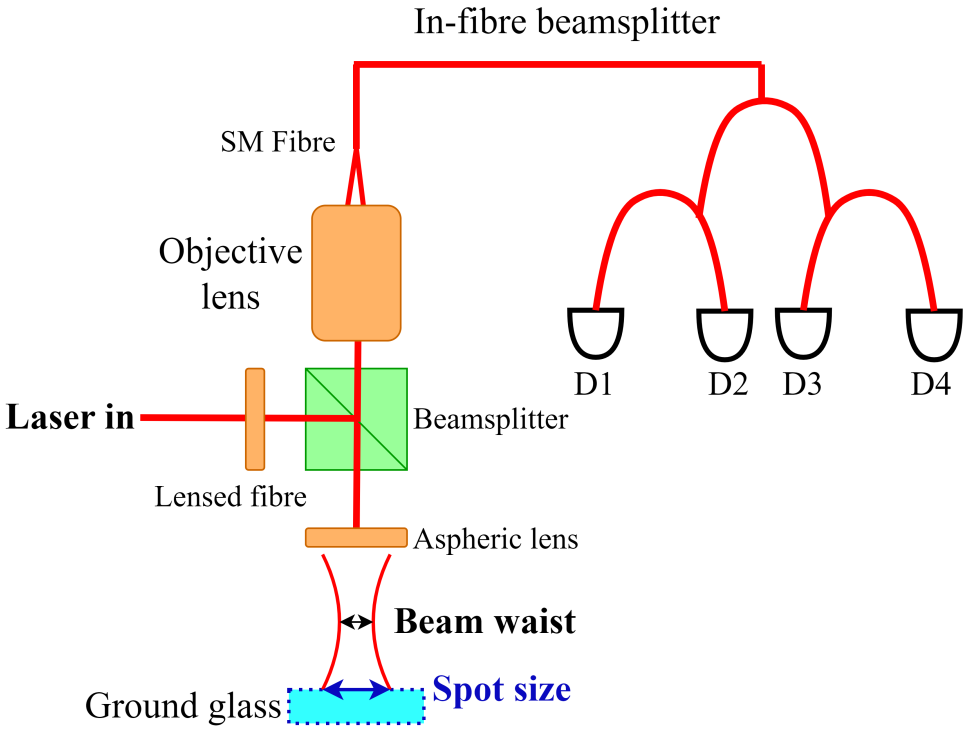

Figure 3.6.2: The experimental set-up for the pseudothermal light experiment. 850 nm continuous wave laser light was coupled into the experiment via a lensed fibre and a cube beamsplitter. The aspheric lens focussed the light onto the ground glass, which was mounted onto a translational z-stage for fine control of the focus. The speckle was collected into single-mode fibre via a 0.26 NA Mitutoyo objective lens, and counted over four SNSPD detection channels.

It is possible to recreate the statistics of thermal light by scattering laser with a rotating *ground glass*, first demonstrated by Martienssen and Spiller.[226] Ground glass is a type of optical component with some associated surface roughness or 'grit'. Incoming light is reflected off or transmitted through the glass depending on its coating, and each grit acts as a randomly-distributed scattering centre. The emerging beam has spatial fluctuations as a result. If the ground glass is also rotated, the beam fluctuates in time and its coherence time is related to this speed of rotation.[227] The interference pattern of light scattered off the rough surface depends on the ratio between the grit size d_{grit} and the spot size d_{spot} of the incoming light. In the limit of a large number of scattering centres, such that $d_{\text{spot}} \gg d_{\text{grit}}$, a complex interference pattern known as *speckle* is formed. The correlation of speckle has thermal statistics, characterised by Gaussian intensity fluctuations, where the associated correlation timescale τ_c is inversely proportional to the

in-plane velocity of the ground glass.[228] If the spot is too small, the intensity fluctuations become abrupt and the speckle pattern is not formed. Hence, by adjusting the optical components of the experiment and changing the spot size, it is possible to vary the bunching lifetime of the pseudothermal light source. This results in a highly versatile experiment that can be used to emulate thermal light statistics with monochromatic light.

In this experiment, a 1500-grit reflective ground glass with protective silver-coating was glued to a small motor, which was connected to a power supply to control the rotation speed. Laser light (850 nm PicoQuant diode laser) was coupled into the experiment via a lensed fibre, and focussed onto the ground glass with a convex lens. The speckle pattern was collected into a 0.26 NA Mitutoyo objective lens and focussed into single-mode fibre, which was incident on four SNSPD detection channels via an in-fibre beamsplitter network. This experiment is shown in Figure 3.6.2. To investigate the relationship between spot size and bunching lifetime, in a manner similar to the study by Kuusela,[229] the correlation for different spot sizes was investigated. Figure 3.6.3 demonstrates the

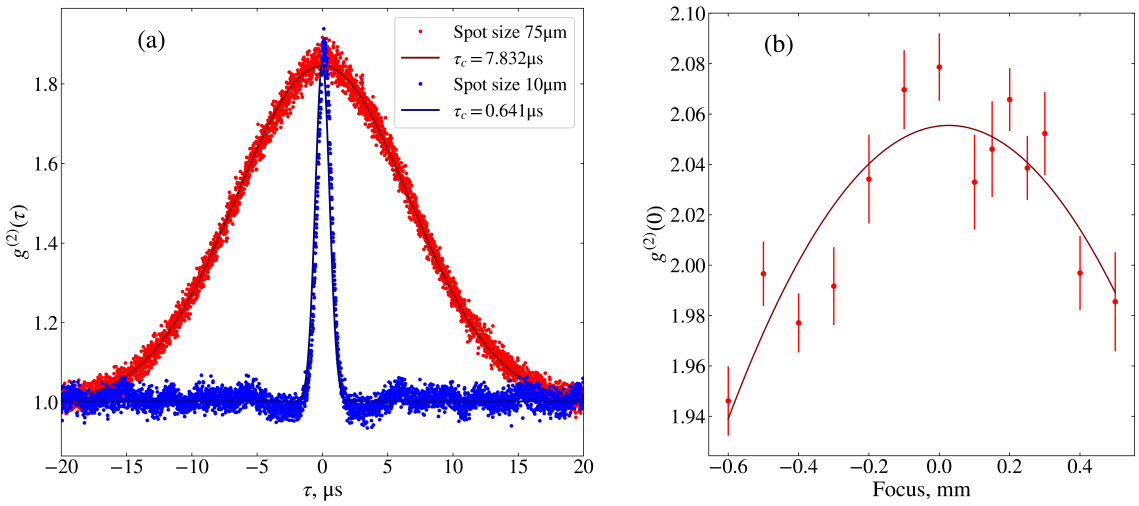

Figure 3.6.3: Tunable characteristics of the pseudothermal light experiment. **(a)**: The change in correlation timescale as the spot size changes. As $\tau \to \infty$, there are periodic oscillations visible in the $g^{(2)}(\tau_{12})$ function. These features are related to the roughness of the mirror. **(b)**: The change in the peak value of the $g^{(2)}(\tau_{12})$ function with spot size. The error bars on the red data points are estimated with counting error, and the dark red line is a fit based on a parabolic function.

tunable nature of the pseudothermal light experiment. In Figure 3.6.3(a), the change in correlation timescale τ_c with a coarse change in spot size is shown. Here, the spot size was changed by swapping out the convex lens used to focus the incident light onto the ground glass for one with a longer focal length. Oscillations in correlation for $\tau > \tau_c$ are observed - this is due to periodic intensity fluctuations of the speckle pattern, related to the rough surface of the mirror as it rotates through 360°. In Figure 3.6.3(b), the change

in the speckle statistics with fine changes in the spot size is shown. Here, the ground glass is being translated along its z-axis stage in order to move through the beam waist. This shows how it is possible to coarsely and finely adjust the spot size to obtain the desired correlation timescale τ_c as well as statistics $g^{(2)}(0)$.

3.6.2 Extending timestamping script

Once the code had been developed to extract $g^{(2)}(\tau_{12})$ from the pseudothermal light experiment described in Section 3.6.1 - it was extended to read in a third detection channel, and find the triple coincidences between the three channels. The main algorithm was the same, except now the correlation algorithm had three key steps:

1. Step 1: Find two-fold coincidences between channel 1 and channel 2, and bin the time differences with `histcounts`;
2. Step 2: Find two-fold coincidences between channel 1 and channel 3, and bin the time differences with `histcounts`;
3. Step 3: Find three-fold coincidences between channel 1, channel 2 and channel 3, and bin the time differences with the bivariate histogram function `histcounts2`.
4. Step 4: When updating the three-fold coincidence count vector, ensure that each combination of coincidences between channel 1 and 2, and channel 1 and 3, is correctly combined and counted separately with a nested `for` loop.

So the 'g3 timestamping' script was able to correlate three detection channels, C1, C2, C3 - finding two second-order correlation functions, $g^{(2)}(\tau_{12})$ and $g^{(2)}(\tau_{13})$, and one $g^{(3)}(\tau_{12}, \tau_{13})$. This script was tested on the pseudothermal light experiment, as well as some antibunched light sources. Figure 3.7.1 shows an example of a third-order correlation function for a colour centre in AlN. Interesting features are described in the caption. In Chapter 5, some third-order correlations of QD will also be shown.

3.7 Discussion of results and future outlook

Figures 3.7.1 and 3.7.2 show some second- and third-order correlation functions that have been extracted with the timestamping script for antibunched and bunched light sources respectively. In Section 3.4, experimental factors that may affect correlation functions in real experiments were discussed. Several of these factors are demonstrated in Figure 3.7.1. Firstly, the low count rate meant that even over a four-hour measurement it was difficult to build up histogram counts for the $g^{(3)}(\tau_{12}, \tau_{13})$, with the average count per bin at infinite delay time being ~ 12. Secondly, by using SPADs and recording a low count rate measurement the correlation is affected by backreflections on detection channel 2,

which are evident in both measurements correlated to this channel. The pseudothermal

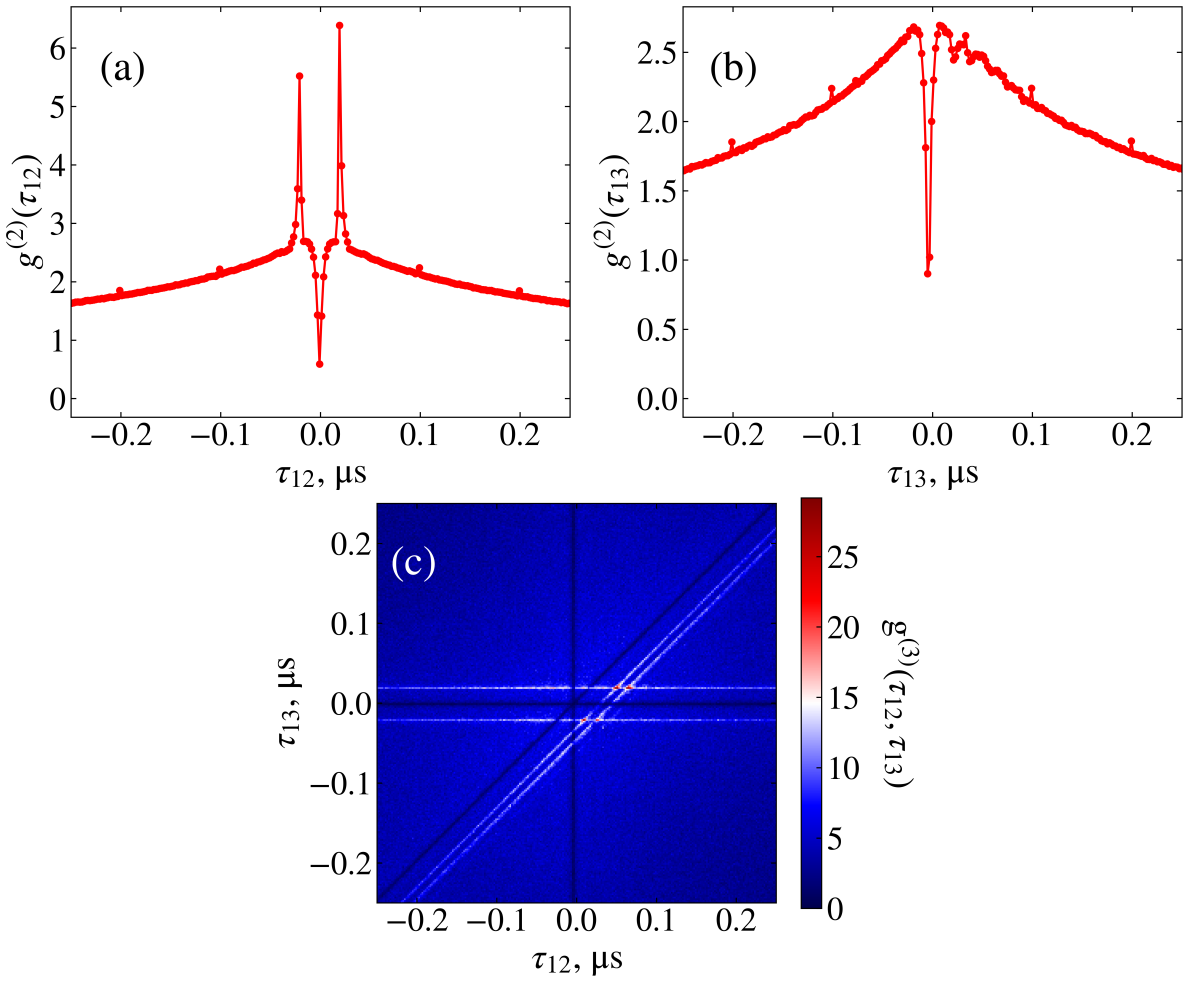

Figure 3.7.1: Antibunching from a colour centre in AlN. These emitters are three level systems which exhibit antibunching and bunching over two characteristic timescales[51] at room temperature, over a wavelength range between 550 to 650nm. The second-order correlation function for delay τ_{12} and τ_{13} shown in **(a)** and **(b)** respectively, and the third-order correlation function shown in **(c)**. In **(a)** and **(c)** we observe backreflections causing bunching at approximately ±20 ns. This measurement was integrated for four hours and average channel count rates were 6 kcps, 39 kcps and 36 kcps for channels 1, 2 and 3 respectively - unbalanced count rates are due to an asymmetric beamsplitter network. In **(a)** and **(b)** small periodic peaks at multiples of ∼100 ns are visible; this is caused by an aliasing effect between the edges of the timestamp bins (dictated by the detector electronics) and the histogram bins (dictated by the script).

light set-up was an optical experiment that can produce a tunable correlation timescale, monochromatic source that exhibits thermal statistics, with careful adjustment of the optics. With this, insights into the physics of speckle and its associated statistics were provided. Figure 3.7.2(c) shows a $g^{(3)}(\tau_{12}, \tau_{13})$ of the pseudothermal light source. As expected according to theory, we observe $g^{(n)}(0) \to n!$ with $g^{(3)}(0,0)$ being ≈ 6. Since the count rate of this source was related to the incoming laser intensity, this experiment was also highly tunable in count rate - this advantage is explored in more detail in the following

Chapter 4, where we examine some rate-dependent properties of single-photon detectors. The timestamping script established a simple algorithm for reading in timetagged data

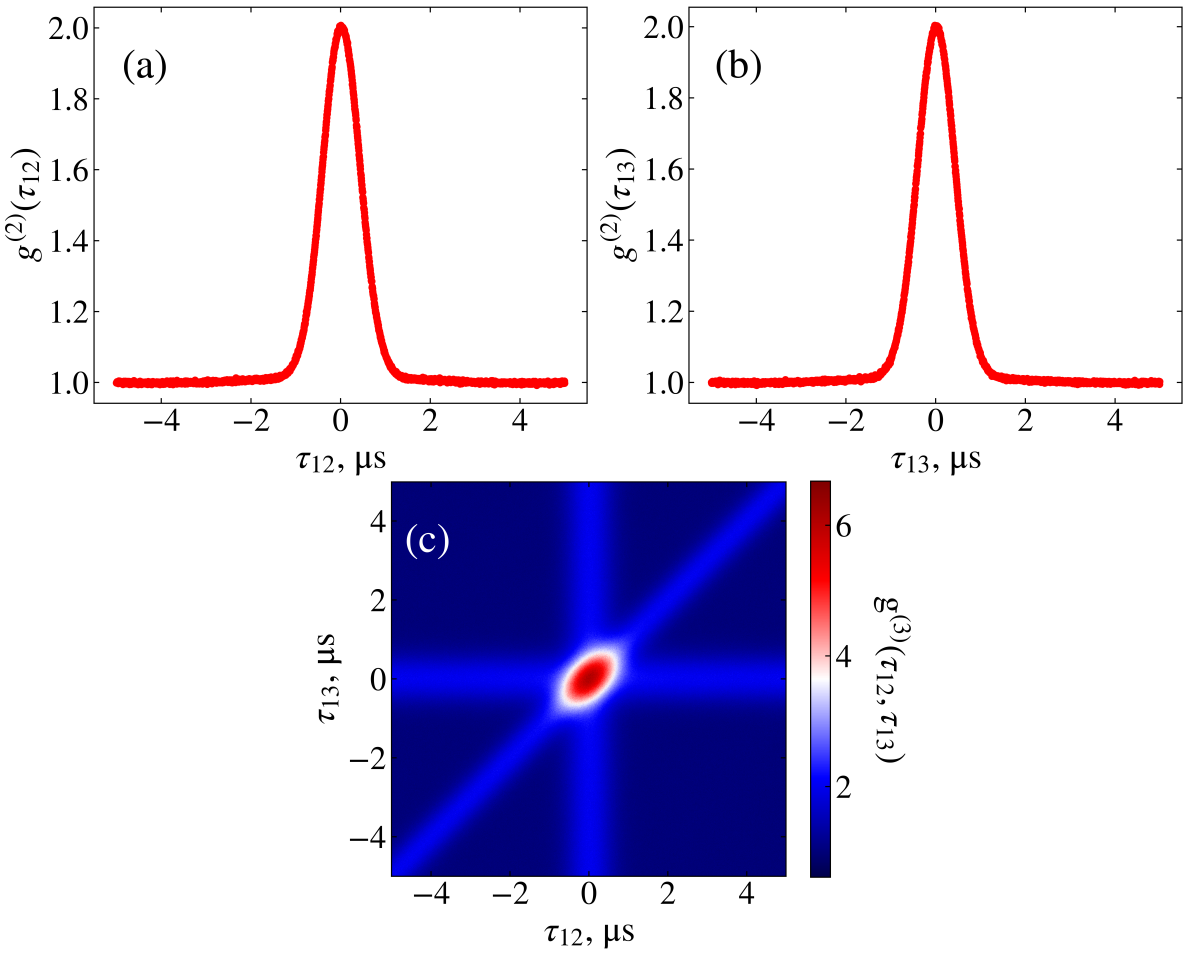

Figure 3.7.2: Bunching from the pseudothermal light experiment. The second-order correlation function for delay τ_{12} and τ_{13} shown in **(a)** and **(b)** respectively, and the third-order correlation function shown in **(c)**. This measurement was integrated for one hour and the average channel count rates were all approximately 100 kcps.

files containing timestamps of photon arrivals and extracting a second- and third-order correlation function, with a user-defined search window and bin size. The timestamping script was used throughout the work presented in this thesis for different light sources, so further examples of its use will be shown in later chapters. Testing this script on light sources with different correlation behaviour provided insight into the limitations of the chunking method, and allowed different edge cases to be adjusted for. For example, when using the timestamping script on files from a very high rate ($> 10^7$ cps), the chunk size must be adjusted to avoid a pile-up effect. Future work on the timestamping code should focus on further testing of 'edge case' measurements, to test its resilience and any as yet undiscovered bugs. For example, in Figure 3.7.1 periodic peaks are visible in the second-order correlation function - this data was processed with an earlier version of the code that did not correctly align the bins of the histogram with those of the

detector e.g. present in the timestamps. This bug was corrected in a later version, for example in Figure 3.7.2 the periodic peaks are not visible. Given the simple nature of the calculation being performed - finding time differences of ordered lists is computationally simple - I think that a worthwhile study would be to parallelise the script somehow, in an automatic or 'smart' way based on the metrics of the files being read in. There may also be merit in developing this script in a lower-level language, such as C, since MATLAB is an interpreted language.

In this chapter, the theory of photon statistics and correlation was outlined, and a discussion on experimental considerations and computational analysis was presented. The potential limitations of practical experiments with imperfect efficiencies and real single-photon detectors were described, and the experimental techniques will be applied in the remaining chapters of this thesis on the various second- and third-order correlation functions that are measured. The next chapter uses both the pseudothermal light experiment and the timestamping script to investigate the impact of detector dead time on photon counting and correlation.

CHAPTER 4

MEASURING CORRELATIONS ON IMPERFECT SINGLE-PHOTON DETECTORS

4.1 Introduction

Chapter 3 presented an overview of photon correlation. This chapter will demonstrate how real single-photon detectors are limited in their ability to accurately measure photon correlation. Single-photon detectors are an essential tool in quantum optics, enabling photon counting and a variety of quantum technologies. All single-photon detectors have a *dead time* - a finite time following a detection event for which the detector cannot register subsequent photons - limiting its maximum counting rate. The effect of dead time on a detector's ability to accurately count photons has previously been mathematically modelled.[230–233] Recent work has focussed on estimating single-photon detection efficiency by developing a dead time correction.[234–237] In these works, the detection efficiency is assumed as a Heaviside function, and only the Poissonian case is treated. There remains to be a generalised model that can correct the counting distribution of correlated light sources for detectors with a time-dependent detection efficiency recovery.

In this chapter I will present a model describing the rate-dependent detection efficiency of a single-photon detector with finite dead time for the three statistical distributions of light. The real detector recovery is experimentally verified for an SNSPD detection system and used for a numerical simulation of the detected rate. The impact of the real detector recovery on the second-order correlation function is described mathematically, and experimental data is presented to demonstrate how high photon rates alter the second, third and fourth-order correlation functions.

4.2 Detector dead time

Introduced in Chapter 1, the dead time is one of a few key metrics used to describe and compare single-photon detectors. The physical mechanism behind it depends on the detector, explained in more detail in Chapter 2. In a SPAD, the dead time is a result of the active quenching required to lower the voltage response and sweep away carriers in the p-n junction. In a SNSPD, the dead time is associated with the recovery of the supercurrent in the nanowire as the photon hotspot is reduced. In both systems, the dead time is typically on the order of tens of nanoseconds. Both of these detectors are described in more detail in Chapter 2.

In this first section, we will introduce two interpretations of detector dead time according to various models and definitions in literature. The first is a simplistic model based on a Heaviside function, and the second is a more complex time-dependent model based on experimental measurements.

4.2.1 Heaviside detector dead time

As described in the previous section, many current reports in the literature for dead time correction models assume that the detection efficiency is described by a Heaviside function, i.e.

$$\eta(t) = \begin{cases} 0 & \text{if } t \leqslant T_{\text{dead}} + t_{\text{detection}} \\ 1 & \text{if } t > T_{\text{dead}} + t_{\text{detection}} \end{cases}. \tag{4.2.1}$$

Equation 4.2.1 describes the function shown in Figure 4.2.1. Considering the definition of

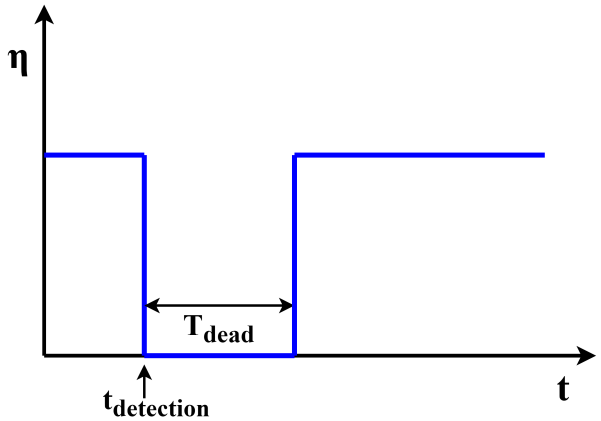

Figure 4.2.1: Detection efficiency η versus time since detection as a Heaviside function. The detector is assumed to instantaneously recover to 100% of its normal detection efficiency following the dead time.

efficiency in terms of measured photons: we can define time-averaged detection efficiency $\varepsilon = \langle \eta(t) \rangle$ simply as the ratio of detected photons R' to incident photons R. Following a detection event, as indicated in Figure 4.2.4, the detector enters its deadtime, after

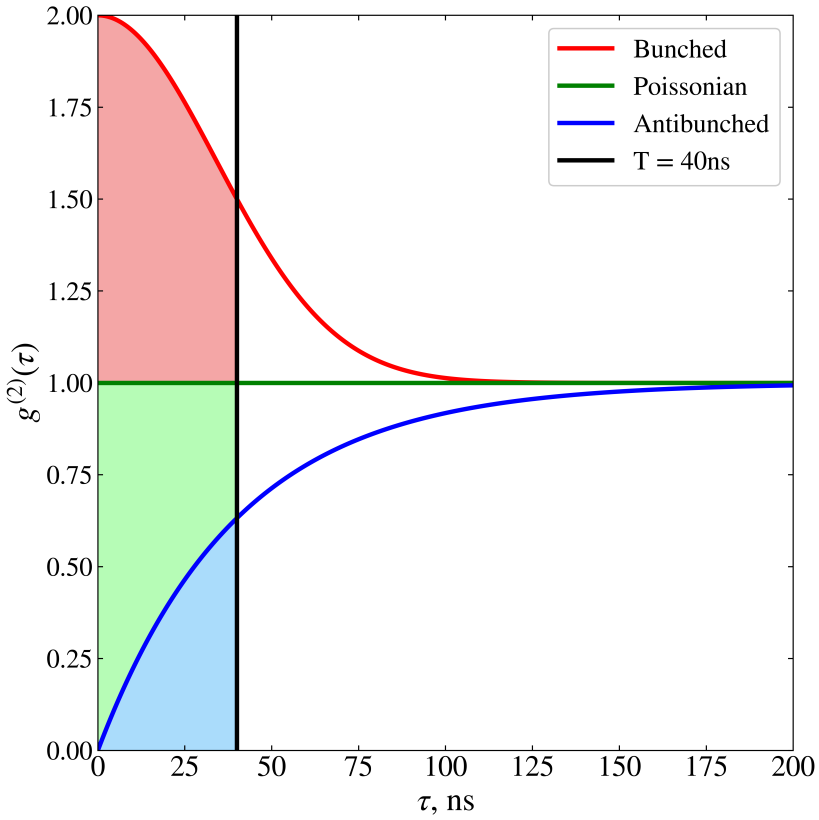

Figure 4.2.2: Photons that go undetected during the deadtime for bunched, Poissonian and antibunched light sources. The bounded area between the $g^{(2)}(\tau_{12})$ and the black line indicating the detector dead time represents the photons missed for each type of source.

which it immediately recovers to its normal response. The detection efficiency during the dead time is zero, thus before T_{dead} has elapsed the detector will miss some number of incoming photons. For sources with different statistics, the photons that go undetected during the dead time will vary, in accordance with the relative conditional probability of subsequent detection - the second-order correlation function, $g^{(2)}(\tau_{12})$. Figure 4.2.2 shows the $g^{(2)}(\tau_{12})$ for bunched, antibunched and Poissonian light, where the equations for the bunched and antibunched correlation functions are

$$g^{(2)}(\tau) = 1 + \exp\left[\frac{-\ln|2| \cdot \tau^2}{T^2}\right], \tag{4.2.2}$$

$$g^{(2)}(\tau) = 1 - \exp\left[\frac{-|\tau|}{T}\right], \tag{4.2.3}$$

respectively. The characteristic correlation timescales have been set to 40 ns, also marked on the axis with the vertical black line, as the dead time.

Chapter 3 presented that, for an uncorrelated light source, the number of coincidence counts N_{counts} in a correlation histogram is proportional to the incoming rate on each detection channel - $N_{counts} = R_1 \times R_2 \times t_{bin} \times T_{int}$. This is a consequence of the denominator of the $g^{(2)}(\tau_{12})$ function in the limit $\tau \to \infty$. The number of undetected photons can

be estimated using a similar argument for the Poissonian case, where the conditional probability of a subsequent detection is equal at all τ. The total number of incident photons R is equal to the detected rate R' plus the photons that are missed during the dead time. The dead time is triggered by a detected photon, and the number of photons missed is proportional to the incident rate R multiplied by the dead time T_{dead}, so the total missing photons are given by $R \cdot R' \cdot T_{\text{dead}}$. Hence we have that

$$R = R' + R' \cdot R \cdot T_{\text{dead}}, \tag{4.2.4}$$

which we can rewrite in terms of detected rate R'

$$R' = \frac{R}{1 + R \cdot T_{\text{dead}}}. \tag{4.2.5}$$

This simplistic model is only valid in the case where $g^{(2)}(\tau_{12}) = 1$. In order to find an expression for R' in the case of a time-dependent $g^{(2)}(\tau_{12})$ i.e. non-Poissonian light sources, we must consider the real detector recovery, which in fact is time-dependent following a detection event.

4.2.2 Time-dependent detector recovery

As mentioned in Section 4.2, the recovery of the supercurrent in SNSPDs typically takes tens of nanoseconds. The response of the superconducting state can be described by a model based on an electrical circuit.[209] The SNSPD can be represented as an inductor with some series resistance, a bias current, a load impedance and a switch - shown in Figure 4.2.3(a). The inductor represents the superconducting state which has a large kinetic inductance[208] and the resistor R_n has a time-dependent resistance and represents the hotspot. The detector operates in the following way: upon absorption of a photon, the switch opens and diverts the bias current onto some load impedance Z_0, where the output pulse is measured. An example of an SNSPD output pulse is shown in Figure 4.2.3(b). This output pulse has a rise time τ_{out} related to the circuit parameters by the following expression:

$$\tau_{\text{out}} = \frac{L_k}{Z_0 + R_n(t)}. \tag{4.2.6}$$

As the switch closes to remove $R_n(t)$, the current in the nanowire recovers to I_{bias} over some time period τ_R given by:

$$\tau_R = \frac{L_k}{Z_0}. \tag{4.2.7}$$

The sum of the output pulse rise time τ_{out} and the supercurrent reset time τ_R result in the overall *recovery time* of the detector. From Equations 4.2.6 and 4.2.7 we see that the nanowire kinetic inductance L_k is the principal limitation of the detector recovery time. The effect of this recovery time is to limit the maximum count rate and to induce a

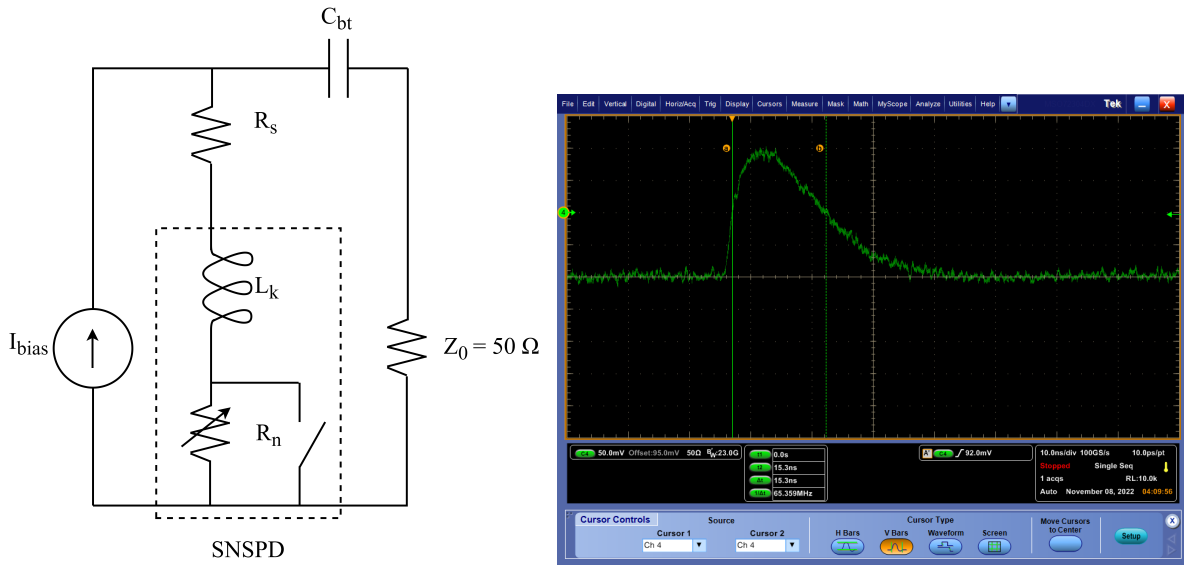

Figure 4.2.3: **(a)**: Adapted from Figure 1b in Yang *et al.*, an electrical circuit describing the operation of an SNSPD. The inductor represents the large kinetic inductance of the superconducting nanowire L_k and the resistor represents the hotspot with a time-dependent resistance, $R_n(t)$. **(b)**: The output pulse of an SNSPD system measured on an oscilloscope. The falling edge of the pulse

time-dependent detector recovery, where the time taken to recover to the time-averaged detection efficiency is not described by a Heaviside function, as detailed in the previous Section, but instead has a smooth time-varying response. The definition of the total

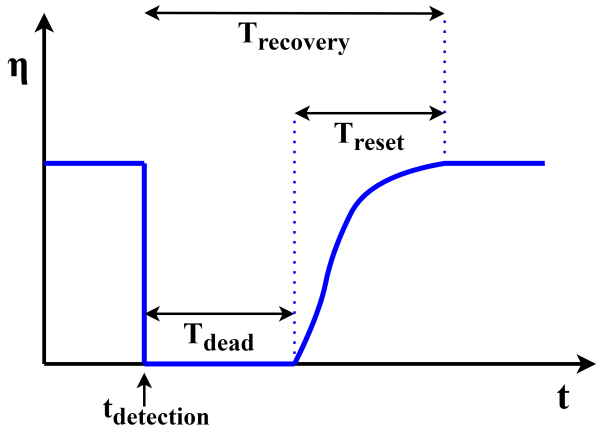

Figure 4.2.4: Some key terms in defining a single-photon detector's detection efficiency recovery following a detection event at $t_{detection}$. The detection efficiency is zero for the duration of T_{dead}, the detector dead time. There is a smoothly varying recovery to the average detection efficiency over some time T_{reset}, the detector reset time. The total recovery time of the detector $T_{recovery}$ is the sum of the dead time and the reset time.

detector recovery time for a general single-photon detection system is depicted in Figure 4.2.4, based on a definition in the European Telecommunications Standard Institute (ETSI) group specification document for QKD.[238] The fact that over this reset time, the detection efficiency is smoothly varying, is an important factor that has consequences

at high photon rate. In the following sections, we show how the real detector recovery $\eta(\tau)$ can be experimentally determined, used to more accurately model the detected rate and overall averaged detection efficiency ε, and finally its impact on the measured correlation function $g^{(n)}(\tau)$ for $n = 2, 3, 4$.

4.3 The waiting time distribution

The *waiting time distribution* is the distribution of the time interval between two successive (random) events.[239] In statistics it is used to relate the exponential distribution to the time between events that can be described by Poissonian statistics. In terms of photon counting, it is a similar concept to the second-order correlation function but with a subtle difference. An important distinction to recall, is that τ_{12} refers to a time *difference* between two detection channels, $\tau_{12} = t_2 - t_1$. The $g^{(2)}(\tau_{12})$ denotes the probability of detecting a photon at any time difference τ_{12} given that a photon was detected at $\tau_{12} = 0$, relative to the Poissonian distribution where $g^{(2)}(\tau_{12}) = 1 \ \forall \ \tau_{12}$. Hence, as $\tau \to \infty$, all second-order correlation functions tend to 1, since subsequent photons become uncorrelated at long timescales. The waiting time distribution is obtained from the probability of detecting a second photon at some time t given that the last detected photon was at $t = 0$, and no other photons have been detected since, which thus drops off exponentially, with an exponent determined by the average rate. As described in Chapter 3, timetagged data files provide a list of every single photon arrival per detection channel. It is possible to use this data to provide information on the real detector recovery as a function of time since previous detection, which is denoted as τ. By finding the time differences between each consecutive pair of detected photons arriving at one channel, and obtaining the histogram of these subsequent time differences, $\eta(\tau)$ can be measured for each detection channel. Figure 4.3.1(b) shows the experimentally measured time-dependent recovery for the four near-infrared detection channels of our SNSPD system (IDQuantique ID281 SNSPD detectors with ID900 Time Controller photon counter and timetagger) when illuminated with Poissonian light (highly attenuated 850 nm PicoQuant diode laser). Differences across the four detection channels can be attributed to slight differences in efficiency, caused by SNSPD polarisation sensitivity and different detector bias values, as well as experimental features such as unbalanced beamsplitters. Detailed discussion of the SNSPDs can be found in Chapter 2, and the experiment for generating the Poissonian and bunched light in this study can be found in Chapter 3. Here, τ is the time difference between the first detection event at $t_1 = 0$ and the next detection event at some time $t_2 = t$. The exponent of each dataset in Figure 4.3.1(a) indicates different rates in accordance $\Omega = e^{-R \cdot \tau}$. In Figure 4.3.1(b) this has been normalised out to obtain the real detector recovery. The average time over the four channels at which the signal has recovered to 50% of its average detection efficiency

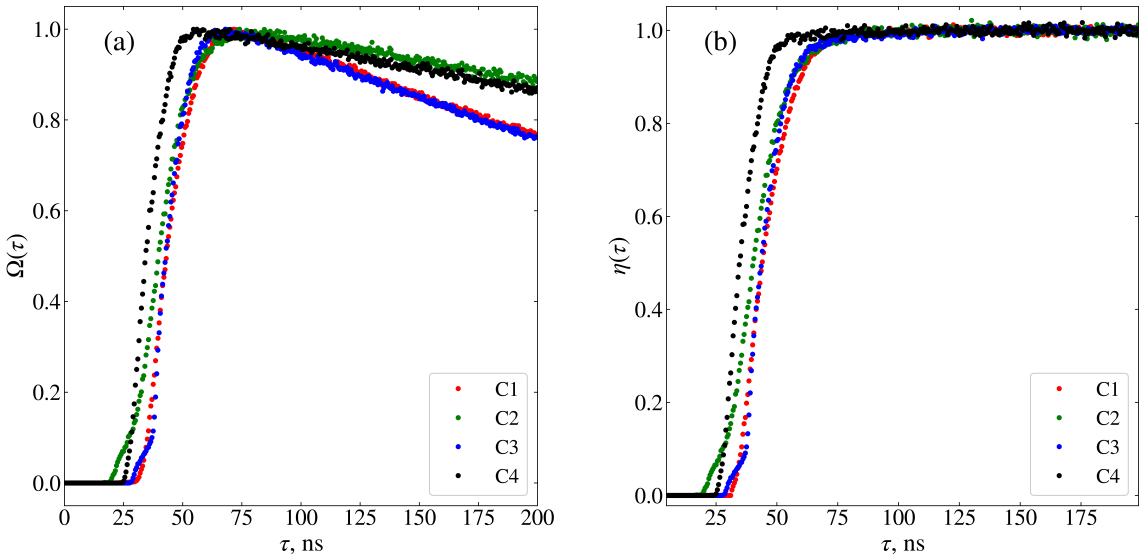

Figure 4.3.1: Experimentally verifying the time-dependent detector recovery. **(a)**: The waiting time distribution for each detection channel on the SNSPD system. This function is generated by plotting the histogram of time differences between consecutive photon arrivals. The count rate has been normalised to the maximum value for each channel for scaling purposes. **(b)**: The real detector recovery, where the rate-dependent exponents have been normalised out to obtain $\eta(\tau)$. When $\eta(\tau) = 1$, the detector has recovered to its time-averaged detection efficiency value ε.

is 40 ns. The waiting time distribution $\Omega(\tau)$ is modelled using a numerical simulation described by Equation 4.3.1, where

$$\Omega(\tau + \delta\tau) = \Omega(\tau) - \Omega(\tau) \cdot \eta(\tau) \cdot P(\tau) \cdot \delta\tau. \tag{4.3.1}$$

Here: τ is the time since initial detection, $\delta\tau$ is an infinitesimal time interval, $\eta(\tau)$ is the detector recovery and $P(\tau)$ is the probability of a second photon arriving at the detector. The detection probability $P(\tau)$ is assumed to be related to the second-order correlation function and the incoming intensity I,

$$P(\tau) = A \cdot g^{(2)}(\tau) \cdot I, \tag{4.3.2}$$

where A is a constant related to the detection efficiency ε. The mean waiting time $\bar{\tau}$ is given by

$$\bar{\tau} = \frac{\int_0^\infty \tau \cdot \Omega(\tau) \cdot \delta\tau}{\int_0^\infty \Omega(\tau) \cdot \delta\tau}. \tag{4.3.3}$$

For a detector with no dead time and hence no recovery, $\eta(\tau) = \eta_0$. For Poissonian light with $P(\tau) = P_0$, we can use a trial function $\Omega(\tau) = e^{-R \cdot \tau}$. Substituting this into

Equation 4.3.3 and integrating the numerator by parts yields:

$$\bar{\tau} = \frac{\int_0^\infty \tau \cdot e^{-R\cdot\tau} \cdot \delta\tau}{\int_0^\infty e^{-R\cdot\tau} \cdot \delta\tau}, \tag{4.3.4}$$

$$\therefore \bar{\tau} = \frac{\frac{1}{R^2}}{\frac{1}{R}} = \frac{1}{R}. \tag{4.3.5}$$

So for Poissonian light, the mean waiting time τ is the inverse of the incident rate R, where $R = \eta_0 P_0$.

4.3.1 Detected rate

The measured detector recovery $\eta(\tau)$ and the probability of a second photon arriving at the detector $P(\tau)$ are implemented in Equation 4.3.1 to simulate the waiting time distribution, $\Omega(\tau)$. From this numerical simulation, it is possible to obtain the mean waiting time $\bar{\tau}$ and thus build up the detected rate R' as a consequence of Equation 4.3.5. The function $\Omega(\tau + \delta\tau)$ is built up in an iterative way based on previous values of $\Omega(\tau)$, in

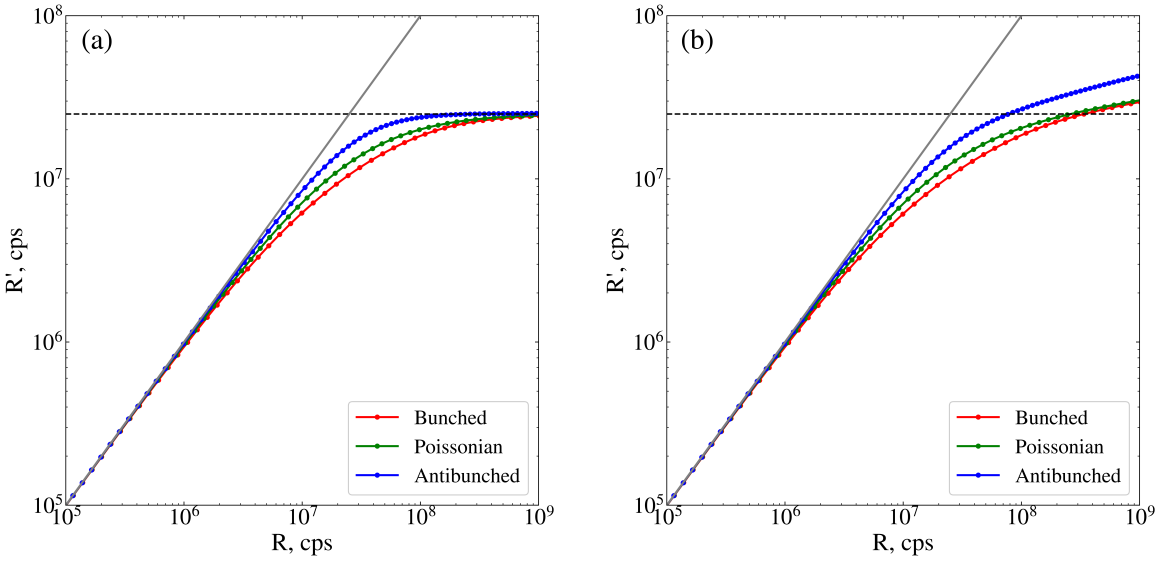

Figure 4.3.2: The detected rate simulation for (a): a detection efficiency described by a Heaviside function η_H; (b): a detection efficiency described by the experimentally verified detector recovery η_{real}. In both simulations, the correlation timescale for each statistical signature is set to the dead time, $\tau_c = T_{dead}$.

steps of $\delta\tau$, and the waiting time distribution is obtained by taking its numerical derivative $\Omega(\tau) = \frac{d}{d\tau}(\Omega(\tau + \delta\tau))$. To obtain a function that describes the detected rate R' versus incident rate R, the waiting time simulation is applied in two cases. Firstly, the $\Omega(\tau)$ is simulated for detectors that have a time-dependent detector recovery $\eta = \eta(\tau)$, i.e. real detectors, to obtain the mean waiting time $\bar{\tau}$ and hence the detected rate R' as a function of incident intensity I. In this step, the detector recovery can either be input as the real,

experimentally verified function η_{real}, or a simple Heaviside function η_{H}. Secondly, the same simulation is applied but for detectors with no time-dependent detector recovery, to obtain the mean waiting time $\bar{\tau}$ and the incident rate R as a function of incident intensity I. The difference between detected rates for the three types of statistics are maximally different when the correlation timescales τ_c are on the order of, or smaller than, T_{dead}. When $\tau_c \gg T_{\text{dead}}$, the correlated detected rates converge to that of the

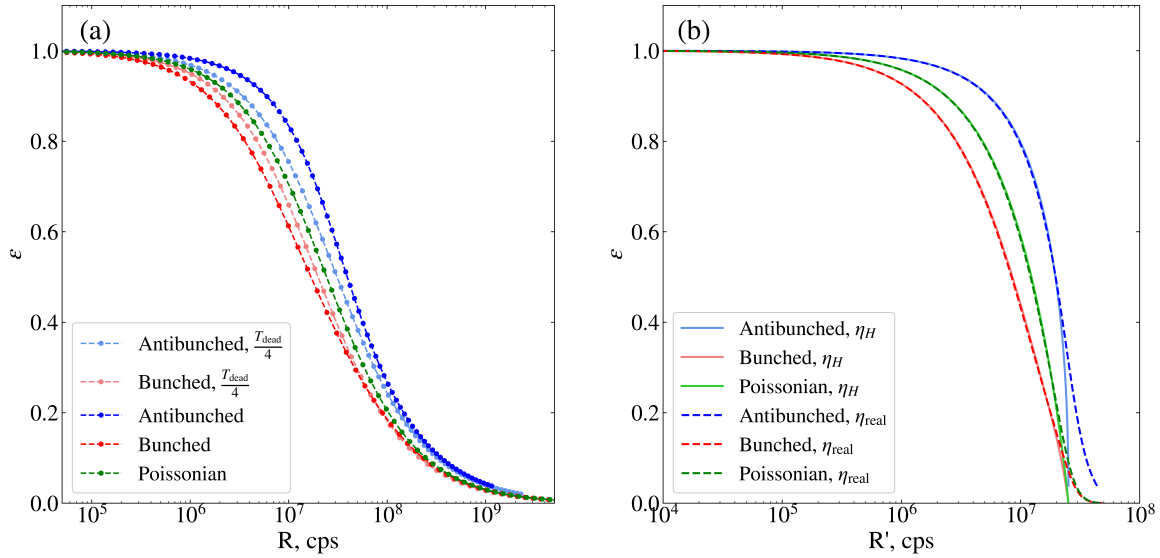

Figure 4.3.3: Detection efficiency, $\epsilon = R'/R$, against **(a)** incident rate R, for two different values of τ_c; **(b)** detected rate R', for a Heaviside detector response, η_H, and a real detector response, η_{real}. Correlation timescales all set to T_{dead} unless specified.

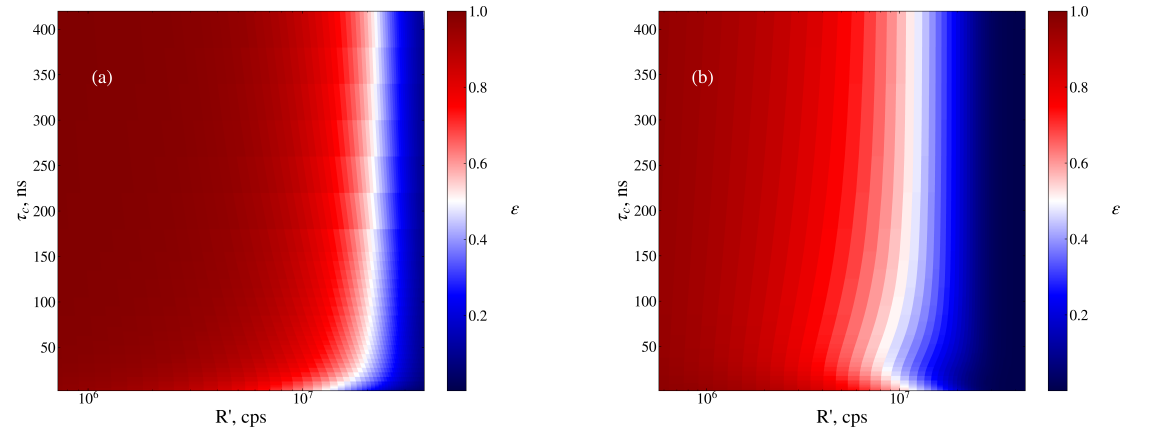

Figure 4.3.4: Detection efficiency, $\epsilon = R'/R$, against detected rate R', for different values of τ_c for **(a)**: antibunched light and **(b)** bunched light. In this figure the same relation as in Figure 4.3.3(a) is shown but for a range of τ_c from 100 ps to 400 ns. Below T_{dead} the behaviour of the bunched and antibunched sources diverge, as expected from the second-order correlation function.

Poissonian case. Figure 4.3.2(a) shows the results of the simulation for a detector with

a detection efficiency described by a Heaviside function, while Figure 4.3.2(b) is for the real experimentally verified detector recovery of the SNSPDs. We see that Figure 4.3.2(a) saturates such that the detected rate R' never exceeds $\frac{1}{T_{\text{dead}}}$, whereas for the real detector recovery which has a low but finite probability of detection for $t < T_{\text{dead}}$, the detected rate R' can exceed this limit. With this simulation, the change in detection efficiency $\varepsilon = R'/R$ can be investigated with respect to both incident rate R and detected rate R'. Figure 4.3.3(a) shows ε against R for two different timescales - firstly, $\tau_c = T_{\text{dead}}$ for Poissonian, bunched and antibunched light, and secondly $\tau_c = T_{\text{dead}}/4$ for bunched and antibunched light. In Figure 4.3.3(b) the change in ε against R' is shown for the three light statistics, with a real detector recovery η_{real} and a Heaviside detector recovery η_{H}. Again, there is a discrepancy between the two detector recovery models that is maximal at high count rates, $R' > 10^7$, and for mid-range count rates, $R' \sim 10^6$ the Heaviside model overestimates the detection efficiency. Figure 4.3.4 shows (a) the antibunched case and (b) the bunched case for a wider range of correlation timescales, from 100 ps ($T_{\text{dead}}/400$) up to 400 ns ($100 \times T_{\text{dead}}$). Both cases approach that of the Poissonian when $\tau_c \gg T_{\text{dead}}$. When $\tau_c = T_{\text{dead}}$ maximum discrepancy between the bunched and antibunched case is observed; this can be understood with the 'missing photons' depicted in Figure 4.2.2, where the antibunched case has slightly better efficiency due to missing fewer photons, and vice versa for bunched, than the Poissonian case. Thus, the model demonstrates (i) the importance of assessing the real detector recovery $\eta(\tau)$ to more accurately predict the detection efficiency behaviour as a function of rate; (ii) the impact of finite dead time in terms of correlation timescale.

4.3.2 Real detector saturation

To further characterise the SNSPD, a measurement to infer the real detector saturation was set up. Using a motorised fibre attenuator detected rate for bunched and Poissonian light can be measured for a range of different incident rates, as determined by a power meter. This allows comparisons between the real detector characteristics and the numerical simulation. For this measurement, the pseudothermal light experiment described in Chapter 3 was used. Figure 4.3.5 shows the arrangement for obtaining the experimental saturation curves, achieved by sweeping the power through the fibre using a motorised mechanical attenuator able to attenuate between 10 to 45dB. In order to safely examine the detected rate on the SNSPD whilst simultaneously extracting the power in the fibre above the noise floor of the power meter (few hundred picowatts), a manual in-fibre attenuator A_2 was connected after the sweeping attenuated light source and before the SNSPD. A comparison between the two light sources was valid as long as A_2 remained fixed for the entire experiment, between bunched and Poissonian. However, this issue was compounded by the lower intensity (around three orders of magnitude) of

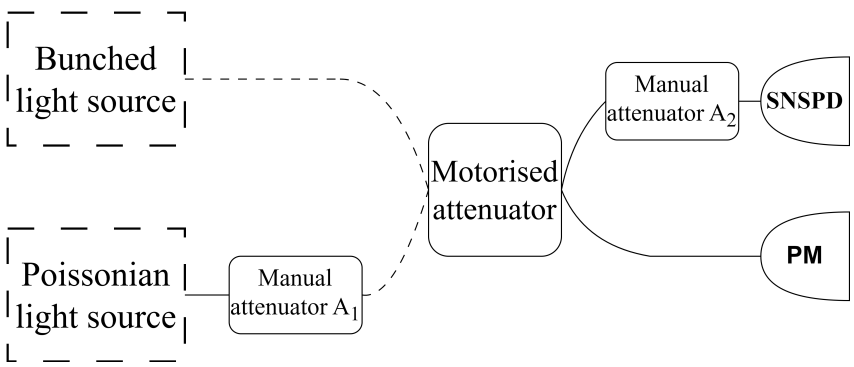

Figure 4.3.5: A schematic of the arrangement used for examining the detected rate of the bunched and Poissonian light sources, where 'PM' is a Thorlabs PM100D power meter. The bunched light was generated with the pseudothermal light experiment described in Chapter 3 and the Poissonian light source was a highly attenuated 850 nm PicoQuant diode laser.

the bunched light source. To accurately measure the saturation, between 10 and 15 Mcps at the detector was required. The experiment was set up in the following way. First, the motorised attenuator was set to fully open. The bunched light source was connected, and the manual attenuator in front of the SNSPD, A_2, was set to a position where no more than $\sim$ 12 Mcps was being counted at the detector. Then, the manual attenuator after the Poissonian source, A_1, was fully closed. Next, the Poissonian source was connected, and A_1 was slowly opened to a safe level, so that the count rate was comparable to that of the bunched light. By ensuring this, it was assumed that the optical power reaching the power meter is also equivalent, as long as the manual attenuators $A_{1,2}$ remain fixed for the duration of the experiment. Although this was the only way to obtain comparable count rates for both sources across the full range of the motorised attenuator, at high attenuations the power of both sources was too low to register on the power meter. However, by assuming the motorised attenuator was linear, the 'real' power could be extracted with the following expression

$$P = P_{\max} \times 10^{-\frac{A_m - 10}{10}}, \tag{4.3.6}$$

where A_m is the set position of the motorised attenuator in decibels and $P_{\max}$ is the maximum power measured, i.e. the lowest uncertainty value. Using this relation, the saturation curves were corrected, and the measured detected rates for the bunched and Poissonian sources is shown in Figure 4.3.6(a). As expected, the detected rate begins to saturate at high incident rates, $P > 10$ nW (equivalent to $> 10^9$ cps at 850 nm) and the saturation behaviour of the two light sources differs beyond $P \sim 10$ nW. Since the power meter being used in this study is only sensitive down to hundreds of picowatts, it was not possible to measure an antibunched source over this range. Using a low-power $g^{(2)}(\tau_{12})$ measurement of the bunched light source we can estimate its correlation timescale with a fit (shown in Figure 4.4.1(a)), which was determined to be $\tau_c \approx$500 ns. According

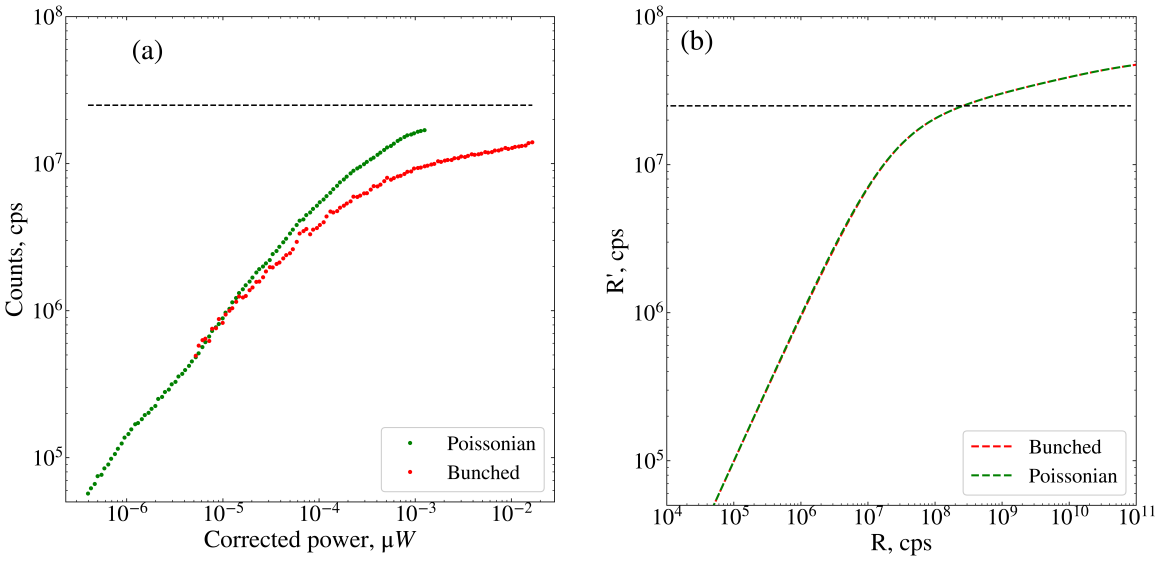

Figure 4.3.6: Detector saturation for correlation timescale $\tau_c = 500$ns. **(a)** The experimental data obtained with the schematic shown in Figure 4.3.5. The x-axis has been extrapolated based on the highest power-value for each curve using the attenuation in decibels of the motorised attenuator and Equation 4.3.6. **(b)** A simulation of the expected detected rate for Poissonian and bunched light source using the numerical simulation outlined in Section 4.3.1.

to the numerical simulation, for a correlation timescale of ∼500 ns when measured on detectors with $T_{\text{dead}} = 40$ ns, the saturation behaviour of a bunched and Poissonian light source is identical, but the detected rate R' in both cases still exceeds $1/t_d$ due to the non-zero detection efficiency, as before. The simulation for these timescales is shown in Figure 4.3.6(b). There are discrepancies between the experimentally measured data and the numerical simulation. Firstly, the experimental data implies that bunched sources saturates at $\approx 10^7$ cps and the Poissonian source slightly higher, whereas the simulation shows that for the time-dependent recovery measured on the SNSPDs, both sources should saturate at almost 4×10^7 cps. In addition, for a correlation timescale of 500 ns the simulation predicts that there will be no discrepancy between a bunched and Poissonian light source, although according to the corrected data shown in Figure 4.3.6(a), there is a difference when the incident power is >10 pW. I believe that the combination of assumptions made to correct the power with Equation 4.3.6 has resulted in this discrepancy between saturation curves. Repeating this measurement using a power meter that has a lower noise floor would be ideal as it would negate the correction factor which may be incorrect - alternatively, a brighter bunched light source would achieve the same outcome, and remove the need for the first manual attenuator, A_1, since for similar power ranges both sources could be attenuated with A_2 alone. Alternatively, using a motorised attenuator that has been properly calibrated at the power range of interest would help to identify whether or not the assumption of linearity is correct. Since the motorised attenuator used in this experiment was a fibre-coupled beam block, we

may expect the attenuation to be non-linear particularly at the minimum and maximum attenuation values, based on the Gaussian mode beam profile in a single-mode fibre.

4.4 Detected higher-order correlations

In Section 4.3.1 we have seen how for real detectors with finite dead time, the detected rate for each of the three statistical signatures of light can be simulated based on the real detector recovery and the probability of detection, given by the expected $g^{(2)}(\tau_{12})$. However - since measuring a correlation function relies on the measured intensity, it must also be the case that correlations are affected by finite dead time. To examine

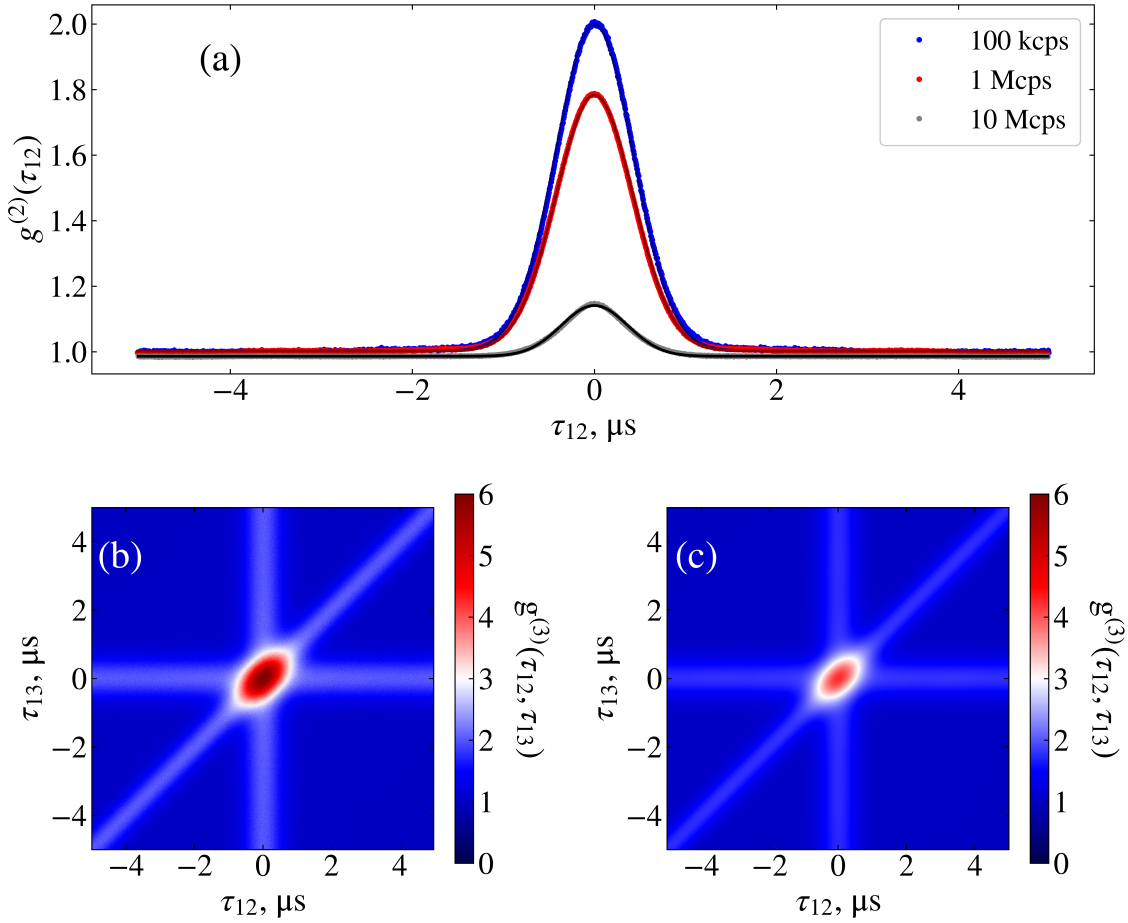

Figure 4.4.1: Change in the $g^{(2)}(\tau_{12})$ and $g^{(3)}(\tau_{12},\tau_{13})$ of the pseudothermal source with detected rate. **(a)**: As the detected rate increases from 100 kcps up to 10 Mcps, the value of $g^{(2)}(0)$ reduces from 2.00 to 1.16. Each of these $g^{(2)}(\tau_{12})$ functions has 10 ns bin widths. The darker lines on each dataset are fits based on Equation 4.2.2. The correlation timescale based on this fit is ~500 ns. The third-order correlation function for an average channel rate of **(b)**: 100 kcps and **(c)**: 1 Mcps, where the $g^{(3)}(\tau_{12},\tau_{13})$ reaches a maximum of 6.7 and 4.3 respectively.

the measured correlation function, we can consider the definition of the second-order

correlation function in terms of the detected rate R'. For detector i the detected rate R'_i is given by the product of the incident rate R_i and the rate-dependent efficiency $\varepsilon_i(R_i)$, where we have assumed equivalence between the incident rate R and the incident intensity I. From the standard expression for $g^{(2)}(\tau_{12})$ in terms of intensity we can now write:

$$g^{(n)}_{\text{measured}}(0,0,...) = \frac{\langle \sum_{i=1}^{n} \varepsilon_i(R_i) \cdot R_i \rangle}{\sum_{i=1}^{n} \langle \varepsilon_i(R_i) \cdot R_i \rangle}, \tag{4.4.1}$$

where n is the total number of detectors and hence the order of correlation. By assuming that the detectors have equal efficiencies $\varepsilon_i(R_i) = \varepsilon_d(R_i)$ and that they all receive an equal photon rate R, Equation 4.4.1 can be simplified to

$$g^{(n)}_{\text{measured}}(0,0,...) = \frac{\langle (\varepsilon_d(R) \cdot R)^n \rangle}{\langle \varepsilon_d(R) \cdot R \rangle^n} = \frac{\int_0^\infty [\varepsilon_d(R) \cdot R]^n \cdot \xi(R) \cdot \mathrm{d}R}{\left[\int_0^\infty \varepsilon_d(R) \cdot R \cdot \xi(R) \cdot \mathrm{d}R\right]^n}, \tag{4.4.2}$$

where $\xi(R)$ is the rate-dependent intensity distribution of a particular light source. Using

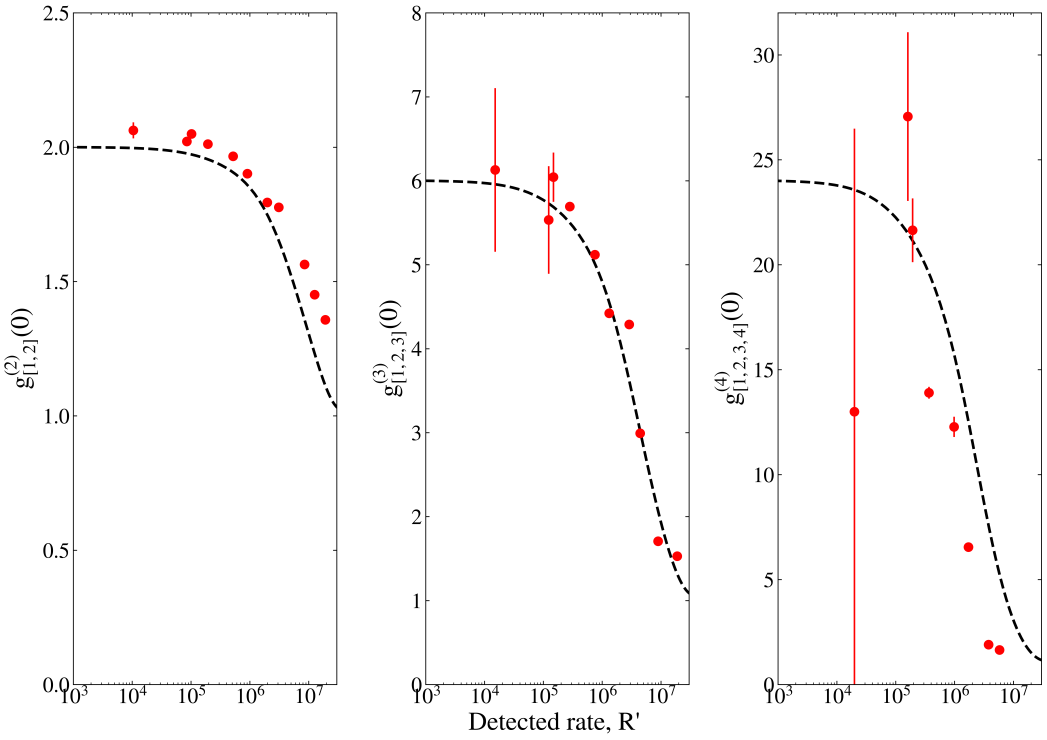

Figure 4.4.2: Changes in the peak heights of $g^{(2)}(\tau_{12})$,$g^{(3)}(\tau_{12},\tau_{13})$ and $g^{(4)}(\tau_{12},\tau_{13},\tau_{14})$ of the pseudothermal source. The black dashed line is obtained from a simulation that uses the real detector recovery and detected rates. The red dots are experimentally obtained values. The errors are estimated based on counting error as defined in Equation 3.6.4.

the determined detector efficiency response it is possible to numerically evaluate Equation 4.4.2 for a known intensity distribution of light - here, with the pseudothermal light source we can approximate its intensity distribution with the well-known formula[221] given by $\xi(I) = \langle I \rangle^{-1} e^{\frac{-I}{\langle I \rangle}}$. Figure 4.4.1(a) shows the $g^{(2)}(\tau_{12})$ of the pseudothermal light

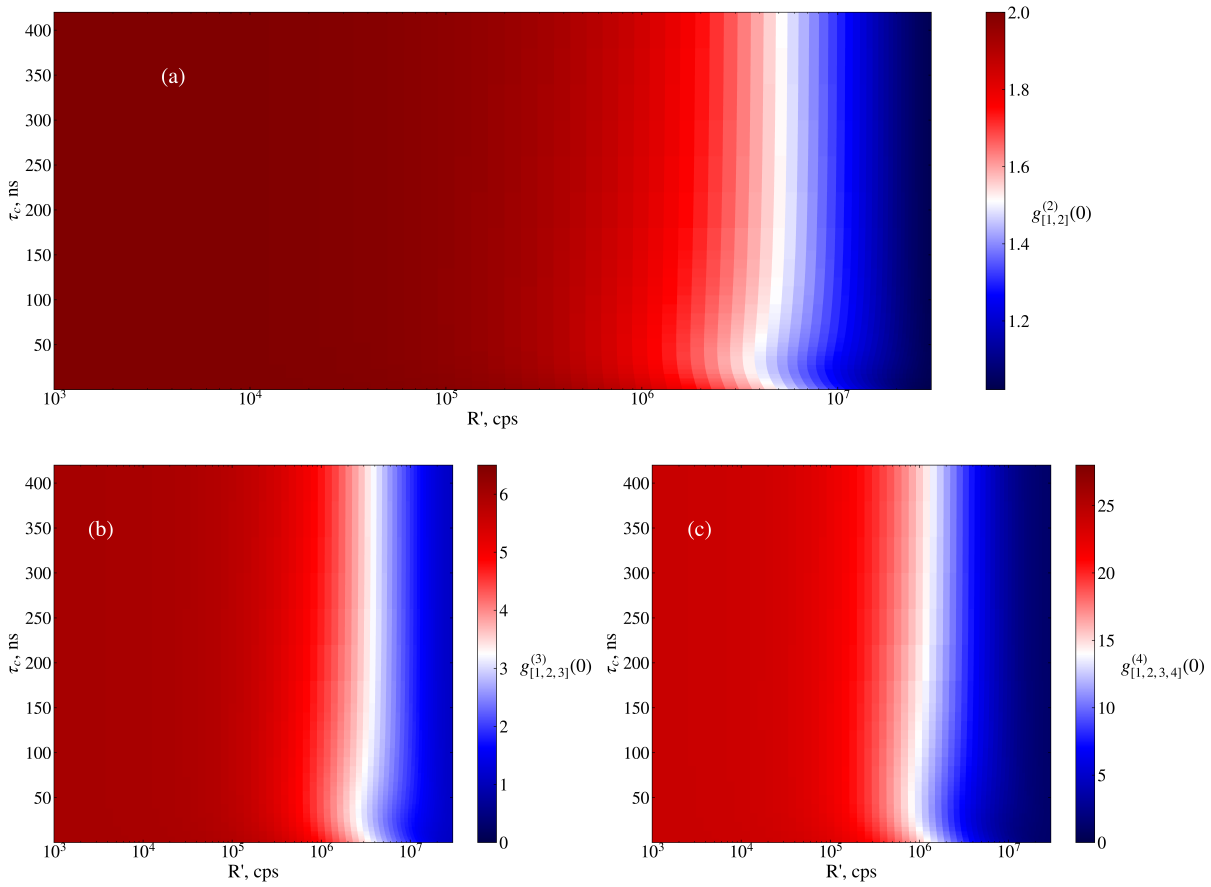

Figure 4.4.3: The simulated change in **(a)**: $g^{(2)}(\tau_{12})$, **(b)**: $g^{(3)}(\tau_{12}, \tau_{13})$ and **(c)**: $g^{(4)}(\tau_{12}, \tau_{13}, \tau_{14})$ for varying detected rate R' and correlation timescale τ_c.

configuration used for this study, at different detected rates. The correlation timescale remains the same for each dataset, but the peak ($g^{(2)}(0)$) falls below the expected value of 2 for thermal light. This is a consequence of the changing detection efficiency at high rates. In Figure 4.4.1(b) and (c), the same effect is observed in the $g^{(3)}(\tau_{12}, \tau_{13})$. Figure 4.4.2 shows the expected change in the value of $g^{(2,3,4)}(0)$ with detected rate R'. The black dashed line is the results of the simulation based on Equation 4.4.2, and the red data points are experimentally obtained values from the pseudothermal light experiment (Section 3.6.1) using the timestamped analysis script (Section 3.5). To obtain values for $g^{(4)}(0)$, a more compact script based on the timestamped code was developed - in this script, correlations were only calculated for two single time bins - at $[\tau_{12}, \tau_{13}, \tau_{14}]$ equals $[0, 0, 0]$ and $[\tau_{\text{inf}}, \tau_{\text{inf}}, \tau_{\text{inf}}]$ where $\tau_{\text{inf}} \gg \tau_c$, when τ_c was the correlation timescale. The normalised correlation value for $g^{(4)}(0)$ was obtained by taking the ratio of these two individual bins. By only finding four-fold coincidences in one time bin, and not finding cross-correlations between all channels, the correlation algorithm could be simplified to a conditional search with `if` statements, such that each detection channel did not need to have a binary search as is the case for the full timestamped script. The error bars on these data points is estimated using the counting error (Equation 3.6.4) from the histogram

counts in the bins post-processing. The increase in counting error moving from $g^{(2)}(0)$ through to $g^{(3)}(0)$ and $g^{(4)}(0)$ increases to the power of n for the same rate, as expected from Equation 3.6.3. Finally, Figure 4.4.3 extends the simulation shown in Figure 4.4.2 for a range of correlation timescales - from this, we conclude that the n^{th} order correlation function is not strongly dependent on the correlation timescale at high rates.

4.5 Discussion of results and future outlook

In this chapter, the impact of a finite dead time for single-photon detectors has been explored. In Section 4.3.1 a numerical simulation of detected rate based on a Heaviside detector recovery (η_{H}) versus a real detector recovery (η_{real}) was presented. In Figure 4.3.1 the experimentally-verified time-dependent recovery of the SNSPDs was shown, and Figure 4.3.6 presents the (a) experimentally determined and (b) numerically simulated saturation behaviour for a Poissonian and bunched light source on the SNSPDs. With this experimental set up, it was not possible to experimentally verify the saturation of an antibunched source, since the power meter did not have a low enough noise floor to register such low optical fluxes. This would be a useful measurement to obtain in future, to see if the saturation does follow the expected behaviour observed in Figure 4.3.2(b). Section 4.4 expanded the detected rate simulation to consider the effect of real detectors measuring photon correlation, for $g^{(n)}(\tau_{12}, ..., \tau_{1n})$ with $n = 2, 3, 4$. The difference in the value of $g^{(n)}(0)$ was observed in experimental data as shown for $g^{(2)}(\tau_{12})$ in Figure 4.4.1(a), and for $g^{(3)}(\tau_{12}, \tau_{13})$ in Figures 4.4.1(b) and (c). These experimentally obtained results highlight the necessity of careful calibration when measuring correlation on detectors. Finally, a model of the measured $g^{(2)}(\tau_{12})$, $g^{(3)}(\tau_{12}, \tau_{13})$ and $g^{(4)}(\tau_{12}, \tau_{13}, \tau_{14})$ based on the detected rate simulation shows the change in these values at zero time-delay in Figure 4.4.2 for a bunched light source. This trend was verified with experimental data. Figure 4.4.3 shows simulation results for a range of correlation timescales.

The numerical model presented in this chapter permits a simple yet powerful analysis method that can be easily implemented and have high impact in single-photon source metrology and high-precision measurements. Measuring a bunched $g^{(2)}(\tau_{12})$ and higher-order correlations is of importance when measuring entangled photon states where we expect two photons arriving simultaneously. Future work on this topic may focus on extended the treatment, both experimental and simulation, to antibunched light sources, to understand the impact of finite dead time on antibunched sources with a range of correlation timescales. In the following chapters, work on single-photon source and detector metrology will be presented, highlighting the potential applications and importance of the field.

CHAPTER 5

QUANTUM DOTS IN MICROPILLARS

5.1 Introduction

As described in Chapter 1, an ideal single-photon source is a crucial element of many quantum technologies. Semiconductor quantum dots (QDs) are zero-dimensional structures that can be grown epitaxially and integrated into optical resonator structures. The three-dimensional confinement of the QD introduces a delta-function-like density of states for the charge carriers which allows optical transitions to be individually addressed. Their energy is defined by the band gap of the semiconductor and the size and strain of the QD, leading to a theoretically tunable single-photon source. Generally these structures are fabricated with molecular beam epitaxy or metal-organic chemical vapour deposition using *self-assembled* growth, in particular the Stranski-Krastanov method.[240] QDs grown in this manner exhibit promising optical properties but at the cost of random, non-deterministic locations on the substrate, as well as non-uniform size. Controlled, deterministic growth of QDs is an active research area.[241–244] QD single-photon sources based on a range of materials and structure geometry have been demonstrated from deep UV[61,245–247] up to the telecommunications band in IR (1550 nm).[248–252] The most mature fabrication techniques exist for the III-arsenide material systems which emit in the near-infrared region, typically 850 to 1000nm. The first single-photon emission from a QD was reported in this material system[43] soon followed by *indistinguishable* single-photons from an epitaxial QD;[44] since then, many studies have reported high indistinguishability.[79,80,253–255] The brightest[36] and most pure[71] single-photon sources reported are III-arsenide QDs in microcavity structures.

In this chapter, the development of a fabrication process for defining semiconductor micropillar QDs-containing structures will be presented, and single-photon characteristics of the sample will be demonstrated with high-power resonant fluorescence experiments.

5.1.1 Two-level systems

A two-level system is the most simplistic model used to approximate the dynamics of many different quantum systems, including atoms, qubits, and QDs. Here we will introduce the mathematical description of light interacting with an electronic two-level system, and provide the theoretical framework for a phenomenon that will appear in experimental data shown in Section 5.3.1. The following treatment can be found in Fox[223] and Loudon.[221]

The two-level system introduced here is comprised of energy levels, $|1\rangle$ and $|2\rangle$, separated by some energy $\hbar\omega_0$ and centred on E_0, such that $E_1 = E_0 - \hbar\omega_0$, $E_2 = E_0 + \hbar\omega_0$. A pure state $|\psi\rangle$ of this two-level system can written in the Bloch representation, a geometric description based on the coefficients of the state wavefunction which satisfy $|c_1|^2 + |c_2|^2 = 1$:

$$
\begin{aligned}
|\psi\rangle &= c_1\,|1\rangle + c_2\,|2\rangle\,, \\
x &= 2\mathrm{Re}\langle c_1 c_2\rangle, \\
y &= 2\mathrm{Im}\langle c_1 c_2\rangle, \\
z &= |c_2|^2 - |c_1|^2.
\end{aligned}
$$

Using the mathematical expression above and the visual aid of Figure 5.1.1, we can see

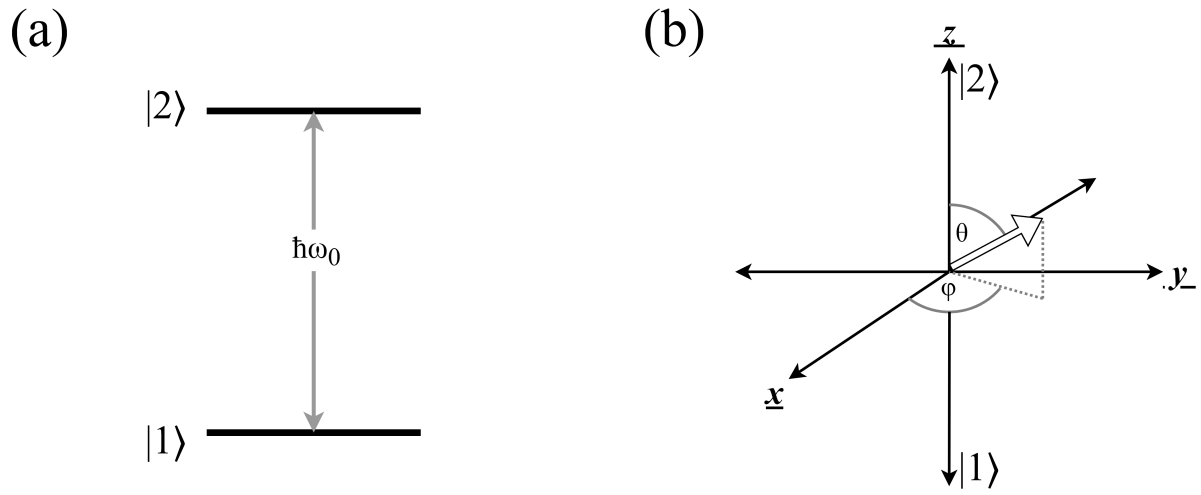

Figure 5.1.1: Illustrations of the models used in this section. **(a)**: The two level system. **(b)** The Bloch sphere representation of the two-level system.

that the *ground* (or unexcited) state $|1\rangle$ has a Bloch vector representation $(0, 0, -1)$ i.e. pointing straight down along $\underline{\mathbf{z}}$, while the excited state $|2\rangle$ is $(0, 0, 1)$. We can describe any mixed state $|\psi_r\rangle$ using this co-ordinate system, where we have defined θ as the azimuthal angle between the positive $\underline{\mathbf{z}}$ and $|\psi_r\rangle$, and ϕ as the angle between the positive $\underline{\mathbf{x}}$ and $|\psi_r\rangle$.

To examine the interaction of such a two-level system with light, we will first assume that any incoming light is close to resonance, such that $\omega = \omega_0 + \delta\omega$ where $\delta\omega << \omega_0$. This condition allows us to solve the time-dependent Schrödinger equation using time-dependent perturbation theory. The electric field of the incoming light perturbs the electric dipole of the two-level system. A full treatment can be found in Appendix B. The general solution yields:

$$\Psi\left(\underline{\mathbf{r}}, t\right) = c_1\left(t\right)\psi_1\left(\underline{\mathbf{r}}\right)e^{\frac{-iE_1t}{\hbar}} + c_2\left(t\right)\psi_2\left(\underline{\mathbf{r}}\right)e^{\frac{-iE_2t}{\hbar}}, \tag{5.1.1}$$

where we note that the wavefunction amplitudes associated with each energy level, $c_1\left(t\right)$ and $c_2\left(t\right)$, are time-dependent. The two first-order differential equations describing the evolution of these amplitudes are given by:

$$\dot{c_1}\left(t\right) = \frac{i}{2}\Omega\left(e^{i(\omega-\omega_0)t} + e^{-i(\omega+\omega_0)t}\right)c_2\left(t\right), \tag{5.1.2}$$

$$\dot{c_2}\left(t\right) = \frac{i}{2}\Omega\left(e^{-i(\omega-\omega_0)t} + e^{i(\omega+\omega_0)t}\right)c_1\left(t\right), \tag{5.1.3}$$

where we have introduced the *Rabi frequency*:

$$\Omega = \left|\frac{\mu_{12}\varepsilon_0}{\hbar}\right|, \tag{5.1.4}$$

which depends on the *electric dipole moment* of the two level system, μ_{12}. To solve these equations we can consider the strong field limit: considering the case of exact resonance, such that $\delta\omega = 0$, and using the rotating wave approximation to neglect terms that oscillate at $\pm\left(\omega + \omega_0\right)$, we obtain

$$\dot{c_1}\left(t\right) = \frac{i}{2}\Omega c_2\left(t\right), \tag{5.1.5}$$

$$\dot{c_2}\left(t\right) = \frac{i}{2}\Omega c_1\left(t\right). \tag{5.1.6}$$

Differentiating either line and substituting into the other, we can solve for a particle that begins in lower level ($c_1\left(0\right) = 1$, $c_2\left(0\right) = 0$) to obtain the probability coefficients

$$\left|c_1\left(t\right)\right|^2 = \cos^2\left(\frac{\Omega t}{2}\right), \tag{5.1.7}$$

$$\left|c_2\left(t\right)\right|^2 = \sin^2\left(\frac{\Omega t}{2}\right). \tag{5.1.8}$$

This result demonstrates that the probability amplitudes for the ground and excited states $|1,2\rangle$ oscillate in time with a frequency of $\Omega/2\pi$ - this behaviour is a Rabi oscillation, and is observed in any two-level system under strong resonant excitation.

5.1.2 Emitters in cavities

The previous section described the interaction between the canonical two-level system and some light of near-resonance using perturbation theory in free space. In this section, we will discuss the same physical system but now with our two-level system inside an optical cavity. In general, an optical cavity is used to confine light of a particular wavelength, defined by its length. Therefore they are typically implemented in devices that either seek to improve the interaction length for the light and the active region, or require a specific spectral range. Optical cavity structures are desirable for single-photon sources as they are able to enhance the source brightness via the Purcell effect,[256] and deliver the fluorescence in a well-defined spatial mode, hence improving the efficiency. We will examine the physics behind both of these attributes.

To discuss the coupling between our two-level system and an optical cavity we must introduce a simple cavity model and some characteristics. For a cavity with some length L_{cav} we can define a set of resonant modes ω_{cav}

$$\omega_{\text{cav}} = m\frac{\pi c}{nL_{\text{cav}}}, \tag{5.1.9}$$

where n is the refractive index of the cavity medium and m is an integer. Equation 5.1.9 defines the frequencies of light that will be preferentially confined by the cavity, since light of this frequency will be in-phase after a round trip. The cavity *finesse* $\mathcal{F}$ is given by Equation 5.1.10

$$\mathcal{F} = \frac{\pi\left(R_1R_2\right)^{\frac{1}{4}}}{1-\sqrt{R_1R_2}}. \tag{5.1.10}$$

The finesse is inversely proportional to the square root of the transmission of light through the cavity over one round trip, and also determines the spectral width of the resonant modes, $\Delta\omega_{\text{cav}}$, as given in Equation 5.1.11

$$\Delta\omega_{\text{cav}} = \frac{\pi c}{n\mathcal{F}L_{\text{cav}}}, \tag{5.1.11}$$

and so, physically, we can consider the finesse as some measure of the cavity lossiness - a higher finesse leads to a lower transmission, and sharper spectral modes. For a non-planar cavity, it is helpful to have a general parameter that describes how sharp the cavity resonant mode is - for this, we introduce the *quality* factor, Q:

$$Q = \frac{\omega_{\text{cav}}}{\Delta\omega_{\text{cav}}}. \tag{5.1.12}$$

The numerical value varies depending on the type of cavity, but generally speaking a 'high' Q-value indicates a photon will complete more round trips before escaping than in a 'low' Q cavity. We can introduce the (average) photon lifetime, τ_{cav} and photon decay

rate Γ, as in Equation 5.1.13

$$\Delta\omega_{\text{cav}} \equiv (\tau_{\text{cav}})^{-1} \equiv \Gamma. \tag{5.1.13}$$

A cavity of central wavelength ω_{cav} and full width at half maximum $\Delta\omega_{\text{cav}}$ will have a spectrum of a Lorentzian shape centred on ω_{cav} with width $\Delta\omega_{\text{cav}}$. Now, we can consider the interaction between some general two-level system and an optical cavity, where the transition frequency of the two-level system ω_0 is equal to the resonant cavity mode ω_{cav}. In this thesis, the work focusses on a cylindrical cavity known as a semiconductor

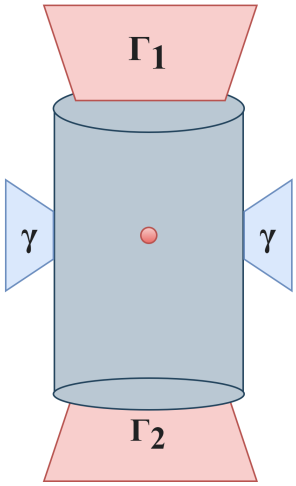

Figure 5.1.2: A schematic of a cylindrical cavity with non-resonant decay rates emitting at the sides (so-called *leaky modes*) and photon decay rates at the top and bottom Γ_1 and Γ_2 respectively.

micropillar. The cavity structure defines three possible radiative decay routes, labelled in Figure 5.1.2. The top decay route is the preferred decay mode, labelled Γ_1. The bottom is labelled Γ_2 and together, $\Gamma = \Gamma_1 + \Gamma_2$ define the cavity mode decay rate. Any emission out of the cavity sidewalls are non-cavity modes - 'leaky' modes - which we have designated as γ. We can now introduce the spontaneous emission coupling factor, β:

$$\beta = \frac{\Gamma}{\Gamma + \gamma}, \tag{5.1.14}$$

which gives the proportion of emission in a preferred mode. For a perfect cavity, $\beta \to 1$. The ratio of top emission over total cavity mode emission is defined by η given in Equation 5.1.15

$$\eta = \frac{\Gamma_1}{\Gamma} \tag{5.1.15}$$

The Q factor can be determined by measuring the spectrum of the cavity mode. We introduce some new parameters: the atom-photon coupling parameter g_0, and the cavity mode volume V_0. The atom-photon coupling g_0 is related to the electric dipole interaction

μ_{12} and the cavity mode volume V_0. These parameters allow us to define two limits of atom-cavity behaviour, the *strong-coupling* limit when $g_0 \gg (\Gamma, \gamma)$, and the *weak-coupling* limit when $g_0 \ll (\Gamma, \gamma)$. Physically, the strong coupling limit corresponds to cyclic re-absorption and re-emission of the photon within the cavity, before it decays out. The system will undergo many Rabi oscillations before eventually leaking out of the cavity. The dynamics of this system are described by the Jaynes-Cummings model. In the weak coupling limit, spontaneous decay happens more quickly than reabsorption, but the decay rate is modified.[257] Now, we introduce the *Purcell factor* F_P[256] as the ratio of the spontaneous emission rate of the emitter in the cavity to that in free space:[258]

$$F_P = \frac{3Q\left(\lambda/n\right)^3}{4\pi^2 V_0} \frac{\Delta\omega_{\mathrm{cav}}^2}{4\left(\omega_0 - \omega_{\mathrm{cav}}\right)^2 + \Delta\omega_{\mathrm{cav}}^2} \frac{\left|\underline{\mathbf{p}} \cdot \underline{\mathbf{E}}\right|^2}{\left|\underline{\mathbf{p}}\right|^2 \cdot \left|\underline{\mathbf{E}}\right|^2} \frac{\left|\underline{\mathbf{E}}\left(\underline{\mathbf{r}}\right)\right|^2}{\left|\underline{\mathbf{E}}_{\mathrm{max}}\right|^2}. \tag{5.1.16}$$

where the second, third and fourth term modify the originally derived first term. The first term indicates that a high Q and small V_0 cavity will enhance the spontaneous emission rate of an emitter. The second term accounts for how far detuned the emitter transition ω_0 may be from the central cavity mode ω_{cav}. The third term considers the orientation of the dipole, and the final term accounts for how spatially close to resonance the emitter is within the cavity mode volume.

5.1.3 Semiconductor quantum dots

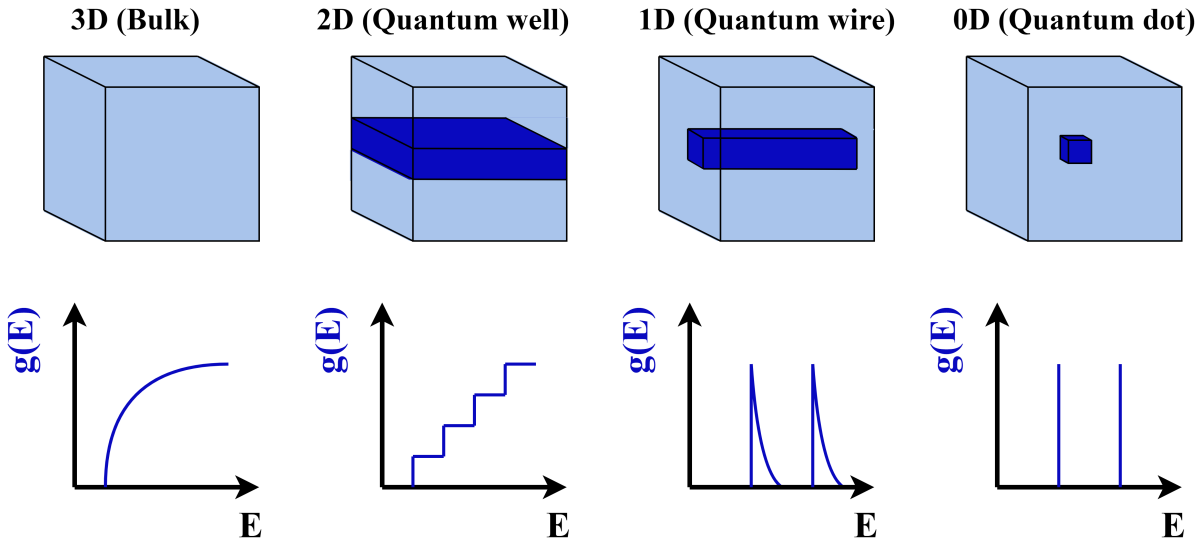

Figure 5.1.3: The density of states for different degrees of confinement. Charge carriers can move in: 3 dimensions in bulk; 2 dimensions in a quantum well; 1 dimension in a quantum wire; 0 dimensions in a QD.

In this section, the optical transitions of QDs will be presented based on the band theory of semiconductors. Any bulk semiconductor has a conduction band (CB) and

valence band (VB), separated by a band gap, which each contain electrons and holes (absence of an electron) respectively. Combining two (or more) different semiconductors together can form a *heterostructure*, where a mismatch in bandgap leads to a confining potential barrier. The available states for charge carriers in either band is described by the density of states - this function, describing the number of available energy states for charge carriers to populate, changes with the degree of confinement, as shown in Figure 5.1.3. Thus populations will change as the bands experience different degrees of confinement. QDs grown in strained material systems with heteroepitaxy will grow via the Stranski-Krastanov growth mode.[240] In this regime, a highly-strained *wetting layer* will form a 2-dimensional plane on top of the substrate. Then, at some critical thickness, *island growth* - the mode that forms the QDs - begins on top of the wetting layer.[259] With typical scales of tens of nanometres, charge carriers are completely confined. An electron in the CB and a hole in the VB form an *exciton*, a quasiparticle that forms an optically addressable dipole. The confinement of excitons within the QD leads to a discretised density of states, resulting in a ladder of energy levels, much like in atoms - hence the common moniker for QDs, 'artificial atoms'.[260] The resulting energy structure is complex, depending on a range of structural properties such as the material bandgap, and the local strain, size and symmetry of the QD. The spin of the charge carriers also results in an underlying fine structure for all optical transitions, complicating the energy structure further. The rest of this section will examine this energy structure in more detail. Note that the following treatment only applies in zero magnetic field, a condition which applies to all experimental results in this chapter. Furthermore - while more complicated charge complexes exist, in this thesis only the neutral exciton was measured - so discussion here will be limited to this specific case.

The simplest optical transition in this system is formed by a single electron and hole, referred to as the *neutral exciton*. This will henceforth be denoted X^0. The ground state comprises an empty QD, while the excited state consists of all possible configurations of an electron-hole pair. For a direct bandgap semiconductor such as gallium arsenide (GaAs) and indium arsenide (InAs), in bulk the low-lying states in the CB are s-type with angular momentum $L = 0$, and the upper states in the VB are p-type with angular momentum $L = 1$.[260] This results in angular momentum projections of $l = 0$ for electrons in the CB and $l = 0, \pm 1$ for holes in the VB. Electrons and holes, being fermions, have spin $S = 1/2$. The total angular momentum projection J for electrons (e) and holes (h) in the CB and VB is therefore $J = 1/2$ and $J = 1/2,\ 3/2$ respectively. The VB states at $J = 3/2$ with projections $J_z = \pm 3/2$ and $J_z = \pm 1/2$ are known as the *heavy hole* (hh) and *light hole* (lh) respectively. These states are degenerate at the *gamma point*, the centre of the crystal Brillouin zone.[261] The degeneracy of these states is lifted by compressive strain during the growth process.[259] The states at $J = 1/2$ form the *split-off* band, which is separated from the hh and lh by an energy gap Δ_{SO} due to spin-orbit

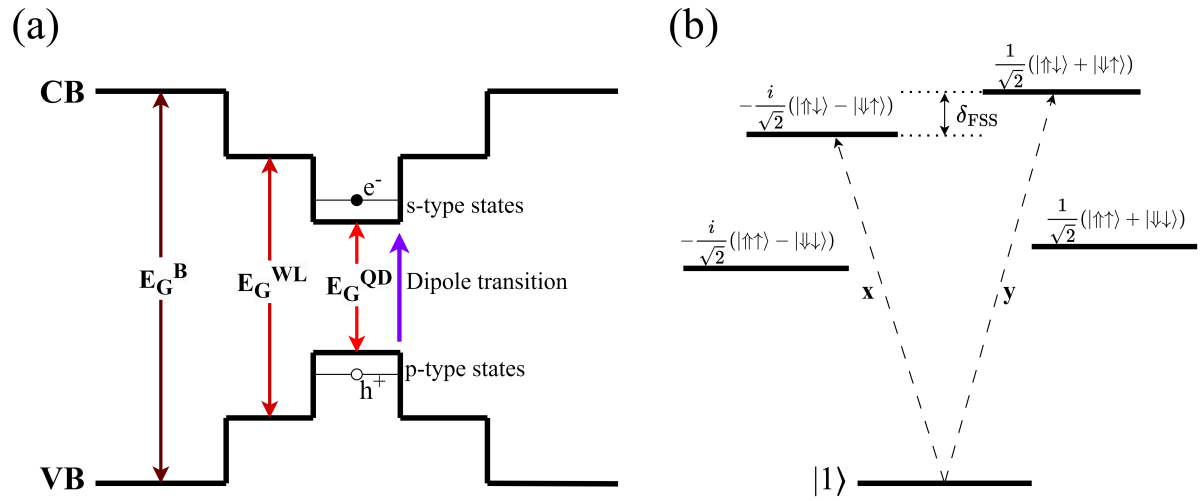

Figure 5.1.4: The underlying energy structure of a QD. **(a)**: The energy diagram of a QD structure in a direct bandgap semiconductor, where **CB** and **VB** denote the conduction and valence band edge respectively. The bulk has a band gap E_G^B, the wetting layer energy $E_G^{WL} < E_G^B$ and the optically addressable QD levels are confined to $E_G^{QD} < E_G^{WL}$. **(b)**: The fine structure of the neutral exciton, X^0, where the dashed arrows indicate allowed optical transitions. The bright doublet is separated in energy by δ_{FSS} due to spin-orbit interaction, and results in the circularly polarised transitions being mixed into orthogonally linearly polarised transitions, $|x\rangle$ and $|y\rangle$.

coupling.[262] The major contribution in shifting the lh band at lower energies in this quantum dot system (InAs) is usually attributed to strain.[263] Typically for III-V QDs, excitons comprising of hh are more energetically favourable.[264] For the combination of e-hh, there are four possible arrangements of the spins - (↑⇑), (↓⇓), (↑⇓), (↓⇑) - where a single arrow indicates the e spin, a double arrow indicates the hh spin, and the direction of the arrow represents spin 'up' or 'down' respectively. The first two arrangements are forbidden by optical selection rules, as they result in $J = \pm 2$. The latter two are the allowed or 'bright' transitions[265] where $J = \pm 1$, which is allowed via a circularly polarised photon exchanging one quantum of angular momentum. The energy diagram of this fine structure configuration is depicted in Figure 5.1.4(b). The two states are separated by some small energy $\delta_{\text{FSS}} << E_0$ - this is fine structure splitting, in zero magnetic field this occurs due to the exchange interaction between the electron and hole,[266] resulting from properties including local strain field, crystal inversion symmetry and structural anisotropy.[267,268] Typically this splitting is on the order of μeV. This lifted degeneracy of the optically allowed states results in a mixture of the circularly polarised transitions becoming orthogonally linearly polarised states, represented by $|x\rangle$ and $|y\rangle$ in Figure 5.1.4(b).

5.1.4 Resonant fluorescence of quantum dots

The previous section discussed that the dipole transition of the QD states has a smaller energy gap than its surrounding bulk material, and so it follows that we can address all available optical transitions in a QD by directly exciting the wetting layer or bulk semiconductor. This is experimentally convenient, as it allows for spectral filtering, for example with dichroic mirrors or band-pass filters, to separate the excitation from the emitted fluorescence in a confocal microscope system. However, as has already been alluded to in Section 5.1.1 resonant excitation of QDs leads to an assortment of interesting physics.

The features of QD fluorescence depend strongly on the features of the incoming light field that interacted with the QD transition. Resonant light can have two main interactions[269] with the QD transition; these are generally referred to as coherent and incoherent excitation. Incoherent excitation will promote an electron to the QD CB, forming the exciton or excited state, which will radiatively decay and spontaneously re-emit a photon.[1] This regime, henceforth referred to as *resonant photoluminescence* (RPL), can lead to a homogeneous broadening of the emission linewidth which reduces its coherence time T_2.[183] Coherent excitation, or the *resonant Rayleigh scattered* (RRS) regime, will result in fluorescence that exhibits spectral properties of the excitation field itself.[184] Resonant excitation generally will result in fluorescence that contains both components; under particular experimental conditions, one may be suppressed. RRS is the dominant emission mechanism when exciting at low power or when in the Heitler regime, i.e. in the limit of small Rabi frequency $\Omega^2 < (\gamma^2/2)$ where the linewidth $\gamma = 1/T_1$, while the RPL becomes dominant in the high power limit. The ratio of these two components in a particular resonant excitation signal is given by:[184]

$$\frac{I_{RSS}}{I_{RPL}} = \frac{T_2}{2T_1} \times \frac{1}{1 + \Omega^2 T_1 T_2}, \tag{5.1.17}$$

where T_1 is the radiative lifetime and T_2 is the coherence time. It was first theoretically predicted[270,271] and later demonstrated experimentally[272] that antibunching of resonant fluorescence is the result of interference between these two individual components - if either is suppressed, the antibunching vanishes, and it is impossible to observe antibunching and subnatural linewidth photons simultaneously.

In the limit of large Rabi frequency, Ω, the resonant fluorescence spectrum emerges as the Mollow triplet, a set of states 'dressed' by the coherent laser excitation with two sidebands and a degenerate central band. Figure 5.1.5 shows an illustration of this 'dressed state' picture and the corresponding transitions. In this limit, the antibunching timescale of the fluorescence T_A is equivalent to the excited state lifetime T_1, and the

[1] This is also the mechanism for emission with non-resonant excitation.

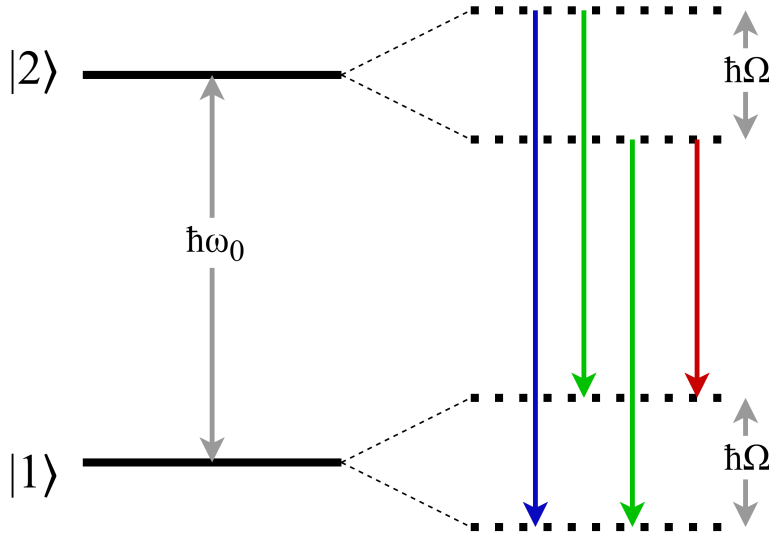

Figure 5.1.5: Dressed states of the two level system separated by $\hbar\omega_0$ under resonant continuous-wave excitation. Each level splits into two, which results in four possible transitions, two of which are degenerate (green arrows).

coherence time T_2 is limited by T_A. When examining the photon statistics of the neutral exciton transition under increasing pump power, oscillations in the second-order correlation function are apparent - this is evidence of Rabi oscillations between the Mollow triplet sidebands. These Rabi oscillations are modulated by a decay corresponding to the transition radiative lifetime, where both the Rabi frequency and decay rate are power-dependent features. The second-order correlation function in this physical regime can be described by Equation 5.1.18:

$$g^{(2)}(\tau) = 1 - \exp\left[-\eta\,|\tau|\right]\left(\cos(\mu\,|\tau|) + \frac{\eta}{\mu}\sin(\mu\,|\tau|)\right), \tag{5.1.18}$$

where $\eta = (1/T_1 + 1/T_2)/2$ and $\mu = \sqrt{\Omega^2 + (1/T_1 - 1/T_2)^2}$.[273]

The first demonstration of coherent resonant excitation for semiconductor QDs employed an 'orthogonal excitation-detection geometry',[182] where the fluorescence is emitted in some orthogonal direction to the excitation beam. The development of the dark-field microscope[186] allows parallel beams and uses polarising optics for filtering. The incident excitation light is set at some polarisation orthogonal to that which is collected and analysed. This is achieved using a combination of optics such as linear polarisers and waveplates, such that the system is excited with an excitation beam of a particular polarisation, and only fluorescence of an orthogonal polarisation to this is collected. As described in Chapter 2, this is a challenging experimental feat and a minimum extinction ratio is required to observe the interesting features of the fluorescence.

5.1.5 Semiconductor fabrication

The process flow for the samples described in the remainder of this chapter includes hardmask deposition, direct-write lithography and inductively-coupled plasma (ICP) etching to form micropillars from III-V semiconductor materials. In this section, before moving onto the methods and results of this chapter, a brief overview of these techniques will be provided.

Masking of a material for etching is typically achieved with the patterning of a photoresist, however when the required etchant for a material will also react with the photoresist, or a deep etch with small feature sizes is required, then an extra mask is necessary. This is a layer of metal or dielectric known as a hardmask, which can be fabricated with techniques such as evaporation or deposition, or grown via chemical vapour deposition techniques.[274] In the early stages of this process development, both electron-beam physical vapour deposition (EBPVD) and plasma-enhanced chemical vapour deposition (PECVD) were tested to deposit silicon dioxide (SiO_2) and silicon nitride (SiN). EBPVD requires a high vacuum (at least 1×10^{-2} Pa), and uses a high voltage applied to a tungsten filament to generate a high-energy electron beam. This electron beam is focussed onto the deposition material, which typically sits inside a crucible.[275] The deposition material sublimates and coats a target substrate within its path. PECVD is a similar high vacuum deposition process to EBPVD, but instead of creating a physical deposition process by bombardment, the generation of a plasma by radio frequency discharge accelerates the ionised deposition material towards a target substrate.

Photolithography uses high-energy (deep UV) light to define patterns on substrates using photosensitive polymers known as photoresists. First, the photoresist is applied to the sample with spin coating, followed by a hotplate bake. Next, the photoresist is exposed to light while being masked with the desired pattern, and then dissolved in a solvent known as a developer. A positive tone photoresist is one that is broken down by exposure to light, leaving a gap or hole, and a negative tone photoresist is one that is strengthened by exposure to light, leaving an etch-resistant mask. The pattern can be applied with a physical mask, for example with a specifically designed piece of quartz and a mask-aligning tool under direct exposure. Alternatively, a direct write-projection lithography tool may be used, which creates the pattern with a digital micrometer device. This creates the pattern using a series of optics and mirrors without requiring contact on the device. This method of patterning allows on-the-fly mask redesign and faster exposure times than alternative non-contact patterning processes such as electron-beam lithography. For certain resists, after exposure, another bake on the hot plate is required - post-exposure bake (PEB). This densifies the resist and improves adhesion to the surface. The key parameters in optimising the patterning process are:

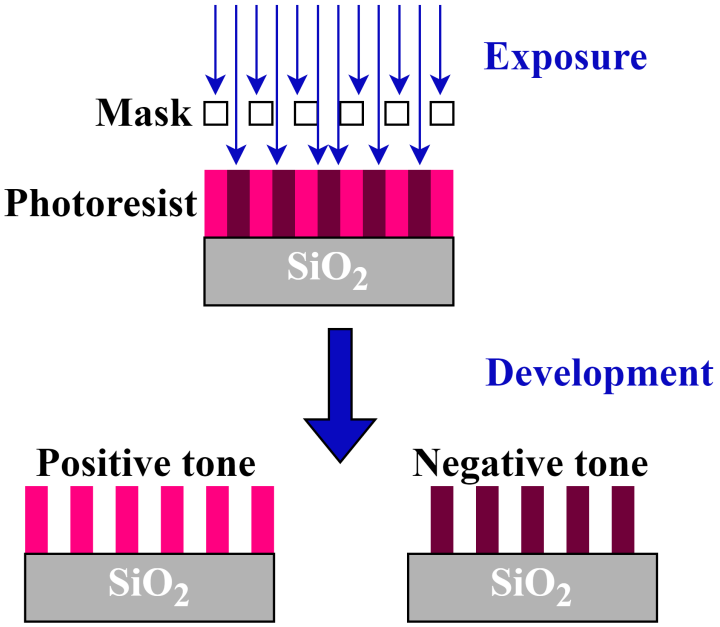

Figure 5.1.6: An illustration of positive versus negative tone resist. For a positive tone resist, the exposed area is weakened and removed following exposure and development. For a negative tone resist, the exposed area is strengthened and the surrounding areas are removed following exposure and development.

- Choice of tone: the pattern feature sizes and shapes will dictate whether a positive or negative tone resist is more appropriate. For example if small features with relatively large spacing in between are required, then negative tone will make the resist stripping more straightforward since most of it is being removed. Furthermore, in most processes using a negative tone resist means that a lift-off process is not required.

- Resist thickness: if no other masking is being used, then generally a thicker mask is required for bigger etch depths. However smaller feature sizes are easier to define on thinner layers of photoresist. The thickness is controlled by the spin speed and time.

- Edge-bead removal: the spinning process can often lead to thicker resist layers at the edges of the sample, which can be removed with a second step.

- Post-exposure bake: especially for negative tone resist, the temperature and time of the PEB is important in defining the verticality of the remaining resist.

- Development: both the developer used and the development time will impact the feature sizes.

After a sample has been masked and patterned using a lithography process, this pattern needs to be transferred to the semiconductor material - this is achieved with etching. Wet

etching uses wet chemicals, such as acid or base solutions, and is a relatively simple and cheap process which results in isotropic etch profiles. Dry etching uses gas etchants, some of which can be noxious, and is a complex process requiring expensive equipment such as vacuum chambers and liquid nitrogen cooling, which results in anisotropic etch profiles. Examples of dry etching include reactive ion etching (RIE), capacitively coupled plasma

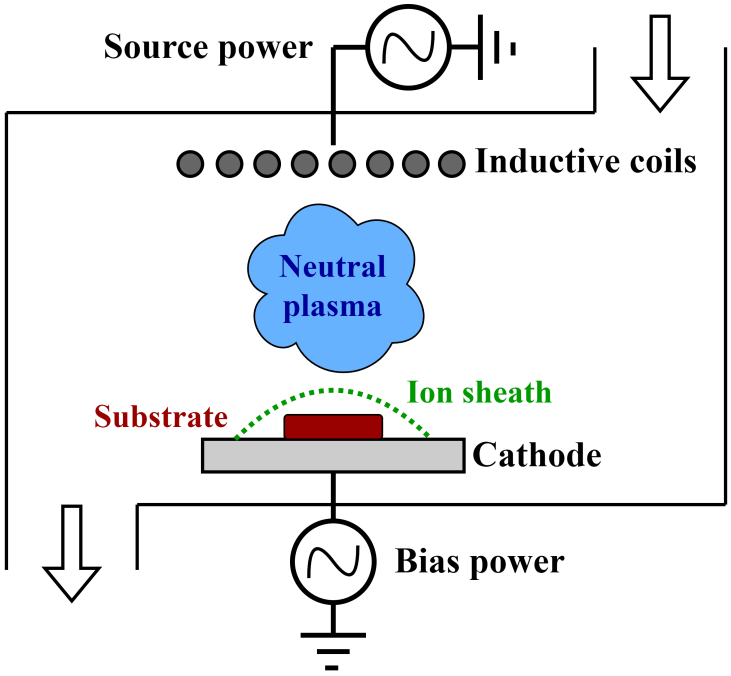

Figure 5.1.7: An illustration of an ICP etcher. Two separate RF fields control the plasma and bias respectively.

or inductively coupled plasma (ICP). Dry etching can result in three specific etch profiles: with *physical ion beam* etching, the material is sputtered away under bombardment; using *chemical plasma* etching, neutral particles hit the target substrate and some volatile product is ejected; *reactive ion* etching combines physical and chemical etching to give vertical sidewalls. Using a plasma, which can be considered as a quasi-neutral gas of electrons and ions, the ions can be controlled with electric fields. The plasma is generated by applying an RF field across a cathode and anode plate inside a vacuum chamber which contains a source gas, reaction products, excited neutrals and ions.[276] The source gas is selected depending on the required etch chemistry - it is required to react with the substrate material and also create volatile reaction products. The relatively light and mobile electrons produce ionisation states and excited radicals, while the heavy and slow ions tend to gather at the cathode creating an ion sheath. The plasma is sustained by ionisation events between electrons and neutral particles on the substrate, while excitation events produce the free radicals required for etching. Most of the RF voltage is dropped across the sheath; any reactant that suddenly 'feels' the large electric field of the sheath is slammed into the substrate, where it does the etching.[277] In ICP etching, an extra RF generator breaks the connection between the DC bias and the plasma pressure. One RF

generator creates the plasma in the chamber, while the other applies a DC bias. This method has the fastest anisotropic etching rates since a high power, high pressure regime is available.

5.2 Fabrication of semiconductor micropillars

In this section onwards, the main fabrication and experimental results of this chapter will be presented. I will describe the development of a process flow for defining microcavity structures in III-V semiconductor materials containing QDs, optimised for the mass-production of thousands of optically active devices. In the following section, single-photon characteristics will be demonstrated with hallmark measurements, and a higher-order correlation under high power excitation will be presented. A pair of

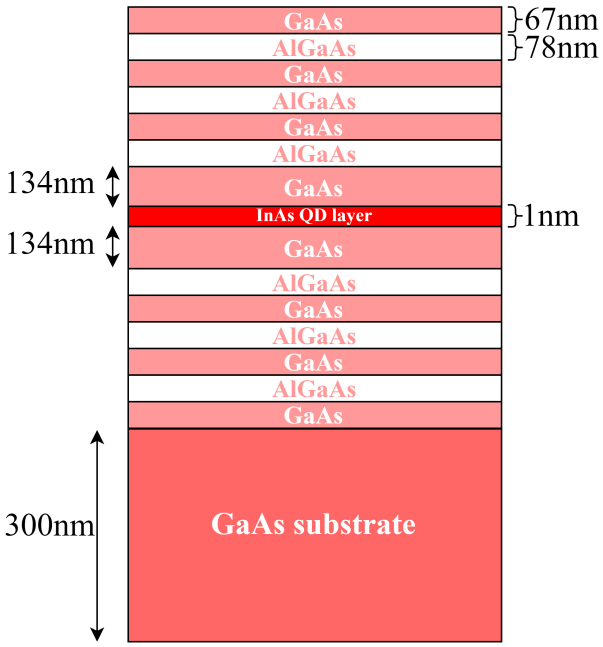

Figure 5.2.1: A schematic of the DBR samples grown via MBE. The Bragg mirror pairs are grown on top of a 300 nm GaAs substrate. A 1 nm InAs layer in between DBR stacks hosts the QDs and is surrounded on top and bottom by a 134 nm GaAs buffer layer.

distributed Bragg reflector (DBR) mirrors can form an easily manufacturable microcavity using well established semiconductor fabrication techniques. These structures are formed of alternating layers of semiconductor material with different refractive indices, with a thickness chosen to preferentially reflect light of a particular wavelength and constructively interfere.[278] For the devices developed in this thesis, these alternating layers were gallium arsenide (GaAs) and aluminium gallium arsenide (AlGaAs) with a thickness resulting in a central planar cavity mode of 940 nm. By varying the number of upper and lower Bragg pairs, the cavity Q-factor was modified. Three inch wafers were grown via MBE at the National Epitaxy Facility, Sheffield, with a varying number

of upper and lower Bragg pairs. Over the course of this project, samples investigated included upper and lower pair numbers of 7/26, 17/26 and 20/30 respectively. The process involved three principal stages: the hardmask deposition, the patterning, the three-step etch. All processing was undertaken at the Institute for Compound Semiconductors (ICS) at Cardiff University, unless specified otherwise.

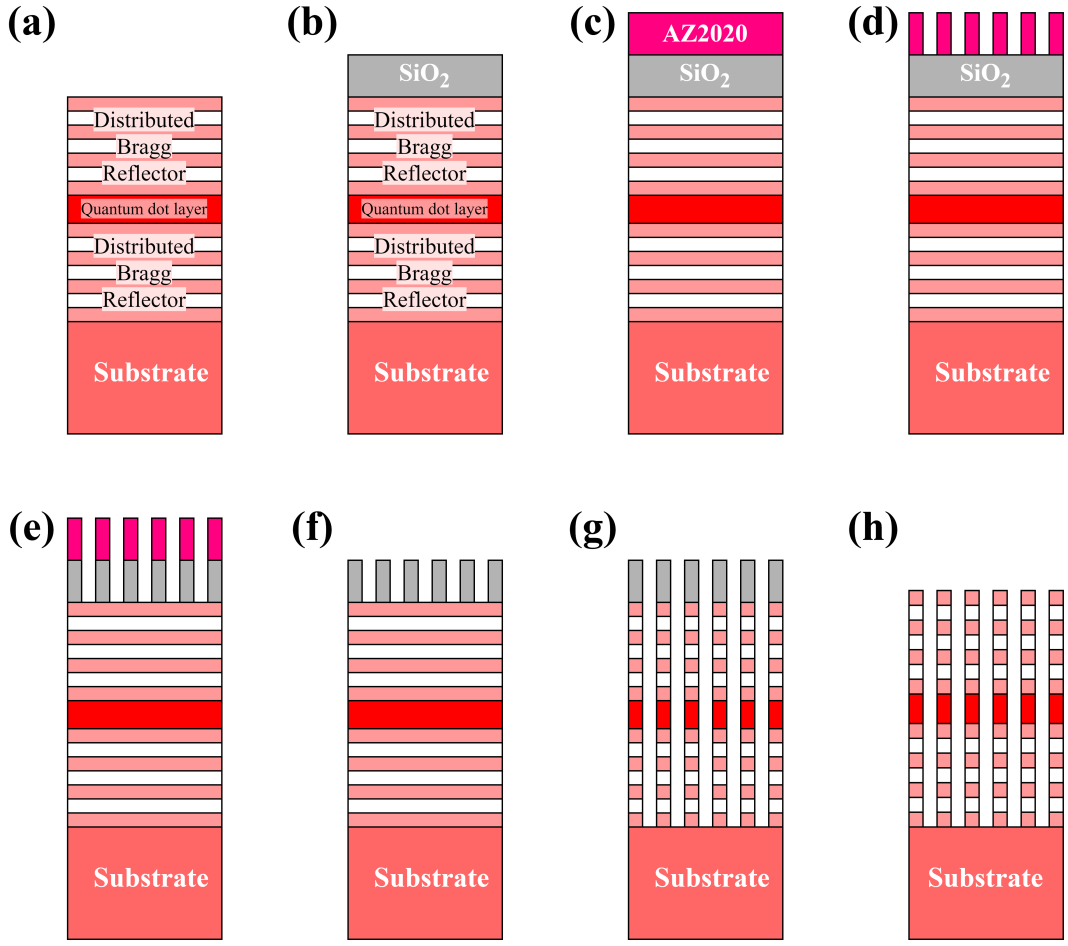

Figure 5.2.2: The micropillar fabrication process flow. **(a)** Three inch wafers of a planar cavity on a GaAs substrate are grown with MBE. The cavity is formed of alternating GaAs and AlGaAs layers around a QD layer of InAs. **(b)** 750 nm of SiO_2 is deposited via plasma-enhanced chemical vapour deposition (PECVD) to form the hardmask. **(c)** An adhesive layer followed by 2 µm of negative-tone photoresist, AZ2020, is spun and baked on in a two-step process. **(d)** The photoresist is exposed using direct-write projection lithography. After this step the samples have a post-exposure bake (PEB) followed by a double-dip in AZ276 developer and de-ionised water (DI). **(e)** After patterning, the first dry etch occurs. The hardmask is etched with C_4F_8 and O_2 with inductively-coupled plasma (ICP). **(f)** The samples are stripped of resist with NMP and then undergo a three-step clean with acetone, methanol and isopropyl alcohol (IPA) in a warm ultrasonic bath. **(g)** After resist strip and clean, the second dry etch occurs. The DBR stack is etched with BCl_3 and N_2 with ICP. Immediately after being removed from the loadlock the sample is submerged in DI. **(h)** Finally the remaining hardmask is removed with a third etch step that is identical in etch parameters to the first. After etching, the samples are coated in 10 nm tantalum pentoxide with an atomic layer deposition (ALD) process.

5.2.1 Hardmask deposition

For this process, silicon nitride (SiN) and silicon dioxide (SiO_2) hardmask depositions were tested, initially with EBPVD and later, PECVD. An ellipsometer was used to measure the deposited thickness and uniformity, and the software returns a 'goodness of fit' parameter R, where ideally R approaches one. The initial estimate of required

Sample	**Thickness, d (nm)**	**Thickness change, Δd**	**Refractive index, n**	**Fit parameter, R**
A	907	-10	1.4576	0.99396
B	987	-43	1.4362	0.99311
C	832	-12	1.4583	0.99217
D	892	-13	1.4564	0.99362

Table 5.2.1: The results of the first EBPVD test after annealing.

hardmask thickness based on the desired etch depth was 1 µm. In the ICS, the largest possible thickness of SiN and SiO_2 achievable with evaporation was 300 nm and ∼1 µm respectively, so evaporation and various annealing conditions were tested. The first test was on four $10 \times 10 mm^2$ samples of bulk GaAs, named A, B, C and D. After evaporation, the samples underwent rapid thermal annealing (RTA). This process shrinks and thus densifies the deposited layer. The samples were examined on the ellipsometer before and after to calculate changes in layer thickness. The obtained thicknesses and fit parameters from the ellipsometer are summarised in Table 5.2.1. However after following through the patterning and etching process on these samples, it was determined that the quality of the SiO_2 was not adequate, since we were unable to define the smallest pillar sizes and withstand the deep etch. Repeating the evaporation and anneal test on SiN was attempted using a two-step evaporation process, however the SiN delaminated after the second evaporation and anneal step, both on wafers and cleaved samples. After these results, the hardmask deposition was outsourced to the University of Bristol to deposit 1 µm of SiO_2 via PECVD. This yielded positive results, with the hardmask of sufficient quality and thickness to withstand the etch and permit feature definition down to 1.55 µm. This point is discussed further in Section 5.2.3 when describing the etch optimisation.

5.2.2 Direct-write projection photolithography

The desired high-aspect ratio of the pillars of up to 1.55 µm by 8 µm posed a difficult trade-off for resist thickness and so the patterning of these samples was the longest optimisation of the entire process. The first lithography trials were performed on Samples A, B, C, D mentioned in Section 5.2.1. A quartz mask was designed by Dr Petros Androvitsaneas and Dr Tomas Peach for a positive tone resist. The pattern was comprised of regular 5 × 5 arrays of pillars, with diameters from 1.55 µm to 5 µm. An adhesion

promoter layer improves the adhesion between the substrate and the photoresist, reducing the likelihood of accidentally removing the exposed areas.

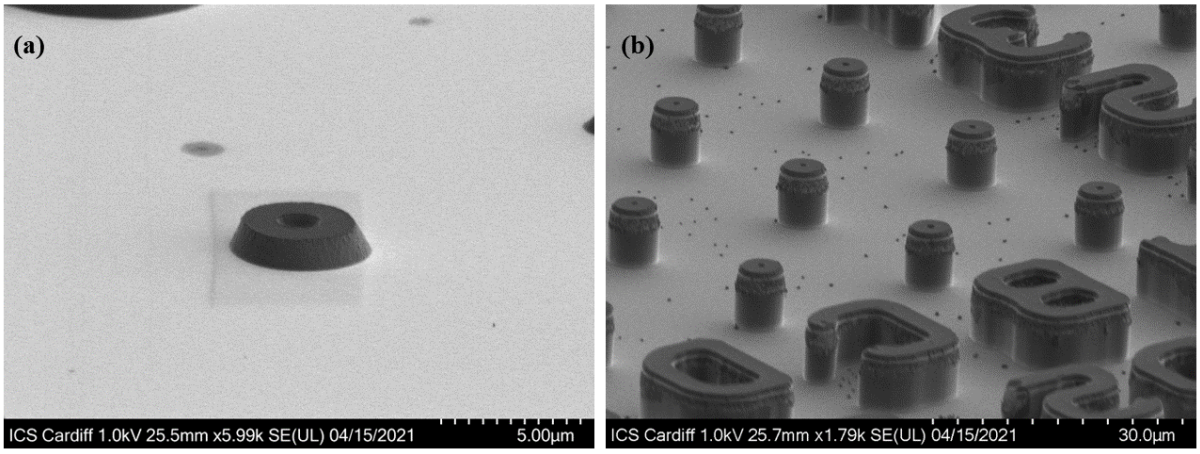

Figure 5.2.3: A scanning electron microscope (SEM) image showing the 'doughnut' interference pattern shown on Sample A as a result of masked photolithography. **(a)**: The sample following the hardmask etch. The pyramidal shape is thought to be caused by a non-optimal PEB. **(b)**: The sample following the semiconductor etch. Sidewall roughness and non verticality has been transferred onto the top of the pillar, and the hollowed centre is still visible.

The first trial was done on Sample B. Photoresist AZ ECI 3027 was used, with a spin recipe to coat 3 µm. The exposure was done with a lamp power of 442 W, where 12.94 mW cm^{-2} was the measured power at the sample by the optometer. The suggested dosage for this photoresist was given on the data sheet as 260 mJ cm^{-2} and requiring the exposure to be ∼20 seconds. The resist was baked at 120 °C for 1 minute and then developed for 1 minute 50 seconds. Upon examining the sample after development with an optical microscope, it was noted that no features smaller than 3 µm had survived, implying that it had been overdeveloped. Furthermore, some of the features had visible 'doughnut' shapes; an example is shown in an etched sample in Figure 5.2.3. This is due to interference between the substrate and the mask - for close-contact physical masking, interference effects can result in an uneven distribution of exposure light intensity at the photoresist, leading to an uneven resist post exposure and development. For Sample A, the dosage was lowered to ∼195 mJ cm^{-2} by exposing for 15 seconds. The PEB and development time were the same as for Sample B. This sample was underdeveloped and the doughnut shapes were still visible - see Figure 5.2.3. For Samples C and D, a negative tone resist was tested. For this, a quartz mask in the ICS with similar feature sizes designed for negative tone resist was used as a temporary placeholder. The AZ 2020 photoresist was used, with the same adhesion promoter, and a ∼2 µm thickness was spin coated. The optometer measured 12.1 mW cm^{-2} and the required dosage for this photoresist was initially estimated at 60 mJ cm^{-2}. Sample C was exposed for 5.2 seconds and the PEB was 115 °C for 2 minutes; Sample D was exposed for 6 seconds and the PEB was 112 °C for 2 minutes. The development took 1 minute 30 seconds

and again was followed by a DI rinse. Both samples showed features down to 1.5 µm, with no visible interference effects. The development proceeded with the negative tone photoresist, which required a mask redesign.

The next round of optimisation was done on GaAs material, and 'real' material i.e. DBR stacks of GaAs/AlGaAs with 1 µm of SiO_2 hardmask deposited by PECVD. The exposure tool was also changed - from the photolithography mask aligner (Suss MJB4) to a new direct-write maskless projection lithography tool (MicroWriter ML3 Pro). As before, 2 µm of TI adhesion promoter and negative resist AZ 2020 was spun and baked on to our samples. Initial exposure tests were run on a GaAs sample to test required dosage - the optimal dose was determined to be 80 mJ cm^{-2} for 2 minutes to resolve the smallest feature sizes. Following exposure, the PEB was performed on a wafer-scale hotplate with improved sensors and an automatic timing system. During the dosage optimisation it became clear that for this particular photoresist, the PEB was a key part of defining the verticality of the sidewalls, and so controlling the temperature more efficiently with a better hotplate was particularly advantageous. The developer was AZ 726 and the samples were developed for a total of 90 seconds in two separate beakers, followed by a DI rinse. This process resulted in a well-defined pattern and was therefore tested next on the real material, which also yielded positive results. The direct write settings were as listed in Table 5.2.2. The development and PEB were the same parameters as for the

Parameter	Value
Quality	'Normal'
Dose correction	0.8
Focus	0
Resolution	0.6 µm
Wavelength	365 nm
Microscope magnification	×20
Resist sensitivity	100

Table 5.2.2: The DMO parameters.

GaAs sample test - the smallest pillars on this run also survived. The final lithography recipe was then as follows:

1. **Cleaning**: solvent clean in ultrasonic bath at 50 °C for 5 minutes each in acetone and IPA.
2. **PECVD**: deposit 1 µm of SiO_2.
3. **TI adhesion primer**: spin on 2 µm, bake at 115 °C for 2 minutes.
4. **AZ2020**: spin on 2 µm, bake at 110 °C for 1 minute.
5. **Direct-write exposure**: 80 mJ cm^{-2} dosage for 2 minutes, parameters as listed in Table 5.2.2.

6. **Post-exposure bake**: 112 °C for 2 minutes on digital hotplate.

7. **Development**: 90 second 'double dip' followed by DI rinse.

5.2.3 Inductively-coupled plasma etching

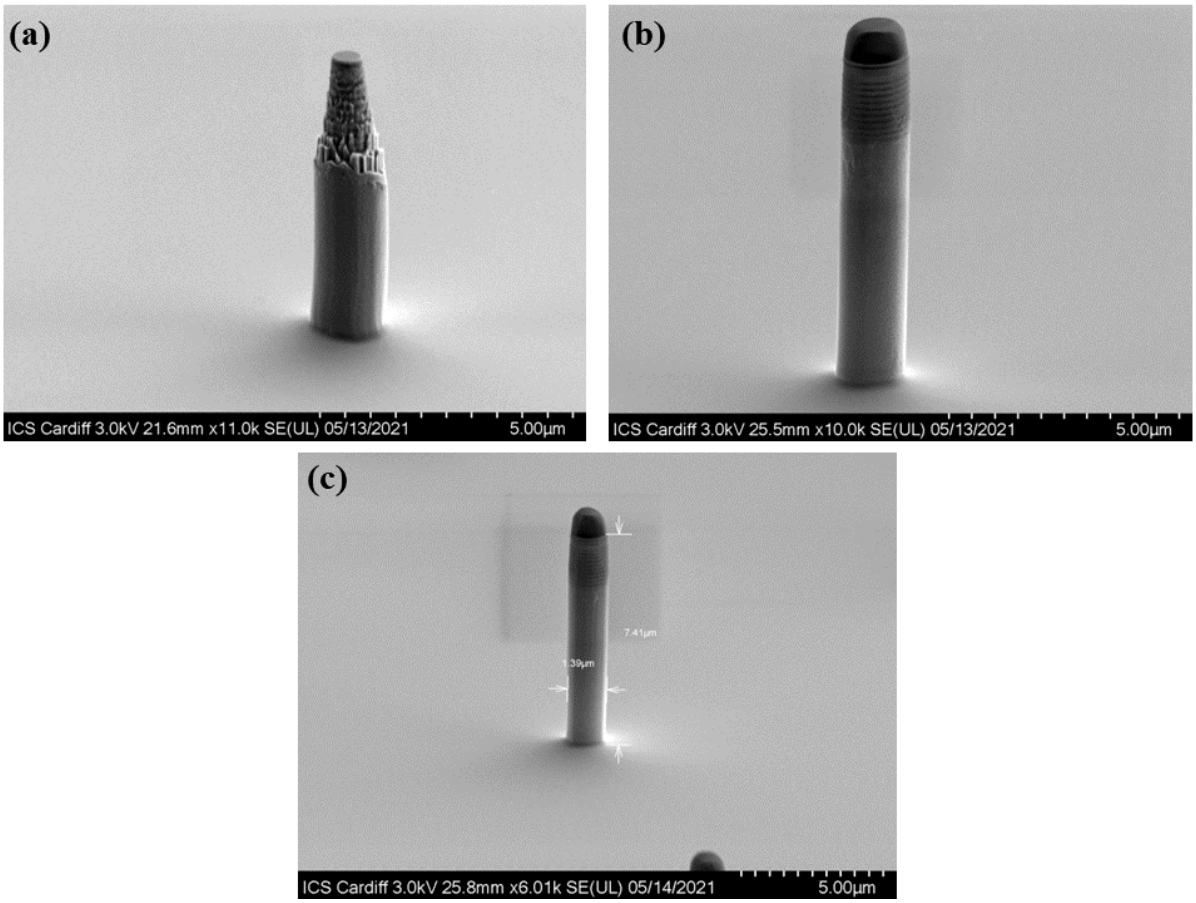

Figure 5.2.4: A SEM image showing three etch tests for the first two etch steps described in Section 5.2.3. **(a)**: The sample with no hardmask after two etches. The selectivity was too low and the top of the pillar was destroyed. **(b)**: The sample with photoresist removed after the first etch. The selectivity of the hardmask is high as there is plenty remaining. **(c)**: The sample with hardmask and photoresist for both etches. The labels show the achieved aspect ratio.

To define the micropillar structures after patterning the resist, three separate etch steps were undertaken. The first step to define the pattern on the hardmask was a fluorine-based ICP etch, and the second step to etch the DBR layers is a chlorine-based ICP etch. The selectivity of the hardmask was tested with some DBR material with different coatings - a sample with photoresist but no hardmask, a sample with hardmask but no photoresist, and a sample with hardmask and photoresist. Before the first etch step, the samples are ashed at 50 W for 1 minute. The fluorine hardmask etch was a high-power etch that ran for approximately 18 minutes. The chlorine semiconductor etch was around 4 minutes. After the semiconductor etch step, the samples were immediately

submerged in DI water after being taken out of the ICP loadlock. This is to reduce sidewall corrosion caused by chlorine from leftover etchant residue, and reduces the oxidation of the aluminium-rich DBR layers in atmosphere. Figure 5.2.4 shows the results of each test. Without a hardmask, the top of the pillar was destroyed as the selectivity was too low. Both etches with the hardmask had a high enough selectivity, as the required etch depth was reached with some hardmask remaining, with the sidewalls remaining vertical. Removing the photoresist with a strip and clean before the second etch resulted in a thinner layer of hardmask being left over, and so this step was taken forward in the process as it made removing the hardmask later on easier. The strip and clean is an hour long procedure in total. The photoresist is removed by sitting in NMP resist stripper for 30 minutes at 80 °C, and then for 5 minutes in the sonnicator at 50 °C, 30 W, 80 Hz. Then the samples are put in acetone, first on the 80 °C hotplate for 5 minutes, and then in the sonnicator for 5 minutes at 50 °C, 30 W, 80 Hz; the same process is repeated in IPA. After cleaning the sample is ashed once again, at 100 W for 1 minute. The final

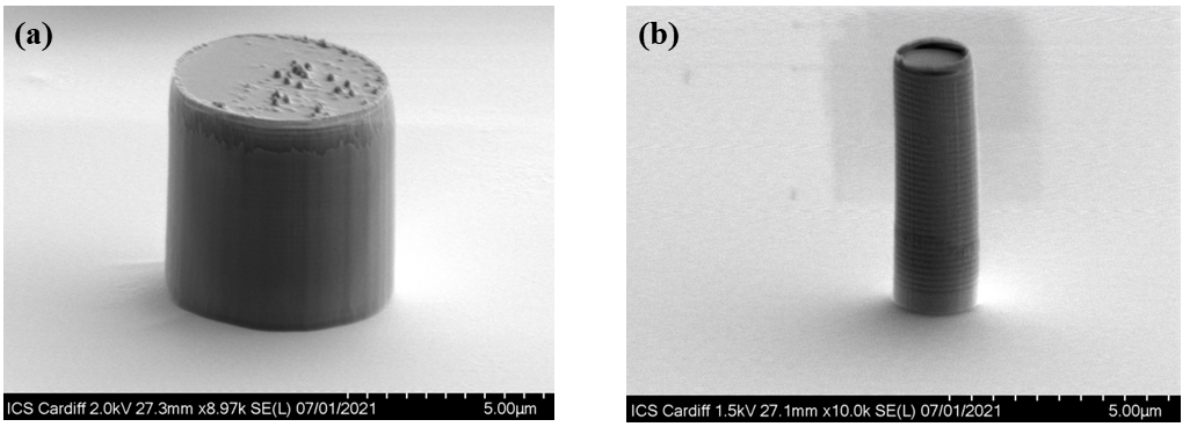

Figure 5.2.5: A SEM image showing two etch tests for the final etch step described in Section 5.2.3. **(a)**: The RIE appeared to deposit a polymer-like substance on the pillar sidewalls. **(b)**: The ICP etch, after some optimisation was more successful and did not result in redeposition.

part of the process to be developed was the hard mask removal step. To optimise this, RIE and ICP etching were tested. RIE was attempted with etch chemistry CHF_3 + Ar for 20 minutes. This resulted in a reasonably smooth top of the pillar, however there was redeposition of some polymer-like substance that coated the sidewalls, which could not be removed with cleaning, shown in Figure 5.2.5(a). The same ICP etch recipe for the first etch step was also tested. This required some tweaking of parameters such as ICP power to alter the balance of physical versus chemical etching but ultimately resulted in smooth surfaces with no redeposition or attacking of the GaAs/AlGaAs sidewalls, as shown in Figure 5.2.5(b). A deep clean with a high power oxygen plasma, and a conditioning with the fluorine etch chemistry for the ICP etch chamber resulted in the best results. Sometimes contaminants from previous etch processes by other users were evident in the SEM images of the samples, either by corrosion or sidewall deposition, similar the

sidewall deposition shown in Figure 5.2.5(a). After some full processing runs had been trialled, the hardmask thickness was reduced from 1 µm to 750 nm as this was easier to remove in this final step. Finally, after defining the micropillar structures and removing the remaining hardmask, a 10 nm layer of tantalum pentoxide (Ta_2O_5) coated the sample with ALD. This is because aluminium-rich alloys, such as the one comprising the DBR stack in this sample, oxidise quickly in atmosphere and corrode the sidewalls. As well as keeping the samples under vacuum, the ALD step reduces possible oxidation when in atmosphere and aims to improve the longevity of the samples.

5.3 Micropillar characteristics

The final process flow is illustrated in Figure 5.2.2, and Figure 5.3.1 shows a scanning-electron microscope image of a processed sample. The results of this process flow were reported in a paper published in 2023.[279] The mask design results in $\sim 14,000$ unetched pillars of varying diameter. Sample characterisation began by searching the

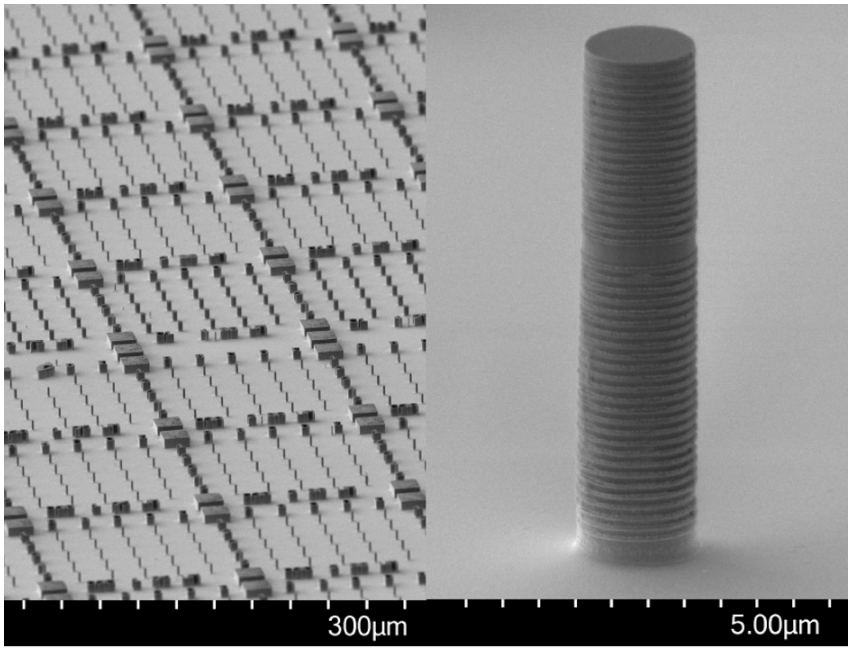

Figure 5.3.1: A scanning electron microscope (SEM) image of the micropillar structures. On the left, a wide-field image of the 5×5 arrays ordered by pillar diameter size. On the right, a close-up image of an individual micropillar of diameter 1.75 µm and etch depth of ∼7 µm

pillars one-by-one under non-resonant optical excitation at 850 nm. A camera and white light source allows navigation of the sample, and initially the collection fibre was directed to a spectrometer, so that relatively bright and spectrally isolated transitions can be located. Switching between white light reflectivity and laser photoluminescence was achieved with a beamsplitter cube secured to a flip-mount. For the low-Q sample with 7 upper and 26 lower layers, the proportion of optically active pillars - pillars that

containing some QD transitions close to the centre of the cavity mode - approached unity. Non-resonant photoluminescence revealed many narrow transitions per pillar, shown in 5.3.2(a). The cavity mode was probed with white light reflectivity measurements. The central cavity mode ω_{cav} according to the Lorentzian fit shown in Figure 5.3.2(b) is (925.37 ± 0.02)nm, and the mode width $\Delta\omega_{\text{cav}}$ is (2.15 ± 0.06)nm. This yields a Q-factor of 430 ± 11. The transition of interest - around 925.5 nm - was successfully isolated and identified as a neutral exciton transition by resonant excitation measurements of lifetimes and linescans. The next section onwards will describe resonant excitation experiments.

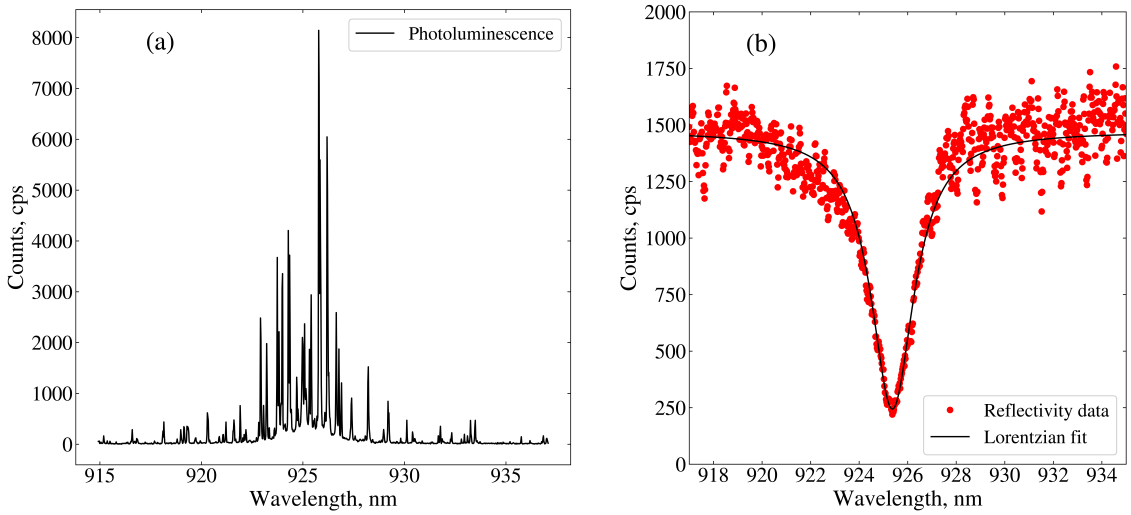

Figure 5.3.2: Spectra of the sample with 7 upper and 26 lower DBR layers. Data collected by Dr Petros Androvitsaneas. **(a)**: Photoluminescence (PL) spectrum of the QD transitions in the C1A 1.7 µm 2E micropillar. **(b)**: White light reflectivity measurement of the cavity mode.

5.3.1 Resonant fluorescence microscope

The experimental set up is shown in Figure 5.3.3. The sample is illuminated with both white light and laser light: the former allows reflectivity measurements of the cavity mode, and the latter is used for both non-resonant and resonant excitation to examine photoluminescence. linear polariser (LP) set the incoming polarisation to $|H\rangle$ - denoted by $\|$ in Figure 5.3.3 - and to set the cross- ($\perp$) and co- ($\|$) polarised collection paths. Laser light launching into $|H\rangle$ passed through a HWP which was mounted onto an individually addressable motorised rotation stage, before being coupled into fibre, to control attenuation of the beam. The laser power is monitored by the power meter labelled 'PM', where the first beamsplitter has a 90:10 ratio, with 90% going onto the power meter. The incoming excitation light is transmitted through the polarising beam splitter (PBS) and through another beamsplitter which also couples in the white light - this second beamsplitter is on a flip-mount, such that the white light can be de-coupled as

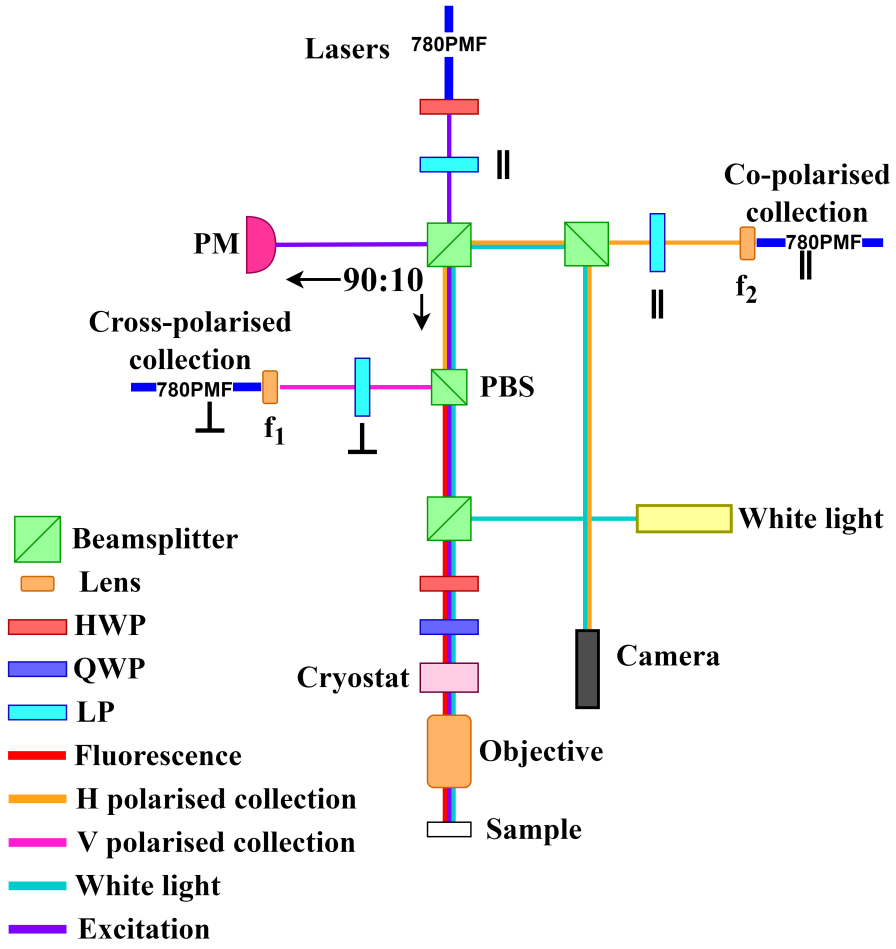

Figure 5.3.3: A schematic of the microscope used for pillar searching and resonant fluorescence measurements. The 850 nm PicoQuant, the M2 and the Mira laser were all coupled into the fibre labelled "Lasers". In the key, LP stands for linear polariser; HWP for half waveplate; QWP for quarter waveplate; BS for beamsplitter. The beamsplitter for coupling in the white light source was on a flip-mount, allowing it to be easily coupled in and out as required. The objective in the cryostat is 0.81NA, f =2.89 mm This microscope was built by Dr Petros Androvitsaneas.

required. Before going through the cryostat window onto the sample, the incoming light travels through a HWP and QWP in turn, both mounted onto motorised rotation stages and also tip-tilt stages. This combination enables the projection of any polarisation state on the Poincaré sphere onto our sample; for a HWP aligned to a particular QD transition, the QWP corrects for any ellipticity introduced by the cryostat window and extinguishes the laser. The tip-tilt stages allow fine adjustment of the waveplates to ensure normal incidence and therefore expected retardance.

The outgoing light travels back through the cryostat window, the QWP, the HWP, optionally the white-light beamsplitter, and then to the PBS. Upon reaching the PBS, all light with an orthogonal polarisation to the input light is directed towards a LP and focussing lens onto the 'cross-polarised' collection fibre. The focussing lens has a focal length $f_1 = 7.5$ mm. All light with some component of polarisation parallel to the input light is directed towards a LP and a focussing lens onto the 'co-polarised' collection fibre.

The focussing lens here has a focal length $f_2 = 8\,\text{mm}$. A non-polarising beamsplitter diverts some of the co-polarised channel to the camera for imaging. The cross-polarised and co-polarised collection fibres could be connected to any required instrument, for example a spectrometer or single-photon detectors.

To resonantly excite a particular transition of interest, a continuous-wave tunable titanium sapphire (Ti:Sapph) laser (M2 Equinox) was tuned to the transition wavelength as observed on a spectrometer. The waveplate positions were chosen as follows. Any transition will have a preferred orientation, related to the crystal structure, and so we aim to excite with a linear polarisation 45° away from this which we control with the HWP. With reference to Figure 5.1.4(b), this effectively means we excite and collect at some polarisation in between $|x\rangle$ and $|y\rangle$. Next, the QWP is rotated to minimise the background noise. This is done initially using the CCD in the optical spectrometer to estimate the minimal background peak. Once on resonance with the transition, the QWP position can be selected by detuning the laser slightly and rotating to minimise the counts at large pump power. This can also give an estimate of the current experimental extinction. To take a linescan, the M2 software would be set to 'Terascan' mode where the start wavelength, end wavelength and scanning speed can be defined. This enables smooth scanning of the laser wavelength over a desired range. We recorded the count rates of both the cross-polarised and co-polarised channels on SNSPDs via a National Instruments data acquisition box. A LabVIEW programme built by Dr JP Hadden and Dr Sam Bishop was used to record both the M2 wavelength and the count rates of each channel over a scan.

5.3.2 Higher-order correlations under high-power excitation

In this section, the photon statistics of the high-power limit of continuous-wave resonant excitation will be explored in detail. First, some characteristics of the particular transition under investigation will be shown to demonstrate that this transition is a neutral exciton. A particular transition at approximately 925 nm in a 1.7 µm diameter micropillar was identified as spectrally isolated and bright. Upon resonantly exciting this transition and measuring the time-resolved photon emission of the emitter, oscillations in the radiative decay were observed, shown in Figure 5.3.4(a). This is a hallmark of the neutral exciton, since the spin of the exciton state begins to precess between the fine-structure split states on the Bloch sphere after excitation, and quantum beats are observed.[222] The period between beats in this figure is ∼370 ps, this has an energy equivalence of 11.2 µeV. The fine structure splitting can also be observed with a laser linescan - Figure 5.3.4(b) shows the cross- and co-polarised collection count rates as the laser is scanned from 925.1 to 925.135 nm. Differences in the count rate between the cross- and co-polarised channel occur as a result of unbalanced efficiencies, due to unbalanced beamsplitters used in

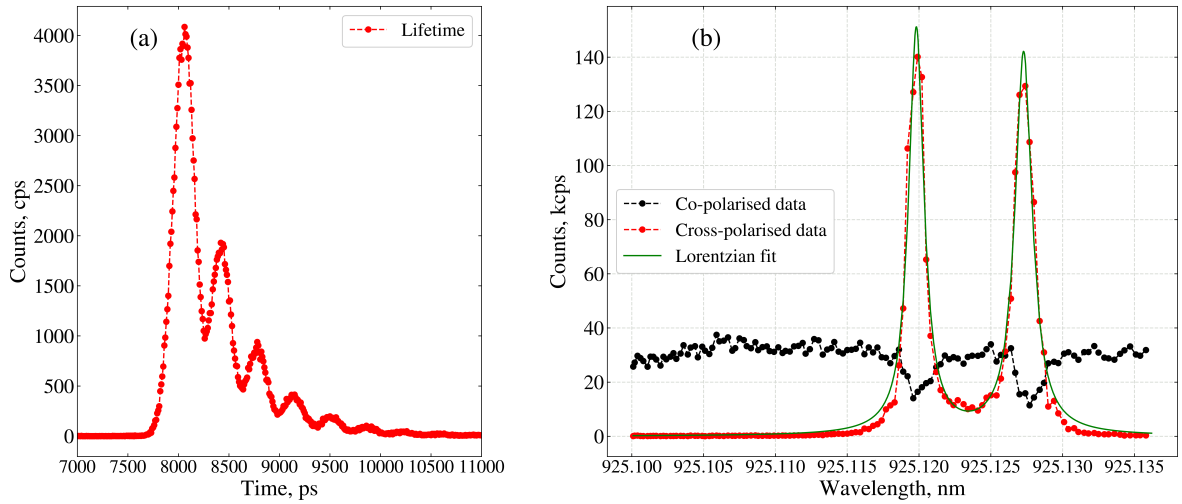

Figure 5.3.4: Resonant excitation characteristics of the 925 nm transition in a 1.7 µm pillar. **(a)**: A time-correlated photoluminescence measurement shows oscillations in the lifetime, characteristic of a neutral exciton. **(b)**: A linescan showing the fine-structure splitting of the neutral exciton transition. The red data is the count rate on the cross-polarised channel which collects the single-photon fluorescence, and the black data is the co-polarised channel which collects the scattered laser signal. The green line is a Lorentzian fit to the fine-structure split doublet.

the experimental set up shown in Figure 5.3.3. The linewidths in Figure 5.3.4(b) are 1.28 pm and 1.44 pm for the blue and red transition respectively, which corresponds to energies of 1.97 µeV and 2.31 µeV respectively. The difference between the peak centres to estimate the fine-structure splitting is 7.47 pm, or 10.8 µeV - similar to the periodicity observed in Figure 5.3.4(a). Once this neutral exciton transition had been identified, power-dependent second-order correlation functions were measured. For the dataset in Figure 5.3.5, the pump power was varied from 76 nW up to 30 µW to investigate the power dependence of the oscillatory $g^{(2)}(\tau_{12})$. As discussed in Section 5.1.4, under high-power resonant excitation the spectrum of a two-level system is dressed and the Mollow triplet emerges. In the time domain this presents as Rabi oscillations in the second-order correlation. Figure 5.3.5 shows a range of power-dependent second-order correlation functions that have been fit with Equation 5.1.18. We expect that the Rabi frequency Ω is proportional to the square of the input power, P. As the transition is pumped harder, the oscillations increase in frequency and also the instrument response further limits the resolution obtained on the anti-bunching dip. This can be overcome by convolving the correlation function with a simple Gaussian function, of a width equivalent to the detector jitter, as described in Chapter 3. This convolution has been applied to the two highest power datapoints in Figure 5.3.6. An imperfection visible in the data presented in Figure 5.3.5 is a very small component of modulation from a second frequency. The fine structure splitting of the neutral exciton orthogonal transitions in this experiment was 7.47 pm, shown in Figure 5.3.4(b). The overlap of the two tails of each Lorentzian

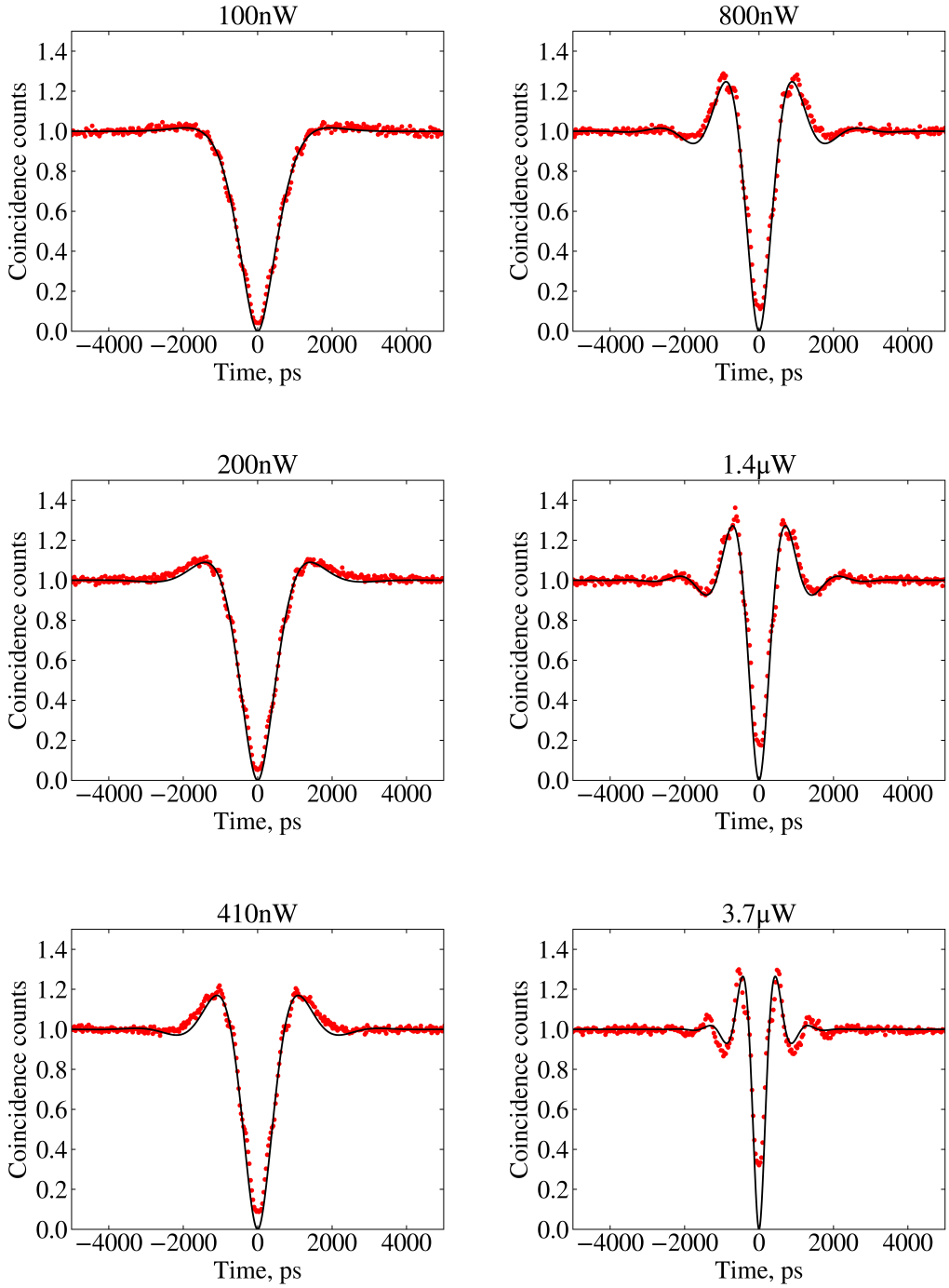

Figure 5.3.5: Power-dependent second-order correlation functions under continuous-wave, resonant excitation. Rabi oscillations appear in the correlation as a result of interactions with the Mollow triplet sidebands. The black line on each subplot is Equation 5.1.18 fitted to the data in red.

peak is visible between them - this implies that when on resonance with one peak, it is possible to weakly excite the other. As a result, we may expect that the modulation of the second-order correlation function is independent of power and related to the beat

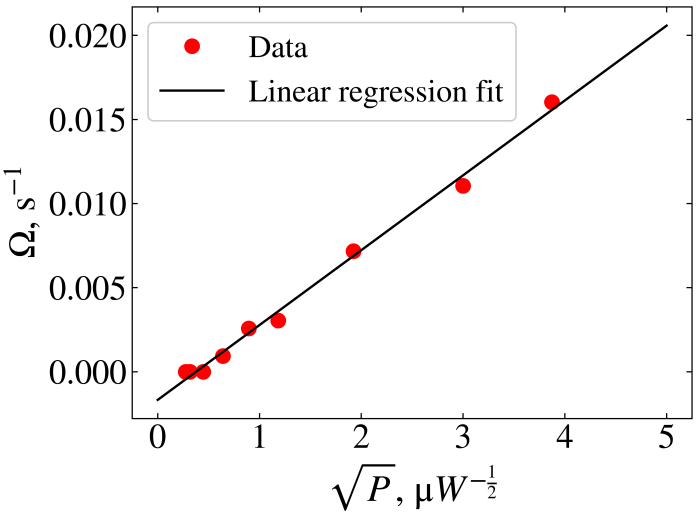

Figure 5.3.6: The square root of pump power versus the Rabi frequency obtained from the fits shown in Figure 5.3.5. The data points in red are fit with a linear function, the black line.

frequency introduced by the fine structure splitting, as exhibited in Figure 5.3.4(a). In Figure 5.3.7, the time-correlated photoluminescence from Figure 5.3.4(a) and three of the low-power second-order correlation functions from Figure 5.3.5 are shown side-by-side, with lines marked at the periodicity of the beating. Another imperfection noted in this

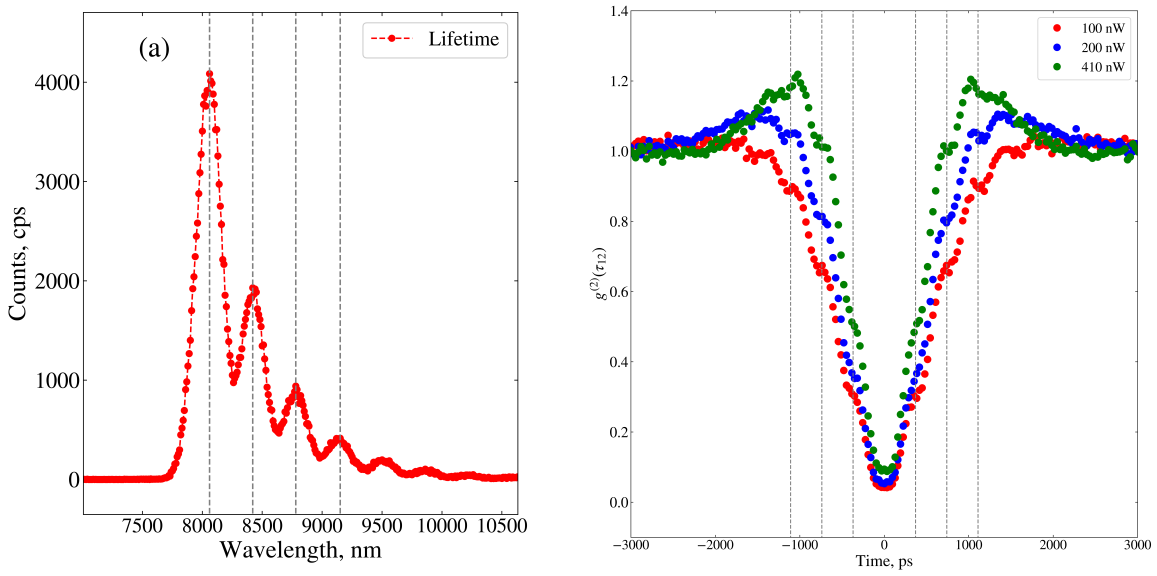

Figure 5.3.7: Fine structure beating in the time-correlated measurements. **(a)**: The data presented in Figure 5.3.4(a) with lines marked on the beat period. **(b)**: Three of the power-dependent $g^{(2)}(\tau_{12})$ shown in Figure 5.3.5 with lines of the same period marked. The periodic modulation of the $g^{(2)}(\tau_{12})$ shown here is not power-dependent.

data set is demonstrated by Figure 5.3.6. We would expect this data to go through the origin - at zero pump power, there should be zero Rabi frequency. The fact that according to the data, we have a non-zero Rabi frequency at zero power implies that

there is some systematic error in our power reading. This is attributed to the noise floor of the power meter being a few hundred picowatts. Finally, a third-order correlation

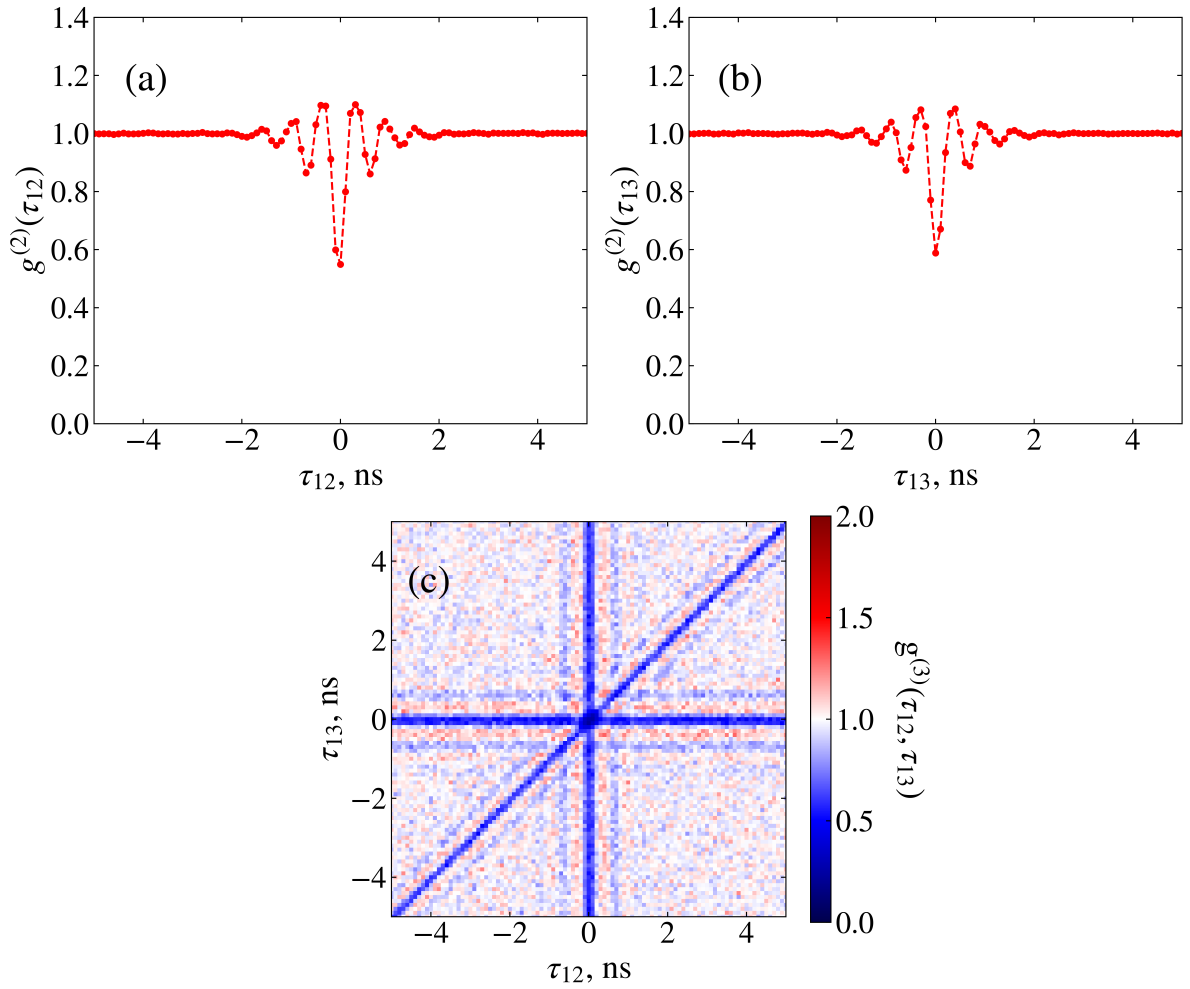

Figure 5.3.8: Oscillatory correlation functions at high power excitation. **(a)** and **(b)** show second-order correlation functions at 8 µW pump power, and **(c)** shows a third-order correlation across the same channels and under the same pump power. The oscillations are symmetric and visible in the $g^{(3)}(\tau_{12},\tau_{13})$.

function under the same experimental conditions as in Figure 5.3.5 was measured using the analysis script described in Chapter 3. For this experiment, the cross-polarised collection fibre was split across four channels using the beamsplitter network described in Chapter 3 and events were timetagged over fifteen minutes. Each channel counted ∼3 Mcps. In Figure 5.3.8(a) and (b) the second-order correlation function for τ_{12} and τ_{13} respectively are shown, and in Figure 5.3.8(c) the third-order correlation between channels 1, 2 and 3 is shown. This yielded the same oscillatory behaviour as observed in the second-order correlations, all symmetric about time zero. For this excitation power the raw second-order correlation function at zero time delay is equal to 0.55 and 0.59 for channel 1-2 and channel 1-3 respectively, and the raw third-order correlation function at zero time delay is equal to 0.22. The Rabi frequency in the third-order correlation remains

constant at this excitation power as expected. Figure 5.3.9 shows the anti-diagonal slice of the 2D $g^{(3)}(\tau_{12}, \tau_{13})$ from Figure 5.3.8 overlaid with the corresponding channel $g^{(2)}(\tau_{12})$ functions. The $g^{(3)}(\tau_{12}, \tau_{13})$ slice exhibits much higher counting noise, as expected. This measurement could be improved by integrating for a longer time period to increase the histogram counts per bin. The third-order correlation of the transition under high-power

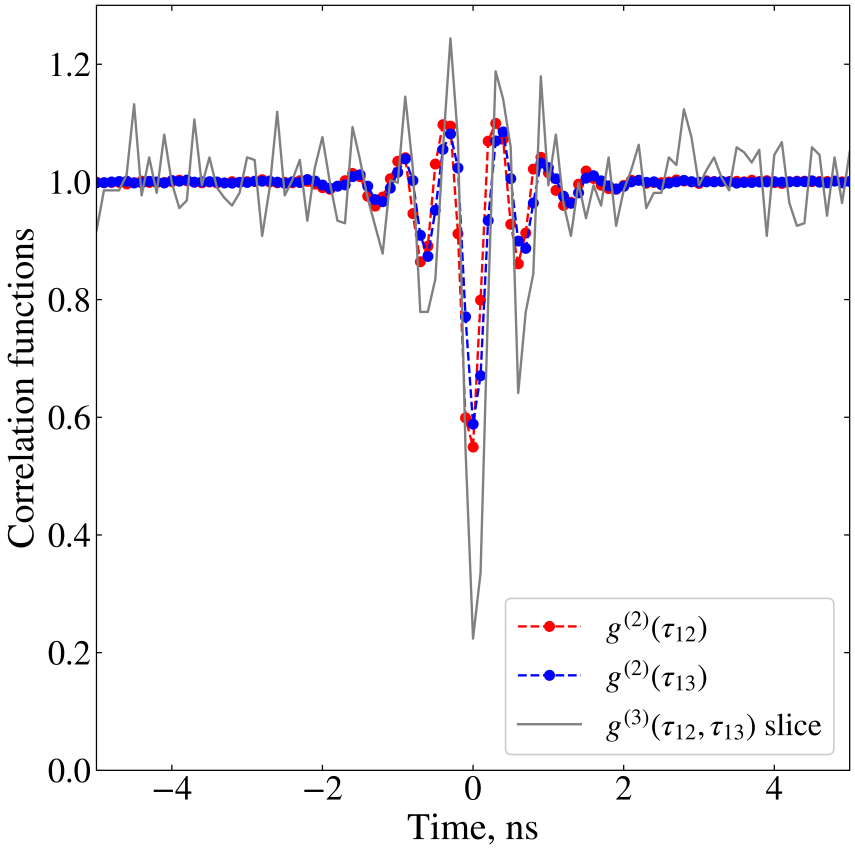

Figure 5.3.9: The correlations shown in Figure 5.3.8 where an antidiagonal slice of the third-order correlation has been overlaid on the second-order correlations. The period of the Rabi oscillation for each correlation remains constant at this excitation power as expected.

resonant excitation provides a direct way of measuring the multi-photon probability by recording the three-fold coincidences.

5.4 Discussion of results and future outlook

In this Chapter, I have presented a semiconductor fabrication process intended for the mass-manufacture of embedded QDs in micropillars as single-photon sources. Direct-write lithography allows the patterning of up to 14,000 devices in 240 seconds[279] with feature sizes defined down to 1.55 µm. Inductively-coupled plasma (ICP) etching allows the definition of smooth-sidewall and high-aspect ratio semiconductor micropillar cavities of different Q-factors. By characterising a low-Q sample with resonant excitation,

I presented results demonstrating that the QD in micropillar samples emit a bright and pure flux of single photons, with the hallmark measurements of correlation functions confirming both the antibunched statistics and the expected two-level system behaviour of Rabi oscillations under high power excitation.

Over the course of my research, I examined low-Q cavities and neutral excitons only. As outlined in Section 5.1.2, high Q cavities result in a higher Purcell factor and therefore a larger enhancement of the spontaneous decay rate. Furthermore, a high-Q cavity results in different photon dynamics as a result of the Jaynes-Cummings model[221] - repeating the higher-order correlations and analysing differences in the Rabi oscillation behaviour may be of interest. Studying Rabi oscillations with frequency-resolved photon correlations, such as in the studies by Nieves and Muller,[280,281] would provide further insight to the three-fold coincidence probability across the Mollow triplet. Also extending the study to charge complexes such as charged trions and biexcitons could lead to interesting photon statistics, examining higher-order correlations of the biexciton cascade, for example as reported in Bounouar *et al.*[282]

Future work could focus on extending the resonant excitation study to the Heitler regime to examine the features of coherent scattering. Photon bunching and non-conventional lineshapes as a function of detuning have been reported when operating in the Heilter regime[283–285] but higher-order correlations in this field are yet to be reported. Extending this work to examine the higher-order statistics of the coherently scattered photons has the potential to provide further insights into the dynamics of the QD complexes.

CHAPTER 6

A METROLOGICAL STUDY OF QUANTUM DOTS IN MICROPILLARS

6.1 Introduction

In Chapters 4 and 5, work on single-photon detector and source characterisation was presented. Now, we approach the fundamental field of single-photon metrology. The advancing capability of single-photon sources and detectors leads to more challenging measurement requirements,[286] for example picosecond resolution and femtowatt sensitivity. To maintain traceability to the Système Internationale (SI) units, characterisation techniques must extend to the few-photon level. Improving the realisable uncertainty of the candela, the SI unit of luminous intensity, also motivate advances in this area.[287,288] The prospect of using an ideal single-photon source for calibrating single-photon detectors and an expanded definition of the candela, has been recently discussed by metrologists.[289] The field of *quantum radiometry* maps the development of this endeavour,[177] moving from the classical regime of electromagnetic radiation to the single-photon regime of light quanta with proof-of-concept measurements on a variety of quantum light sources being demonstrated.

In this chapter, a metrological study on a QD source will be presented. First, an overview of metrology will be given, describing the chain of traceability and calibrated measurements. Then low optical flux detector (LOFD) will be introduced, with a description of pioneering work aiming to close the gap between classical and quantum radiometry. Finally the main experimental results of the chapter will be presented: first, a measurement of the QD single-photon flux on three LOFD, two of which are traceably linked to the SI; and second, applying the calibrated single-photon flux to calibrate a superconducting nanowire single-photon detector (SNSPD).

6.1.1 Traceability and calibrated measurements

The concepts of traceability and calibration are complementary and fundamental to metrology. Metrology is concerned with the development of scientific standards, and the improvement of measurement techniques to ensure accurate realisation of these standards. Figure 6.1.1(a) shows the 'traceability' pyramid, demonstrating the hierarchical structure of metrology. The arrow of traceability on the left hand side indicates that any measurement, no matter how imprecise, can be traced back to some measurement standard. Typically this is an international standard, such as the SI units. The arrow of calibration on the right hand side indicates what level of calibration is required at each stage - this gives an estimate of uncertainty at each level. Any measurement that is performed on calibrated equipment is said to be 'traceably' linked to the SI. The length of this chain of traceability is determined by the number of calibrated instruments between the primary standard and the end measurement. Traceability is important as it ensures that the accuracy of measurements around the world can be compared, and international standards maintained. Metrology is a dynamic field; scientific and technological advancements create ever-changing measurement requirements and capabilities.

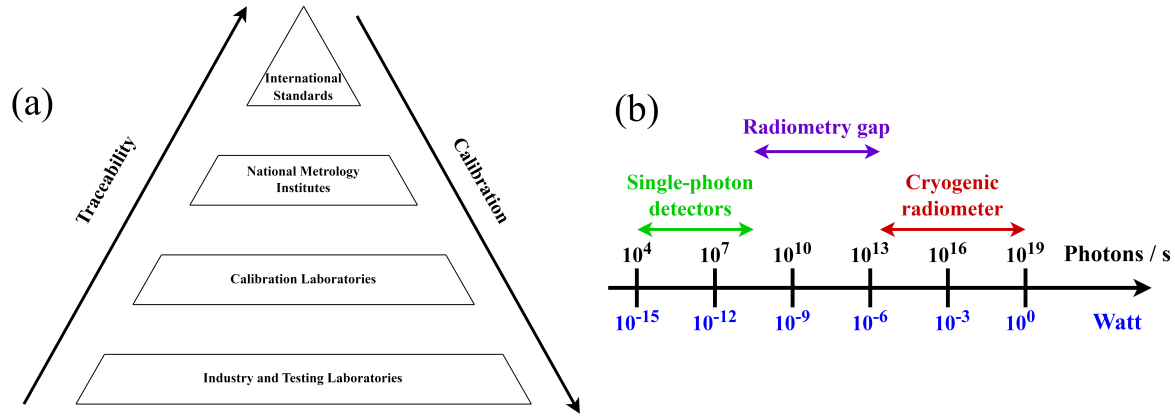

Figure 6.1.1: Central concepts in single-photon metrology. **(a)**: The traceability pyramid. **(b)**: The traceability gap between classical and quantum radiometry.

The SI base unit definitions are maintained and agreed upon by National Metrology Institutes around the world. Their definitions can and do evolve, at the Conférence Générale des poids et mésures (CGPM). When first introduced, many of the SI base units were defined in terms of physical artefacts - for example the kilogram and the metre. Efforts have been made to move away from this convention, and revise definitions to be based on experiments and fundamental physical constants, since artefacts can be lost, damaged or degrade over time. This is also advantageous as, in most cases, it improves the realisable uncertainty on the absolute value. Six of the seven base units are now realisable to accuracies of 1 part in a few million[290] at the UK's National Metrology Institute, the National Physical Laboratory (NPL). The seventh - the candela - is at

best realised with an accuracy of 1 part in a few thousand. According to the Bureau International de Poids et Measures[290] (BIPM):

> "The candela, symbol cd, is the SI unit of luminous intensity in a given direction. It is defined by taking the fixed numerical value of the luminous efficacy of monochromatic radiation of frequency 540 THz, K_{cd}, to be 683 when expressed in the unit $lm\,W^{-1}$, which is equal to $cd\,sr\,W^{-1}$, or $cd\,sr\,kg^{-1}\,m^{-2}\,s^3$, where the kilogram, metre and second are defined in terms of h, c and $\Delta\nu_{Cs}$."

This definition of the candela relates photometry - the sensitivity of the human eye to visible light - to radiometry. At its conception, it was defined with reference to a blackbody radiator as a *standard candle* or *lamp*. Now, its definition is based on a fixed luminous intensity that the human eye is most sensitive to (approximately 555 nm in air), and is realised using a detector-based definition - and is therefore source-independent.[288] It is realised experimentally via cryogenic radiometry. This technique relates the heat generated by incident radiation to an amount of electrical Joule heating that can be measured against a primary electrical standard.[291] The cryogenic radiometer[292] is the self-calibrating absolute detector that carries the primary standard of optical flux, and is used to calibrate other instruments and pass along traceability. As mentioned in Section 6.1, metrologists have been examining the possibility of an expanded definition of the candela based on photon number rather than optical power. This would allow a definition related to fundamental physical constants, where the only experimental uncertainty for the realisation comes from the photon number N - theoretically reducing the uncertainty on its realisation by orders of magnitude.[287] However, this ambition puts rigorous requirements on the single-photon source, which would need a sharply defined spectral extent to minimise uncertainty $\Delta\lambda$ and unprecedented brightness ($> 10^{15}$ photons per second).[288] The semiconductor QD is currently the brightest[36] and most pure[58] single-photon source reported. However, plenty of challenges remain to bring about an expanded definition of the candela. In particular - perfect internal quantum efficiency and collection efficiency are experimentally demanding.

Another application of single-photon sources in metrology is for calibrating single-photon detectors. A particular method used to achieve an SI-traceable calibration of the detection efficiency of a single-photon detector is the *substitution method*. In this calibration technique, an SI-traceable *reference detector* measures the optical flux of a source; this optical flux is then directed to some device under test (DUT) to infer its detection efficiency.[293] Most commonly this technique is performed using a pulsed laser source, attenuated to different levels in order to build up a rate-dependent detection efficiency function.[234] However, this method requires a correction for Poissonian statistics and detector dead time.[294] Proposals to use a single-photon source to apply in these calibrations have suggested this method may improve measurement uncertainties.[295]

Firstly, a single-photon source that emits one photon per excitation pulse, when excited at a rate lower than the inverse of the dead time, would negate the requirement of a dead time corrected factor. In addition, the lower intensity fluctuations that are only achievable with a quantum light source, such as an intensity-squeezed source,[296] could lead to a 'quantum advantage' gained in the uncertainty on its flux value.

Linking antibunched light sources to the SI in a directly traceable way is challenging - there is a substantial gap between the power ranges used in conventional cryogenic radiometry and the maximum signals obtained in photon counting experiments - illustrated in Figure 6.1.1(b). It is only in the last decade that the radiometry gap is starting to close and proof-of-principle measurements are being demonstrated, thanks to improved single-photon sources and detectors. The next sections will explore these LOFD, discuss their applications in single-photon detector calibration, and finally, recent results in the field of quantum radiometry will be presented.

6.1.2 Low optical flux detectors

Low optical flux detector (LOFD) are classical photodetectors, based on photodiodes, that aim to bridge the gap between a typical power meter and single-photon detector. Photodiodes produce a measurable electrical output based on incoming radiation. An important property of a photodiode for LOFDs is its *responsivity*: this quantity depends on the frequency of incoming radiation and gives the electrical output over the optical input. The internal quantum efficiency (IQE) of such a detector is given by the ratio of the number of electron-hole pairs generated in the detector active region to the number of incident photons. The external quantum efficiency (EQE) is related to the IQE via the detector active area's reflectance, absorption coefficient, trap states, resistance and thickness. For radiometric applications that aim to pass traceability to new instruments, it is the detector's responsivity that is calibrated against the cryogenic radiometer.[297] Importantly, when the responsivity is calibrated against the primary standard, it is crucial that the incident beam underfills the detector aperture, such that the detector is measuring the total power in the beam. If this is not the case - the detector is instead measuring the beam *irradiance*, a quantity which depends on the beam area and has units $\mathrm{A\,W^{-1}\,cm^{-2}}$. At NPL, several *trap detectors* are calibrated against the cryogenic radiometer to extend the traceability chain and perform detector calibrations. These detectors, first described by Fox,[299] have ideal properties for this application, and indeed were developed for this specific aim. Their construction is based on an arrangement of silicon photodiodes that direct reflected radiation from each photodiode onto another, reducing polarisation sensitivity and enhancing the IQE to near unity. The disadvantage of a multiple-element detector in this way is that the collective dark current of each element sums together, leading to an overall higher noise floor. Other LOFDs may use

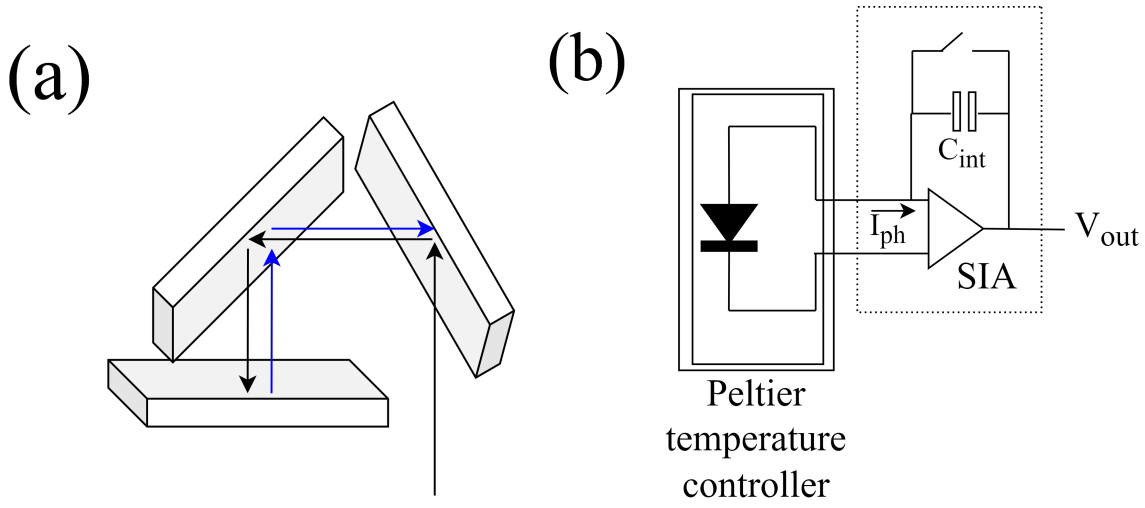

Figure 6.1.2: Schematics of the SI-traceable low optical flux detector (LOFD) used in this study. **(a)**: Three-element trap (3ET) detector. **(b)**: Cooled silicon photodiode from the Czech Metrology Institute (CMI); recreated from Porrovecchio *et al* Fig. 5.[298]

cooled germanium photodiodes, and most require an additional amplification process, such as a transimpedance or switch-integrator amplifier. Detectors may be operated with or without an electrical bias - this changes its characteristics. For an unbiased detector, the responsivity is linear with optical power. However the responsivity of a biased detector is non-linear and therefore the calibration is more complex, especially when extrapolation is required. To this end, when using these LOFDs for passing traceability, typically one endeavours to operate in a 'linear region' of wavelength.

In this chapter, three LOFDs were used for a metrological study. The three-element trap (3ET) detector is a free-space reflection trap detector based on an arrangement of three Hamamatsu (S1337) photodiodes used for single-photon detector calibration in NPL. A fibre-coupled photodiode with a cooling fan, thermoelectric controller and integrating capacitor, provided by Geiland Porrovecchio and Dr Marek Šmíd at the Czech Metrology Institute (CMI), was able to realise a lower noise floor than the 3ET.[298] Both of these detectors are unbiased and directly SI-traceable, as their responsivity has been linked to the cryogenic radiometer at NPL and the CMI respectively. A schematic of both is shown in Figure 6.1.2. Their photocurrents are amplified by a switch integrator amplifier (SIA).[300] Typically, low flux optical measurements employ a transimpedance amplifier (TIA), which offers advantages such as high accuracy and stability, large operational range of current, and can work with biased photodiodes. Drawbacks of TIAs include its complex design (high-cost precision resistors and high-quality field-effect transistor amplifiers), its sensitivity to capacitance in the photodiode junction, and having low bandwidth at high gains.[301] Contrastingly SIAs offer better performance specifically at low current amplification,[302] can be more cost effective, and are not sensitive to photodiode capacitance. A commercial photoreceiver (Femto) based on a low noise silicon

photodiode and an integrated TIA exhibited excellent sensitivity (down to femtowatts) and stable output, but was not directly traceable to the SI - although this is a calibration that could be performed in hindsight of any experimental results. This specific model of detector was calibrated by a group at the Physikalisch-Technische Bundesanstalt (PTB),[295] who stated that despite the detector being biased, its responsivity was calibrated and found to be linear in the ultra-low power regime (between 57 fW and 12.3 pW).

6.1.3 Experimental demonstrations in quantum radiometry

As explored in Section 6.1.1, the traceability gap between classical and quantum radiometry has only recently begun to close, thanks to brighter, more efficient single-photon sources, and more sensitive detectors, LOFD, that are traceably linked to the SI. This section will provide a brief review of the recent advancements in quantum radiometry.

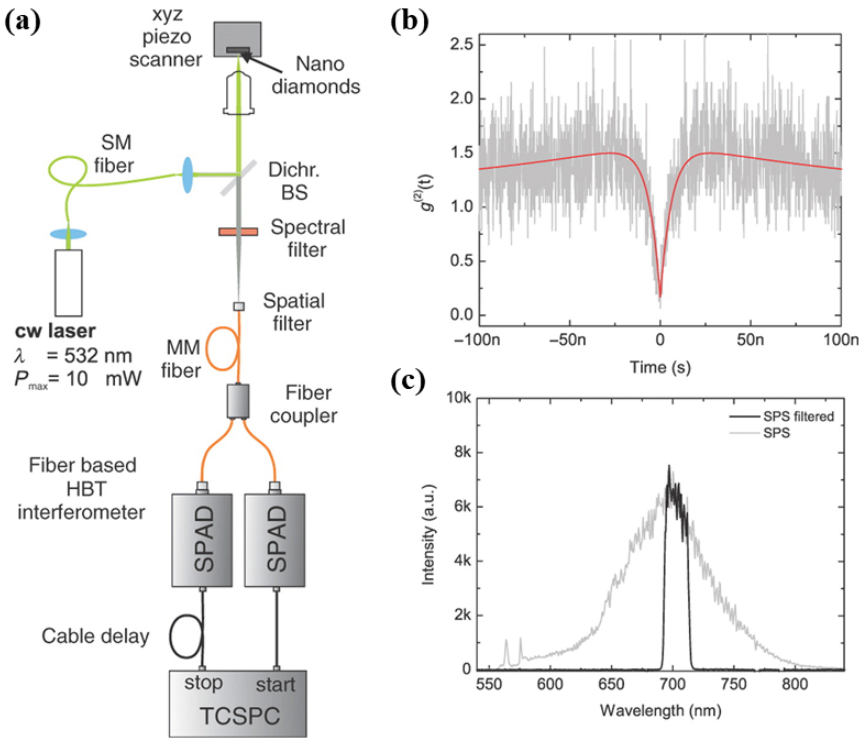

Figure 6.1.3: Taken from Schmunk *et al.*[294] **(a)** The LSCM system used to examine the NV centres. **(b)** The second-order correlation function and **(c)** the full and filtered spectrum of the diamond NV source respectively.

An absolute metrological calibration of a single-photon source involves a traceable measurement of its optical power on an instrument calibrated against the cryogenic radiometer. This was first demonstrated for the diamond NV centre,[303] which was calibrated with reference to its optical flux and spectral power density. An absolute

metrological calibration of a single-photon detector involves illuminating the detector with some known optical power, as determined with a calibrated measurement of the optical flux and any attenuation factors, to determine its detection efficiency. An overview of single-photon detectors is given in Chapter 1, and in Chapter 4, the dead time in single-photon detectors leads to a detection efficiency that not only depends on the incoming rate, but also on the source statistics. Thus a full detector characterisation should consider all of these metrics. Many absolute detector calibrations using single-photon sources have been demonstrated already for single-photon avalanche diode (SPAD). Schmunk *et al.* presented a SPAD calibration technique based on a commercially available diamond NV centre.[294] Details of the experiment are shown in Figure 6.1.3. A 700 ± 19nm bandpass filter was implemented to filter the broadband emission and the single-photon purity was measured to be $g^{(2)}(0) = 0.15 \pm 0.002$. Lombardi *et al.* traceably measured a maximum single-photon flux of 334 fW from a

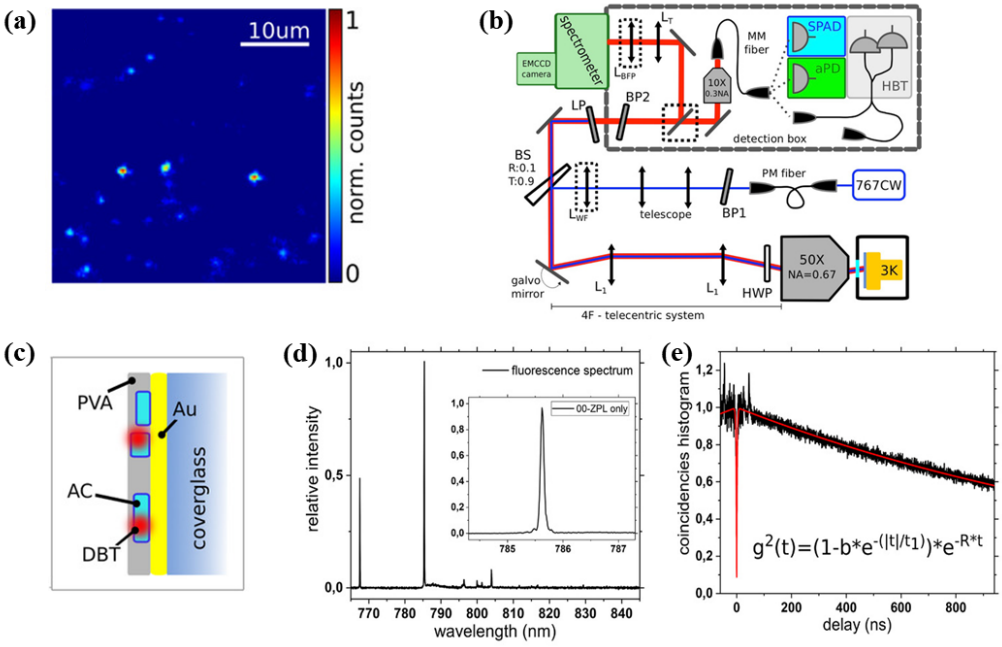

Figure 6.1.4: Taken from Lombardi *et al.*[55] Figure **(a)** shows a wide-field image showing bright regions indicating nanocrystals. Figure **(b)** is a schematic of the device based on dibenzoterrylene (DbT) molecules in anthracene (Ac) nanocrystals, suspended in a polyvinyl alcohol (PVA) substrate on a reflective gold (Au) layer. Figure **(c)** is a schematic of the epifluorescent microscope, and Figures **(d)** and **(e)** show the sample spectrum and second-order correlation function respectively.

dibenzoterrylene (DbT) molecule in an anthracene nanocrystal (DbT:Ac).[55] This was achieved with 200 nm DBT:Ac nanocrystals grown with a re-precipitation method, and fabricated into a resonator structure based on a gold mirror to optimise the direction of emission. Details of this experiment are summarised in Figure 6.1.4. At a maximum count rate of 1.4×10^6 photons per second the single-photon purity remained high, with

$g^{(2)}(0) = 0.08 \pm 0.01$; the single-photon flux is also shown to be stable, with an overall drift of around 2% over a 10-minute timescale. A SPAD was calibrated with the substitution method, where the traceably calibrated flux of 334 fW was measured on a classical silicon photodetector, and the detection efficiency was determined to be $\eta_{\mathrm{SPAD}} = (0.603 \pm 0.012)$ over a range of 10^5 to 10^6 photons per second incident flux. Georgieva *et al.* perform

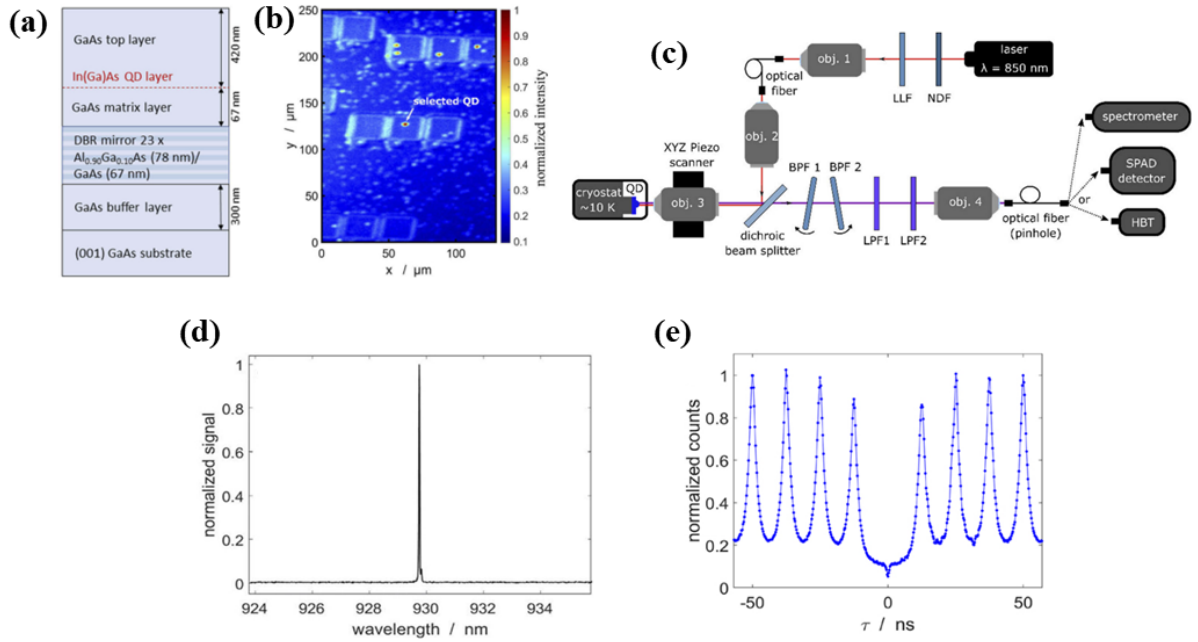

Figure 6.1.5: Taken from Georgieva *et al.*[295] Figure **(a)** and **(b)** show a schematic and micro-photoluminescence scan of the quantum dot sample structure respectively. In **(b)** the deterministically patterned micro-mesa structures are visible as squares. Figure **(c)** shows a schematic of the confocal microscope set-up for investigating the sample, while **(d)** and **(e)** are the filtered source spectrum and pulsed second-order correlation function respectively.

a similar study to Lombardi *et al.* with a triggered InGaAs QD, traceably measuring a maximum single-photon flux of (545 ± 4)fW.[295] In this work, a deterministic process is used to create resonant structures around self-assembled InGaAs QD with electron-beam lithography and etch fabrication techniques. An absolute calibration of a SPAD was performed in a similar manner to Lombardi *et al.* using the substitution technique and a commercially available low-noise photoreceiver from Femto, which was traceably calibrated. A weighted mean for detection efficiency of $\eta_{\mathrm{SPAD}} = (0.3263 \pm 0.0022)$ was calculated.

In the remainder of this chapter, our work applying a QD micropillar sample for the absolute calibration of SNSPDs will be presented. At the time of measurement, the calibrated single-photon flux measured on the 3ET, an SI-traceable detector, was the highest reported in this field.[1] Section 6.2 describes the experimental set-up

[1] In the months since this experimental work, a study from the Korean Institute of Standards and Science[304] has reported a higher single-photon flux traceably linked to the SI.

for establishing a bright and pure single-photon flux in a low-temperature confocal microscope, and shows the results from measuring this optical flux on three different LOFD. Section 6.3 explains the calibration of SNSPD based on applying the substitution method and using both the single-photon source and an attenuated pulsed laser as a comparative study.

6.2 Metrological characterisation of single-photon flux

6.2.1 Single-photon characteristics

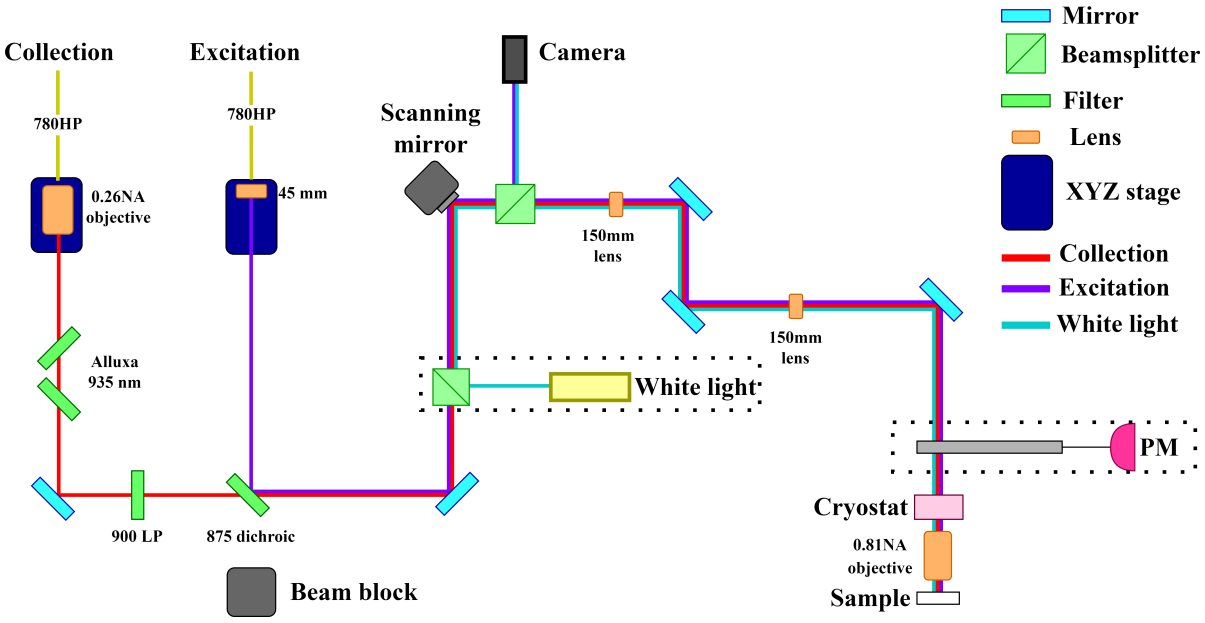

Figure 6.2.1: Schematic of the low-temperature laser scanning confocal microscope (LSCM) used for all measurements shown in this chapter. The dotted boxes indicate components that can be placed and removed as required; the white light was typically only used to navigate the sample and realign the microscope, and the power meter (PM) was only used when calibrating the laser power controlled by a LabVIEW VI. The details of the microscope can be found in Section 6.2.1.

For this study, a QD in low-Q micropillar sample was used - a sample from the same wafer and fabrication run as the results shown in Chapter 5. This was held at 4 K in an attoDRY close-cycle cryostat. The following LSCM system and all associated LabVIEW software for obtaining measurements was implemented by Dr Philip Dolan; I was responsible for maintaining and aligning it during this study. To navigate the sample and choose a $\sim 100\times100$ µm^2 area to investigate, white light illumination was coupled into the system with a pellicle and LED source on magnetic mounts, and a camera collected light reflected from the sample. Non-resonant excitation and collection of fluorescence was achieved with the LSCM, a schematic of this system is shown in Figure 6.2.1. This system allowed wide-field, high-resolution raster scanning of up to 25 micropillars at a time via

custom LabVIEW software. The raster scanning was achieved with a steering mirror, a 4f focal system and SPADs; a 0.81 NA objective lens focussed the excitation light onto, and collected fluorescence from the sample. The excitation source was launched onto the breadboard via a 780HP single-mode fibre and 45 mm achromatic doublet, and then directed towards the LSCM with a 875 nm dichroic mirror. The other end of the launch fibre was coupled to a fibre connector, meaning that any choice of laser could be coupled in - over the course of the experiments, 780 nm and 850 nm CW diode lasers and a pulsed tunable titanium sapphire laser (Spectra Physics Tsunami) were used for non-resonant excitation. The emitted fluorescence of 920 to 940nm is transmitted through the dichroic mirror, filtered with a 900 nm long pass filter, collected by a 0.26 NA Mitutoyo objective and focussed onto a 780HP single-mode fibre. This could be coupled, via a 10 m long 780HP fibre, into the spectrometer, a Hanbury-Brown and Twiss experiment, or both via an in-fibre 50:50 beamsplitter. This configuration is shown in Figure 6.2.2.

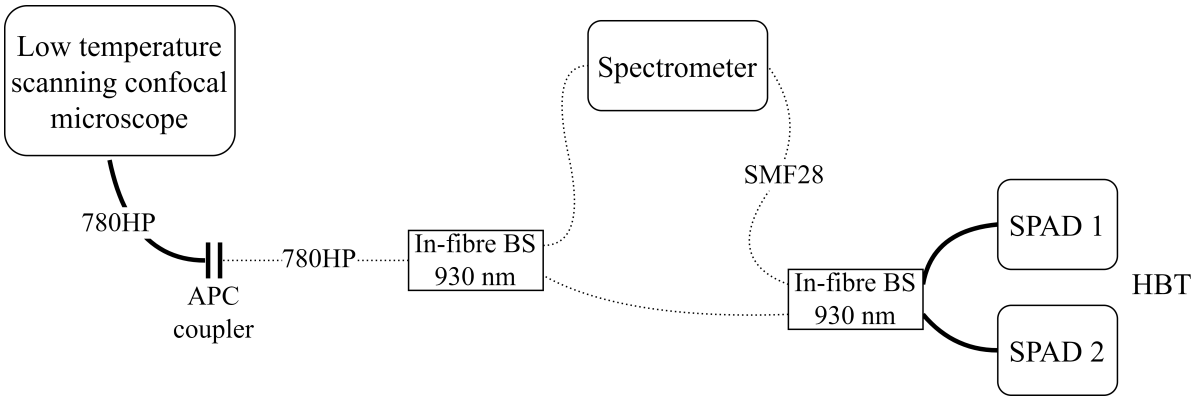

Figure 6.2.2: A schematic of the table layout. The dotted lines indicate fibres that can be swapped over. The 780HP coupled into the collection fibre can be connected directly to the spectrometer, directly to the Hanbury-Brown and Twiss, or to both through an in-fibre beamsplitter.

To filter the fluorescence down to a single transition, two methods were investigated. First, spectrometer filtering was implemented and collected into SMF28. The collection fibre was launched back onto the table and coupled in through the spectrometer slit via an $f = 30$ and $f = 40$mm achromatic doublet respectively. The grating was 1200 lines per mm with 900 nm blaze, and during alignment the entrance and exit widths were varied. The spectrometer was aligned with a 780 nm CW diode laser and the output was coupled into SMF28 via an achromatic doublet lens. The resolution and coupling of the spectrometer filtering is shown in Figure 6.2.3(a). The second filtering method was with two ultra-narrow bandpass filters (Alluxa 935.0-0.45 OD5). These filters were secured on motorised rotation stages and mounted before the collection objective. The achievable bandwidth and transmission of the Alluxa filter pair was determined with a white-light source and the spectrometer, shown in Figure 6.2.3(b).

After completing a scan, the laser focus point could be redirected to each pillar

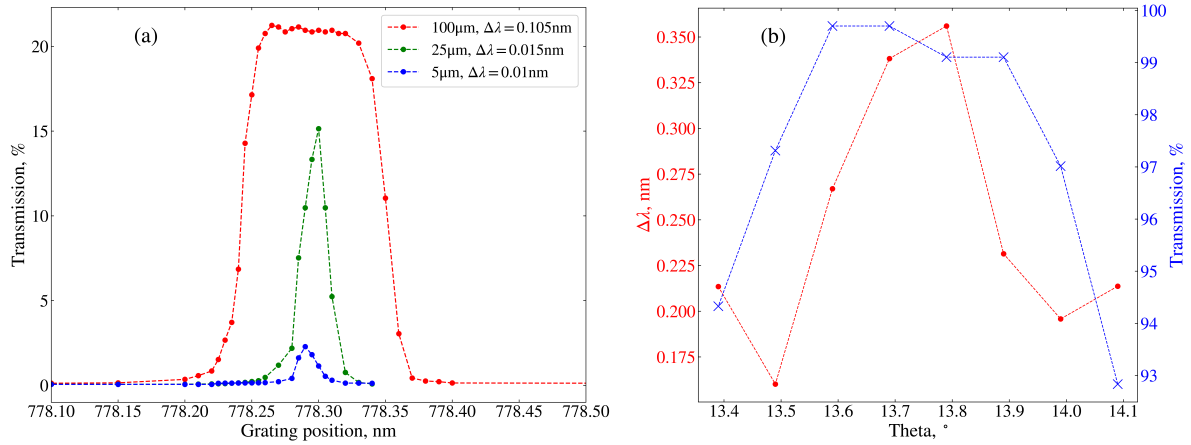

Figure 6.2.3: Comparing the coupling and resolution of the spectrometer and a pair of Alluxa filters. **(a)**: Varying the exit slit width to estimate the spectrometer resolution. After aligning the 780 nm source, the grating was jogged through 778 to 778.5nm and the transmission at the exit port recorded, for different exit slit widths. **(b)**: Rotating one Alluxa filter with respect to another on a motorised rotation mount and measuring the filtered white-light spectrum on a spectrometer. The transmission and bandwidth for each position measured.

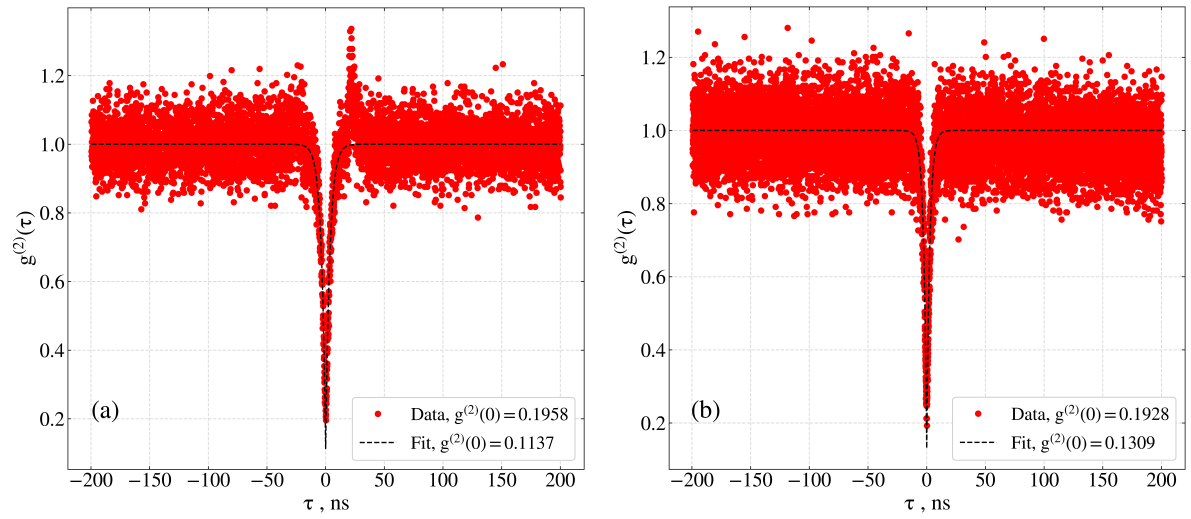

Figure 6.2.4: Comparing second-order correlation functions on SPADs for each method. The fit displayed in black corrects for the SPAD instrument response function with a convolution fitting routine, described in detail in Section 3.4.2. **(a)**: A $g^{(2)}(\tau_{12})$ taken with spectrometer filtering. The transition was pumped with 5.1 μW, the count rate was $\leq$ 20kcps at the SPADs and the integration time was 16 hours. Due to the substantially lower count rate, bunching due to back reflections is visible at ∼20 ns **(b)**: A $g^{(2)}(\tau_{12})$ taken with Alluxa filtering. The transition was pumped with 5.7 μW, the count rate was ∼330kcps and the integration time was 5 minutes.

one-by-one, and the micropillar spectrum was recorded with the Alluxa filters removed. Similarly to the search process described in Section 5.3, bright, narrow and spectrally isolated transitions were noted for further investigation. Once identified, the fluorescence was filtered and a $g^{(2)}(\tau_{12})$ was measured on SPADs. A $g^{(2)}(\tau_{12})$ was measured with each filtering method for a particular transition in order to compare - the results of these measurements are shown in Figure 6.2.4. In the $g^{(2)}(\tau_{12})$ with spectrometer filtering,

we see some asymmetric peaks - this is caused by back reflections (see Section 3.4.3 in Chapter 2 for further discussion). This measurement took approximately 16 hours longer to integrate. It was expected that filtering with the higher resolution provided by the spectrometer would improve the $g^{(2)}(0)$ substantially, but Figure 6.2.4 shows that actually the raw data gave a similar value for both methods, but a huge difference in integration time. This data has been fitted with a function comprised of a $g^{(2)}(\tau_{12})$ convolved with an IRFs that describes the SPADs jitter. We attribute the non-zero $g^{(2)}(\tau_{12})$ value after convolution for both datasets to some mixture of coherent background, and also potentially collecting photons from other nearby QD transitions. This measurement confirmed that spectrally filtering with the Alluxa filters was the most efficient way to proceed, and so they were implemented for the remainder of the results in this Chapter.

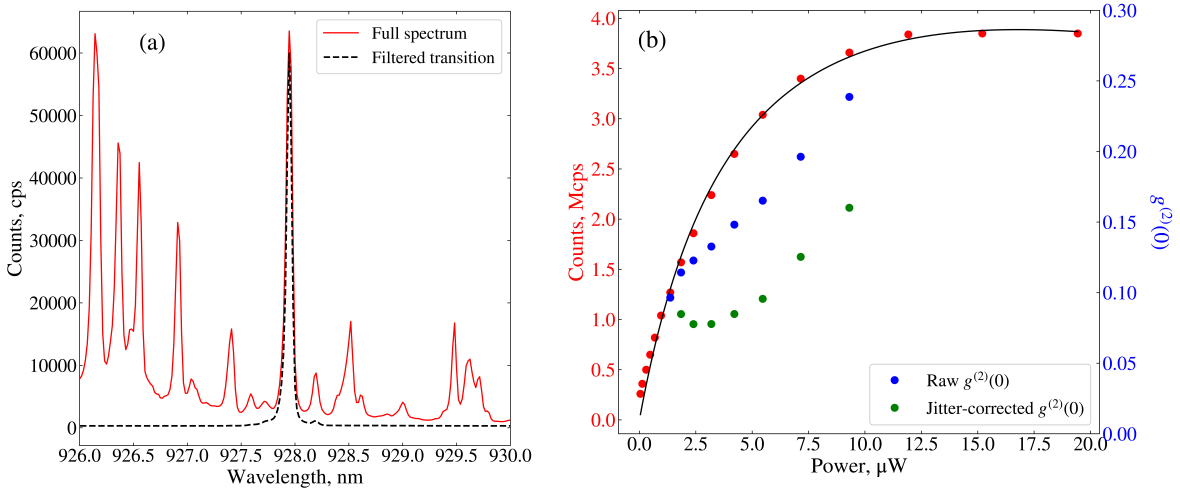

Figure 6.2.5: The transition emission characteristics. **(a)**: The spectrum of the micropillar, filtered and unfiltered, when excited with 850 nm CW excitation. **(b)**: The saturation behaviour of the 928 nm transition on SNSPDs. In red, the count rate versus pump power, and in blue, the raw $g^{(2)}(0)$ versus pump power.

The 928 nm transition in pillar 2D, section C3D 1.6 µm was chosen as the brightest and most pure candidate measured in the search period, during which approximately 200 micropillars were investigated, each with anywhere between 5 and 15 sharp spectral lines to examine. For further single-photon characterisation, measurements were also taken on SNSPDs, which have lower dark counts and jitter, and better detection efficiencies at this wavelength. The filtered spectrum, saturation behaviour and power-dependent second-order correlation function of this particular transition measured on SNSPDs is shown in Figure 6.2.5. Figure 6.2.5(a) shows the full micropillar and filtered transition spectra, while Figure 6.2.5(b) shows the filtered transition saturation behaviour and power-dependent $g^{(2)}(0)$, both raw and corrected for jitter. The saturation curve has

been fit with the expression:

$$C = \frac{C_\infty P_p}{P_p + P_{\text{sat}}} + I_{\text{bg}} \cdot P_p, \tag{6.2.1}$$

where C is the count rate, P_p is the pump power, P_{sat} is the saturation power and C_∞ is the count rate at the saturation power. The term $I_{\text{bg}} \cdot P_p$ is a correction term to account for background counts that increase linearly with pump power. Based on the data shown in Figure 6.2.5(a), a lower bound for $g^{(2)}(0)$ can be estimated by considering the SNR as described in Section 3.4.1. The mean of the background counts in the filtered spectrum is 310 cps, and the maximum of the peak is $\sim$ 60 kcps, giving an overall SNR of $\sim$ 193. According to Equation 3.4.1 this gives the lower bound of the experimentally-obtainable $g^{(2)}(0)$ of 0.010. The best raw $g^{(2)}(0)$ obtained in the power-dependent $g^{(2)}(\tau_{12})$ shown in Figure 6.2.5(b) was 0.104, around ten times bigger than this lower bound. The $g^{(2)}(\tau_{12})$ was fitted with an IRF-convolved function based on measurements of the SNSPD jitter. Measurements of the SNSPD jitter for the two channels used in measurements - detection

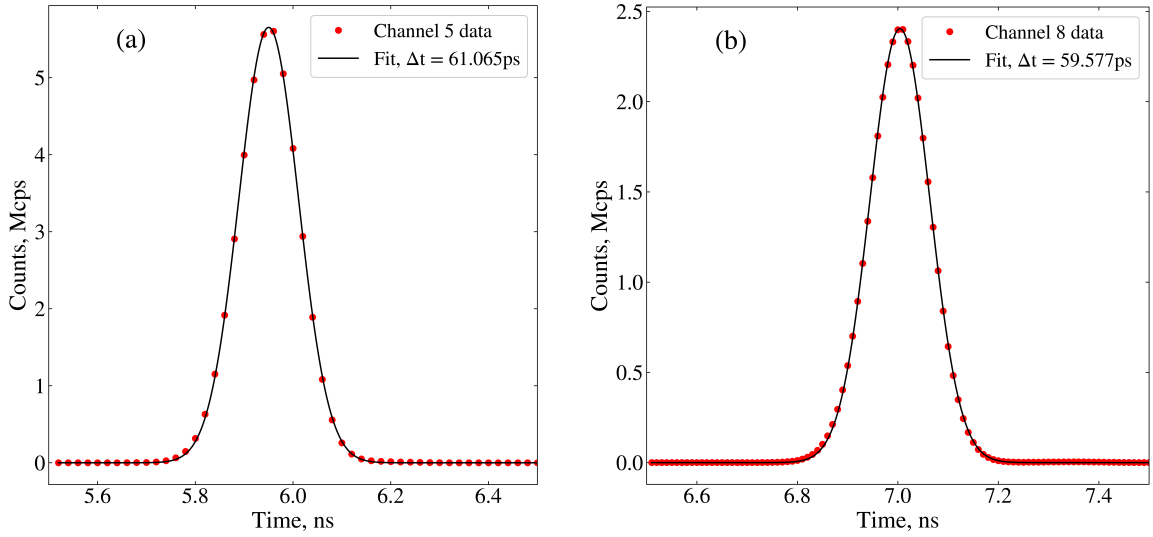

Figure 6.2.6: The jitter of the two SNSPD channels used for measuring correlations. For this measurement, a pulsed laser tuned to 850 nm was split onto a fast photodiode (Thorlabs DXM30AF) and a variable optical attenuator (VOA). The output of the fast photodiode was connected to a channel on the timetagger and used as the clock 'start', and the attenuated pulsed laser coming off the VOA was connected to detection channels 5 and 8 in turn. **(a)**: The data and Gaussian fit for detection channel 5. **(b)**: The data and Gaussian fit for detection channel 8.

channels 5 and 8 on the PhotonSpot SNSPD system at NPL - were taken at a fixed bias value of 20 µA and an incident count rate of $\sim$ 3 Mcps. The results of fitting these measurements with Gaussian functions are shown in Figure 6.2.6. To fit the measured $g^{(2)}(\tau_{12})$ and extract the expected $g^{(2)}(\tau_{12})$ as per the description in Section 3.4.2, values of 61 ps and 60 ps were taken as the jitter for the two channels. As seen in Figure 6.2.5(b)

the best jitter-corrected value was 0.078.

After quantifying the single-photon characteristics of this transition as above, the single-photon flux was coupled into the three LOFD described in Section 6.1.2 and the voltage response of each was recorded. Any LOFD will have some non-zero dark current - analogous to dark counts in single-photon detectors, this is a signal caused by something other than incoming light, for example thermal excitation of electrons, which is a source of noise. Because of this, and also to correct for any signal drift over the measurement, the dark current was intermittently sampled over the length of the measurement. The output of each detector was recorded on custom LabVIEW software used in the detector calibration facility at NPL. This software would record a datapoint each second, comprised of sampling five measurements every 200 ms and taking the mean and standard deviation. A schematic of the experimental set-up for these measurements is shown in Figure 6.2.7. The single-photon flux was collected into

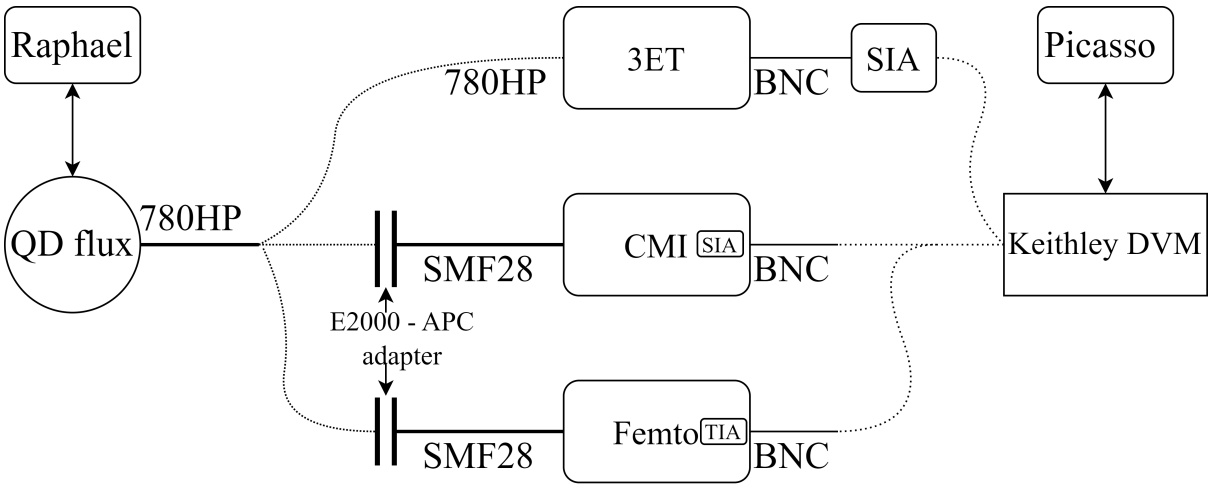

Figure 6.2.7: A schematic of the experimental set-up used for measuring the quantum dot flux on three LOFD. Here, Raphael and Picasso are two independent computers used for data acquisition, where Raphael controlled the shutter for the flux, and Picasso recorded the detector responses. The single-photon flux collected into 780HP fibre could be directed to the three LOFD in turn, where the amplification electronics are labelled for each. All detector outputs were recorded on a digital voltmeter (DVM).

780HP single-mode fibre, as shown in Figure 6.2.1, which was securely connected via E2000-E2000 coupler on a breadboard and taped down to keep the collection fibre still during measurements. Another 780HP fibre was coupled at the other side, and this could be connected to the three connectors in turn. For the 3ET this fibre could be directly connected to the E2000 launch and collimating lens adapter. For the CMI and Femto, which had APC connectors, an extra SMF28 fibre with E2000-APC fibre connectors was required. The pump power of the sample was controlled by a LabVIEW VI on the computer labelled 'Raphael', which would adjust the voltage through a variable optical attenuator (VOA) on the excitation path. This VI had a 'software shutter' feature that would toggle the pump power on and off for the required light and dark measurements,

to intermittently sample the dark current. Each of the detector outputs were connected in turn to the same Keithley digital voltmeter (DVM), and the data acquisition was performed on the computer labelled 'Picasso', using the detector calibration software. A lack of computerised synchronisation between the software shutter controlling the optical flux, and the data acquisition software, resulted in some anomalous datapoints between the signal and the background. To correct for this issue, the following data processing algorithm for the voltage response of each detector was implemented, where a user-defined threshold between the expected dark and light signal value was defined:

1. For all datapoints except the first and the last, calculate the 'gradient' of the previous and next datapoint, where gradient is defined as the change in voltage over the change in time.

2. If:

    - The gradients do not have the same sign, move onto the next datapoint.
    - The gradients do have the same sign, check if they are larger than the user defined threshold. If:
        - The difference between gradients is larger than the threshold, move onto the next datapoint.
        - The difference between gradients is smaller than the threshold, delete the current datapoint.

This algorithm worked on the assumption that, fluctuations due to noise would have a small magnitude relative to the overall change in voltage between a light and a dark measurement, therefore allowing the removal of anomalous datapoints that lay in between these thresholds.

In the following three sections, the measurements on each detector will be described in detail and the main results presented. This data was all collected at the NPL by myself, Adam Parke and Luke Arabskyj, both of whom assisted the analysis described here and in the following sections.

6.2.2 Three-element trap detector

As introduced in Section 6.1.2, the 3ET is a detector built to enhance quantum efficiency by arranging three highly uniform photodiodes (Hamamatsu S1337) to retroreflect an incoming beam. These photodiodes are windowless to reduce interference effects. Fibre-coupling is implemented with a fibre-launch and collimating lens mount that attaches to the detector and focusses the incoming light onto the active area of the first photodiode. The collimating lens had to be carefully adjusted to ensure that all incident photons are collected, so that the optical power is not underestimated. The 3ET

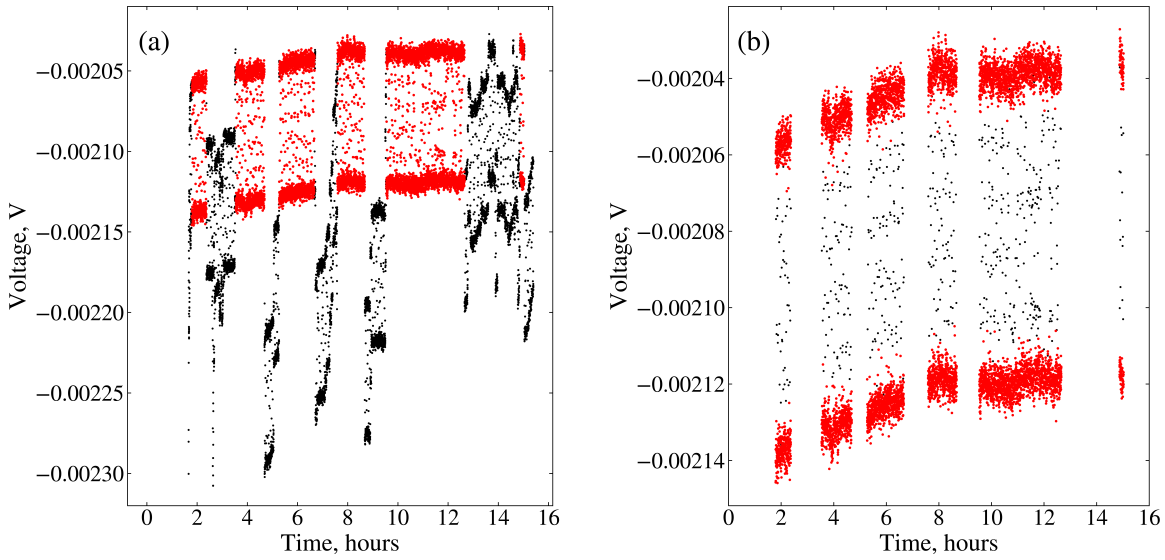

Figure 6.2.8: The voltage response of the 3ET over a 16 hour measurement. There is a severe jump in the voltage between 0 and 2 hours which has been omitted from the axis for rescaling. **(a)**: The raw data of the 3ET measurement. There are random periods of systematic jumps in voltage response affecting both the signal (light) and noise (dark) measurements, shown in black, which are removed. **(b)**: The voltage response of the 3ET after removing periods of shifted voltage response. The slow drift is observed in the steady change of both the signal and noise, but the difference between the two remains approximately constant over the measurement. Anomalous datapoints in between light and dark measurements, shown in black, are also removed based on the algorithm described in Section 6.2.2.

should be underfilled on all photodiode elements, since its responsivity calibration is only valid when all optical power is collected. Upon illumination the photodiodes produce a photocurrent, this is amplified by a SIA[300] and connected to the digital voltmeter for data acquisition, as shown in Figure 6.2.7. This dataset was recorded over a sixteen-hour measurement, and Figure 6.2.8 shows the sampled data from the acquisition software on Picasso. The SIA was connected to a power supply unit and grounded. Despite this, there was still a slow drift over long timescales, and also sharp systematic jumps, in the voltage response. The sporadic jumping in magnitude (shown in Figure 6.2.8(a) as black datapoints) by eye gives a similar magnitude to the 'steady-state' regions - i.e. the difference between light and dark measurements appears to remain constant. Although the exact origin of the periods of systematic jumping is unknown, we can hypothesise that it is related to the amplifier, since the signal and noise are affected in a similar way. However since the origins are not well understood, these regions were omitted from the dataset. The slow drift was thought to be due to ambient conditions such as slow changes in temperature. This drift is evident in the simultaneous changing of the noise and the signal as shown in Figure 6.2.8(b). The detector response to the optical flux is given by the absolute voltage, i.e. the 'light' measurements or signal (shutter open) subtracted from the 'dark' measurements or noise (shutter closed). The signal and noise is extracted from

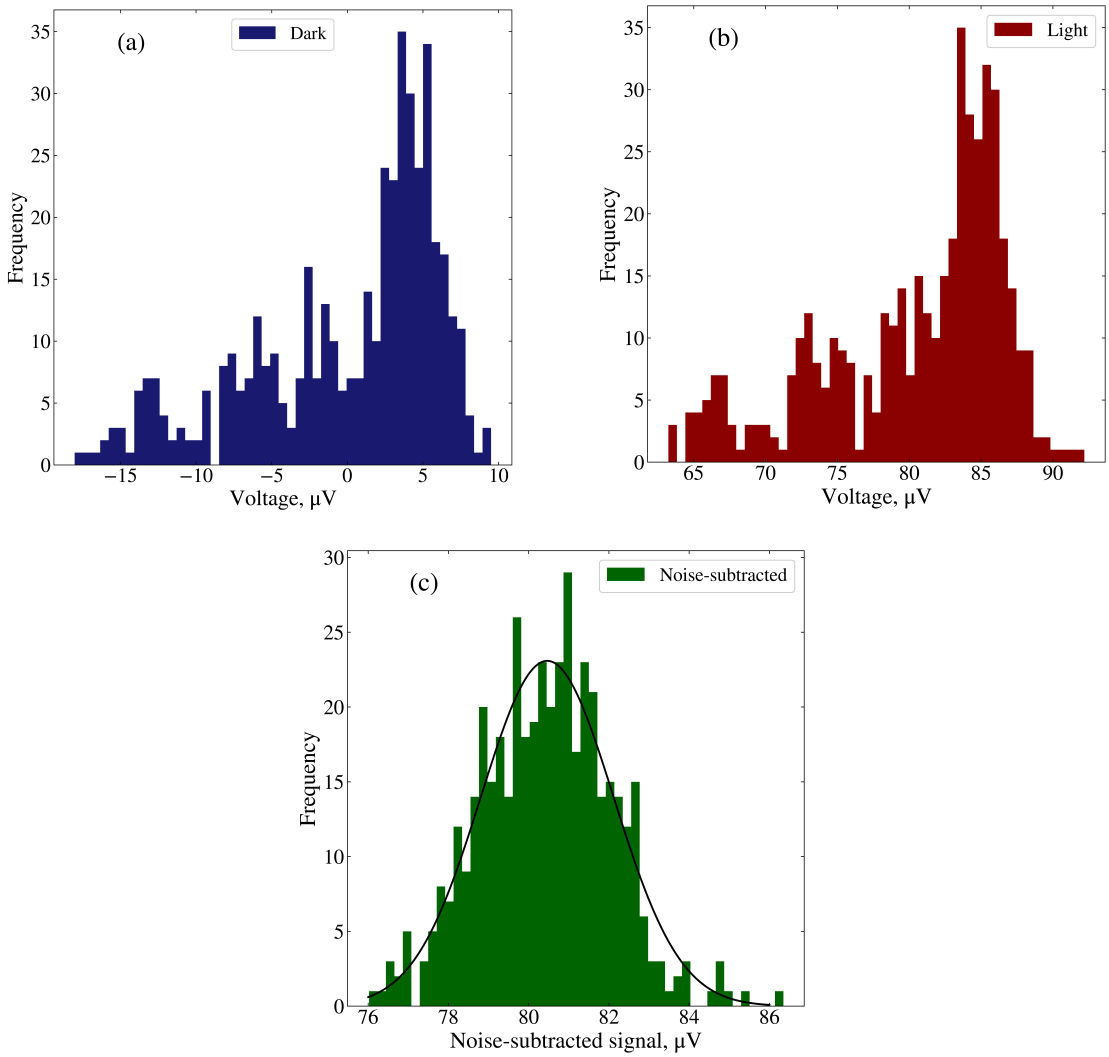

Figure 6.2.9: Histograms of the 'dark' measurements (blue) in **(a)** and the 'light' measurements (red) in **(b)** from the processed 3ET data shown in Figure 6.2.8(b). The tail in the distribution is due to the long timescale drift. **(c)**: A Gaussian fit to the noise-subtracted or 'absolute' voltage response.

the dataset by iterating through each datapoint and determining whether the difference between subsequent voltages was large enough to indicate a change from light to dark or vice versa. The mean and standard deviation are obtained for each from their histograms. It is expected that the signal and noise will follow a Gaussian distribution, but there is a tail to the distribution, shown in Figure 6.2.9(a) and 6.2.9(b). This is because the drift in the data has not been corrected, or 'flattened' out, which is possible with a spline interpolant. This was not necessary for the analysis of this particular dataset - since the background was intermittently sampled for the duration of the measurement, the noise can be directly subtracted from the proximal signal sections and the drift cancels, as demonstrated in Figure 6.2.8(c). This figure shows the noise-subtracted 3ET response,

fitted with a Gaussian function. The subtraction centres the noise histogram around 0, and the mean of the signal histogram is taken as the absolute value of the detector response to the single-photon flux. From this, the total optical power in the fibre can be estimated by relating this voltage response to the detector responsivity and gain. The gain is set on the switch integrator amplifier in the experiment, and the responsivity of the detector is determined by the calibration at the wavelength of interest. The optical power is given by

$$P = \frac{V \cdot C_{\text{div}}}{R \cdot G}, \tag{6.2.2}$$

where $G = (1.00090126 \pm 0.0002) \times 10^8 \text{V A}^{-1}$ and $R = (0.7356 \pm 0.0004) \text{A W}^{-1}$, and the mean voltage response was determined to be $V = (8.0428 \pm 0.0077) \times 10^{-5} \text{V}$. C_{div} here is a correction factor for the reflectivity of the collimating lens (achromatic doublet with near-infrared antireflection coating) that means we will be underestimating the total power in the fibre. This is estimated to be 1.0019 ± 0.004 based on a reflectivity value of 0.1935 at this wavelength given by the datasheet from Thorlabs. This gives a total optical power in the fibre of $P = (1.0924 \pm 0.0012) \text{pW}$. The signal-to-noise ratio of the measurement can be calculated using the mean and standard deviation of the noise-subtracted response - this gave a SNR of 49. The standard uncertainty on the power is calculated by taking the quadrature of errors on each dependent variable, in accordance with Equation 6.2.3

$$\sigma_P = \sqrt{\left(\frac{\partial}{\partial V}P\right)^2 \sigma_V^2 + \left(\frac{\partial}{\partial R}P\right)^2 \sigma_R^2 + \left(\frac{\partial}{\partial G}P\right)^2 \sigma_G^2 + \left(\frac{\partial}{\partial C}P\right)^2 \sigma_C^2}, \tag{6.2.3}$$

where $\sigma_{V,R,G,C}$ is the error on, and $\partial P/\partial V, R, G, C$ the partial derivative of P with respect to, the voltage, responsivity, gain and correction factor respectively.

6.2.3 Femto photodiode

The Femto detector is a commercially available fibre-coupled low noise photoreceiver (Femto, FWPR-20-SI) with a single electronic output. It is comprised of a silicon photodiode and integrated TIA, able to detect optical powers down to 50 fW and with a peak spectral sensitivity around 950 nm. A schematic of the experimental set-up is shown in Figure 6.2.7. The fibre-coupler is an APC connector; since the collection fibre of the confocal microscope was E2000, we needed an additional fibre between the collection and the detector. The collection fibre was connected to an SMF-28 with one E2000 connector and an APC connector at the other side, which was connected to the Femto input. The Femto output is a single female BNC jack - this output was, as before, connected to the DVM for data acquisition. The voltage response of the Femto exhibited no obvious drift over time, and due to the lower noise floor, the SNR was much larger. Since the signal

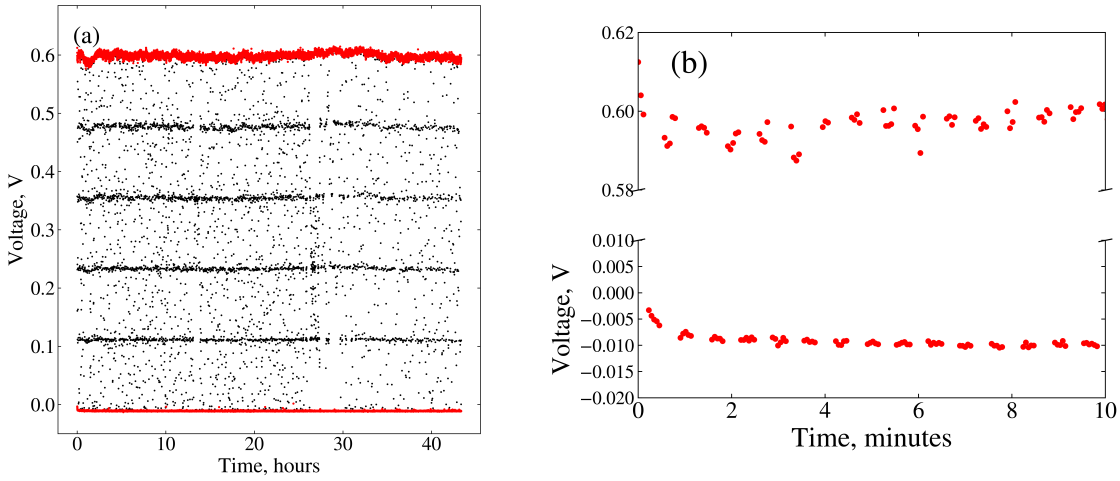

Figure 6.2.10: **(a)**: The voltage response of the Femto over a 40 hour measurement. The anomalous datapoints in black were determined using the same algorithm as for the 3ET and removed before being binned. An aliasing effect caused by asynchronous recording results in 'shadows' of the main signal at five different spacings. **(b)**: A 10-minute section of the Femto measurement showing the intermittent light and dark sampling, toggling every 15 seconds. The axis has been broken for scaling purposes.

was so stable, and the detector robust to external disturbances, a weekend-long (>40 hour) measurement of the single-photon flux was recorded. During this measurement the software shutter toggled between light and dark every 15 seconds, and as for the 3ET data acquisition, the voltage response of the Femto was sampled every 200 ms and the mean and standard deviation of five samples at a time was recorded for each datapoint. The raw and post-processed data is shown in Figure 6.2.10. Some anomalous datapoints were recorded over the long measurement. As with the 3ET measurement, the biggest contribution to this is lack of timing synchronisation between the software shutter and the voltage response data acquisition. In particular for this measurement, a 'stepping' of the signal is observed with five discrete values. This is thought to be some kind of aliasing effect due to the asynchronous sampling, although further investigation is required. The dark measurements for estimating the noise were remarkably stable and with a low standard deviation. The distribution of both the noise and signal are shown in the histograms of Figure 6.2.11. As before, the total optical power in the fibre is estimated based on the measured absolute voltage response, which was $V = (0.609940 \pm 0.000076)\text{V}$. The Femto spectral responsivity in units of V W^{-1} as characterised by a group in PTB[295] is given by $s = (0.5886 \pm 0.0031) \times 10^{12}\text{V W}^{-1}$. The power in the fibre is given by the $P = \frac{V}{s}$ and so the measured power was $P = (1.036 \pm 0.005)\text{pW}$, with a SNR of 128. The standard uncertainty was calculated with the same method as for the 3ET, with standard error propagation on each dependent variable.

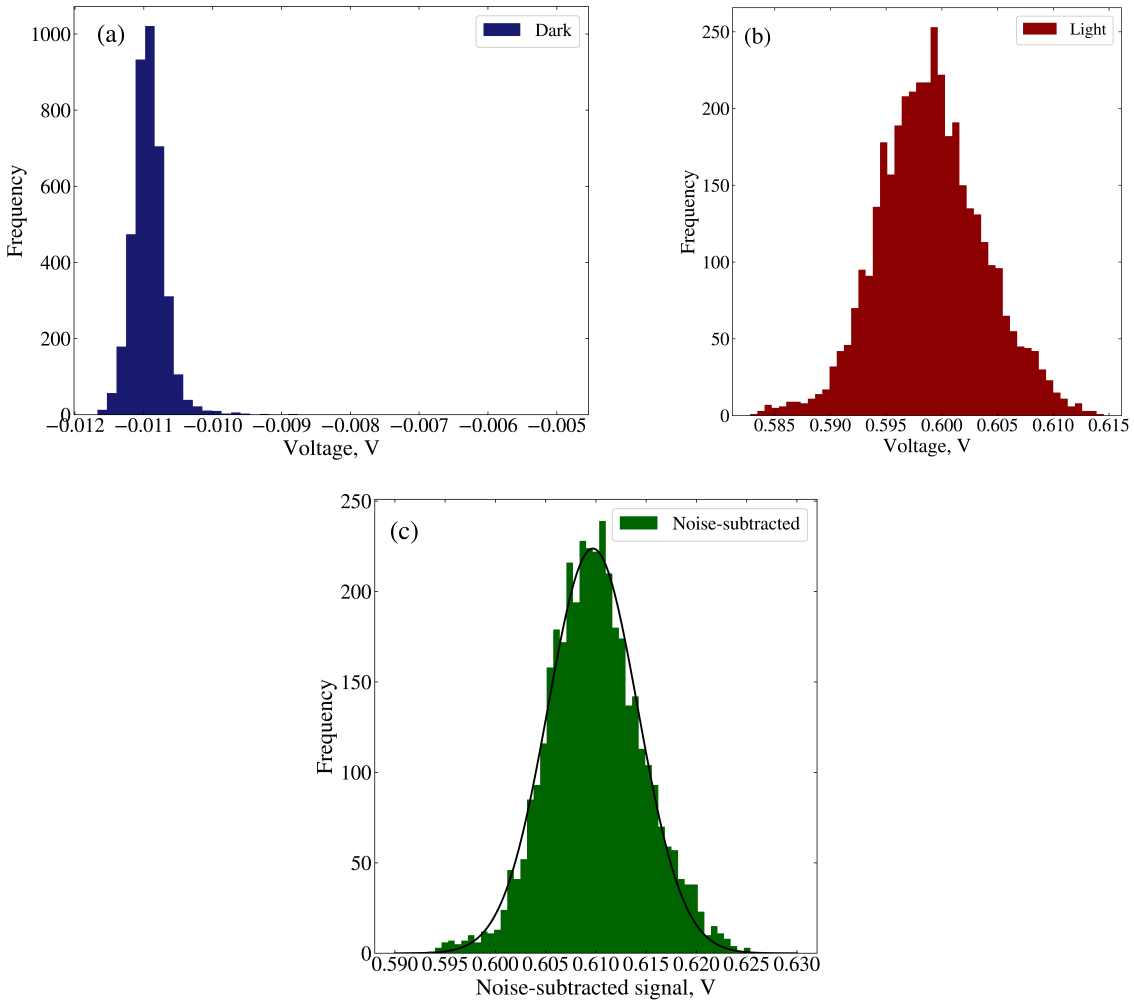

Figure 6.2.11: The histograms of the Femto measurements. Because of differences in distribution size, they have been plotted on separate figures and with different bin widths. **(a)**: The histogram of the Femto noise or dark measurement. Because the noise is so low in this instrument its signal behaves more like a delta function. **(b)**: The histogram of the Femto signal or light measurement. This data has a larger width compared to the noise. **(c)**: The background subtracted absolute voltage response with fitted Gaussian.

6.2.4 Low optical flux detector from CMI

The LOFD from the CMI was a cooled, fibre-coupled silicon photodiode. The collection fibre was connected via SMF-28 with an APC connector in the same manner as for the Femto measurement, shown in Figure 6.2.7. The fibre launch had been designed to screw in to an exact distance that meant the detector active area is underfilled, ensuring validity of the responsivity calibration. The detector is stabilised by a PID loop and coupled to a heatsink, which is connected to a thermoelectric controller via an aluminium-wrapped cable. The heatsink reduces the temperature of the detector cylinder to 12 °C. The thermoelectric controller is biased at 12 V and the detector was connected to a linear power supply at ±20V and grounded, and the DVM for data acquisition. The response

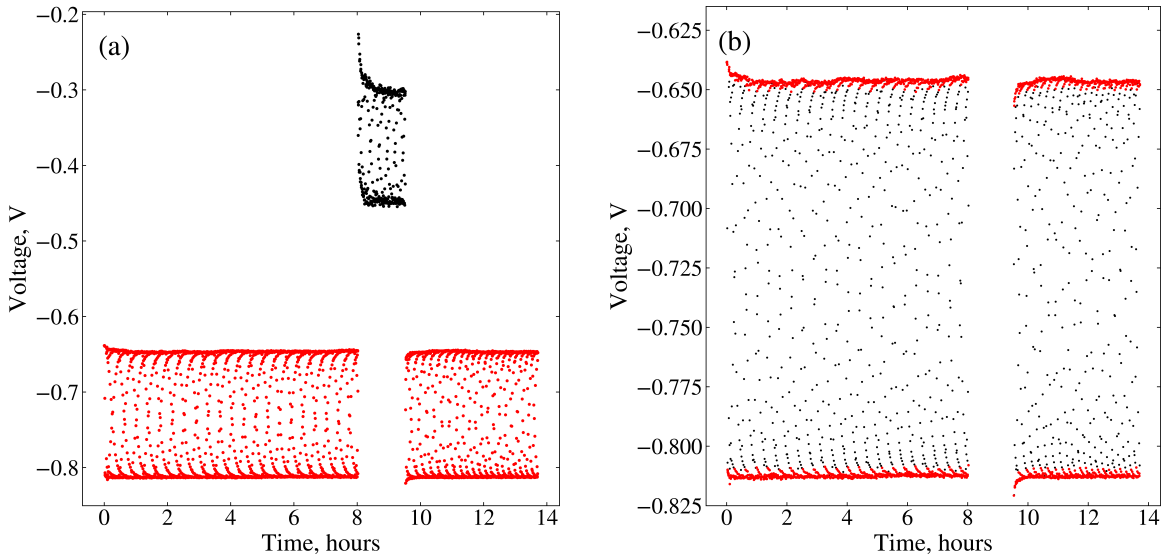

Figure 6.2.12: **(a)**: The raw data of the overnight CMI measurement. Between 8 and 10 hours there is some kind of systematic anomalous behaviour in the detector response, shown in black. These datapoints were excluded from the analysis. **(b)**: The post-processed CMI data, where anomalous datapoints due to asynchronicity are shown in black, and the data between 8 and 10 hours has been excluded.

of this detector between light and dark measurements was slower than the 3ET and Femto, due to an integrating capacitor being used in the internal amplification process. The integration time of the capacitor could be set with a LabVIEW VI when the detector was connected to an RS232 port. A quicker response time resulted in a lower sensitivity - from $1 \times 10^{12}\,\mathrm{A\,W^{-1}}$ to $1 \times 10^{9}\,\mathrm{A\,W^{-1}}$ for 1 s and 1 ms integration time respectively. For these measurements it was operated at 1 s integration time to have maximum sensitivity. At this integration time, the capacitor time constant is ∼20 s. To account for this slower response, the software shutter toggle between light and dark was extended to one minute. Similarly to the 3ET measurement, some unusual periods of severe drift occurred over the long measurement - as before, this is hypothesised as an issue with the internal amplification process, and will be investigated further in future studies. For the purposes of this study, as with the 3ET and Femto measurements, data outside of the expected response for both signal and noise was excluded, and the voltage response was sampled at a rate of 200 ms with each data point being the mean of five samples. The absolute voltage response was $V_{\mathrm{abs}} = (0.16560 \pm 0.00062)\mathrm{V}$. For this detector, to calculate the optical power we must use Equation 6.2.4

$$P = \frac{V_{\mathrm{abs}} \times C}{R \times T}, \tag{6.2.4}$$

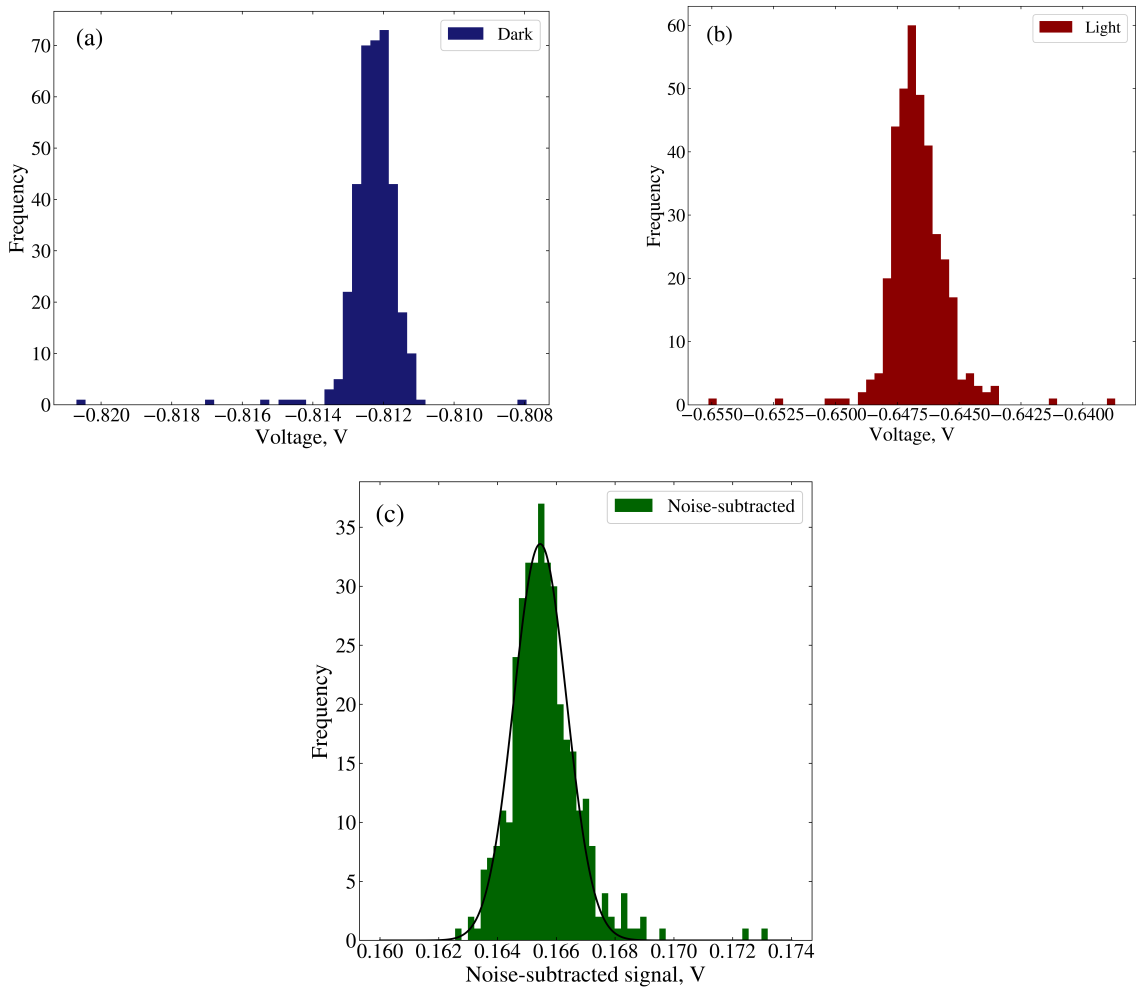

Figure 6.2.13: **(a)**: The histogram of the CMI noise. **(b)**: The histogram of the CMI signal. **(c)**: The background-subtracted absolute voltage response fitted with a Gaussian.

where C =1.045 $\times$ 10^{-12} F[2] is the integrating capacitor inside the detector; R is the detector responsivity and T is the integration time, which was set to 1 s. The responsivity R had been calibrated by the Czech Metrology Institute (CMI) and at this wavelength was $R = 0.1628\text{A W}^{-1}$. Substituting these values resulted in an estimated optical power of $P = 1.063\text{pW}$, measured with a SNR of 140.

6.2.5 Expanded uncertainty analysis and detector comparison

In this section, the tools required for developing the uncertainty analysis beyond the standard uncertainty will be outlined, and use this to present a comparison between the three detectors. So far, only the standard uncertainty on each power measurement has been quoted, based on combining the measurement errors in quadrature. For a metrological study it is common to consider an *expanded* uncertainty. The BIPM defines

[2] 1 F$\equiv$ 1 A s V^{-1}.

the following terms for uncertainty analysis:[305]

- **Standard uncertainty**: "Uncertainty of the result of a measurement expressed as a standard deviation".
- **Type A evaluation (of uncertainty)**: "Method of evaluation of uncertainty by the statistical analysis of series of observations".
- **Type B evaluation (of uncertainty)**: "Method of evaluation of uncertainty by means other than the statistical analysis of series of observations".
- **Combined standard uncertainty**: "Standard uncertainty of the result of a measurement when that result is obtained from the values of a number of other quantities, equal to the positive square root of a sum of terms, the terms begin the variances or the covariances of these other quantities weighted according to how the measurement result varies with changes in these quantities."
- **Expanded uncertainty**: "Quantity defining an interval about the result of a measurement that may be expected to encompass a large fraction of the distribution of values that could reasonably be attributed to the measurand".

Using the above definitions we can outline the concept of expanded uncertainty. Any measurement that we make will have some associated uncertainty that we can estimate. If we calculate a value based on measurements that have multiple contributions to the uncertainty then we can obtain the combined uncertainty by propagating the errors on each; if the values are combined with a linear function then this is as simple as combining the uncertainties in quadrature. Another important concept in metrology but more widely, in statistics, is the idea of a confidence interval. This uses the uncertainty and the expected values of a measurement to define a set of limiting values that we expect a certain proportion of most measurement values to fall within. For metrologists, the aim of establishing an expanded uncertainty is to use the combined standard uncertainty alongside a desired confidence interval. This confidence interval is more commonly referred to as the amount of coverage, or *coverage factor*, k. Once a combined uncertainty has been calculated for a particular measurement, the expanded uncertainty is simply obtained by multiplying together the combined uncertainty and the coverage factor k when $k > 1$.[306]

For a measurement comprised of multiple elements with associated uncertainties, we can estimate the combined degrees of freedom of the measurement - which approximates the overall degrees of freedom in a measurement after propagating the uncertainties - using the Welch Satterthwaite Equation,[306] given in Equation 6.2.5

$$v_{\text{eff}} = \frac{U^4}{\sum_{i=0}^{i=\infty} \left(c_i u_i\right)^4 / v_i}, \tag{6.2.5}$$

where U is the total standard uncertainty (as combined in quadrature), u_i, c_i and v_i are the uncertainty, value and effective number of degrees of freedom respectively, for each quantity labelled with index i. Then, using the combined degrees of freedom we can calculate the coverage factor k for the measurement with the inverse of the Student's t-distribution. This is a probability distribution that generalises the Gaussian distribution and is given by Equation 6.2.6

$$f\left(x, v_{\text{eff}}\right) = \frac{\Gamma\left(\left(v_{\text{eff}}+1\right)/2\right)}{\sqrt{\pi v_{\text{eff}}}\Gamma\left(v_{\text{eff}}/2\right)}\left(1+x^2/v_{\text{eff}}\right)^{-(v_{\text{eff}}+1)/2}, \tag{6.2.6}$$

where Γ is the Gamma function, and v_{eff} as before is the effective degrees of freedom. The coverage factor $k = 1$ encompasses 68% of the distribution of measurements, and $k = 2$ 95% of measurements. It is analogous to the number of standard deviations away from the mean in a Gaussian distribution. Its inverse is obtained by using the percent point function, where we specify an argument of 5% for our desired confidence coverage. This calculated value of k gives us our multiplicative factor for moving between 68-95-99% coverage. It is conventional to state that we have the expanded uncertainty ($k = 2$) if the calculated k is < 2.04.[307] For the CMI detector, we were given a conservative estimate of 2% expanded uncertainty on the power value based on repeatability tests and the calibration performed at the Czech Metrology Institute (CMI). For the 3ET and Femto measurements, this can be calculated based on the measured responses and the standard uncertainties. The results for the parameters of both is presented in Table 6.2.1.

	Power, pW	**Standard uncertainty**	**Effective degrees of freedom**	**Coverage factor**	**Expanded uncertainty**
3ET	1.0924	0.0012	753	1.96	0.00236
Femto	1.036	0.0055	1001	1.96	0.0107
CMI	1.063	-	-	2	0.021

Table 6.2.1: The results of the expanded uncertainty calculation. The effective degrees of freedom is calculated using Equation 6.2.5, where the degrees of freedom for the voltage is based on the number of measurements taken in the experiment, and the effective degrees of freedom for the responsivity of the detector in each case is effectively set to infinity because they have been calibrated.

Figure 6.2.14 shows the histograms from each detector, where the x-axis has been rescaled to show calculated optical power for the noise-subtracted light and dark histograms of each detector. This plot shows the difference in signal-to-noise ratios, given by the ratio of the signal width to the its mean. When comparing the measured optical power for each detector, we note there is a discrepancy between the three detectors. As shown in Figure 6.2.7, the 3ET measurement was taken with only one single-mode fibre between the collection fibre and the detector active area, whereas the Femto and CMI required an extra fibre and coupler. A minimum insertion loss of between 5 and

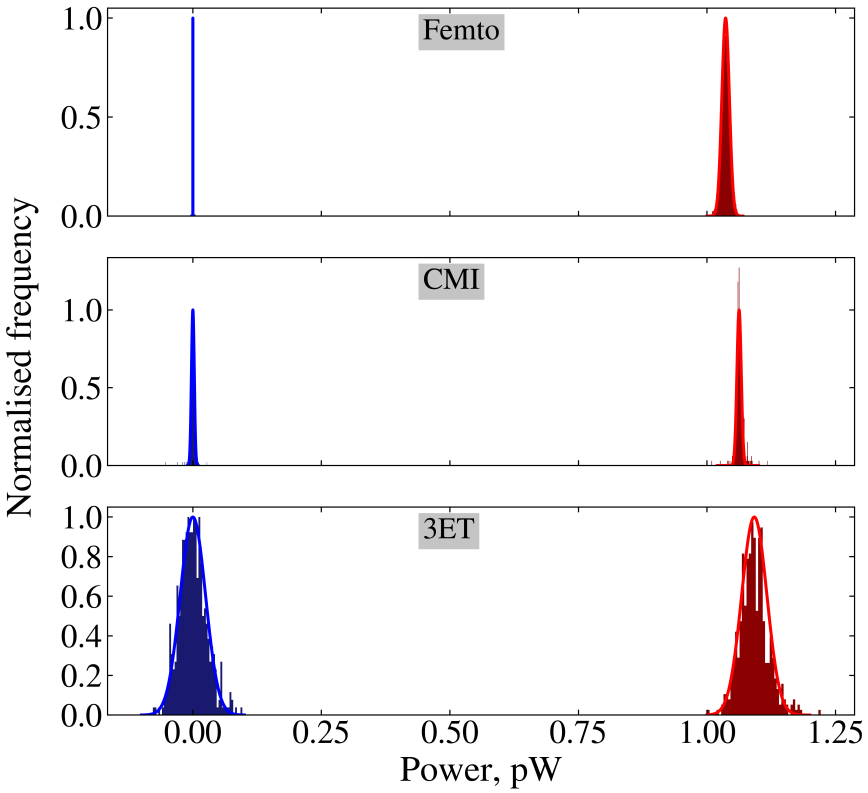

Figure 6.2.14: For the Femto, CMI and 3ET detectors, the noise-subtracted light signal (red) and dark signal (blue) of the three measurements, where the x-axis indicates the optical power. Each has been fit with a Gaussian function. The width of the peaks indicates the relative signal-to-noise of each measurement.

10% is to be expected for standard FC and APC mating sleeves. In addition, the discrepancy between the Femto and CMI outside of expanded uncertainty was found to be contamination of the second fibre during an insertion-loss repeatability study, after the presented measurements had been recorded. This means that the measured voltage response and the calculated optical power are a lower bound of the real value. In future, this can be accounted for with an extra uncertainty term on the power value which considers a higher fibre loss. Furthermore, the 2.5% discrepancy could be avoided by adapting the experiment to perform measurements in free-space, or designing new fibre-launch adapters for the detectors that allows a single, unmoved fibre to run from collection to each detector in turn, minimising the risk of contamination or coupling losses.

After measuring the optical power of the single-photon flux on three LOFD, two of which were traceably calibrated, we had successfully demonstrated a method of closing the radiometry gap and linked our single-photon flux to the SI via a traceability chain to the cryogenic radiometer. A single-photon flux that carries SI-traceability and is delivered

in single-mode fibre can be used to traceably calibrate SNSPDs, a demonstration not yet reported in quantum radiometry literature. In the next section, the experimental methods and analysis for performing this calibration will be described.

6.3 Metrological characterisation of single-photon detectors

For the final section in this chapter, two calibration techniques for the detection efficiency of SNSPDs will be presented. All measurements in this chapter were taken at the National Physical Laboratory (NPL), and the following section focussed on the PhotonSpot SNSPD system. The dark count rate of these detectors were determined to be ∼100 Hz, and initially the polarisation sensitivity of the SNSPDs was assumed to be negligible for our system - the consequences of this are discussed in the final results section. As discussed in Section 6.1.3, studies such as this have been demonstrated for SPADs,[55,294,295] but are yet to be done on SNSPDs. As with these studies, this calibration was performed with the substitution method, where the 3ET was used as the reference detector, the SNSPD was the device under test (DUT), and the source was the single-photon flux. In order to ascertain the efficacy of this technique, a calibration was also performed using the pulsed attenuated laser technique, where the pulsed laser replaces the single-photon flux in the previously mentioned calibration set-up. Results from both will be described and compared in this section. For this preliminary study, the detector calibration facility techniques as applied to SPADs were adapted for the SNSPDs system and low-temperature confocal microscope.

6.3.1 Calibration with attenuated pulsed laser

When calibrating the detection efficiency of any single-photon detector using a laser as the source, it must be highly attenuated to avoid saturating the detector, but we also want to infer the optical flux of the fibre directly. This is achieved with a beamsplitter network for attenuation and a monitor photodiode, where the monitor records the flux before attenuation. Once the attenuation factor of the system has been calibrated and measured to be constant for some linear region of VOA 2, the reading at the monitor can be used to infer the real optical flux leaving the breadboard and going onto the detectors. For this measurement, a Spectra-Physics Tsunami Ti:Sapph laser was tuned to 928 nm, the same central wavelength of the single-photon flux from the quantum dot. The attenuation was achieved with two electronic VOA that are controlled with power supply units (PSU), and a set of in-fibre beamsplitters, arranged as shown in Figure 6.3.1. A monitor photodiode is attached to output A, its response amplified by a TIA set to a particular gain, and the fibre used for the reference and DUT can be connected to outputs

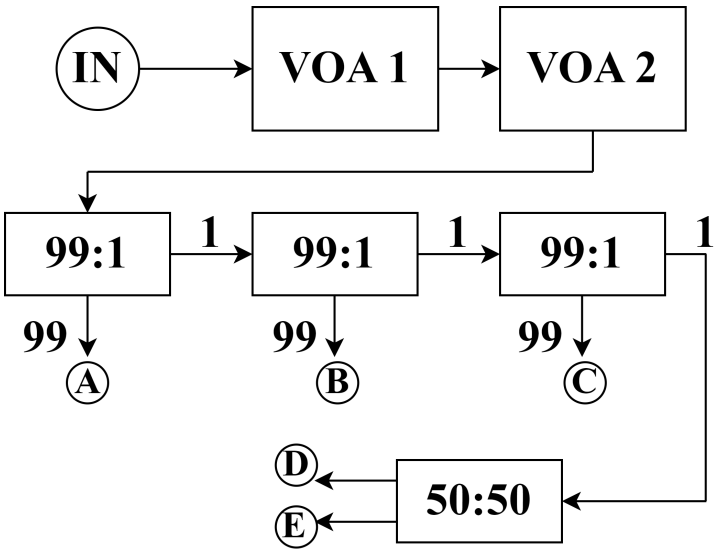

Figure 6.3.1: Schematic of attenuation breadboard. VOA 1 acts as the light/dark switch and VOA 2 sweeps through 0 to 5V. Three 99:1 beamsplitters in series attenuate the signal by approximately -50 dB.

B, C, D or E depending on desired attenuation level. The input is a long 780HP fibre affixed to a gantry from the lab table to the bench, which is taped down securely. The output is another long 780HP fibre going back the other way to the reference detector and DUT on the table. It is important to secure both of these fibres during the calibration so that there are no changes to the system losses and light in the fibre. One VOA acts as a light/dark switch for obtaining the absolute voltage response (as in previous sections), and the other acts as a sweep from low to high attenuation.

The first step of this calibration is to determine the attenuation factor, β, of this system and make sure that it is constant when changing the sweep VOA voltage. This is achieved by a simultaneous measurement of the voltage response for a particular gain on the reference detector and a monitor photodiode, where β is then given by Equation 6.3.1

$$\beta = \frac{V_{\text{ref}}}{G_{\text{ref}}} \cdot \frac{G_{\text{mon}}}{V_{\text{mon}}}. \tag{6.3.1}$$

The VOA voltage was swept between 0 and 5 V and the response of the monitor and the reference was recorded. Some fine-tuning of the attenuation factor was required, as it was difficult to operate at a power that was measurable on the 3ET without saturating the monitor photodiode. After some optimisation, measurements were taken with just two 99:1 beamsplitters, rather than three as depicted in Figure 6.3.1 and the attenuation factor was determined to be $\beta = (1.5466 \pm 0.0005) \times 10^{-4}$.

The next stage of the measurement is to record a range of 10 optical fluxes on the reference and the DUT. For each flux, we can use our calibrated β to estimate the power on the reference detector P using Equation 6.3.2

$$P = \frac{V_{\text{mon}}}{G_{\text{mon}}} \cdot \frac{\beta}{R_{928}}. \tag{6.3.2}$$

The detection probability P_{det} is the ratio of registered detector clicks to incident counts per pulse,

$$P_{\text{det}} = \frac{N_{\text{det}}}{N_{\text{in}}}, \tag{6.3.3}$$

where $N_{\text{det}} = N_{\text{counts}} - N_{\text{bg}}$, N_{counts} is the mean number of incident photons during the light measurements and N_{bg} is the mean number of incident photons during the dark measurements, and N_{in} is given by P/E where E is the energy of the photons at this wavelength, $\lambda = 928$nm. The detection efficiency when the detector is on and able to detect, η, is then estimated with Equation 6.3.4. This corrects for incident photons missed during dead time, based on a model developed by Georgieva *et al.*[236]

$$\eta = \frac{N_{\text{det}}}{N_{\text{in}}\left(1 - N_{\text{det}} \cdot T_{\text{dead}}\right)}, \tag{6.3.4}$$

where T_{dead} is the detector dead time. This model assumes Poissonian statistics and that the detection efficiency can be modelled as a Heaviside function. The flux was varied over two and a half orders of magnitude based on the count rate observed at the DUT, from 10kcps up to $\sim$ 3Mcps. For each of the 10 fluxes, five light and dark measurements were recorded and the mean and standard uncertainty of each was calculated. Five values of N_{det} were determined using these measurements, and the mean and standard uncertainty of that quantity was used for each flux measurement in determining η. The results are summarised in Figure 6.4.1. The apparent increase in detection efficiency η at high count rates is unexpected, and discussed in detail in Section 6.4. The uncertainty on P_{det} and η are propagated from the standard uncertainties measured at the reference and DUT. A full discussion of the uncertainty analysis is presented in Section 6.4.

6.3.2 Calibration with single-photon flux

Performing the calibration of the SNSPD detection efficiency with the QD flux and the 3ET detector is, experimentally, more straightforward than the pulsed laser, since no attenuation is required. Firstly, the QD flux is measured on the 3ET - since at maximum pump power, the signal on the 3ET was close to its noise floor, this was the only data point we were able to obtain for this calibration. As described in the previous section, the power as measured on the 3ET and then N_{det} is measured on the DUT. The $g^{(2)}(\tau_{12})$ and the count rate were recorded before and after the substitution measurement, to verify whether the single-photon flux was stable and if the experiment alignment had drifted.

Over five light and dark measurements, the mean and standard uncertainties were propagated, and an average of $N_{\text{counts}} = 3.9$ Mcps was measured. The 3ET measurement

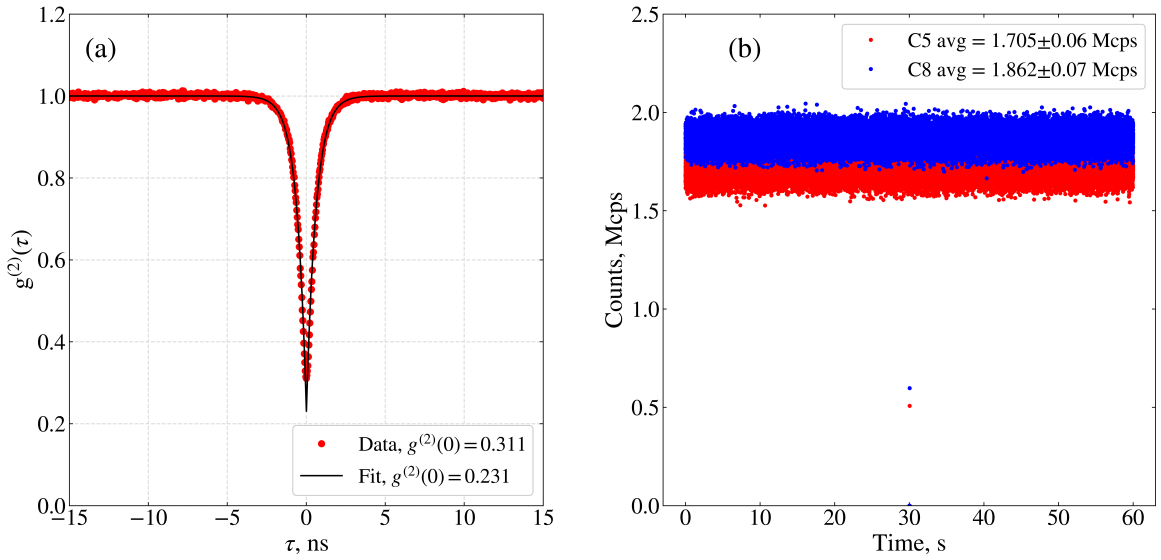

Figure 6.3.2: **(a)**: A timetagged $g^{(2)}(\tau_{12})$ taken immediately after the substitution measurement. The dashed black line is a fit based on convolving the $g^{(2)}(\tau_{12})$ with the SNSPD IRF, as described in Section 3.4.2. **(b)**: The count rate over 60 seconds extracted from the same timetagged data as the second-order correlation function in **(a)**. The average rate and standard deviation of each channel is labelled in the legend. Around 30 seconds in, the count rate drops and recovers within ∼0.5 seconds - this is due to SNSPD delatching. This data is binned over 1 ms timescales.

determined the power of the single-photon flux to be $P = 1.0924$pW. At 928 nm this is equivalent to 5.1 Mcps. This resulted in a detection probability $P_{\text{det}} = 76.4\%$, and a detection efficiency $\eta = 82.7\%$. These results are plotted alongside P and η as measured with the pulsed laser calibration method in Figure 6.4.1. The uncertainty on each value was again propagated with standard uncertainties on all measurands, this is described in detail in Section 6.4.

6.4 Discussion of results and future outlook

The uncertainty on the values for P_{det} and η can be propagated using the values and standard uncertainties on N_{in}, N_{det}, and T_{dead}. The contribution to each error depends on the standard errors of each dependent variable, as well as the partial derivative of the function with respect to each variable. The expressions for $\sigma_{P_{\text{det}}}$ and σ_η are

$$\sigma_{P_{\text{det}}} = P_{\text{det}} \cdot \sqrt{\left(\frac{\sigma_{N_{\text{in}}}}{N_{\text{in}}}\right)^2 + \left(\frac{\sigma_{N_{\text{det}}}}{N_{\text{det}}}\right)^2}, \tag{6.4.1}$$

$$\sigma_\eta = \sqrt{\left(\frac{\partial \eta}{\partial N_{\text{in}}}\sigma_{N_{\text{in}}}\right)^2 + \left(\frac{\partial \eta}{\partial N_{\text{det}}}\sigma_{N_{\text{det}}}\right)^2 + \left(\frac{\partial \eta}{\partial T_{\text{dead}}}\sigma_{T_{\text{dead}}}\right)^2}. \tag{6.4.2}$$

N_{det} and $\sigma_{N_{\text{det}}}$ can be obtained directly from the counts at the detector and the

counting error respectively. N_{in} is calculated from the measured power on the 3ET and wavelength on the spectrum analyser, and so $\sigma_{N_{\text{in}}}$ is calculated with

$$\sigma_{N_{\text{in}}} = \sqrt{\left(\frac{\partial N_{\text{in}}}{\partial P}\right)^2 \sigma_P^2 + \left(\frac{\partial N_{\text{in}}}{\partial \lambda}\right)^2 \sigma_\lambda^2}, \tag{6.4.3}$$

where σ_P is given by Equation 6.2.3. A full treatment of the uncertainty analysis can be found in Appendix C. The contribution from dark counts is neglected since the average rate is four orders of magnitude smaller than that of the single-photon flux, $N_{\text{dark}} \sim 100\text{Hz}$. The results for P_{det} and η, for both the pulsed attenuated laser and the

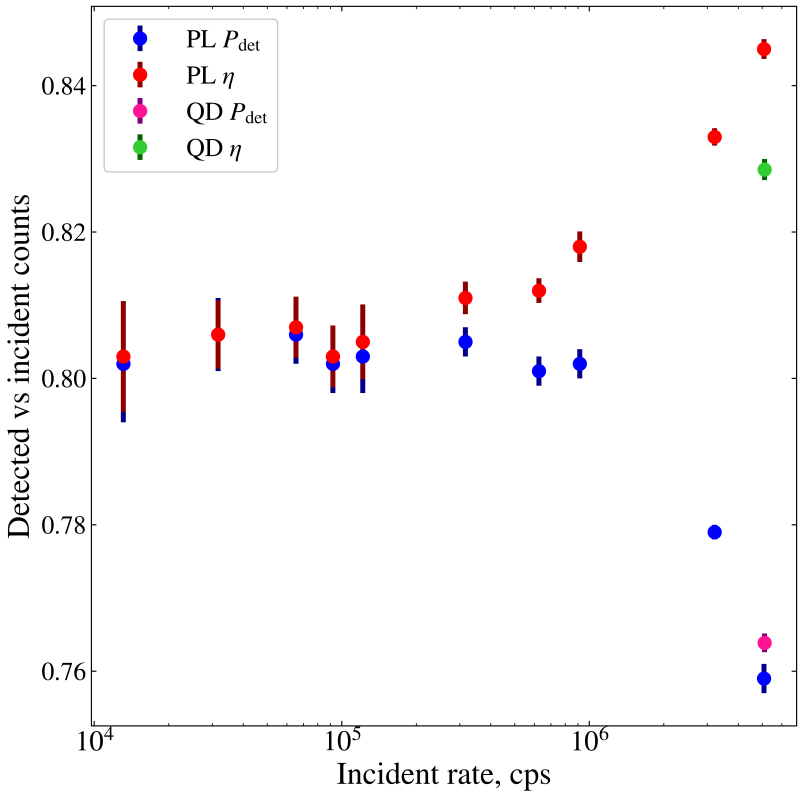

Figure 6.4.1: The calibration results for the pulsed laser method (PL) and the quantum dot method (QD). The detection probability P is given by the ratio of the number of registered counts to the number of incident counts, while the detection efficiency η corrects for the photons missing during the deadtime.

single-photon flux, are shown in Figure 6.4.1. P_{det} for the pulsed laser shows the expected trend - at higher fluxes P_{det} decreases as the detector saturates due to a finite dead time. It is expected that using the dead time correction factor described in Equation 6.3.4 to go from P_{det} to η will result in a flat line, that is, a rate-independent η - because it physically represents the detection efficiency when the detector is on and able to detect. This correction is well-documented[236] and used in literature for pulsed-laser calibrations previously. The fact that Figure 6.4.1 shows an increasing η at higher rates post-correction implies that N_{in} is unexpectedly increasing. We hypothesise that this is a result of the

SNSPD polarisation sensitivity. During this experiment, as explained in Section 6.3.1, the incident flux of the pulsed laser was being varied with a VOA. This component is comprised of an in-fibre MEMS switch that uses a mirror to reduce the transmitted power in the fibre. The use of this, as well as using non polarisation-maintaining fibres, means that some polarisation optimisation of the fibres before the SNSPDs is absolutely required to obtain physically meaningful estimates of the detection efficiency. This could be achieved using fibre polarisation controllers, which comprise rotatable fibre squeezers with fibre-holding clamps. Between measurements, these controllers could be re-optimised to ensure that the count rate is maximised. The polarisation dependence may also explain why the efficiency result for the QD also did not agree with the result of the pulsed laser at the same power. Furthermore, the Poissonian correction applied to obtain the efficiency value may not be valid for antibunched light - additional analysis would be required to verify this. In addition, using a reference detector with a lower noise floor may result in improved uncertainty values - repeating this study with the CMI would be of interest.

Given more time on my secondment at NPL, there are two ways in which I would improve the existing experiment, and two possible extended analyses that may yield more detailed results. Firstly, retaking data for the detector calibration on the CMI detector would maintain SI-traceability whilst permitting a larger range of data of the single-photon flux to be measured, given its lower noise floor. Secondly, making adjustments to the fibres as mentioned in previous sections may help to minimise the likelihood of unexpected results. In terms of future work, I think there are two key areas that may yield more precise results for the calibration. Firstly, Chapter 4 presented evidence that modelling detector dead time as a Heaviside function with respect to time is unphysical and leads to imperfect estimates of detected rates, as well as correlation. If it was possible to characterise the SNSPDs used at NPL in the same way, and build up their detector recovery function alongside the real detected rates for antibunched light, it may be possible to more accurately correct for the CW calibration. Secondly, in Chapter 5 the enhanced count rate and single-photon purity when using resonant excitation was discussed. In addition, the preference of using pulsed excitation with a repetition rate that alleviates the need for a dead time correction was discussed in Section 6.1.3. Repeating the study with pulsed, resonant excitation of the QD sample would potentially result in a brighter and more pure single-photon source, in turn leading to lower uncertainties and demonstrate the impact of a detector calibration using a single-photon source. Hopefully, these avenues will be explored in future by NPL and other students working on single-photon detector calibrations. The work presented in this chapter has provided a route to closing the radiometry gap, by traceably linking the single-photon flux of our devices to both commercial and research LOFD. In addition, the methods and analysis required for using this flux to traceably calibrate a commercial SNSPD have been described as a proof-of-concept measurement.

CHAPTER 7

CONCLUSION

The burgeoning interest in single-photon sources and detectors, especially for applications in quantum technology, has resulted in a wealth of research activity in their design, fabrication, characterisation and application. In this thesis, characterisation techniques for both single-photon sources and detectors were explored, with a specific application of quantum radiometry outlined for our sources processed with semiconductor fabrication techniques.

The thesis began in Chapter 1 with a general overview of single-photon technology, including a summary of the development and current state-of-the-art for both single-photon sources and detectors. Motivations for quantum technology proposed by theory and recent experimental demonstrations were reviewed, as a context for the rest of the thesis. Chapter 2 gave a brief description of experimental techniques and tools used throughout the thesis for source characterisation. Chapter 3 began with a description of the second-order correlation function of light. Computational requirements for building up second- and higher-order correlation functions were described, and an algorithm for obtaining this from timetagged data was presented. Experimental considerations identified how imperfect sources and detectors result in non-ideal correlation functions, and analysis routines for correcting this. The main study chapters, Chapter 4 through 6, presented the main outcomes and results of this research.

Chapter 4 presented a model of the rate-dependent detection efficiency of single-photon detectors with finite dead time. The distinction between Heaviside and real detector dead time was stated, and the real detector recovery of the four detection channels in our SNSPD system was experimentally verified. From this, a numerical simulation was used to determine the detected rate for bunched, Poissonian and antibunched light. This simulation was then implemented in an analysis of the detected correlation function, and experimental data was able to verify the discrepancy

between $g^{(2,3,4)}(0)$ for pseudothermal light at high photon rate. This study introduces a new model to enhance those existing in literature - based on a real detector recovery rather than an assumed Heaviside response - and demonstrates how source statistics will result in different detector saturation. Furthermore, we have demonstrated how real single-photon detectors with a finite dead time are impacted at high incident photon rates, which can render them incapable of accurately counting, and measuring correlation. These conditions and measurements will be critical in many systems for viable quantum technologies, highlighting the need for an appropriate model that accounts for real detector imperfections.

Chapter 5 presented an overview of quantum dots as single-photon sources. The process flow for fabricating semiconductor micropillars based on III-arsenide materials was outlined. This included the use of negative tone resist and direct-write lithography for a high-throughput, mass-manufacturable technique whilst maintaining high resolution down to 1.55 µm, and inductively-coupled plasma etching for high aspect-ratio and smooth-sidewalled micropillar cavities based on distributed Bragg reflector structures. Focussing on a low-Q cavity structure, as defined by the ratio of upper and lower alternating Bragg layers of the structure, I presented some single-photon characteristics under resonant excitation. This includes second- and third-order correlations, including Rabi oscillatory behaviour under high-power excitation. This study presents a fabrication process flow for mass-producing high purity, bright single photon sources with well known III-arsenide etch techniques. These sources were examined under high-power resonant excitation and demonstrated the hallmark behaviour of two-level systems including Rabi oscillations evident in third-order correlation functions.

Finally, Chapter 6 presented an application of our quantum dot in micropillar cavities for quantum radiometry. I presented work on calibrating the single-photon flux from our quantum dot in micropillar sources. This involved three measurements on low optical flux detectors, two of which were traceably linked to the SI. The experimental considerations and analysis techniques for these measurements were discussed in detail. Following on from these measurements, the methods for applying this single-photon flux in the calibration of SNSPDs were outlined. An experiment to compare the results of a calibration using an attenuated pulsed laser and the single-photon source was performed, with the results highlighting experimental considerations for future work.

In summary, this research has provided new insights and tools for single-photon source and detector characterisation. Namely - a versatile script for extracting second- and third-order correlations from timetagged data files with user-defined search windows and bin widths, and a numerical model of the detected rate and correlation function with respect to incident rate. In addition, single-photon sources based on semiconductor quantum dots in micropillar cavities were fabricated, characterised, and traceably linked to the SI in a proof-of-concept measurement for quantum radiometry. Given more time

there are several paths which I would like to explore, as a recommendation for future students.

- **Timestamping script**: while highly adaptable and able to calculate reproducible correlation functions, this script was not computationally efficient, especially for third-order correlations. There is a lot of room for improvement with processing speed, which could be approached either with a new calculation algorithm, or with some parallelisation of the main loop. Due to the nature of the data - being an ordered list, and the main process flow - splitting a large file into chunks based on events, I believe there is likely to be a more efficient algorithm by pre-chunking the file before calculation.

- **Dead time model**: the work presented in this thesis demonstrated the impact of finite dead time on measured correlation with a simulation, verified by experimental measurements of a pseudothermal source. In future, obtaining an experimental saturation curve and rate-dependent second-, third- and fourth-order correlation function for antibunched light would provide further insights, especially relevant for emerging quantum technologies that rely on accurately performing those types of measurements. The challenge with this would be to find a source of antibunched light that has a correlation timescale similar to the detector dead time.

- **Quantum dot in micropillar fabrication and characterisation**: this process flow was optimised for a variety of Q-factor pillars and showed consistent results across a sample containing $\sim 12,000$ devices. For the work presented in this thesis, a low-Q sample was characterised. A potential avenue of interest may be to repeat the low- and high-power resonant excitation measurements for a high-Q sample, to investigate the dependence of these behaviours on the Purcell factor. In addition, deterministic patterning of pillars over pre-selected quantum dots would allow precise matching of the cavity mode, spatially and spectrally, to enhance the coupling efficiency and promote the source brightness.

- **Calibration of superconducting nanowire single-photon detectors with a single-photon source**: As alluded to in Section 6.4, the results for the detector calibration were erroneous due to a limited amount of time for developing the experimental considerations. However this study was very insightful in highlighting several factors of importance - including polarisation control and fibre management. With this knowledge, it would be straightforward to continue optimising this experiment and obtain meaningful results. Furthermore, repeating the study with pulsed resonant excitation would allow a more relevant comparison to be drawn between a calibration with a single-photon source and a pulsed Poissonian source. If the source efficiency and experimental uncertainty can be optimised, achieving

sub-Poissonian error on the intensity may provide a feasible path to reducing the experimental uncertainty on the determination of the candela in an expanded definition.

As a final remark: the applications of single-photon technology have the potential to be enormously impactful, within metrology and beyond. Continuing to improve our understanding of single-photon detectors with more accurate models, and using the quantum advantage posed by sub-Poissonian light sources for their calibration, offers new insights into quantum information processing and its possible implementations. Looking far into the future - the next stages of the quantum revolution, akin to the development of microelectronics and the birth of the Internet, are already afoot. The integration of quantum optics experiments in photonic circuits on CMOS-compatible microchips is required in order to make these proposed technologies truly scalable and competitive with classical computing.

BIBLIOGRAPHY

[1] Planck, M. Über eine Verbesserung der Wienschen Spectral Gleichung. *Annalen der Physik* **309**, 553–563 (1901). 1

[2] Einstein, A. Über einen die erzeugung und verwandlung des lichtes betreffenden heuristischen gesichtspunkt. *Annalen der Physik* **322**, 132–148 (1905). https://onlinelibrary.wiley.com/doi/pdf/10.1002/andp.19053220607. 1

[3] Bohr, N. On the constitution of atoms and molecules. *The London, Edinburgh, and Dublin Philosophical Magazine and Journal of Science* **26**, 1–25 (1913). 1

[4] Dirac, P. A. M. The quantum theory of the emission and absorption of radiation. *Proceedings of the Royal Society of London. Series A, Containing Papers of a Mathematical and Physical Character* **114**, 243–265 (1927). 1

[5] Lewis, G. N. The conservation of photons. *Nature* **118**, 874–875 (1926). 1

[6] Einstein, A. Zur quantentheorie der strahlung. *Phys Zeit* **18**, 121 (1917). 1

[7] Compton, A. H. A quantum theory of the scattering of x-rays by light elements. *Physical Review* **21**, 483 (1923). 1

[8] Shockley, W. The theory of p-n junctions in semiconductors and p-n junction transistors. *Bell System Technical Journal* **28**, 435–489 (1949). 1

[9] Gordon, J. P., Zeiger, H. J. & Townes, C. H. The maser—new type of microwave amplifier, frequency standard, and spectrometer. *Physical Review* **99**, 1264 (1955). 1

[10] Maiman, T. H., Hoskins, R., D'Haenens, I. J., Asawa, C. K. & Evtuhov, V. Stimulated optical emission in fluorescent solids. II. spectroscopy and stimulated emission in ruby. *Physical Review* **123**, 1151 (1961). 1

[11] Brown, R. H. & Twiss, R. Q. Correlation between photons in two coherent beams of light. *Nature* **177**, 27–29 (1956). 1, 26

[12] Iams, H. & Salzberg, B. The secondary emission phototube. *Proceedings of the Institute of Radio Engineers* **23**, 55–64 (1935). 1

[13] Glauber, R. J. Coherent and incoherent states of the radiation field. *Physical Review* **131**, 2766 (1963). 1

[14] Glauber, R. J. The quantum theory of optical coherence. *Physical Review* **130**, 2529 (1963). 1

[15] Glauber, R. J. Photon correlations. *Physical Review Letters* **10**, 84 (1963). 1

[16] Mandel, L. & Wolf, E. *Optical coherence and quantum optics* (Cambridge university press, 1995). 1, 26

[17] Clauser, J. F. Experimental distinction between the quantum and classical field-theoretic predictions for the photoelectric effect. *Physical Review D* **9**, 853 (1974). 1, 3

[18] Kimble, H. J., Dagenais, M. & Mandel, L. Photon antibunching in resonance fluorescence. *Physical Review Letters* **39**, 691 (1977). 1, 3

[19] Deutsch, D. Quantum theory, the Church–Turing principle and the universal quantum computer. *Proceedings of the Royal Society of London. A. Mathematical and Physical Sciences* **400**, 97–117 (1985). 1

[20] Thompson, M. T., Mosca, M., Jozsa, R., Steane, A. & Ekert, A. Quantum enhanced information processing. *Philosophical Transactions of the Royal Society of London. Series A: Mathematical, Physical and Engineering Sciences* **358**, 261–279 (2000). 1

[21] Jozsa, R. Characterizing classes of functions computable by quantum parallelism. *Proceedings of the Royal Society of London. Series A: Mathematical and Physical Sciences* **435**, 563–574 (1991). 2

[22] Deutsch, D. & Jozsa, R. Rapid solution of problems by quantum computation. *Proceedings of the Royal Society of London. Series A: Mathematical and Physical Sciences* **439**, 553–558 (1992). 2

[23] Rivest, R. L., Shamir, A. & Adleman, L. A method for obtaining digital signatures and public-key cryptosystems. *Communications of the ACM* **21**, 120–126 (1978). 2

[24] Shor, P. W. Polynomial time algorithms for discrete logarithms and factoring on a quantum computer. In Adleman, L. M. & Huang, M.-D. (eds.) *Algorithmic Number Theory*, 289–289 (Springer Berlin Heidelberg, Berlin, Heidelberg, 1994). 2

[25] Mayers, D. Unconditional security in quantum cryptography. *Journal of the ACM (JACM)* **48**, 351–406 (2001). 2

[26] Inamori, H., Lütkenhaus, N. & Mayers, D. Unconditional security of practical quantum key distribution. *The European Physical Journal D* **41**, 599 (2007). 2

[27] Bennett, C. H. & Brassard, G. Quantum cryptography: Public key distribution and coin tossing. In *Proceedings of IEEE International Conference on Computers, Systems, and Signal Processing*, 175–179 (1984). 2, 9

[28] Ekert, A. K. Quantum cryptography based on Bell's theorem. *Physical Review Letters* **67**, 661 (1991). 2, 9

[29] Wootters, W. K. & Zurek, W. H. A single quantum cannot be cloned. *Nature* **299**, 802–803 (1982). 2

[30] DiVincenzo, D. P. The physical implementation of quantum computation. *Fortschritte der Physik: Progress of Physics* **48**, 771–783 (2000). 2

[31] Knill, E., Laflamme, R. & Milburn, G. J. A scheme for efficient quantum computation with linear optics. *Nature* **409**, 46–52 (2001). 2

[32] Oxborrow, M. & Sinclair, A. G. Single-photon sources. *Contemporary Physics* **46**, 173–206 (2005). 2

[33] Kim, S. H. *et al.* Color centers in hexagonal boron nitride. *Nanomaterials* **13**, 2344 (2023). 4

[34] Tran, T. T., Bray, K., Ford, M. J., Toth, M. & Aharonovich, I. Quantum emission from hexagonal boron nitride monolayers. *Nature Nanotechnology* **11**, 37–41 (2016). 3, 4, 5

[35] Bishop, S. *et al.* Enhanced light collection from a gallium nitride color center using a near index-matched solid immersion lens. *Applied Physics Letters* **120** (2022). 4

[36] Tomm, N. *et al.* A bright and fast source of coherent single photons. *Nature Nanotechnology* **16**, 399–403 (2021). 3, 4, 5, 61, 93

[37] Babinec, T. M. *et al.* A diamond nanowire single-photon source. *Nature Nanotechnology* **5**, 195–199 (2010). 4, 5

[38] Walls, D. Evidence for the quantum nature of light. *Nature* **280**, 451–454 (1979). 3

[39] De Martini, F., Di Giuseppe, G. & Marrocco, M. Single-mode generation of quantum photon states by excited single molecules in a microcavity trap. *Physical Review Letters* **76**, 900 (1996). 3

[40] Kitson, S., Jonsson, P., Rarity, J. & Tapster, P. Intensity fluctuation spectroscopy of small numbers of dye molecules in a microcavity. *Physical Review A* **58**, 620 (1998). 3

[41] Brunel, C., Lounis, B., Tamarat, P. & Orrit, M. Triggered source of single photons based on controlled single molecule fluorescence. *Physical Review Letters* **83**, 2722 (1999). 3

[42] Lounis, B. & Moerner, W. E. Single photons on demand from a single molecule at room temperature. *Nature* **407**, 491–493 (2000). 3

[43] Michler, P. *et al.* A quantum dot single-photon turnstile device. *Science* **290**, 2282–2285 (2000). 3, 61

[44] Santori, C., Fattal, D., Vučković, J., Solomon, G. S. & Yamamoto, Y. Indistinguishable photons from a single-photon device. *Nature* **419**, 594–597 (2002). 3, 61

[45] Yuan, Z. *et al.* Electrically driven single-photon source. *Science* **295**, 102–105 (2002). 3

[46] Zwiller, V., Aichele, T., Seifert, W., Persson, J. & Benson, O. Generating visible single photons on demand with single InP quantum dots. *Applied Physics Letters* **82**, 1509–1511 (2003). 3

[47] Kuhn, A., Hennrich, M. & Rempe, G. Deterministic single-photon source for distributed quantum networking. *Physical Review Letters* **89**, 067901 (2002). 3

[48] Hennrich, M., Legero, T., Kuhn, A. & Rempe, G. Photon statistics of a non-stationary periodically driven single-photon source. *New Journal of Physics* **6**, 86 (2004). 3

[49] Maurer, C., Becher, C., Russo, C., Eschner, J. & Blatt, R. A single-photon source based on a single Ca+ ion. *New Journal of Physics* **6**, 94 (2004). 3

[50] McKeever, J. *et al.* Deterministic generation of single photons from one atom trapped in a cavity. *Science* **303**, 1992–1994 (2004). 3

[51] Kurtsiefer, C., Mayer, S., Zarda, P. & Weinfurter, H. Stable solid-state source of single photons. *Physical Review Letters* **85**, 290 (2000). 3, 42

[52] Beveratos, A., Brouri, R., Gacoin, T., Poizat, J.-P. & Grangier, P. Nonclassical radiation from diamond nanocrystals. *Physical Review A* **64**, 061802 (2001). 3

[53] Gaebel, T. *et al.* Stable single-photon source in the near infrared. *New Journal of Physics* **6**, 98 (2004). 3

[54] Wu, E. *et al.* Room temperature triggered single-photon source in the near infrared. *New Journal of Physics* **9**, 434 (2007). 3

[55] Lombardi, P. *et al.* A molecule-based single-photon source applied in quantum radiometry. *Advanced Quantum Technologies* **3**, 1900083 (2020). 5, 97, 116

[56] Bishop, S. *et al.* Evanescent-field assisted photon collection from quantum emitters under a solid immersion lens. *New Journal of Physics* **24**, 103027 (2022). 5

[57] Castelletto, S. *et al.* Room temperature quantum emission from cubic silicon carbide nanoparticles. *ACS Nano* **8**, 7938–7947 (2014). 5

[58] Wang, H. *et al.* Towards optimal single-photon sources from polarized microcavities. *Nature Photonics* **13**, 770–775 (2019). 3, 5, 93

[59] Senellart, P., Solomon, G. & White, A. High-performance semiconductor quantum-dot single-photon sources. *Nature Nanotechnology* **12**, 1026–1039 (2017). 3

[60] Bishop, S. G. *et al.* Room-temperature quantum emitter in aluminum nitride. *ACS Photonics* **7**, 1636–1641 (2020). 3

[61] Holmes, M. J., Choi, K., Kako, S., Arita, M. & Arakawa, Y. Room-temperature triggered single photon emission from a III-nitride site-controlled nanowire quantum dot. *Nano Letters* **14**, 982–986 (2014). 3, 61

[62] Castelletto, S. *et al.* A silicon carbide room-temperature single-photon source. *Nature Materials* **13**, 151–156 (2014). 3

[63] Tonndorf, P. *et al.* Single-photon emission from localized excitons in an atomically thin semiconductor. *Optica* **2**, 347–352 (2015). 3

[64] Barnes, W. *et al.* Solid-state single photon sources: light collection strategies. *The European Physical Journal D-Atomic, Molecular, Optical and Plasma Physics* **18**, 197–210 (2002). 4, 5

[65] Koyama, K., Yoshita, M., Baba, M., Suemoto, T. & Akiyama, H. High collection efficiency in fluorescence microscopy with a solid immersion lens. *Applied Physics Letters* **75**, 1667–1669 (1999). 4

[66] Liu, Z. *et al.* High resolution, high collection efficiency in numerical aperture increasing lens microscopy of individual quantum dots. *Applied Physics Letters* **87** (2005). 4

[67] Hadden, J. *et al.* Strongly enhanced photon collection from diamond defect centers under microfabricated integrated solid immersion lenses. *Applied Physics Letters* **97** (2010). 4

[68] Hekmati, R. *et al.* Bullseye dielectric cavities for photon collection from a surface-mounted quantum-light-emitter. *Scientific Reports* **13**, 5316 (2023). 4

[69] Butcher, A. & High, A. A. All-dielectric multi-resonant bullseye antennas. *Optics Express* **30**, 12092–12103 (2022). 4

[70] Sapienza, L., Davanço, M., Badolato, A. & Srinivasan, K. Nanoscale optical positioning of single quantum dots for bright and pure single-photon emission. *Nature Communications* **6**, 7833 (2015). 4

[71] Wang, H. *et al.* On-demand semiconductor source of entangled photons which simultaneously has high fidelity, efficiency, and indistinguishability. *Physical Review Letters* **122**, 113602 (2019). 4, 61

[72] Meunier, M. *et al.* Telecom single-photon emitters in GaN operating at room temperature: embedment into bullseye antennas. *Nanophotonics* **12**, 1405–1419 (2023). 4

[73] Zheng, J., Liapis, A. C., Chen, E. H., Black, C. T. & Englund, D. Chirped circular dielectric gratings for near-unity collection efficiency from quantum emitters in bulk diamond. *Optics Express* **25**, 32420–32435 (2017). 4

[74] Andersen, S. K. *et al.* Hybrid plasmonic bullseye antennas for efficient photon collection. *ACS Photonics* **5**, 692–698 (2018). 4

[75] Duong, N. M. H. *et al.* Enhanced emission from WSe2 monolayers coupled to circular bragg gratings. *ACS Photonics* **5**, 3950–3955 (2018). 4

[76] Vahala, K. J. Optical microcavities. *Nature* **424**, 839–846 (2003). 4

[77] Gerard, J. *et al.* Quantum boxes as active probes for photonic microstructures: The pillar microcavity case. *Applied Physics Letters* **69**, 449–451 (1996). 4

[78] Rivera, T. *et al.* Optical losses in plasma-etched AlGaAs microresonators using reflection spectroscopy. *Applied Physics Letters* **74**, 911–913 (1999). 5

[79] Ding, X. *et al.* On-demand single photons with high extraction efficiency and near-unity indistinguishability from a resonantly driven quantum dot in a micropillar. *Physical Review Letters* **116**, 020401 (2016). 5, 61

[80] Somaschi, N. *et al.* Near-optimal single-photon sources in the solid state. *Nature Photonics* **10**, 340–345 (2016). 5, 61

[81] Natarajan, C. M., Tanner, M. G. & Hadfield, R. H. Superconducting nanowire single-photon detectors: physics and applications. *Superconductor Science and Technology* **25**, 063001 (2012). 6, 23

[82] Dautet, H. *et al.* Photon counting techniques with silicon avalanche photodiodes. *Applied Optics* **32**, 3894–3900 (1993). 6, 7

[83] Ghioni, M., Cova, S., Lacaita, A. & Ripamonti, G. New silicon epitaxial avalanche diode for single-photon timing at room temperature. *Electronics Letters* **24**, 1476–1477 (1988). 7

[84] Cova, S., Lacaita, A., Ghioni, M., Ripamonti, G. & Louis, T. 20-ps timing resolution with single-photon avalanche diodes. *Review of Scientific Instruments* **60**, 1104–1110 (1989). 7

[85] Ceccarelli, F. *et al.* Recent advances and future perspectives of single-photon avalanche diodes for quantum photonics applications. *Advanced Quantum Technologies* **4**, 2000102 (2021). 7

[86] Tosi, A., Calandri, N., Sanzaro, M. & Acerbi, F. Low-noise, low-jitter, high detection efficiency InGaAs/InP single-photon avalanche diode. *IEEE Journal of Selected Topics in Quantum Electronics* **20**, 192–197 (2014). 7, 8

[87] Cabrera, B. *et al.* Detection of single infrared, optical, and ultraviolet photons using superconducting transition edge sensors. *Applied Physics Letters* **73**, 735–737 (1998). 7

[88] Zhang, W. *et al.* NbN superconducting nanowire single photon detector with efficiency over 90% at 1550 nm wavelength operational at compact cryocooler temperature. *Science China Physics, Mechanics & Astronomy* **60**, 1–10 (2017). 7, 8

[89] Ejrnaes, M. *et al.* A cascade switching superconducting single photon detector. *Applied Physics Letters* **91** (2007). 7, 8, 23

[90] Dorenbos, S. *et al.* Superconducting single photon detectors with minimized polarization dependence. *Applied Physics Letters* **93** (2008). 7, 23

[91] Foord, R., Jones, R., Oliver, C. & Pike, E. The use of photomultiplier tubes for photon counting. *Applied Optics* **8**, 1975–1989 (1969). 6

[92] Buller, G. & Collins, R. Single-photon generation and detection. *Measurement Science and Technology* **21**, 012002 (2009). 6, 38

[93] Antognetti, P., Cova, S. & Longoni, A. A study of the operation and performances of an avalanche diode as a single-photon detector. Tech. Rep. (1975). 6

[94] Cova, S., Ghioni, M., Lacaita, A., Samori, C. & Zappa, F. Avalanche photodiodes and quenching circuits for single-photon detection. *Applied Optics* **35**, 1956–1976 (1996). 6, 21

[95] Zhang, J., Itzler, M. A., Zbinden, H. & Pan, J.-W. Advances in InGaAs/InP single-photon detector systems for quantum communication. *Light: Science & Applications* **4**, e286–e286 (2015). 7

[96] Itzler, M. A. *et al.* Single photon avalanche diodes (SPADs) for 1.5 μm photon counting applications. *Journal of Modern Optics* **54**, 283–304 (2007). 7

[97] Lacaita, A., Francese, P., Zappa, F. & Cova, S. Single-photon detection beyond 1 μm: performance of commercially available germanium photodiodes. *Applied Optics* **33**, 6902–6918 (1994). 7

[98] Buller, G. S. *et al.* Time-resolved photoluminescence measurements of InGaAs/InP multiple-quantum-well structures at 1.3 μm wavelengths by use of germanium single-photon avalanche photodiodes. *Applied Optics* **35**, 916–921 (1996). 7

[99] Warburton, R. E. *et al.* Ge-on-Si single-photon avalanche diode detectors: design, modeling, fabrication, and characterization at wavelengths 1310 and 1550 nm. *IEEE Transactions on Electron Devices* **60**, 3807–3813 (2013). 7

[100] Vines, P. *et al.* High performance planar germanium-on-silicon single-photon avalanche diode detectors. *Nature Communications* **10**, 1086 (2019). 7

[101] Lita, A. E., Miller, A. J. & Nam, S. W. Counting near-infrared single-photons with 95% efficiency. *Optics Express* **16**, 3032–3040 (2008). 7

[102] Fukuda, D. *et al.* Titanium-based transition-edge photon number resolving detector with 98% detection efficiency with index-matched small-gap fiber coupling. *Optics Express* **19**, 870–875 (2011). 7

[103] Peacock, A. *et al.* Single optical photon detection with a superconducting tunnel junction. *Nature* **381**, 135–137 (1996). 8

[104] Semenov, A. D., Gol'tsman, G. N. & Korneev, A. A. Quantum detection by current carrying superconducting film. *Physica C: Superconductivity* **351**, 349–356 (2001). 8

[105] Gol'Tsman, G. *et al.* Picosecond superconducting single-photon optical detector. *Applied Physics Letters* **79**, 705–707 (2001). 8

[106] Gol'tsman, G. *et al.* Fabrication of nanostructured superconducting single-photon detectors. *IEEE Transactions On Applied Superconductivity* **13**, 192–195 (2003). 8, 23

[107] Korneev, A. *et al.* Sensitivity and gigahertz counting performance of NbN superconducting single-photon detectors. *Applied Physics Letters* **84**, 5338–5340 (2004). 8

[108] Divochiy, A. *et al.* Superconducting nanowire photon-number-resolving detector at telecommunication wavelengths. *Nature Photonics* **2**, 302 (2008). 8

[109] Korneeva, Y., Florya, I., Semenov, A., Korneev, A. & Goltsman, G. New generation of nanowire NbN superconducting single-photon detector for mid-infrared. *IEEE Transactions on Applied Superconductivity* **21**, 323–326 (2011). 8

[110] Marsili, F. *et al.* Single-photon detectors based on ultranarrow superconducting nanowires. *Nano Letters* **11**, 2048–2053 (2011). 8, 23

[111] Excelitas. NIR-optimized single photon counting module (2020). URL https://www.excelitas.com/file-download/download/public/67136?filename=PD_SPCM%20Family_brochure_June2019.pdf. 8

[112] Sanzaro, M. *et al.* InGaAs/InP single-photon detector with low noise, low timing jitter and high count rate. In *Quantum Sensing and Nanophotonic Devices XII*, vol. 9370, 386–392 (SPIE, 2015). 8

[113] Verma, V. B. *et al.* High-efficiency superconducting nanowire single-photon detectors fabricated from MoSi thin-films. *Optics Express* **23**, 33792–33801 (2015). 8

[114] Marsili, F. *et al.* Detecting single infrared photons with 93% system efficiency. *Nature Photonics* **7**, 210–214 (2013). 8

[115] Vajner, D. A., Rickert, L., Gao, T., Kaymazlar, K. & Heindel, T. Quantum communication using semiconductor quantum dots. *Advanced Quantum Technologies* **5**, 2100116 (2022). 9

[116] Waks, E., Santori, C. & Yamamoto, Y. Security aspects of quantum key distribution with sub-poisson light. *Physical Review A* **66**, 042315 (2002). 9

[117] Beveratos, A. *et al.* Single photon quantum cryptography. *Physical Review Letters* **89**, 187901 (2002). 9

[118] Alléaume, R. *et al.* Experimental open-air quantum key distribution with a single-photon source. *New Journal of Physics* **6**, 92 (2004). 9

[119] Waks, E. *et al.* Quantum cryptography with a photon turnstile. *Nature* **420**, 762–762 (2002). 9

[120] Aichele, T., Reinaudi, G. & Benson, O. Separating cascaded photons from a single quantum dot: Demonstration of multiplexed quantum cryptography. *Physical Review B* **70**, 235329 (2004). 9

[121] Collins, R. *et al.* Quantum key distribution system in standard telecommunications fiber using a short wavelength single photon source. *Journal of Applied Physics* **107** (2010). 9

[122] Intallura, P. *et al.* Quantum communication using single photons from a semiconductor quantum dot emitting at a telecommunication wavelength. *Journal of Optics A: Pure and Applied Optics* **11**, 054005 (2009). 9

[123] Takemoto, K. *et al.* Quantum key distribution over 120 km using ultrahigh purity single-photon source and superconducting single-photon detectors. *Scientific Reports* **5**, 14383 (2015). 9

[124] Dzurnak, B. *et al.* Quantum key distribution with an entangled light emitting diode. *Applied Physics Letters* **107** (2015). 9

[125] Basso Basset, F. *et al.* Quantum key distribution with entangled photons generated on demand by a quantum dot. *Science Advances* **7** (2021). 9

[126] Schimpf, C. *et al.* Quantum cryptography with highly entangled photons from semiconductor quantum dots. *Science Advances* **7** (2021). 9

[127] Basset, F. B. *et al.* Daylight entanglement-based quantum key distribution with a quantum dot source. *Quantum Science and Technology* **8** (2023). 9

[128] Stucki, D., Brunner, N., Gisin, N., Scarani, V. & Zbinden, H. Fast and simple one-way quantum key distribution. *Applied Physics Letters* **87** (2005). 10

[129] Korzh, B. *et al.* Provably secure and practical quantum key distribution over 307 km of optical fibre. *Nature Photonics* **9**, 163–168 (2015). 10

[130] Hadfield, R. H., Habif, J. L., Schlafer, J., Schwall, R. E. & Nam, S. W. Quantum key distribution at 1550nm with twin superconducting single-photon detectors. *Applied Physics Letters* **89** (2006). 10

[131] Takesue, H. *et al.* Quantum key distribution over a 40-db channel loss using superconducting single-photon detectors. *Nature Photonics* **1**, 343–348 (2007). 10

[132] Lucamarini, M., Yuan, Z. L., Dynes, J. F. & Shields, A. J. Overcoming the rate–distance limit of quantum key distribution without quantum repeaters. *Nature* **557**, 400–403 (2018). 10

[133] Ma, X., Zeng, P. & Zhou, H. Phase-matching quantum key distribution. *Physical Review X* **8**, 031043 (2018). 10

[134] Wang, S. *et al.* Twin-field quantum key distribution over 830-km fibre. *Nature Photonics* **16**, 154–161 (2022). 10

[135] Moreau, P.-A., Toninelli, E., Gregory, T. & Padgett, M. J. Imaging with quantum states of light. *Nature Reviews Physics* **1**, 367–380 (2019). 10

[136] Paúr, M., Stoklasa, B., Hradil, Z., Sánchez-Soto, L. L. & Rehacek, J. Achieving the ultimate optical resolution. *Optica* **3**, 1144–1147 (2016). 10, 11

[137] Caves, C. M. Quantum-mechanical noise in an interferometer. *Physical Review D* **23**, 1693 (1981). 10

[138] Braunstein, S. L. Quantum limits on precision measurements of phase. *Physical Review Letters* **69**, 3598 (1992). 10

[139] Braunstein, S. L. & Caves, C. M. Statistical distance and the geometry of quantum states. *Physical Review Letters* **72**, 3439 (1994). 10

[140] Lee, H., Kok, P. & Dowling, J. P. A quantum rosetta stone for interferometry. *Journal of Modern Optics* **49**, 2325–2338 (2002). 10

[141] Giovannetti, V., Lloyd, S. & Maccone, L. Quantum-enhanced measurements: beating the standard quantum limit. *Science* **306**, 1330–1336 (2004). 10

[142] Giovannetti, V., Lloyd, S. & Maccone, L. Quantum metrology. *Physical Review Letters* **96**, 010401 (2006). 10

[143] Walls, D. F. Squeezed states of light. *Nature* **306**, 141–146 (1983). 11

[144] Xiao, M., Wu, L.-A. & Kimble, H. J. Precision measurement beyond the shot-noise limit. *Physical Review Letters* **59**, 278 (1987). 11

[145] Dowling, J. P. Correlated input-port, matter-wave interferometer: Quantum-noise limits to the atom-laser gyroscope. *Physical Review A* **57**, 4736 (1998). 11

[146] Holland, M. & Burnett, K. Interferometric detection of optical phase shifts at the heisenberg limit. *Physical Review Letters* **71**, 1355 (1993). 11

[147] Lloyd, S. Enhanced sensitivity of photodetection via quantum illumination. *Science* **321**, 1463–1465 (2008). 11

[148] Brida, G., Genovese, M. & Ruo Berchera, I. Experimental realization of sub-shot-noise quantum imaging. *Nature Photonics* **4**, 227–230 (2010). 11

[149] Gregory, T., Moreau, P.-A., Toninelli, E. & Padgett, M. J. Imaging through noise with quantum illumination. *Science Advances* **6** (2020). 11

[150] Gregory, T., Moreau, P.-A., Mekhail, S., Wolley, O. & Padgett, M. Noise rejection through an improved quantum illumination protocol. *Scientific Reports* **11**, 21841 (2021). 11

[151] Johnson, S. *et al.* Single-pixel imaging with heralded single photons. *Optics Continuum* **1**, 826–833 (2022). 11

[152] Samantaray, N., Ruo-Berchera, I., Meda, A. & Genovese, M. Realization of the first sub-shot-noise wide field microscope. *Light: Science & Applications* **6** (2017). 11

[153] Casacio, C. A. *et al.* Quantum-enhanced nonlinear microscopy. *Nature* **594**, 201–206 (2021). 11

[154] Ndagano, B. *et al.* Quantum microscopy based on hong–ou–mandel interference. *Nature Photonics* **16**, 384–389 (2022). 11

[155] Gili, V. *et al.* Experimental realization of scanning quantum microscopy. *Applied Physics Letters* **121** (2022). 11

[156] Collaboration, T. L. S. A gravitational wave observatory operating beyond the quantum shot-noise limit. *Nature Physics* **7**, 962–965 (2011). 11

[157] Aasi, J. *et al.* Enhanced sensitivity of the LIGO gravitational wave detector by using squeezed states of light. *Nature Photonics* **7**, 613–619 (2013). 11

[158] Schwartz, O. *et al.* Superresolution microscopy with quantum emitters. *Nano Letters* **13**, 5832–5836 (2013). 11

[159] Israel, Y., Tenne, R., Oron, D. & Silberberg, Y. Quantum correlation enhanced super-resolution localization microscopy enabled by a fibre bundle camera. *Nature Communications* **8**, 14786 (2017). 11

[160] Monticone, D. G. *et al.* Beating the abbe diffraction limit in confocal microscopy via nonclassical photon statistics. *Physical Review Letters* **113**, 143602 (2014). 11

[161] O'Brien, J. L. Optical quantum computing. *Science* **318**, 1567–1570 (2007). 11

[162] Barz, S. *et al.* Demonstration of blind quantum computing. *Science* **335**, 303–308 (2012). 11, 12

[163] Zhong, H.-S. *et al.* Quantum computational advantage using photons. *Science* **370**, 1460–1463 (2020). 11, 12

[164] O'Brien, J. L., Pryde, G. J., White, A. G., Ralph, T. C. & Branning, D. Demonstration of an all-optical quantum controlled-NOT gate. *Nature* **426**, 264–267 (2003). 11

[165] Walther, P. *et al.* Experimental one-way quantum computing. *Nature* **434**, 169–176 (2005). 11

[166] Kiesel, N. *et al.* Experimental analysis of a four-qubit photon cluster state. *Physical Review Letters* **95**, 210502 (2005). 11

[167] Lu, C.-Y., Browne, D. E., Yang, T. & Pan, J.-W. Demonstration of a compiled version of Shor's quantum factoring algorithm using photonic qubits. *Physical Review Letters* **99**, 250504 (2007). 11

[168] Lanyon, B. P. *et al.* Experimental demonstration of a compiled version of Shor's algorithm with quantum entanglement. *Physical Review Letters* **99**, 250505 (2007). 11

[169] Prevedel, R. *et al.* High-speed linear optics quantum computing using active feed-forward. *Nature* **445**, 65–69 (2007). 11

[170] Aaronson, S. & Arkhipov, A. The computational complexity of linear optics. In *Proceedings of the forty-third annual ACM symposium on Theory of computing*, 333–342 (2011). 12

[171] Hamilton, C. S. *et al.* Gaussian boson sampling. *Physical Review Letters* **119**, 170501 (2017). 12

[172] Quesada, N., Arrazola, J. M. & Killoran, N. Gaussian boson sampling using threshold detectors. *Physical Review A* **98**, 062322 (2018). 12

[173] Knemeyer, J.-P., Marmé, N. & Sauer, M. Probes for detection of specific DNA sequences at the single-molecule level. *Analytical Chemistry* **72**, 3717–3724 (2000). 12

[174] Berglund, A. J., Doherty, A. C. & Mabuchi, H. Photon statistics and dynamics of fluorescence resonance energy transfer. *Physical Review Letters* **89**, 068101 (2002). 12

[175] Suhling, K., French, P. M. & Phillips, D. Time-resolved fluorescence microscopy. *Photochemical & Photobiological Sciences* **4**, 13–22 (2005). 12

[176] McIlrath, T., Hudson, R., Aikin, A. & Wilkerson, T. Two-photon LIDAR technique for remote sensing of atomic oxygen. *Applied Optics* **18**, 316–319 (1979). 12

[177] Polyakov, S. V. & Migdall, A. L. Quantum radiometry. *Journal of Modern Optics* **56**, 1045–1052 (2009). 12, 91

[178] Paddock, S. W. *An introduction to confocal imaging* (Springer, 1999). 14

[179] Muller, M. *Introduction to confocal fluorescence microscopy*, vol. 69 (SPIE press, 2006). 14

[180] Hecht, E. *Optics* (Pearson Education India, 2012). 14, 25

[181] Sparrow, C. M. On spectroscopic resolving power. *Astrophysical Journal, vol. 44, p. 76* **44**, 76 (1916). 14

[182] Muller, A. *et al.* Resonance fluorescence from a coherently driven semiconductor quantum dot in a cavity. *Physical Review Letters* **99**, 187402 (2007). 15, 70

[183] Ates, S. *et al.* Post-selected indistinguishable photons from the resonance fluorescence of a single quantum dot in a microcavity. *Physical Review Letters* **103**, 167402 (2009). 15, 69

[184] Nguyen, H.-S. *et al.* Ultra-coherent single photon source. *Applied Physics Letters* **99** (2011). 15, 69

[185] Ulhaq, A. *et al.* Cascaded single-photon emission from the mollow triplet sidebands of a quantum dot. *Nature Photonics* **6**, 238–242 (2012). 15

[186] Kuhlmann, A. V. *et al.* A dark-field microscope for background-free detection of resonance fluorescence from single semiconductor quantum dots operating in a set-and-forget mode. *Review of Scientific Instruments* **84** (2013). 15, 70

[187] Collett, E. Field guide to polarization (Spie Bellingham, WA, 2005). 15

[188] attocube. Closed-cycle cryostats: attodry1000 (2023). URL https://www.attocube.com/en/products/cryostats/closed-cycle-cryostats/attodry1000. 17

[189] attocube. Closed-cycle cryostats: attodry800 (2023). URL https://www.attocube.com/en/products/cryostats/closed-cycle-cryostats/attodry800-optical-cryostat. 18

[190] Wolfe, W. L. *Introduction to imaging spectrometers*, vol. 25 (SPIE Press, 1997). 18

[191] Sze, S. M. *Semiconductor devices: Physics and technology* (John wiley & sons, 2008). 18

[192] Aluf, O. *Advance Elements of Laser Circuits and Systems: Nonlinear Applications in Engineering* (Springer Nature, 2021). 19

[193] Squared, M. M Squared lasers: SolsTiS (2023). URL https://m2lasers.com/solstis.html. 20

[194] Migdall, A., Polyakov, S. V., Fan, J. & Bienfang, J. C. *Single-photon generation and detection: physics and applications* (Academic Press, 2013). 21, 22, 24

[195] Newman, R. Visible light from a silicon p- n junction. *Physical Review* **100**, 700 (1955). 22

[196] Villa, S., Lacaita, A. L. & Pacelli, A. Photon emission from hot electrons in silicon. *Physical Review B* **52**, 10993 (1995). 22

[197] Skocpol, W., Beasley, M. & Tinkham, M. Self-heating hotspots in superconducting thin-film microbridges. *Journal of Applied Physics* **45**, 4054–4066 (1974). 22

[198] Testardi, L. R. Destruction of superconductivity by laser light. *Physical Review B* **4**, 2189–2196 (1971). 22

[199] Semenov, A., Nebosis, R., Gousev, Y. P., Heusinger, M. & Renk, K. Analysis of the nonequilibrium photoresponse of superconducting films to pulsed radiation by use of a two-temperature model. *Physical Review B* **52**, 581 (1995). 22

[200] Kadin, A. & Johnson, M. Nonequilibrium photon-induced hotspot: A new mechanism for photodetection in ultrathin metallic films. *Applied Physics Letters* **69**, 3938–3940 (1996). 22

[201] Anant, V. *et al.* Optical properties of superconducting nanowire single-photon detectors. *Optics Express* **16**, 10750–10761 (2008). 23

[202] Burenkov, V., Xu, H., Qi, B., Hadfield, R. H. & Lo, H.-K. Investigations of afterpulsing and detection efficiency recovery in superconducting nanowire single-photon detectors. *Journal of Applied Physics* **113** (2013). 23

[203] Caloz, M. *et al.* High-detection efficiency and low-timing jitter with amorphous superconducting nanowire single-photon detectors. *Applied Physics Letters* **112** (2018). 23

[204] Wu, J. *et al.* Improving the timing jitter of a superconducting nanowire single-photon detection system. *Applied Optics* **56**, 2195–2200 (2017). 23

[205] Bulaevskii, L., Graf, M., Batista, C. & Kogan, V. Vortex-induced dissipation in narrow current-biased thin-film superconducting strips. *Physical Review B* **83**, 144526 (2011). 23

[206] Yang, X. *et al.* Superconducting nanowire single photon detector with on-chip bandpass filter. *Optics Express* **22**, 16267–16272 (2014). 23

[207] Chen, S. *et al.* Dark counts of superconducting nanowire single-photon detector under illumination. *Optics Express* **23**, 10786–10793 (2015). 23

[208] Kerman, A. J. *et al.* Kinetic-inductance-limited reset time of superconducting nanowire photon counters. *Applied Physics Letters* **88**, 111116 (2006). 23, 48

[209] Yang, J. K. *et al.* Modeling the electrical and thermal response of superconducting nanowire single-photon detectors. *IEEE Transactions on Applied Superconductivity* **17**, 581–585 (2007). 23, 48

[210] Kerman, A. J., Yang, J. K., Molnar, R. J., Dauler, E. A. & Berggren, K. K. Electrothermal feedback in superconducting nanowire single-photon detectors. *Physical Review B* **79**, 100509 (2009). 23

[211] Wiersig, J. *et al.* Direct observation of correlations between individual photon emission events of a microcavity laser. *Nature* **460**, 245–249 (2009). 24

[212] Aßmann, M., Veit, F., Bayer, M., van der Poel, M. & Hvam, J. M. Higher-order photon bunching in a semiconductor microcavity. *Science* **325**, 297–300 (2009). 24

[213] Ou, L.-H. & Kuang, L.-M. Ghost imaging with third-order correlated thermal light. *Journal of Physics B: Atomic, Molecular and Optical Physics* **40**, 1833 (2007). 24

[214] Bai, Y. & Han, S. Ghost imaging with thermal light by third-order correlation. *Physical Review A* **76**, 043828 (2007). 24

[215] Zhou, Y., Liu, J., Simon, J. & Shih, Y. Resolution enhancement of third-order thermal light ghost imaging in the photon counting regime. *JOSA B* **29**, 377–381 (2012). 24

[216] Koch, M. *et al.* Three-photon correlations in a strongly driven atom-cavity system. *Physical Review Letters* **107**, 023601 (2011). 24

[217] Elvira, D. *et al.* Higher-order photon correlations in pulsed photonic crystal nanolasers. *Physical Review A* **84**, 061802 (2011). 24

[218] Stevens, M. J. *et al.* High-order temporal coherences of chaotic and laser light. *Optics Express* **18**, 1430–1437 (2010). 24

[219] Agafonov, I., Chekhova, M., Iskhakov, T. S. & Penin, A. High-visibility multiphoton interference of Hanbury Brown–Twiss type for classical light. *Physical Review A* **77**, 053801 (2008). 24

[220] Rundquist, A. *et al.* Nonclassical higher-order photon correlations with a quantum dot strongly coupled to a photonic-crystal nanocavity. *Physical Review A* **90**, 023846 (2014). 24

[221] Loudon, R. *The quantum theory of light* (OUP Oxford, 2000). 25, 58, 62, 90, 149, 157

[222] Scully, M. O. & Zubairy, M. S. *Quantum optics* (American Association of Physics Teachers, 1999). 25, 84

[223] Fox, M. *Quantum optics: an introduction*, vol. 15 (OUP Oxford, 2006). 28, 62, 157

[224] Brouri, R., Beveratos, A., Poizat, J.-P. & Grangier, P. Photon antibunching in the fluorescence of individual color centers in diamond. *Optics Letters* **25**, 1294–1296 (2000). 30

[225] Kurtsiefer, C., Zarda, P., Mayer, S. & Weinfurter, H. The breakdown flash of silicon avalanche photodiodes-back door for eavesdropper attacks? *Journal of Modern Optics* **48**, 2039–2047 (2001). 33

[226] Martienssen, W. & Spiller, E. Coherence and fluctuations in light beams. *American Journal of Physics* **32**, 919–926 (1964). 39

[227] Jakeman, E. The effect of wavefront curvature on the coherence properties of laser light scattered by target centres in uniform motion. *Journal of Physics A: Mathematical and General* **8**, L23 (1975). 39

[228] Pusey, P. Photon correlation study of laser speckle produced by a moving rough surface. *Journal of Physics D: Applied Physics* **9**, 1399 (1976). 40

[229] Kuusela, T. A. Measurement of the second-order coherence of pseudothermal light. *American Journal of Physics* **85**, 289–294 (2017). 40

[230] Johnson, F., Jones, R., McLean, T. & Pike, E. Dead-time corrections to photon counting distributions. *Physical Review Letters* **16**, 589 (1966). 45

[231] Bédard, G. Dead-time corrections to the statistical distribution of photoelectrons. *Proceedings of the Physical Society* **90**, 131 (1967). 45

[232] Cantor, B. & Teich, M. Dead-time-corrected photocounting distributions for laser radiation. *JOSA* **65**, 786–791 (1975). 45

[233] Mandel, L. Inversion problem in photon counting with dead time. *JOSA* **70**, 873–874 (1980). 45

[234] López, M., Hofer, H. & Kück, S. Detection efficiency calibration of single-photon silicon avalanche photodiodes traceable using double attenuator technique. *Journal of Modern Optics* **62**, 1732–1738 (2015). 45, 93

[235] López, M. *et al.* A study to develop a robust method for measuring the detection efficiency of free-running InGaAs/InP single-photon detectors. *EPJ Quantum Technology* **7**, 14 (2020). 45

[236] Georgieva, H. *et al.* Detection of ultra-weak laser pulses by free-running single-photon detectors: modeling dead time and dark counts effects. *Applied Physics Letters* **118** (2021). 45, 118, 120

[237] Raupach, S. M. *et al.* Detection rate dependence of the inherent detection efficiency in single-photon detectors based on avalanche diodes. *Physical Review A* **105**, 042615 (2022). 45

[238] Chunnilall, C. *et al.* Quantum key distribution (QKD); Component characterization: characterizing optical components for QKD systems. 49

[239] Ibe, O. *Fundamentals of applied probability and random processes* (Academic Press, 2014). 50

[240] Stranski, I. N. & Krastanow, L. Zur theorie der orientierten ausscheidung von ionenkristallen aufeinander. *Monatshefte für Chemie und verwandte Teile anderer Wissenschaften* **71**, 351–364 (1937). 61, 67

[241] Jons, K. *et al.* Triggered indistinguishable single photons with narrow line widths from site-controlled quantum dots. *Nano Letters* **13**, 126–130 (2013). 61

[242] Mrowiński, P. *et al.* Directional single-photon emission from deterministic quantum dot waveguide structures. *Physica Status Solidi –Rapid Research Letters* **14**, 2000115 (2020). 61

[243] Große, J., von Helversen, M., Koulas-Simos, A., Hermann, M. & Reitzenstein, S. Development of site-controlled quantum dot arrays acting as scalable sources of indistinguishable photons. *APL Photonics* **5** (2020). 61

[244] Wang, Y. R., Han, I. S., Jin, C.-Y. & Hopkinson, M. Precise arrays of epitaxial quantum dots nucleated by in situ laser interference for quantum information technology applications. *ACS Applied Nano Materials* **3**, 4739–4746 (2020). 61

[245] Kako, S. *et al.* A gallium nitride single-photon source operating at 200 K. *Nature Materials* **5**, 887–892 (2006). 61

[246] Holmes, M. J., Kako, S., Choi, K., Arita, M. & Arakawa, Y. Single photons from a hot solid-state emitter at 350 K. *ACS Photonics* **3**, 543–546 (2016). 61

[247] Arita, M., Le Roux, F., Holmes, M. J., Kako, S. & Arakawa, Y. Ultraclean single photon emission from a GaN quantum dot. *Nano Letters* **17**, 2902–2907 (2017). 61

[248] Miyazawa, T. *et al.* Single-photon generation in the 1.55 μm optical-fiber band from an InAs/InP quantum dot. *Japanese Journal of Applied Physics* **44**, L620 (2005). 61

[249] Birowosuto, M. D. *et al.* Fast Purcell-enhanced single photon source in 1,550 nm telecom band from a resonant quantum dot-cavity coupling. *Scientific Reports* **2**, 321 (2012). 61

[250] Benyoucef, M., Yacob, M., Reithmaier, J., Kettler, J. & Michler, P. Telecom-wavelength (1.5 μm) single-photon emission from InP-based quantum dots. *Applied Physics Letters* **103** (2013). 61

[251] Nawrath, C. *et al.* Coherence and indistinguishability of highly pure single photons from non-resonantly and resonantly excited telecom C-band quantum dots. *Applied Physics Letters* **115** (2019). 61

[252] Musiał, A. *et al.* High-purity triggered single-photon emission from symmetric single InAs/InP quantum dots around the telecom C-band window. *Advanced Quantum Technologies* **3**, 1900082 (2020). 61

[253] He, Y.-M. *et al.* On-demand semiconductor single-photon source with near-unity indistinguishability. *Nature Nanotechnology* **8**, 213–217 (2013). 61

[254] Wang, H. *et al.* Near-transform-limited single photons from an efficient solid-state quantum emitter. *Physical Review Letters* **116**, 213601 (2016). 61

[255] Santana, T. S. *et al.* Generating indistinguishable photons from a quantum dot in a noisy environment. *Physical Review B* **95**, 201410 (2017). 61

[256] Purcell, E. M., Torrey, H. C. & Pound, R. V. Resonance absorption by nuclear magnetic moments in a solid. *Physical Review* **69**, 37 (1946). 64, 66

[257] Dutra, S. M. *Cavity quantum electrodynamics: the strange theory of light in a box* (John Wiley & Sons, 2005). 66

[258] Unitt, D., Bennett, A., Atkinson, P., Ritchie, D. & Shields, A. Polarization control of quantum dot single-photon sources via a dipole-dependent Purcell effect. *Physical Review B* **72**, 033318 (2005). 66

[259] Gywat, O., Krenner, H. J. & Berezovsky, J. *Spins in optically active quantum dots: concepts and methods* (John Wiley & Sons, 2009). 67

[260] Kira, M. & Koch, S. W. *Semiconductor quantum optics* (Cambridge University Press, 2011). 67

[261] Kittel, C. *Introduction to solid state physics* (John Wiley & sons, inc, 2005). 67

[262] Winkler, R., Papadakis, S., De Poortere, E. & Shayegan, M. *Spin-orbit coupling in two-dimensional electron and hole systems*, vol. 41 (Springer, 2003). 68

[263] Ehrhardt, M. & Koprucki, T. *Multi-Band Effective Mass Approximations: Advanced Mathematical Models and Numerical Techniques*, vol. 94 (Springer, 2014). 68

[264] Kowalik, K., Krebs, O., Lemaître, A., Gaj, J. & Voisin, P. Optical alignment and polarization conversion of the neutral-exciton spin in individual InAs/InGaAs quantum dots. *Physical Review B* **77**, 161305 (2008). 68

[265] Bracker, A. S., Gammon, D. & Korenev, V. L. Fine structure and optical pumping of spins in individual semiconductor quantum dots. *Semiconductor Science and Technology* **23**, 114004 (2008). 68

[266] Bayer, M. *et al.* Fine structure of neutral and charged excitons in self-assembled InGaAs/AlGaAs quantum dots. *Physical Review B* **65**, 195315 (2002). 68

[267] Bester, G., Nair, S. & Zunger, A. Pseudopotential calculation of the excitonic fine structure of million-atom self-assembled $In_{1-x}Ga_xAs$/GaAs quantum dots. *Physical Review B* **67**, 161306 (2003). 68

[268] Seguin, R. *et al.* Size-dependent fine-structure splitting in self-organized InAs/GaAs quantum dots. *Physical Review Letters* **95**, 257402 (2005). 68

[269] Mollow, B. Power spectrum of light scattered by two-level systems. *Physical Review* **188** (1969). 69

[270] Dalibard, J. & Reynaud, S. Correlation signals in resonance fluorescence: interpretation via photon scattering amplitudes. *Journal de Physique* **44**, 1337–1343 (1983). 69

[271] Carreño, J. L., Casalengua, E. Z., Laussy, F. P. & del Valle, E. Joint subnatural-linewidth and single-photon emission from resonance fluorescence. *Quantum Science and Technology* **3**, 045001 (2018). 69

[272] Phillips, C. L. *et al.* Photon statistics of filtered resonance fluorescence. *Physical Review Letters* **125**, 043603 (2020). 69

[273] Flagg, E. B. *et al.* Resonantly driven coherent oscillations in a solid-state quantum emitter. *Nature Physics* **5**, 203–207 (2009). 70

[274] Seshan, K. *Handbook of thin film deposition techniques principles, methods, equipment and applications, second editon* (CRC Press, 2002). 71

[275] Harsha, K. S. *Principles of vapor deposition of thin films* (Elsevier, 2005). 71

[276] Ekinci, H. *Plasma and Reactive Ion Etching*. 73

[277] Posseme, N. *Plasma Etching Processes for CMOS Devices Realization* (Elsevier, 2017). 73

[278] Fowles, G. R. *Introduction to modern optics* (Courier Corporation, 1989). 74

[279] Androvitsaneas, P. *et al.* Direct-write projection lithography of quantum dot micropillar single photon sources. *Applied Physics Letters* **123** (2023). 81, 89

[280] Nieves, Y. & Muller, A. Third-order frequency-resolved photon correlations in resonance fluorescence. *Physical Review B* **98**, 165432 (2018). 90

[281] Nieves, Y. & Muller, A. Third-order photon cross-correlations in resonance fluorescence. *Physical Review B* **102**, 155418 (2020). 90

[282] Bounouar, S. *et al.* Path-controlled time reordering of paired photons in a dressed three-level cascade. *Physical Review Letters* **118**, 233601 (2017). 90

[283] Javadi, A. *et al.* Single-photon non-linear optics with a quantum dot in a waveguide. *Nature Communications* **6**, 8655 (2015). 90

[284] Snijders, H. *et al.* Purification of a single-photon nonlinearity. *Nature Communications* **7**, 12578 (2016). 90

[285] Chen, D., Lander, G. R., Solomon, G. S. & Flagg, E. B. Polarization-dependent interference of coherent scattering from orthogonal dipole moments of a resonantly excited quantum dot. *Physical Review Letters* **118**, 037401 (2017). 90

[286] Chunnilall, C. J., Degiovanni, I. P., Kück, S., Müller, I. & Sinclair, A. G. Metrology of single-photon sources and detectors: a review. *Optical Engineering* **53**, 081910 (2014). 91

[287] Cheung, J. *et al.* The quantum candela: a re-definition of the standard units for optical radiation. *Journal of Modern Optics* **54**, 373–396 (2007). 91, 93

[288] Sperling, A. & Kück, S. The SI unit candela. *Annalen der Physik* **531**, 1800305 (2019). 91, 93

[289] Zwinkels, J. C., Ikonen, E., Fox, N. P., Ulm, G. & Rastello, M. L. Photometry, radiometry and 'the candela': evolution in the classical and quantum world. *Metrologia* **47**, R15 (2010). 91

[290] Mises en-pratique for the SI base unit definitions (2019). URL https://www.bipm.org/en/publications/mises-en-pratique. 92, 93

[291] Fox, N. Radiometry with cryogenic radiometers and semiconductor photodiodes. *Metrologia* **32**, 535 (1995). 93

[292] Quinn, T. J. & Martin, J. A radiometric determination of the Stefan-Boltzmann constant and thermodynamic temperatures between -40 °C and+ 100 °C. *Philosophical Transactions of the Royal Society of London. Series A, Mathematical and Physical Sciences* **316**, 85–189 (1985). 93

[293] Chapter 8 - Single-photon detector calibration. In Migdall, A., Polyakov, S. V., Fan, J. & Bienfang, J. C. (eds.) *Single-Photon Generation and Detection*, vol. 45 of *Experimental Methods in the Physical Sciences*, 257–281 (Academic Press, 2013). 93

[294] Schmunk, W., Rodenberger, M., Peters, S., Hofer, H. & Kück, S. Radiometric calibration of single photon detectors by a single photon source based on NV-centers in diamond. *Journal of Modern Optics* **58**, 1252–1259 (2011). 93, 96, 97, 116

[295] Georgieva, H. *et al.* Absolute calibration of a single-photon avalanche detector using a bright triggered single-photon source based on an InGaAs quantum dot. *Optics Express* **29**, 23500–23507 (2021). 93, 96, 98, 109, 116

[296] Chu, X.-L., Götzinger, S. & Sandoghdar, V. A single molecule as a high-fidelity photon gun for producing intensity-squeezed light. *Nature Photonics* **11**, 58–62 (2017). 94

[297] Parr, A. C., Datla, R. & Gardner, J. *Experimental methods in the physical sciences: Optical radiometry*, vol. 41 (Elsevier, 2005). 94

[298] Porrovecchio, G. *et al.* Comparison at the sub-100 fW optical power level of calibrating a single-photon detector using a high-sensitive, low-noise silicon photodiode and the double attenuator technique. *Metrologia* **53**, 1115 (2016). 95

[299] Fox, N. Trap detectors and their properties. *Metrologia* **28**, 197 (1991). 94

[300] Mountford, J., Porrovecchio, G., Smid, M. & Smid, R. Development of a switched integrator amplifier for high-accuracy optical measurements. *Applied Optics* **47**, 5821–5828 (2008). 95, 106

[301] Theocharous, E. & Wareham, E. Ultra-high performance photodetection systems for radiometric applications. *Measurement Science and Technology* **15**, 1216 (2004). 95

[302] Cheung, J. Y., Chunnilall, C. J., Porrovecchio, G., Smid, M. & Theocharous, E. Low optical power reference detector implemented in the validation of two independent techniques for calibrating photon-counting detectors. *Optics Express* **19**, 20347–20363 (2011). 95

[303] Rodiek, B. *et al.* Experimental realization of an absolute single-photon source based on a single nitrogen vacancy center in a nanodiamond. *Optica* **4**, 71–76 (2017). 96

[304] Hong, K. S. *et al.* Towards the realization of single photon sources for radiometry applications at room temperature. *IEEE Transactions on Instrumentation and Measurement* (2023). 98

[305] JCGM. GUM 1995 with minor corrections. In BIPM *et al.* (eds.) *GUM 1995 with minor corrections*, vol. 100 of *Guide to the Expression of Uncertainty in Measurement* (JCGM, 2008). URL http://www.bipm.org/utils/common/documents/jcgm/JCGM_100_2008_E.pdf. 113

[306] Crowder, S., Delker, C., Forrest, E., Martin, N. *et al.* *Introduction to statistics in metrology* (Springer, 2020). 113

[307] Gardner, J. 6. Uncertainty estimates in radiometry. In *Experimental Methods in the physical sciences*, vol. 41, 291–325 (Elsevier, 2005). 114

APPENDIX A

HIGHER-ORDER PHOTON CORRELATIONS

A.1 Quantum optics and photon statistics

At the few-photon level a quantum mechanical description is required to classify the behaviour of some particular forms of light. This description can extend to classical fields, where the idea of beam intensity I can be reformulated as photon number, n, based on the quantum harmonic oscillator (QHO) model. A quantised electromagnetic field based on position and momentum operators $\hat{q}$, $\hat{p}$ is described by a one-dimensional Hamiltonian[221]

$$\hat{H} = \frac{1}{2}\left(\hat{p}^2 + \omega^2\hat{q}^2\right), \tag{A.1.1}$$

where ω is the angular frequency of the field, and $\hat{q}$, $\hat{p}$ obey the commutation relation $[\hat{q}, \hat{p}] = i\hbar$. We can define a pair of operators, $\hat{a}$ and $\hat{a}^\dagger$:

$$\hat{a} = \frac{1}{\sqrt{2\hbar\omega}}\left(\omega\hat{q} + i\hat{p}\right), \tag{A.1.2}$$

$$\hat{a}^\dagger = \frac{1}{\sqrt{2\hbar\omega}}\left(\omega\hat{q} - i\hat{p}\right), \tag{A.1.3}$$

From Equations A.1.2 and A.1.3 we can obtain the commutation relation $\left[\hat{a}, \hat{a}^\dagger\right] = 1$ and rewrite the Hamiltonian in Equation A.1.1 as

$$\hat{H} = \hbar\omega\left(\hat{a}^\dagger\hat{a} + \frac{1}{2}\right). \tag{A.1.4}$$

The commutation relations for $\hat{a}$, $\hat{a}^\dagger$ and $\hat{H}$ can also be calculated,

$$\left[\hat{H}, \hat{a}^\dagger\right] = \hbar\omega\hat{a}^\dagger \tag{A.1.5}$$

$$\left[\hat{H}, \hat{a}\right] = -\hbar\omega\hat{a} \tag{A.1.6}$$

For some wavefunction ψ_n, the time-independent Schrödinger equation satisfies $\hat{H}\psi_n = E_n\psi_n$, where ψ_n is an eigenfunction of the Hamiltonian with some eigenvalue E_n. Consider operating on the wavefunction with a new operator, $\hat{H}\hat{a}^\dagger$:

$$\left(\hat{H}\hat{a}^\dagger\right)\psi_n = \left(\hat{H}\hat{a}^\dagger - \hat{a}^\dagger\hat{H} + \hat{a}^\dagger\hat{H}\right)\psi_n, \tag{A.1.7}$$

$$\implies \left(\left[\hat{H}, \hat{a}^\dagger\right] + \hat{a}^\dagger\hat{H}\right)\psi_n = \left(\hbar\omega\hat{a}^\dagger + \hat{a}^\dagger\hat{H}\right)\psi_n, \tag{A.1.8}$$

$$\hat{H}\psi_n = E_n\psi_n \implies \left(\hat{H}\hat{a}^\dagger\right)\psi_n = \left(\hbar\omega\hat{a}^\dagger + \hat{a}^\dagger E_n\right)\psi_n = \left(\hbar\omega + E_n\right)\hat{a}^\dagger\psi_n. \tag{A.1.9}$$

From Equation A.1.9 - if ψ_n is an eigenfunction of the Hamiltonian, then $\hat{a}^\dagger\psi_n$ is an eigenfunction with eigenvalue $E_n + \hbar\omega$. Similarly, it is possible to show that

$$\left(\hat{H}\hat{a}\right) = \left(E_n - \hbar\omega\right)\hat{a}\psi_n \tag{A.1.10}$$

such that $\hat{a}\psi_n$ is an eigenfunction with eigenvalue $E_n - \hbar\omega$. With this, we have defined a ladder of energy levels, where $\hat{a}^\dagger$ is a raising operator, and $\hat{a}$ is a lowering operator. It

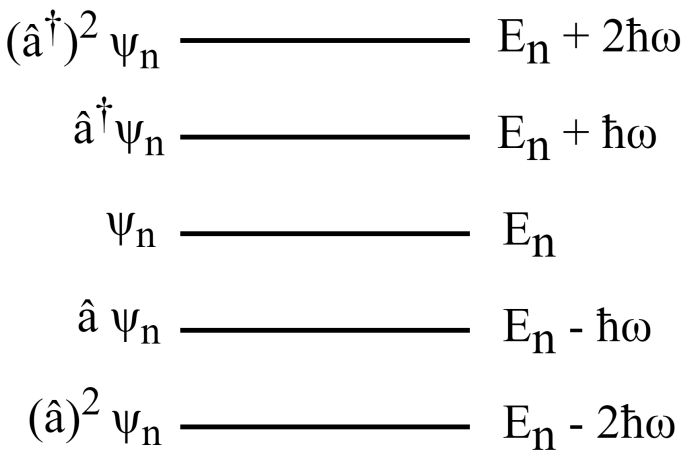

Figure A.1.1: A schematic of the 'ladder' of energy levels centred on E_n, where $\hat{a}^\dagger$ is the raising operator that adds $\hbar\omega$, and $\hat{a}$ is the lowering operator that subtracts $\hbar\omega$.

is possible to obtain the 'bottom rung' of this energy ladder by assuming that $\hat{a}\psi_0 = 0$,

i.e. the lowering operator returns zero when trying to move beyond the ladder.

$$\hat{H}\psi_0 = \hbar\omega\left(\hat{a}^\dagger\hat{a} + \frac{1}{2}\right)\psi_0, \tag{A.1.11}$$

$$\implies \hat{H}\psi_0 = \hbar\omega\hat{a}^\dagger\left(\hat{a}\psi_0\right) + \frac{1}{2}\hbar\omega\psi_0 = 0 + \frac{1}{2}\hbar\omega\psi_0, \tag{A.1.12}$$

$$\hat{H}\psi_0 = E_0\psi_0 \implies E_0 = \frac{1}{2}\hbar\omega. \tag{A.1.13}$$

E_0 is the *zero-point energy* of the harmonic oscillator. If we apply the raising operator we can find the n^{th} energy level defined by E_n:

$$E_n = E_0 + n\hbar\omega = \left(n + \frac{1}{2}\right)\hbar\omega. \tag{A.1.14}$$

From this expression we can define the number operator, $\hat{n}$, which gives the number of excited energy quanta according to $\hat{n}\psi_n = n\psi_n$:

$$\hat{H}\psi_n = \hbar\omega\left(\hat{a}^\dagger\hat{a} + \frac{1}{2}\right)\psi_n = \left(n + \frac{1}{2}\right)\hbar\omega\psi_n, \tag{A.1.15}$$

$$\implies \hat{n} = \hat{a}^\dagger\hat{a}. \tag{A.1.16}$$

The set of number states $\{n\}$ are all eigenstates of the Hamiltonian and form an orthonormal basis $\langle n|n'\rangle = \delta_{n,n'}$. We can redefine the raising and lowering operators in terms of energy quanta $\hbar\omega$:

$$\hat{a}^\dagger|n\rangle = (n+1)^{\frac{1}{2}}|n+1\rangle, \tag{A.1.17}$$

$$\hat{a}|n\rangle = n^{\frac{1}{2}}|n-1\rangle. \tag{A.1.18}$$

also known as the *creation* and *destruction* operators, respectively.

A.2 The timestamping script

```
%% Timestamping code
% g3 integration
% Clark Nov to Jan 2020

clear all;
tic

%% Read in files
%  Define filename root
```

```
fileName = '20230322_925p127nm_64nWg2';

% Build input and output filenames
fileName1 = sprintf('%s_C1.bin',fileName);
fileName2 = sprintf('%s_C2.bin',fileName);
fileName3 = sprintf('%s_C3.bin',fileName);
% File operations begin here
% Set foutName if you wish to write the diagonal histogram to csv
foutName = sprintf('%s_C1C2C3.csv',fileName);
woutName = sprintf('%s_C1C2C3.mat',fileName);
[fid1,fid2,fid3,file1,file2,file3] = ...
    read_3file(fileName1,fileName2,fileName3);

% Hist settings
t_max = 1e5;  %time in ps for search window
d_bin = 100;  %the counter box resolution - IDQ has 100 for high speed
bin_size = d_bin; %hist bin size must be multiple of counter box res
t_offset = 0; %if data is offset remember to subtract in calculation loop
bins = round((2*t_max)/bin_size);
histrange = -t_max:bin_size:t_max;

% Count arrays
N1 = zeros(1,length(histrange)-1);
N2 = zeros(1,length(histrange)-1);
N3 = zeros(length(histrange)-1,length(histrange)-1);
% Set up plots
[C,h] = contourf(histrange(1:length(N3)),histrange(1:length(N3)),N3);
set(h,'LineStyle','none')

% Initialise arrays
% Specify chunk length to read in to workspace from file
% 5e4 recommended
chunk_factor = 5e4;
% Initialise arrays
chunk1 = (file1(2)/chunk_factor);
chunk2 = (file2(2)/chunk_factor);
chunk3 = (file3(2)/chunk_factor);
precision = 'uint64';                %ID900 datatype
chunk_plot = chunk_factor*1e2;
```

```
co_exp = zeros(chunk_factor,1);
t_int = zeros(chunk_factor,1);
t1_int = zeros(chunk_factor,1);
t2_int = zeros(chunk_factor,1);
t3_int = zeros(chunk_factor,1);
chunkrate1 = zeros(chunk_factor,1);
chunkrate2 = zeros(chunk_factor,1);
chunkrate3 = zeros(chunk_factor,1);
chunk1_dt = zeros(chunk_factor,1);
chunk2_dt = zeros(chunk_factor,1);
chunk3_dt = zeros(chunk_factor,1);

%% Main loop
for i1 = 1:chunk_factor
    % Read in chunks of each file
    d_array1 = fread(fid1,chunk1,'uint64');
    d_array2 = fread(fid2,chunk2,'uint64');
    d_array3 = fread(fid3,chunk3,'uint64');
    %% Find correlations
    % Cut down channel 1 by removing first and last t_max events
    st = min(d_array1) + t_max;
    fin = max(d_array1) - t_max;
    indices = find(d_array1>st & d_array1<fin);
    ind = length(indices);
    % Initialise arrays
    dt12_array = NaN(ind,200);
    dt13_array = NaN(ind,200);
    dt_pair = NaN(ind*100,2);
    % Chunk metrics for tracking experiment
    % Average chunk end time
    t_int(i1) = (d_array1(end)+d_array2(end)+d_array3(end))/3;
    t1_int(i1) = (d_array1(end));
    t2_int(i1) = (d_array2(end));
    t3_int(i1) = (d_array3(end));
    % Average chunk time
    chunk1_dt(i1) = d_array1(end)-d_array1(1);
    chunk2_dt(i1) = d_array2(end)-d_array2(1);
    chunk3_dt(i1) = d_array3(end)-d_array3(1);
    % Average chunk rate
```

```
88      chunkrate1(i1) = chunk1/chunk1_dt(i1);
89      chunkrate2(i1) = chunk2/chunk2_dt(i1);
90      chunkrate3(i1) = chunk3/chunk3_dt(i1);
91
92      i123 = 0;
93      for i2 = 1:ind
94          here = indices(i2); % Find index value of this iteration
95          now = d_array1(here); % Find time value of this index
96          hi = now + t_max; % Set upper bound
97          lo = now - t_max; % Set lower bound
98          % Search in next channel using find
99          match2 = find(d_array2<hi & d_array2>lo);
100         if isempty(match2) == false
101             dt12 = d_array2(match2) - now;
102             dt12_array(i2,1:length(dt12)) = dt12;
103         end
104         match3 = find(d_array3<hi & d_array3>lo);
105         if isempty(match3) == false
106             dt13 = d_array3(match3) - now;
107             dt13_array(i2,1:length(dt13)) = dt13;
108         end
109
110         % Find combinations of pairs across channels
111         row12 = dt12_array(i2,:);
112         row12_t = row12(~isnan(row12));
113         i3 = length(row12_t);
114         row13 = dt13_array(i2,:);
115         row13_t = row13(~isnan(row13));
116         i4 = length(row13_t);
117         row123 = i3*i4;
118
119         for i12 = 1:i3
120             for i13 = 1:i4
121                 i123 = i123+1;
122                 dt_pair(i123,1) = dt12_array(i2,i12);
123                 dt_pair(i123,2) = dt13_array(i2,i13);
124             end
125         end
126     end
```

```
127
128     % Count data
129     % Create histogram of pairs file
130     % this command is a bottleneck on program speed
131     % non linear with 'edges' size
132     [n1, histrange_new] = histcounts(dt12_array,histrange);
133     N1 = N1+n1;
134     [n2,histrange_new] = histcounts(dt13_array,histrange);
135     N2 = N2+n2;
136     [n3,histrange_new,histrange_new] = ...
137         histcounts2(dt_pair(:,1),dt_pair(:,2),histrange,histrange);
138     % Combine count pairs for 2D hist
139     for i3 = 1:length(histrange)-1      % Column iterator
140         for i4 = 1:length(histrange)-1  % Row iterator
141             N3(i4,i3) = N3(i4,i3)+n3(i4,i3);
142         end
143     end
144
145     %% Update plot
146     i3 = mod(i1,round(chunk_plot/chunk_factor));
147     if i3==0 % Only update plot every chunk_plot_size iterations
148         h2.ZDataSource = 'N3';
149         refreshdata;
150         shg;
151     end
152
153     % If one of the channels is empty, break main loop to avoid error
154     T2 = isempty(d_array2);
155     T3 = isempty(d_array3);
156     if T2 == 1 | T3 == 1
157         break
158     % Otherwise, move the pointer according to the timestamp gradient
159     elseif T2 == 0 || T3 == 0
160         % Gradient of fid2_file_pos at end of this chunk/channel2(time)
161         grad2 = ftell(fid2)/max(d_array2);
162         % Each timestamp has 8 bytes so find time to nearest 8 units
163         new_posn_2 = 8*round(max(d_array1)*grad2/8);
164         % Move file current position to new_posn
165         fseek(fid2,new_posn_2,'bof');
```

```
166         grad3=ftell(fid3)/max(d_array3);
167         new_posn_3=8*round(max(d_array1)*grad3/8);
168         fseek(fid3,new_posn_3,'bof');
169     end
170 end
171
172 counts = diag(flip(N3));
173 histrange_crop = histrange+bin_size;
174 histrange_crop = histrange_crop(1:(length(counts)));
175 file_out(1:length(histrange_crop),1) = histrange_crop;
176 file_out(1:length(counts),2) = counts;
177 file_out(1:length(counts),3) = sqrt(counts);
178 writematrix(file_out,foutName);
179
180 save(woutName);
181
182 fclose('all');
183 toc
```

APPENDIX B

SOLVING THE TDSE WITH PERTURBATION THEORY

Following the treatment in Fox[223] and Loudon,[221] the transition rate between the two energy levels, $W_{1\to2}$, is given by Fermi's Golden Rule:

$$W_{1\to2} = \frac{2\pi}{\hbar} |M_{12}|^2 \, g(\hbar\omega), \tag{B.0.1}$$

where M_{12} is the *matrix element* for the transition and $g(\hbar\omega)$ is the *density of states* of the transition's final state. The matrix element describes the overlap of the initial and final states with respect to the incoming light perturbation

$$M_{12} = \langle 2| \hat{\mathrm{V}} |1\rangle, \tag{B.0.2}$$

where the incoming perturbation $\hat{\mathrm{V}}$ can be modelled as the field-dipole interaction

$$\hat{\mathrm{V}}(t) = e\underline{\mathbf{r}} \cdot \underline{\boldsymbol{\varepsilon}}(t). \tag{B.0.3}$$

We can rewrite the matrix element more succinctly with the *electric dipole moment* μ_{12} which considers the dipole moment over all $\underline{\mathbf{r}}$:

$$M_{12} = -\underline{\boldsymbol{\mu}}_{12} \cdot \underline{\boldsymbol{\varepsilon}}_0. \tag{B.0.4}$$

The density of states for the final state of a transition depends on the physical system, but for some incoming light field at frequency ω in free space, it depends on the mode volume V_0:

$$g(\omega) = \frac{\omega^2 V_0}{\pi^2 c^3}. \tag{B.0.5}$$

The Hamiltonian can be split into a time-independent term H_0 that describes the two-level system with no light interaction, and a perturbation time-dependent term describing the incoming light.

$$\hat{\mathrm{H}} = \hat{\mathrm{H}}_0 (\underline{\mathbf{r}}) + \hat{\mathrm{V}} (t) . \tag{B.0.6}$$

The unperturbed system will have two solutions, one for each level, $i = 1, 2$.

$$\hat{\mathrm{H}} = \hat{\mathrm{H}}_0 (\underline{\mathbf{r}}) + \hat{\mathrm{V}} (t) ,$$
$$\hat{\mathrm{H}}_0 \Psi_{\mathrm{i}} = i\hbar \frac{\partial \Psi_{\mathrm{i}}}{\partial \mathrm{t}}.$$

The wavefunction can be written as the product of a spatially-dependent and time-dependent function

$$\Psi_{\mathrm{i}} (\underline{\mathbf{r}}, t) = \psi_i (\underline{\mathbf{r}}) \, e^{\frac{-iE_i t}{\hbar}}, \tag{B.0.7}$$

where $\psi_i (\underline{\mathbf{r}})$ is an eigenfunction of the time-independent Hamiltonian term, such that

$$\hat{\mathrm{H}}_0 \psi_i (\underline{\mathbf{r}}) = E_i \psi_i (\underline{\mathbf{r}}) . \tag{B.0.8}$$

The general solution to the TDSE for a two-level system e.g. one with two eigenstates is given by Equation B.0.9:

$$\Psi (\underline{\mathbf{r}}, t) = c_1 (t) \, \psi_1 (\underline{\mathbf{r}}) \, e^{\frac{-iE_1 t}{\hbar}} + c_2 (t) \, \psi_2 (\underline{\mathbf{r}}) \, e^{\frac{-iE_2 t}{\hbar}} . \tag{B.0.9}$$

Now, substituting Equation B.0.9 into the TDSE:

$$\left[\hat{\mathrm{H}}_0 (\underline{\mathbf{r}}) + \hat{\mathrm{V}} (t)\right] \Psi (\underline{\mathbf{r}}, t) = i\hbar \left[\dot{c}_1 (t) - \frac{iE_1}{\hbar}\right] e^{\frac{-iE_1 t}{\hbar}} \psi_1 (\underline{\mathbf{r}}) + i\hbar \left[\dot{c}_2 (t) - \frac{iE_2}{\hbar}\right] e^{\frac{-iE_2 t}{\hbar}} \psi_2 (\underline{\mathbf{r}}) . \tag{B.0.10}$$

Equation B.0.8 gives us the expression

$$\mathrm{H}_0 \Psi (\underline{\mathbf{r}}, t) = E_1 \psi_1 e^{\frac{-iE_1 t}{\hbar}} + E_2 \psi_2 e^{\frac{-iE_2 t}{\hbar}} . \tag{B.0.11}$$

By substituting B.0.11 into Equation B.0.10 and collecting terms to cancel, we arrive at Equation B.0.12

$$\hat{\mathrm{V}} (t) \, \Psi (\underline{\mathbf{r}}, t) = i\hbar \left[\dot{c}_1 (t) \, \psi_1 (\underline{\mathbf{r}}) \, e^{\frac{-iE_1 t}{\hbar}} + \dot{c}_2 (t) \, \psi_2 (\underline{\mathbf{r}}) \, e^{-\frac{iE_2 t}{\hbar}}\right] . \tag{B.0.12}$$

We recall from Equation B.0.2 that we can describe the interaction of the perturbation with the overlap integral between the two states as a matrix element, $\langle \psi_i | \, \hat{\mathrm{V}} \, | \psi_j \rangle = M_{ij}$. Furthermore - for eigenstates ψ_i, ψ_j that form an orthonormal basis, $\langle \psi_i | \psi_j \rangle = \delta_{ij}$ where δ_{ij} here is the Kronecker-delta function. Applying $\langle \psi_1 |$ to both sides of Equation B.0.12,

we obtain:

$$\text{LHS} : \langle\psi_1| c_1(t) e^{\frac{-iE_1 t}{\hbar}} |\psi_1\rangle + \langle\psi_1| c_2(t) e^{\frac{-iE_2 t}{\hbar}} |\psi_2\rangle = c_1(t) \mathrm{V}_{11} e^{-\frac{iE_1 t}{\hbar}} + c_2(t) \mathrm{V}_{12} e^{-\frac{iE_2 t}{\hbar}}, \quad \text{(B.0.13)}$$

$$\text{RHS} : i\hbar \left[\langle\psi_1| \dot{c}_1(t) e^{\frac{-iE_1 t}{\hbar}} |\psi_1\rangle + \langle\psi_1| \dot{c}_2(t) e^{\frac{-iE_2 t}{\hbar}} |\psi_2\rangle \right] = i\hbar \dot{c}_1(t) e^{\frac{-iE_1 t}{\hbar}}, \quad \text{(B.0.14)}$$

$$\implies \dot{c}_1(t) = \frac{-i}{\hbar} \left[c_1(t) \mathrm{V}_{11} + c_2(t) \mathrm{V}_{12} e^{\frac{-i(E_2 - E_1)t}{\hbar}} \right] = \frac{-i}{\hbar} \left[c_1(t) \mathrm{V}_{11} + c_2(t) \mathrm{V}_{12} e^{-i\omega_0 t} \right]. \quad \text{(B.0.15)}$$

Similarly applying $\langle\psi_2|$ to both sides of Equation B.0.12, we obtain:

$$\dot{c}_2(t) = \frac{-i}{\hbar} \left[c_1(t) \mathrm{V}_{21} e^{-i\omega_0 t} + c_2(t) \mathrm{V}_{22} \right]. \quad \text{(B.0.16)}$$

We can insert the explicit form of the light perturbation $\mathrm{V}(t)$ as given in Equation B.0.3 and choose the incoming polarisation to lie along the x-axis:

$$\underline{\boldsymbol{\varepsilon}}(t) = \begin{pmatrix} \varepsilon_0 \\ 0 \\ 0 \end{pmatrix} \cos(\omega t), \quad \text{(B.0.17)}$$

such that the perturbation becomes:

$$\hat{\mathrm{V}}(t) = ex\varepsilon_0 \cos(\omega t) = \frac{ex\varepsilon_0}{2} \left(e^{i\omega t} + e^{-i\omega t} \right), \quad \text{(B.0.18)}$$

and therefore the matrix elements V_{ij} simplify to:

$$\mathrm{V}_{ij}(t) = \frac{e\varepsilon_0}{2} \left(e^{i\omega t} + e^{i-\omega t} \right) \langle\psi_i|\psi_j\rangle. \quad \text{(B.0.19)}$$

Comparing with the matrix element from Fermi's Golden rule M_{12} in Equation B.0.4 and define the *dipole matrix element*:

$$\mathrm{V}_{ij}(t) = \frac{e\varepsilon_0}{2} \left(e^{i\omega t} + e^{i-\omega t} \right) \underline{\mu}_{ij}, \quad \text{(B.0.20)}$$

where

$$\underline{\mu}_{12} = \begin{pmatrix} \mu_{11} & \mu_{12} \\ \mu_{21} & \mu_{22} \end{pmatrix}. \quad \text{(B.0.21)}$$

The dipole matrix element $\underline{\mu}_{12}$ is a real measurable quantity, therefore $\mu_{21} = \mu_{12}$; the position operator $\hat{x}$ is odd, and the Hamiltonian based on the perturbing function given

in Equation B.0.19 is odd, meaning that the odd diagonal matrix elements $\mu_{11} = \mu_{22} = 0$. Now, inserting Equation B.0.20 into Equations B.0.15 and B.0.16, we obtain:

$$\dot{c_1}(t) = \frac{i\varepsilon_0\mu_{12}}{2\hbar}\left(e^{i(\omega-\omega_0)} + e^{-i(\omega+\omega_0)}\right)c_2(t), \tag{B.0.22}$$

$$\dot{c_2}(t) = \frac{i\varepsilon_0\mu_{12}}{2\hbar}\left(e^{-i(\omega-\omega_0)} + e^{i(\omega+\omega_0)}\right)c_1(t). \tag{B.0.23}$$

Here, we define the *Rabi frequency*, Ω:

$$\Omega = \left|\frac{\mu_{12}\varepsilon_0}{\hbar}\right|. \tag{B.0.24}$$

APPENDIX C

COMBINED UNCERTAINTY CALCULATIONS

The dead time-corrected detection efficiency η is given by:

$$\eta = \frac{N_{\text{det}}}{N_{\text{in}}\left(1 - N_{\text{det}} \cdot \tau_d\right)}, \tag{C.0.1}$$

and its combined uncertainty σ_η is given by:

$$\sigma_\eta = \sqrt{\left(\frac{\partial \eta}{\partial N_{\text{in}}}\sigma_{N_{\text{in}}}\right)^2 + \left(\frac{\partial \eta}{\partial N_{\text{det}}}\sigma_{N_{\text{det}}}\right)^2 + \left(\frac{\partial \eta}{\partial \tau_d}\sigma_{\tau_d}\right)^2}. \tag{C.0.2}$$

The expressions for each of the partial derivatives are:

$$\frac{\partial \eta}{\partial \tau_d} = \frac{N_{\text{det}}^2}{N_{\text{in}}} \cdot \left(\frac{1}{1 - N_{\text{det}}\tau_d}\right)^2, \tag{C.0.3}$$

$$\frac{\partial \eta}{\partial N_{\text{in}}} = -\frac{1}{N_{\text{in}}^2}\frac{N_{\text{det}}}{(1 - N_{\text{det}}\tau_d)}, \tag{C.0.4}$$

$$\frac{\partial \eta}{\partial N_{\text{det}}} = \frac{1}{N_{\text{in}}} \cdot \frac{1}{(1 - N_{\text{det}}\tau_d)} + \frac{N_{\text{det}^2}}{N_{\text{in}}} \cdot \frac{1}{(1 - N_{\text{det}}\tau_d)^2}. \tag{C.0.5}$$

The error on the dead time, σ_{τ_d}, is negligible due to the relative contribution from the electronics jitter compared to the fluctuating count rates. The error on the detected rate is given by the Poissonian counting error on the number of detection clicks, and the error on the incident counts $\sigma_{N_{\text{in}}}$ is given by

$$\sigma_{N_{\text{in}}} = N_{\text{in}}\sqrt{\left(\frac{\sigma_P}{P}\right)^2 + \left(\frac{\sigma_\lambda}{\lambda}\right)^2}, \tag{C.0.6}$$

where the error on the power measurement is calculated by the propagating the errors on the relevant variables for each detector, in accordance with Equation C.0.7

$$\sigma_P = \sqrt{\left(\frac{\partial}{\partial V}P\right)^2 \sigma_V^2 + \left(\frac{\partial}{\partial R}P\right)^2 \sigma_R^2 + \left(\frac{\partial}{\partial G}P\right)^2 \sigma_G^2 + \left(\frac{\partial}{\partial C}P\right)^2 \sigma_C^2}, \tag{C.0.7}$$

where $\sigma_{V,R,G,C}$ is the error on, and $\partial P/\partial V, R, G, C$ the partial derivative of P with respect to, the voltage, responsivity, gain and correction factor respectively.